Cubic GaN on Pre-Patterned 3C-SiC/Si (001) Substrates

Dem Department Physik
der Universität Paderborn
zur Erlangung des akademischen Grades eines
Doktors der Naturwissenschaft
vorgelegte

Dissertation

von

Ricarda Maria Kemper

Paderborn, April 2014

Parts of this work have already been published in journals, conference proceedings and a book chapter. The publications are listed on page 153.

Content

Abstract

The influence of growth area reduction towards length scales predicted to be effective for defect reduction by the theory of nanoheteroepitaxy is analyzed. This is studied in detail for the first time in the system of meta-stable cubic GaN (c-GaN) grown by plasma-assisted molecular beam epitaxy on pre-patterned 3C-SiC/Si (001) substrates. It is demonstrated that regardless of the pattern symmetry or size, the cubic phase of GaN nucleates on top of all investigated mesa structures. Electron beam lithography followed by a lift-off and a reactive ion etching process is used for tailoring post-shaped SiC structures. A successful reduction of the {111} stacking fault (SF) density is achieved by reducing the (001) top edge length of the posts from ~500 nm down to ~20 nm. Transmission electron microscopy reveals a nucleation of phase-pure and almost defect-free c-GaN on top of the smallest SiC nanostructures as predicted by theoretical calculations.

The growth of c-GaN on pre-patterned and planar 3C-SiC/Si substrates is also governed by anti-phase domains of the substrate. Two different domains in the c-GaN growing with different densities of planar defects and amounts of hexagonal inclusions have been identified. Furthermore, it is quantified that {111} SFs lower not only the cubic crystal quality but also reduce the cathodoluminescence emission intensity.

The studies presented in this work aim to give more insight into the basic growth mechanisms of c-GaN on pre-patterned 3C-SiC/Si (001).

1 Introduction

Wide band-gap materials, especially group III-nitrides like GaN, AlN, and InN have a great potential for optoelectronic and electronic device applications like laser diodes and transistors [1-3]. Up to date there is a huge interest in nitride technologies to fabricate low dislocation density up to dislocation free epilayers for high-quality GaN-based devices.

Devices show best performance if fabricated on lattice-matched substrates since lattice-mismatch leads to the generation of strain and therefore misfit dislocations at the interface which may cause scattering of charge carriers, reduced carrier mobility, non-radiative recombination in optical devices and device heating. However, the choice of suitable substrate materials is limited and thus additional techniques have to be developed to overcome persistent mismatch issues.

One method for the elimination of misfit dislocations is the reduction of the growth area [4]. Defect reduction in mismatched systems was also demonstrated by the theory of nanoheteroepitaxy (NHE), which describes the selective growth on a nano-patterned (10-100 nm) substrate [5]. In contrast to planar heteroepitaxy, the idea of NHE includes a partitioning of strain between the epilayer and the substrate and a distribution of the mismatch strain in the epilayer in three dimensions. NHE offers the possibility of growing dislocation free epilayers on non-lattice-matched nano-patterned substrates.

So far the most frequently used material among all group-III nitrides is the thermodynamically stable hexagonal polytype of GaN. In hexagonal GaN, due to the crystal symmetry, inherent spontaneous and piezoelectric polarization fields are present along the c-axis, which can be detrimental to device characteristics [6,7]. Therefore, non-polar and semi-polar systems have attracted growing interest in the last years [8]. One method to produce real non-polar materials is the growth of cubic GaN (c-GaN). Although the hexagonal polytype is the thermodynamically favorable phase, it has been shown that there is a narrow window of experimental conditions to achieve the heteroepitaxial growth of c-GaN [9]. As low defect density bulk GaN substrates [10], on which one might grow lattice matched GaN epilayers, are not available, the most adequate substrate is cubic silicon carbide 3C-SiC (001) exhibiting a lattice misfit of -3.25%. The dislocation density [11] of c-GaN deposited on 3C-SiC (001) by plasma assisted molecular beam epitaxy (MBE) is ~ $(10^{9}\text{-}10^{11})$ cm^{-2}, which is in the order of magnitude of what has been achieved in hexagonal GaN epitaxy a few years ago. First field effect transistors [3] and infrared detectors [12] based on c-GaN have been successfully realized. However, a reduction of the dislocation density is a basic step towards the fabrication of high performance devices.

In this work, improved c-GaN growth on 3C-SiC/Si (001) by using pre-patterned substrates is described. For this purpose the theory of NHE is introduced before the experimental methods and results are described. The growth of c-GaN by MBE on patterned 3C-SiC/Si (001) substrates is demonstrated. Nano-patterning of 3C-SiC/Si (001) is either achieved using self-organized colloidal masks or electron beam lithography. Both processes are followed by a lift-off and a reactive ion etching process. Then the c-GaN grown on planar [13] and pre-patterned [14] 3C-SiC substrates is analyzed. It is shown that c-GaN grown on pre-patterned and unstructured 3C-SiC/Si (001) by MBE forms two types of structural domains which are induced by the substrate. The preferential formation of stacking faults (SFs) and hexagonal inclusions in one type of these domains is proven by independent measurement techniques. The main planar defect type in c-GaN, the {111} SFs, lowers the structural quality and reduces the luminesence intensity in c-GaN layers and in c-GaN/AlN multi-quantum wells (MQWs), which is determined by correlated scanning transmission electron microscopy (STEM) and cathodoluminescence (CL) measurements. A reduction of the SF density with increasing film thickness resulting in an increased CL emission intensity towards the film surface is shown in section 7.2.

Finally, the realization of c-GaN films [15] and a c-AlN/GaN MQW layer film [16] on sub-micrometer post-shaped 3C-SiC structures is demonstrated. The final section of this thesis describes the influence of growth area reduction down to ~20 nm on c-GaN. High-resolution transmission electron microscopy (TEM) images show the possibility of growing almost defect-free and phase-pure c-GaN on these smallest nanostructures.

These studies may help to improve the structural quality of upcoming electrical and optoelectronical devices and enable to develop fabrication technologies towards nano-scaled devices based on c-GaN grown on 3C-SiC (001).

2 Fundamentals

This chapter gives an introduction into the fundamentals and the physical properties of cubic group III-nitrides. Subsequently, the growth process and the growth parameter of planar c-GaN films are discussed. This subsection is the basis for the growth of c-GaN and c-AlN/GaN MQWs on pre-patterned substrates. The occurrent defects in c-GaN epilayers are described in an extra subsection. Finally, the theory of nanoheteroepitaxial growth in general and especially for c-GaN grown on 3C-SiC is introduced.

2.1 Properties of Cubic III-Nitrides

Group III-nitrides can crystallize in different polytypes. The most common is the naturally occurring hexagonal wurtzite polytype. Further, there exists the meta-stable cubic phase, which crystallizes in the zinc blende crystal structure. Figure 2.1 shows a schematic drawing of the zinc blende crystal structure with the lattice parameter a in the case of c-GaN, which is based on a face-centred cubic (fcc) unit cell with a base of two atoms. In general, the metal (Ga, dark grey) is incorporated on the origin (0,0,0), and the nitrogen (N, light grey) is placed on the (¼,¼,¼) lattice site. The structure can be described as two interpenetrating fcc sublattices, which are shifted by ¼ of the lattice cell diagonal with respect to each other. Each atom is covalently bonded to four neighboring atoms. For a better understanding the zinc blende structure of c-GaN is schematically shown in Fig. 2.2 with (a) the crystal structure with the (111) and (110) plane marked in dashed lines, (b) the principle directions in the cubic crystal structure, (c) different <111> directions and (d) the view along the [110] direction. The stacking sequence in [001] and [110] directions are *ABABAB* and the stacking sequence of the {111} planes is *ABCABC*, which is the closed-packed arrangement of atoms.

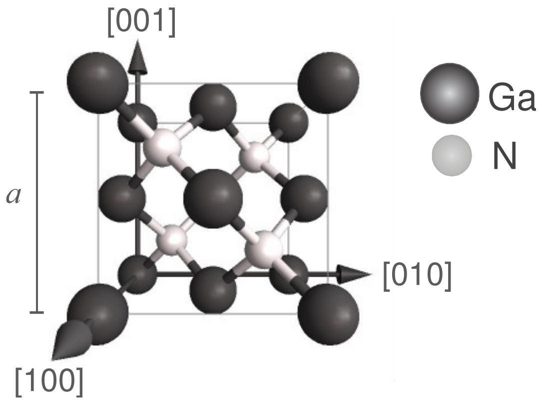

Figure 2.1

Zinc blende crystal structure of c-GaN (simulated by JEMS version 3.6907U2011 [17]).

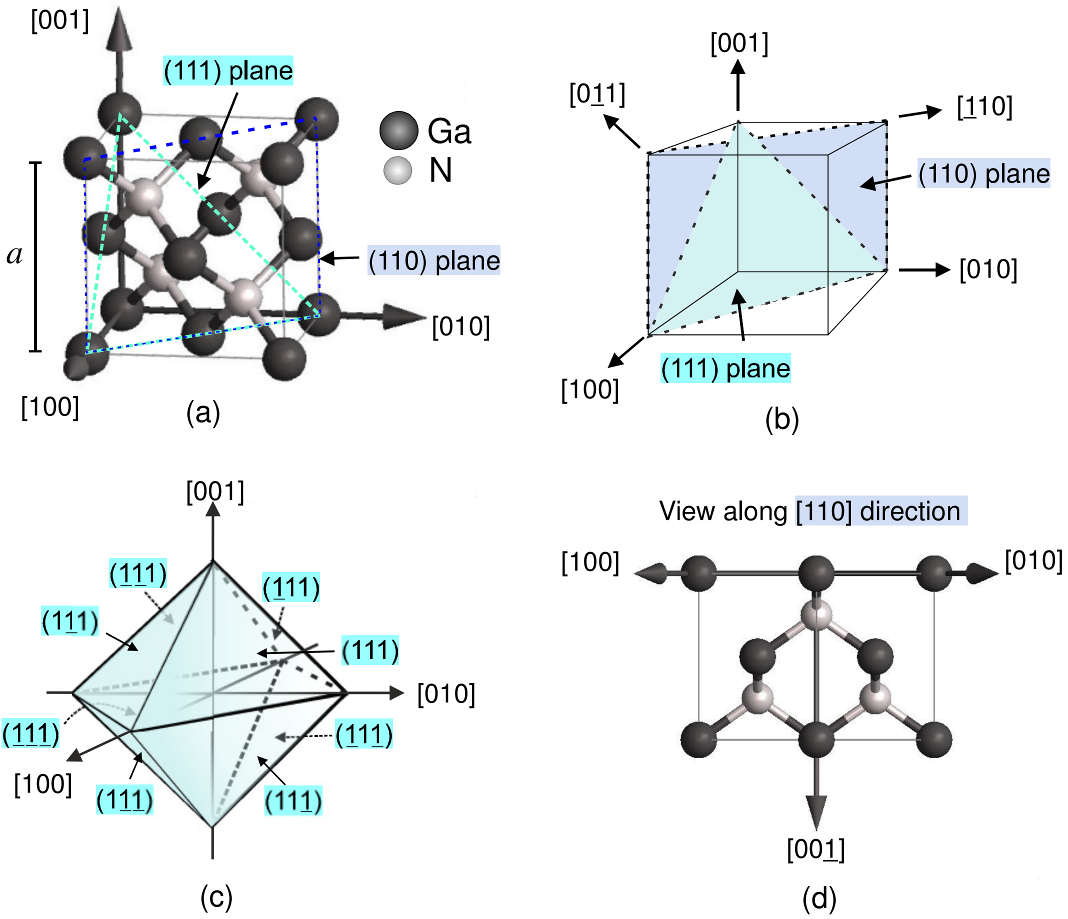

Figure 2.2

(a) Zinc blende crystal structure of c-GaN with lattice parameter *a* and [001] growth direction with the (111) and (110) plane shown in dashed lines, **(b)** the cardinal directions in the cubic crystal structure (after [18]), **(c)** different {111} planes and **(d)** view along the [110] direction.

It has to be mentioned that the (111) plane in the cubic structure is equivalent to the (0001) basal plane of the hexagonal phase. This relation will be become important in chapter 7.

The zinc blende crystal structure, similarly to the diamond structure (e.g. Si, Ge), exhibits strong covalent bonds, but consists of two types of atoms A and B. Both crystal structures are characterized by a high chemical inertness and thermodynamic stability. Due to the symmetrical crystal structure no spontaneous piezoelectric polarization fields along the [001] direction are present. These properties are important advantages for optoelectronic and electronic devices based on the cubic phase of group III-nitrides. The values of the lattice constant and the bandgap of c-GaN and c-AlN are summarized in Table 2.1.

Properties	Cubic GaN	Cubic AlN
Lattice constant [Å]	4.503 [19]	4.37 [21]
Bandgap [eV]	3.2 (direct) [19], [20]	5.93 (direct) [22] 5.3 (indirect) [22]

Table 2.1 Properties of c-GaN and c-AlN at room temperature [19-22].

2.2 Properties of 3C-SiC

Silicon Carbide (SiC) can exist in about 250 polytypes [23], which structurally only differ in the stacking sequence of the hexagonal bilayers of Si and C atoms. The bond length between the Si and the C atom is ~1.889 Å. In all polytypes the atoms are tetrahedrally and covalently bonded with the coordination number 4. The cubic polytype is referred to as 3C-SiC. Here the Ramsdell notation [24] is used, where the 3 indicates the periodicity of the stacking sequence and the C indicates a cubic (zinc blende) crystal structure. SiC is an indirect semiconductor with a bandgap of 2.39 eV and a room temperature lattice constant of 4.359 Å for the 3C-SiC polytype (see Table 2.2). It is also characterized by a high chemical inertness and thermodynamic stability. On the other hand the high chemical inertness makes it difficult to pattern/modify the surface, e.g. 3C-SiC is chemically inert to alkalis and acids. Therefore dry etching methods like reactive ion etching processes are established for e.g. the patterning of the 3C-SiC surface.

Properties	3C-SiC
Lattice constant [Å]	4.359 [25]
Bandgap [eV]	2.36 (indirect) [26] 6.0 (direct) [26]

Table 2.2 Properties of 3C-SiC at room temperature [25], [26].

Inversion Domain Boundaries in 3C-SiC

One possibility to produce 3C-SiC (001) bulk-like substrates is the growth of SiC on Si (001) substrates by low-pressure chemical vapor deposition [27]. In this case, it should be noted that the Si (001) surface exhibits domain terraces with Si dimers on the surface which are orientated along the [110] or the [$\underline{1}$10] direction [28]. These terraces are separated by monatomic steps with a height of *a*/4. In literature it is shown that the presence of these monatomic steps leads to inversion domain boundaries (IDBs), in the

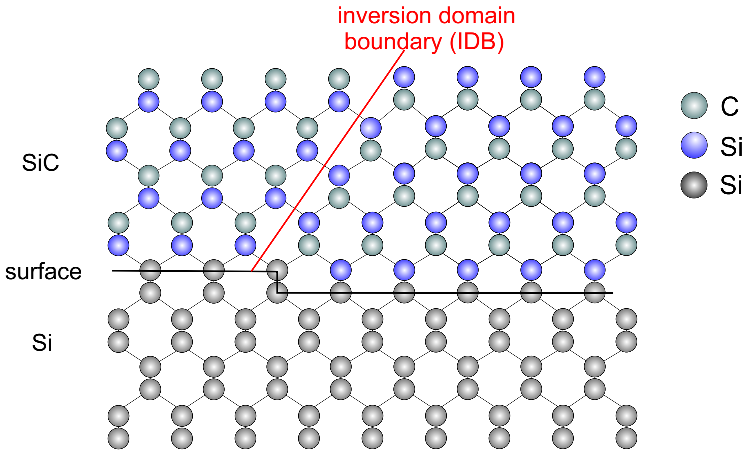

Figure 2.3
Growth of a polar semiconductor (zinc blende SiC) on a Si (001) surface having monatomic steps. Inversion domain boundaries (IDBs) are associated with the monatomic steps (after [29]).

case of a polar semiconductor like SiC being deposited on such a surface [29]. In Fig. 2.3 the growth of cubic SiC on a Si (001) surface having monatomic steps is depicted. It is assumed that the growth of the 3C-SiC starts with a monolayer of Si atoms. If all Si atoms bond to the Si atoms the stepped surface is transmitted to the polar epilayer. As a consequence IDBs are formed in the 3C-SiC during the nucleation on the elementary Si substrate. The domains can be interpreted as 3C-SiC domains, also known as anti-phase domains (APDs), that are rotated by 90° around the [001] axis. IDBs have been also observed in other material systems like GaAs/Si (001). In the case of cubic III-V semiconductors grown on Si the IDBs have an irregular shape [30].

2.3 Principle of Molecular Beam Epitaxy (MBE)

This chapter gives a brief introduction into the basic physical processes in molecular beam epitaxy (MBE). The following section is based on the information given in Ref. [31].

In the MBE technique, epitaxial thin films result from a reaction between an atomic beam of constituent elements like Ga, Al and the substrate surface. Figure 2.4 shows a schematic illustration of the three zones where the basic processes in MBE take place. The heated effusion cells have individual shutters to control the molecular beam. The different vapour elements are mixed in the mixing zone above the substrate, which is heated and usually rotated. The crystallization zone is on the substrate surface.

The deposition takes place under ultrahigh vacuum conditions which lead to growth governed by kinetics of the surface processes which are usually far from thermodynamic equilibrium conditions. This means that the MBE growth is dominated

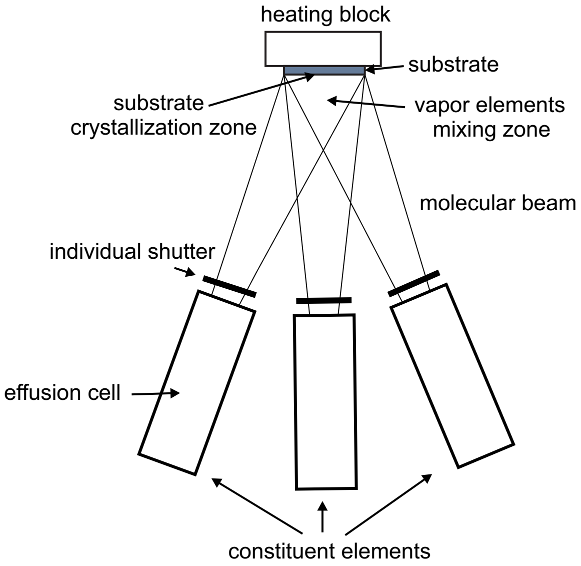

Figure 2.4
Schematic illustration of the three zones where the basic processes in MBE take place (after [31]).

by the kinetics of the surface processes like desorption and adsorption processes. In an atomistic model (see Fig. 2.5) the impinging atomic beam hits the surface of the substrate where several surface processes occur. Besides surface diffusion, the atoms can be incorporated into the lattice, create surface agglomerations, desorb from the surface or interdiffusion can play a role during the epitaxial film growth. The surface ki-

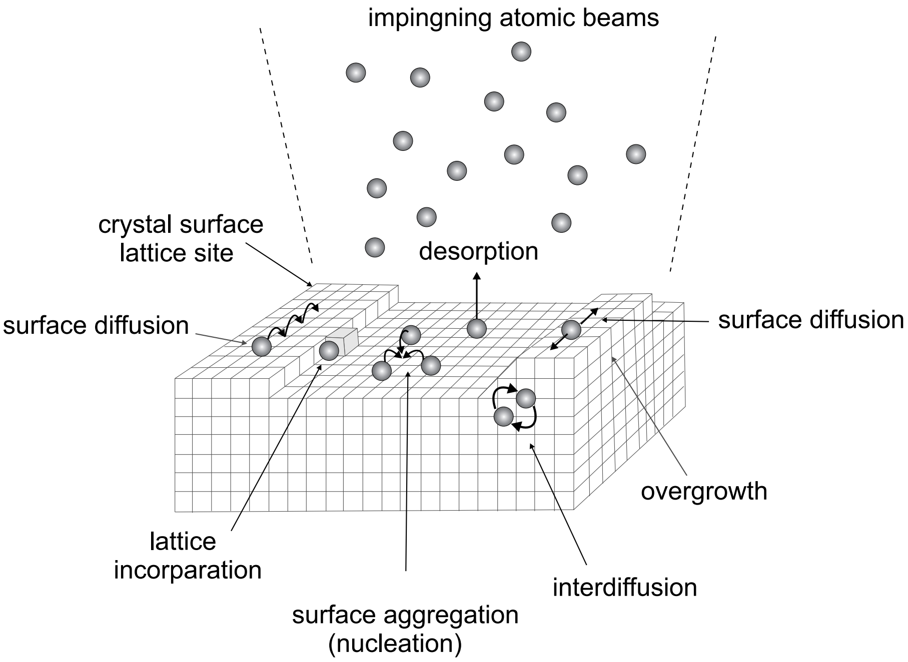

Figure 2.5
Schematic illustration of an atomistic model of the surface processes on the substrate during growth process (after [31]).

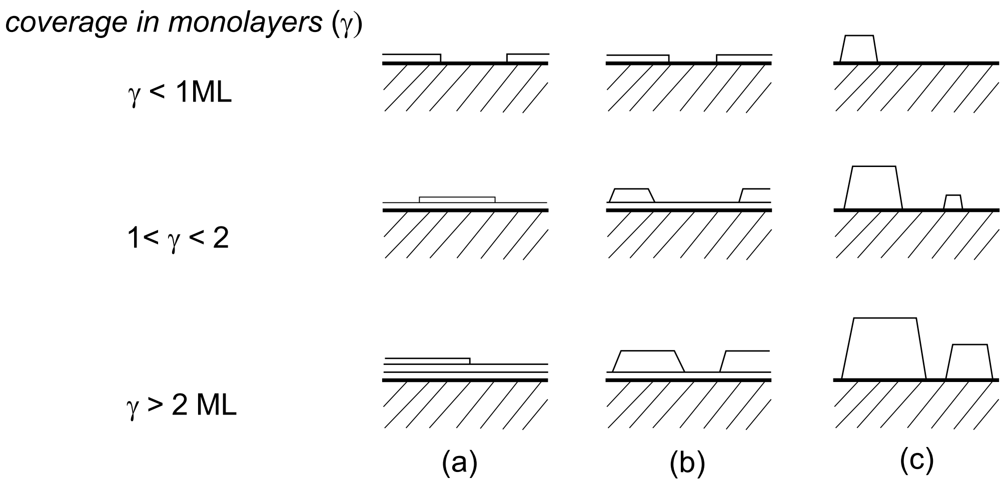

Figure 2.6
Schematic illustration of the three crystal growth modes, **(a)** layer-by-layer (Frank-van der Merwe), **(b)** layer plus island (Stranski-Krastanov), **(c)** island (Volmer-Weber) mode (after [31]).

netics depend on the substrate temperature, the incoming beam flux, the surface diffusion length, the surface roughness and the misfit between the substrate and the growing film. An important parameter describing the surface kinetics is the sticking coefficient S. It describes the ratio between the number of atoms adhering to the surface N_{adh} and the total number of incoming atoms N_{tot}:

$$S = \frac{N_{adh}}{N_{tot}}. \qquad (1)$$

If the sticking coefficient is zero all atoms re-evaporate.

In literature three fundamentally different growth mechanisms are described. Figure 2.6 illustrates the (a) layer-by-layer growth mode (Frank-van der Merwe), (b) the layer plus island growth mode (Stranski-Krastanov) and (c) the island growth mode (Volmer-Weber). These growth modes are displayed for three different monolayer (ML) surface coverages (γ). The layer-by-layer growth is self-explanatory. The first atoms condense to a complete monolayer on the substrate surface. Here the atoms are more strongly bound to the surface than to each other. In the Skranski-Krastanov mode (Fig. 2.6b) initially a complete monolayer is formed. But then it is energetically unfavorable to remain in the layer-by-layer growth mode and 3D islands are formed on the so called “wetting”-layer. The main reason for the island formation of this growth mode is related to strain induced by the mismatch of the lattice constant between the substrate and the epilayer. When an island formation still starts from the beginning, the growth mode is defined as the Volmer-Weber mode (Fig.2.6c). This occurs when the atoms are bound more strongly to each other than to the substrate surface.

2.4 Strain Relaxation in Heteroepitaxial Systems

In heteroepitaxy strain relaxation and the nucleation of misfit dislocations is one of the most important mechanisms which must be considered for the growth of high quality epilayers on non-lattice matched substrates. The description in this section mainly follows [32].

The growth of misfit layers with respect to the substrate passes through initial stages with increasing film thickness. To explain these initial processes a thin cubic epilayer is grown in a two dimensional growth mode on an unstrained thick cubic substrate as illustrated in Fig. 2.7. The growth direction is along the z-axis and the growth plane is the xy-plane. Further it is assumed that the relaxed lattice parameter of the epilayer a_e is larger than the unstrained lattice parameter of the substrate a_s. This is also the case for c-GaN deposited on a 3C-SiC (001) substrate. The resulting lattice mismatch strain (misfit) is defined as:

$$f = \frac{a_s - a_e}{a_e}, \qquad \text{here } a_e > a_s,\ f < 0. \tag{2}$$

The mismatch between c-GaN grown on 3C-SiC (001) is about -3.2% and larger than between c-AlN and 3C-SiC (001) with -0.25%.

When a thin epilayer is grown on an unstrained substrate with smaller lattice parameter the initial layer will be coherently strained as shown in Fig. 2.7a. At the interface the layer matches the substrate lattice constant a_s in the plane, resulting in a tetragonal distortion of the epilayer lattice in z-direction and an out-of-plane lattice constant c.

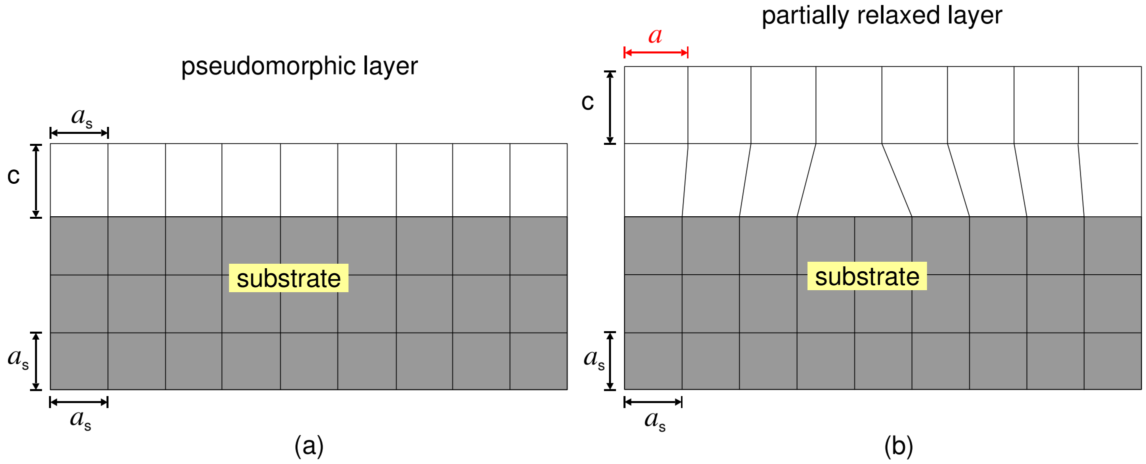

Figure 2.7
(a) Pseudomorphic and **(b)** partially relaxed epilayer grown on a mismatched substrate (after [32]).

The result is an in-plane biaxial compression of the epilayer. The in-plane stresses in the epilayer applied by the substrate are:

$$\sigma_{xx} = \sigma_{yy} = \sigma_{\parallel}. \tag{3}$$

Additionally, the out-of-plane stress σ_{zz} is assumed to be zero

$$\sigma_{zz} = \sigma_{\perp} = 0. \tag{4}$$

(For the growth on low-index planes like the (001) plane in the cubic system shear stresses are also assumed to be zero.) The biaxial stress $\sigma_{\parallel}$ is correlated to the in-plane strain ε_{II}, which for an unrelaxed epilayer corresponds to the mismatch strain *f*:

$$\sigma_{II} = \mathrm{Y}\varepsilon_{\parallel}. \tag{5}$$

The constant of proportionality Y is the biaxial modulus, which is the Young´s modulus in the case of biaxial stress. The elastic moduli for cubic crystals in general are listed in appendix A. With these correlations the total strain energy E_{ε} per unit area in the system can be described as a function of the layer thickness *h* by

$$E_{\varepsilon} = \varepsilon_{\parallel}^{2}\mathrm{Y}h. \tag{6}$$

Furthermore, the in-plane strain $\varepsilon_{\parallel}$ in the layer can be reduced by means of defect formation inducing a relative lattice relaxation δ:

$$\varepsilon_{\parallel} = f - \delta. \tag{7}$$

In a pseudomorphic layer (see Fig. 2.7a) the lattice relaxation is still $\delta = 0$ and therefore $\varepsilon_{\parallel} = f$. In growth direction the epilayer is deformed by an out-of-plane lattice parameter c resulting in an out-of-plane strain

$$\varepsilon_{\perp} = \frac{c - a_e}{a_e}. \tag{8}$$

The in-plane and the out-of plane strains can be related by

$$\varepsilon_{\perp} = -R_B\varepsilon_{\parallel} = -\frac{2C_{12}}{C_{11}}\varepsilon_{\parallel}. \tag{9}$$

Here, R_B is the biaxial relaxation constant of the growing film and C_{ij} are the elastic stiffness constants. The biaxial relaxation constant is the analogon to the Poisson ratio but for the case of biaxial stress in the sample. The out-of-plane strain has the opposite sign compared to the in-plane strain.

If the film thickness is increased the stored strain energy also increases: "As the film thickness increases, the elastic energy stored within the film increases. At some thickness, it becomes energetically favorable to relieve this misfit strain by the formation of dislocations at or near the substrate/film interface. These dislocations destroy the coherency of the interface and, therefore, increase its energy. It is when the elastic energy relieved by the dislocations balances the increase in interfacial energy associated with their formation that becomes thermodynamically favorable to introduce dislocations at the interface. The film thickness at which this occurs is known as the critical thickness." [33].

When the critical film thickness is reached the epilayer starts to relax. In a partially relaxed epilayer, shown in Fig. 2.7b, the in-plane lattice constant of the epilayer increases from a_s to a with $a_e > a > a_s$. It is still larger than the unstrained lattice parameter of the substrate, but still smaller than its relaxed lattice parameter a_e. Some of the mismatch is now accommodated by misfit dislocations (plastic strain). This is illustrated in Fig. 2.7b by an missing half-plane of atoms in the epilayer. The total energy is now the sum of the strain energy and the energy of the incorporated dislocations. The critical film thickness can be determined by minimizing the energy.

In literature several models introduce the calculation of the critical film thickness as a function of the used material parameters. Firstly, van der Merwe used an isotropic elastic analysis to form a continuum theory, but he did not consider the mechanism of dislocation formation [34]. Matthews and Blakeslee [35], for example, supposed that a preexisting threading dislocation in the substrate replicates in the growing film. It is assumed that this dislocation can bend over from the substrate to create a misfit dislocation at the interface when the critical layer thickness is reached. They found an equation to determine the critical layer thickness h_c which is often used:

$$h_c = \frac{b}{2\pi f} \frac{\left(1-\nu\cdot\cos^2(\alpha)\right)}{(1+\nu)\cos(\lambda)} \left(\ln\left(\frac{h_c}{b}\right)+1\right), \tag{10}$$

where b is the the absolute value of the Burgers vector of the dislocation, f the mismatch of the system, ν the Possion ratio, α the angle between the Burgers vector and the line vector of the dislocation and λ denotes the angle between the slip direction and that direction in the film plane which is perpendicular to the line of intersection of the slip plane and the interface. For 60°- dislocations in (001) zinc blende materials it is usually supposed that $b = a/\sqrt{2}$ (see section 2.6) and $\cos\lambda = \cos\alpha = 1/2$ [32]. The equation of Matthews and Blakeslee was also used to determine the critical layer thickness of c-GaN grown on 3C-SiC (001) substrates to be about 0.7 nm [36] ($1\,\text{monolayer (ML)} = 0.5\cdot \text{a}_{\text{c-GaN}} \approx 0.225\text{ nm} \Rightarrow 3\text{ ML} \approx 0.675\text{ nm}$).

An alternative expression for the critical film thickness was found by People and Bean [37]. When the strain energy density of the epilayer exceeds the self-energy of an isolated screw dislocation at a fixed distance from the free surface, misfit dislocations are formed. The theory of nanoheteroepitaxy, which is introduced in subsection 2.7.1 and appendix B, is based on this model.

2.5 MBE of Cubic GaN on Planar 3C-SiC (001)

This section is a brief review of the molecular beam epitaxy (MBE) of c-GaN on 3C-SiC (001) substrates. The fundamentals of the growth process [9] are presented, which is the basis for the growth of cubic III-nitrides on pre-patterned substrates (see chapter 5).

The c-GaN thin films were deposited in a RIBER MBE 32 system. A schematic drawing of the interior of the MBE UHV-chamber is shown in Fig. 2.8a. An Oxford Applied Research HD25 radio frequency plasma source was used to provide activated nitrogen atoms. Gallium and aluminum atoms were evaporated from Knudsen cells (RIBER ABN35 standard elemental sources). The sources have an orifice of 2.5 cm and are arranged in a horizontal semi circle with tiltangles of 33°. The distance between the substrate and the effusion cells is about 12 cm (see Fig. 2.8b). The sample holder facing the effusion sources is located at the cross-over point of the atomic beams of these effusion cells. The holder is heated from the backside and can be rotated by a substrate manipulator to improve the uniformity of the deposition. Furthermore, there is a nitro-

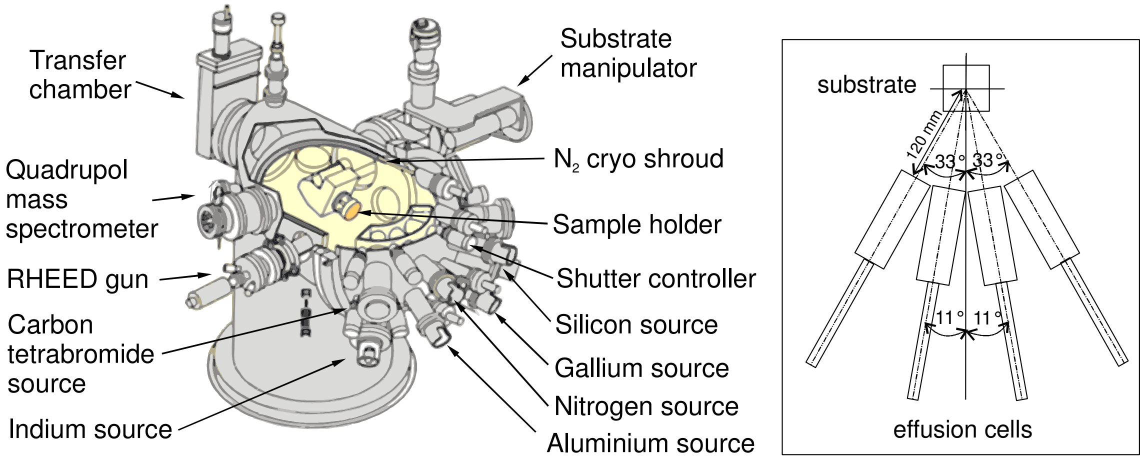

(a) (b)

Figure 2.8
(a) Schematic drawing of a Riber 32 MBE system. **(b)** Cells and substrate geometry in the UHV-chamber (after [38]).

gen cooled shroud around theentire UHV-chamber (active during growth) to minimize residual water vapour and carbon-containing gases in the vacuum chamber.

Cubic GaN layers were deposited at a substrate temperature of 720°C on the rotating 3C-SiC/Si (001) substrates. The adsorption and desorption of metal (Ga, Al) layers on the surface are investigated using the intensity of a reflected high-energy electron beam (RHEED) as a probe. A brief introduction into this measurement method is given in section 3.1.

As an important step to improve the GaN surface morphology and thus the inner structure of films in a systematic way, it is essential to understand the surface structure and the underlying growth process on an atomic scale. In particular, the kinetic processes of adsorption and desorption on the surface (described in section 2.3) are considered as key parameters that govern the surface morphology, incorporation kinetics and consecutively the overall material quality. In MBE of GaN, two dimensional surfaces are commonly achieved under gallium-rich conditions, with theoretical [39] and experimental [40, 41] evidence suggesting that the growth front is stabilized by a metallic Ga adlayer. The optimum conditions for the epitaxial growth of c-GaN are mainly determined by two parameters, the surface stoichiometry and the substrate temperature [42]. Both parameters are interrelated; therefore an in-situ control of substrate temperature and surface stoichiometry is highly desirable. The study of the surface reconstruction by RHEED was one of the key issues in understanding the cubic III-nitride growth [42, 43, 44]. First principle calculations by Neugebauer et al. [45] show that all energetically favoured surface configurations of the non-polar (001) c-GaN surface are gallium-stabilized and therefore optimum growth conditions are expected under slightly gallium-rich conditions. The optimum growth conditions of cubic III-nitrides were found, when one monolayer gallium coverage is formed at the growing surface [9]. This is in contrast to what has been observed with hexagonal GaN (h-GaN), where the optimum growth conditions with regard to surface morphology are related to the formation of a gallium bilayer (c-plane, [46, 47]) or a trilayer (m-plane, [41]), respectively. Under one monolayer gallium coverage the root mean square roughness of the c-GaN surface measured by a 5x5 μm^2 atomic force microscopy (AFM, see chapter 3.2) scan is decreasing to a minimum value of 2.5 nm. The smoother the surface of the epilayer the narrower is also the X-ray rocking curve line width (ω-scan) of the c-GaN and the higher is the structural quality of the cubic epilayer.

In Fig. 2.9 the rocking curve line width of c-GaN epilayers grown on 3C-SiC/Si (001) substrates is plotted *versus* the c-GaN film thickness and the associated dislocation density N_{disl} derived from (002) rocking curves by the method of Gay et al. [11] (see also section 3.5). Two clear effects can be seen from this plot. First a reduction of the full width at half maximum (FWHM) with increasing epilayer thickness is observed. The inset presents the ω-scan of a 450 nm thin c-GaN film. This linewidth dependence is consistent with the defect annihilation process observed in c-GaN grown on GaAs (001) substrates [48]. Since in zinc-blende structure the SFs lie on the (111)

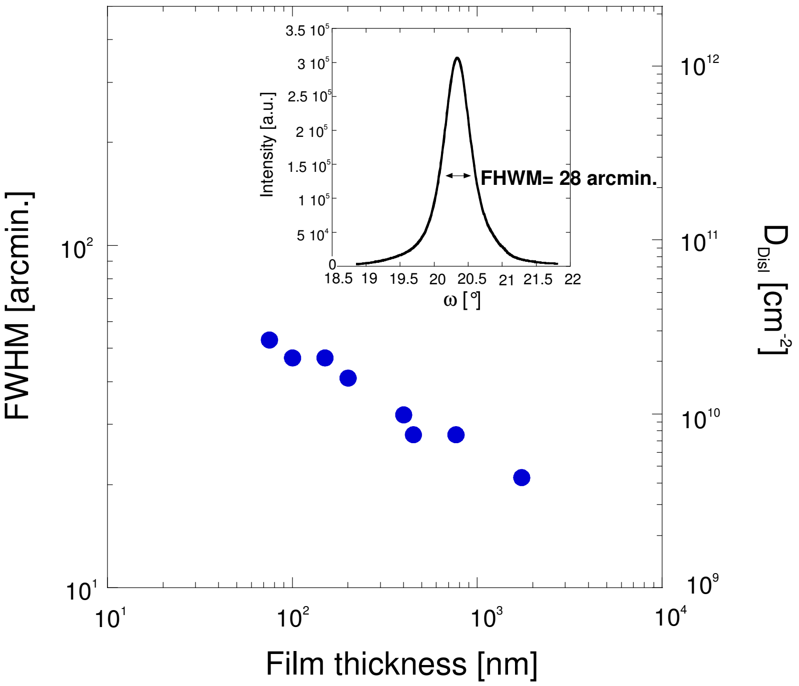

Figure 2.9

X-ray rocking curve line width of c-GaN epilayers grown on 3C-SiC/Si (001) substrates plotted *versus* the film thickness of c-GaN epilayers and the associated dislocation density N_{disl} determined by the method of Gay et al. [11]. The inset shows the ω-scan of a 450 nm thin c-GaN film (sample GNR 2151).

planes, an annihilation mechanism is possible, when two SFs, lying for example on the (111) and on the $(\underline{11}1)$ planes, intersect and annihilate simultaneously with the creation of a dislocation aligned along the [110] direction. This annhilation mechanism of two {111} SFs is studied in detail with high-resolution TEM images at the 3C-SiC/Si (001) interface [49] showing similar behaviour like in the c-GaN/SiC system. The annhilation results from the reaction between two partial dislocations resulting in a partial dislocation which is referred to as Lomer-Cottrell dislocation or stair-rod dislocation [49] along the [110] direction.

The glide model by Ayers [50] implies that the dislocation density N_{disl} is inversely proportional to the layer thickness d and that the FWHM is proportional to $d^{-1/2}$. However, using the method of Gay et al. [11], which correlates the X-ray rocking curve FWHM with the dislocation density, one sees from Fig. 2.9, that a residual dislocation density N_{disl} in the order of some $10^9/cm^2$ remains for about 1 μm thick c-GaN epilayers. In contrast the dislocation density at the interface is in the order of $N_{disl} \sim 10^{11}/cm^2$. For many device applications such a high density of dislocations severely reduces the device performances and it is highly desirable to avoid it. The growth of sufficiently thick films to suppress high dislocation densities – however –is no desirable option, as growth rates are in the order of 160 nm/h.

2.6 Extended Defects in Cubic GaN

In general, three basic types of extended defects in epitaxial c-GaN thin films grown on 3C-SiC (001) should be mentioned. The first typeis misfit dislocations due to relaxation of a pseudomorphically strained thin layer on the substrate. The second type is dislocations originating in the substrate, which extend into the epilayer. The third types are SFs on {111} planes. In this work (and in literature [51]-[54], [18]) it has been revealed by TEM measurements that SFs on the {111} planes are the predominant extended defects in the cubic III-nitrides. On average, the dislocation density of c-GaN determined by high-resolution X-ray diffraction is about ~10^{10}-10^{11} cm^{-2} (see section 2.5 and 3.5) and about ~$10^{9}\mathrm{cm}^{-2}$ in the 3C-SiC substrate [13].

Dislocations are specified by their line vectors $\vec{l}$, the Burgers vectors $\vec{b}$, the angle between these vectors and their glide planes. The Burgers vector can be determined by a so called Burgers circuit as explained in [18]. Figure 2.10 tries to explain the definition of the Burgers vector. In Fig. 2.10a the path *MNOPQ* round an edge dislocation is illustrated. If the same atom-to-atom path is made in an undisturbed crystal, shown in Fig. 2.10b, it would not be a closed loop. The vector which is required to complete the circuit, the closure failor, is named Burgers vector. It indicates the direction and the amount of atomic displacements in the disturbed crystal and is independent of the position and orientation of the dislocation line. For example, in cubic crystals the Burgers vector is the shortest lattice translation vector which joins two points. In zinc blende crystals the shortest lattice vectors are of type $a/2\langle 110\rangle$ and $a\langle 001\rangle$. Therefore, these Burgers vectors $\vec{b}$ are most likely for dislocations in zinc blende structures. In the case of a fcc crystal structure frequently $\vec{b} = \frac{a}{2}\langle 110\rangle$ with the length

$$b = \sqrt{\left(\frac{a}{2}\right)^2 + \left(\frac{a}{2}\right)^2 + 0} = \frac{a}{\sqrt{2}} \qquad (11)$$

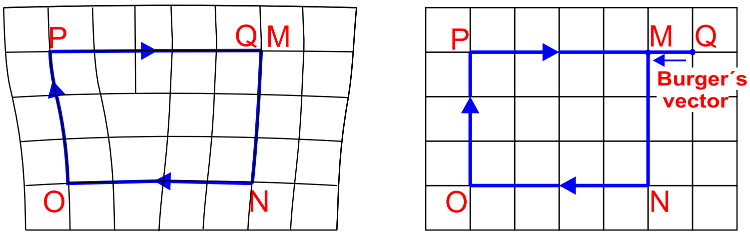

Figure 2.10

Schematical drawing of a Burgers circuit: **(a)** Burgers circuit around an edge dislocation with positive line sense into the paper and **(b)** Burgers circuit in an undisturbed crystal and definition that the closure difference is the Burgers vector (after [18]).

with *a* being the lattice constant.

Because the energy of a dislocation E is proportional to b^2 the energy of the type $a/2\langle 110\rangle$ dislocation is half of that of a $a\langle 001\rangle$ defect ($(a)^2/2$ compared to a^2). The line energy E of a dislocation is determined by Frank´s rule to

$$E \approx CG\, b^2 \tag{12}$$

with *C* a constant depending of the dislocation type and *G* the shear modulus. Frank´s rule reveals that a dislocation reaction is energetically favored if the sum $\sum b^2$ for the products is less than the sum $\sum b^2$ for the reactants [32]. Therefore, the $a/2\langle 110\rangle$ dislocation is energetically very favorable. Further, the closed-packed planes are the {111} planes and there are four {111} planes with three <110> directions in each. They act as glide planes for dislocations, because these are the planes with the highest density of atoms.

After reaching the critical layer thickness lattice relaxation starts by the introduction of misfit dislocations at (or near) the interface. In the cubic system misfit dislocations are formed along the two orthogonal <110> directions in the plane of the interface and have predominantly 60° character [32]. This 60°-dislocation may dissociate into two Shockley partial dislocations

$$\frac{a}{2}[110] \rightarrow \frac{a}{6}[121] + \frac{a}{6}[12\bar{1}], \tag{13}$$

which is energetically favorable, as can be shown by Frank´s rule [32]. The dissociation occurs naturally by glide processes. The two partial dislocations lie on the same (111) glide plane as the 60°-dislocation. Between them, a SF exists on this (111) glide plane. In Fig. 2.11 a sketch of the dissociation of a perfect edge dislocation with a Burgers vector $\vec{b}_{per} = a/2\langle 110\rangle$ into two partial dislocations with Burgers vectors $\vec{b}_S = a/6\langle 12\bar{1}\rangle$ and $\vec{b}_S = a/6\langle 121\rangle$ with a SF in between is shown.

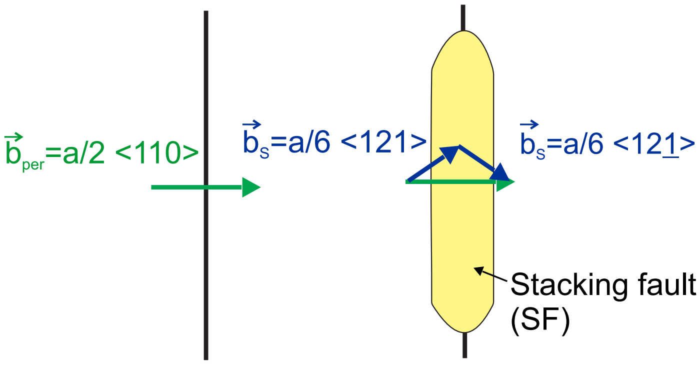

Figure 2.11
Dissociation of a perfect edge dislocation into two Shockley partials with a SF in between (after [55], [56]).

Stacking faults are planar defects which describe a change in the stacking sequence. In the cubic structure the stacking sequence in [111] direction can be described as *ABCABC*. A change of the stacking sequence leads to hexagonal (stacking sequence *ABAB*) inclusions, which locally change the crystal symmetry and result in polar faces. If an additional plane of atoms is inserted into the stacking sequence, like *ABC**B**ABC*, the SF is called extrinsic. If one plane is removed, as in *ABCBC*, it is named an intrinsic SF.

This work shows that the main extended defects in c-GaN and c-AlN/GaN layers grown on pre-patterned 3C-SiC (001) substrates by MBE are SFs on the {111} planes with 57.4° between the {111} planes and the (001) surface of the substrate.

2.7 Defect Engineering for Improved Epilayer Growth

One of the key issues in semiconductor device fabrication is defect engineering, because defects tend to degrade device performances. Along linear defects the interatomic bonding is disturbed leading to dangling bonds and large local strain fields. As a result shallow and deep levels may be introduced into the band gap and can act as recombination centers, or dopant atoms can be attracted into dilation or compression zones leading to locally enhanced concentration of doping atoms.

To avoid these negative effects different techniques of defect engineering in heteroepitaxial layers have been introduced in literature. Here, defect engineering means to control defect densities and defect types. These efforts can be divided into two groups: techniques to remove existing defects and techniques to prevent the nucleation of defects (see Fig. 2.12).

The technique mentioned first includes buffer layer approaches and epitaxial lateral overgrowth (ELO) processes.

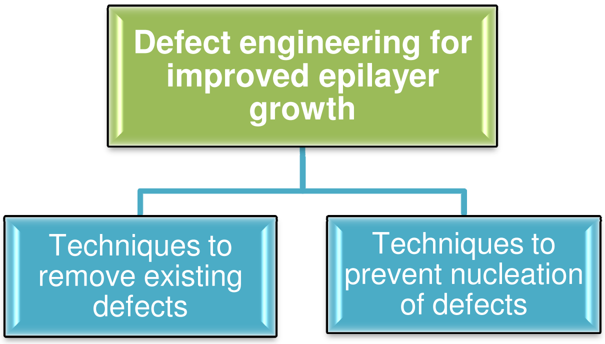

Figure 2.12

The field of defect engineering can be divided into two groups.

Thick buffer layers are usually used to act as virtual substrates and are deposited between the substrate and the device layers. If they are designed to be lattice-matched to the device layer, then the device layer can be grown on a lattice-matched virtual substrate. It has also been shown that the dislocation density decreases with increasing layer thickness. These benefits prevent the nucleation of misfit dislocation in the active layers.

The ELO method is based on the selective growth on seed areas of either pad or stripe shape. Between these pads areas are located which are usually covered with an oxide (e.g. SiO_2). Growth conditions have to be chosen in the way that they prevent the nucleation of material on the areas between the growth seeds and achieve a lateral growth of the material deposited on the seed pads. Then the growth over the opening masks is an extension of the seed pads and leads to a coalescent film. In literature (e.g. in [57]) it has been shown that the overgrown film above the oxide areas contains much less defects compared to conventional growth techniques. On the one hand dislocations are stopped by the oxide mask. On the other hand e.g. threading dislocations can bend over the oxide mask in the lateral growth direction and therefore they cannot reach the top surface of the epilayer. Unfortunately, in the MBE growth of c-GaN the lateral growth rate is much smaller than the vertical growth rate (~40 nm/h compared to ~160 nm/h, estimated from TEM measurements in [58]). Therefore, this technique is not the first choice for defect reduction in the cubic III-nitrides.

Another possibility of defect engineering is to avoid defects in the growing layer right from the start. This group of methods includes the reduced or selected area growth and the nanoheteroepitaxy (NHE) [5]. The reduction of the growth area is a common method for the elimination of misfit dislocations. Even the reduction of the growth area in the µm-range reduces the nucleation sites of dislocations [4]. Additional defect reduction mechanisms become available, if the growth area is further reduced, as proposed in the NHE theory by Zubia and Hersee [5]. This theory deals with the growth on nanostructures with a size of 10-100 nm. NHE offers the possibility of growing dislocation free epilayers on non-lattice-matched nano-patterned substrates if the growth areas are sufficiently small. In this case, the mismatch induced stress leads to a three dimensional strain partitioning between both, the growing film and the substrate. In consequence, the strain within the growing film can be kept below a threshold at which the strain relaxation by the formation of extended defects becomes energetically favourable. Hersee et al. [59] have demonstrated in the h-GaN/SiC system that also additional defect reduction mechanisms are active like filtering of substrate defects, the improved coalescence at the nanoscale, and defect termination at local free surfaces. The improved coalescence occurs when the layer is thin and compliant during coalescence and when the h-GaN nuclei have a highly uniform size and shape [60]. In contrast, the ELO technique the layers are typically thick (~µm) when they coalesce leading to defects generated at the boundaries.

In the following subsection the possibility to avoid extended defects in heteroepitaxial layers by the use of substrates with tailored surface morphologies shall be addressed.

2.7.1 Theory of Nanoheteroepitaxial Growth

The theory of NHE was introduced by Zubia and Hersee [5] and is based on the studies of People and Bean [36] who introduced a possibility to determine the critical layer thickness h_c. Furthermore, it implies the studies of Luryi and Suhir [61] who demonstrated that the critical film thickness h_c^l depends on the lateral dimensions l for a given mismatch f of the system. Zubia and Hersee extended all these results to the theory of NHE [5] by including effects of compliance in the substrate. Over the years there have been further enhancements concerning this topic. For example Ye et al. [62] determined the critical lateral dimensions for a nanoscale-patterned heterostructure using the finite element method. In what follows the basic idea of NHE is briefly introduced followed by a description of the NHE on a non-compliant substrate (Model of Luryi and Suhir) and at the end the theory of NHE on a compliant substrate (Model of Zubia and Hersee) is outlined (see also appendix B). The source for these models can be found in [5], [61], [63] and [32].

Basic Idea of NHE

The basic idea of NHE is that the reduction of the growth area in the nm-range (10-100 nm) offers new mechanisms of strain relaxation compared to a planar heteroepitaxial system. In order to illustrate the difference between conventional epitaxy and NHE, Fig. 2.13 depicts a schematic drawing of a planar epilayer and a selective-area-grown epilayer on a patterned substrate. In conventional planar epitaxy the lattice

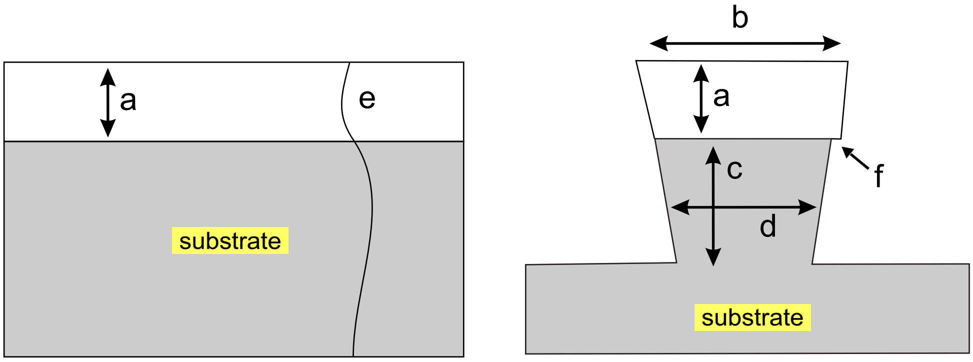

Figure 2.13
Sketch of a planar epilayer and a selective-area-grown epilayer on a patterned substrate (after [5]).

mismatch at the interface leads to lateral strain in the growing film and in consequence to transversal lattice distortions (in growth direction). Vertical deformation of the grown epilayer *(a)* is the only stress-relief mechanism besides the formation of dislocations. In contrast, on a two dimensionally patterned surface both the substrate and the growing film are not subjected to lateral confinements and therefore a three dimensional partitioning of the strain in the epilayer and in the substrate and consequently a reduced strain in the epilayer is expected. Therefore, the stress can also be relieved by lateral deformations *(b)* in the layer and vertical and lateral deformations *(c)* and *(d)* in the substrate island. Even in the case that stress relief should occur partly by the nucleation of misfit dislocations, these dislocations can glide to the sidewalls of the island and there create a sidewall step *(f)*. In the planar layer an assumed threading dislocation *(e)* cannot glide to the mesa edges and therefore the planar epilayer contains those dislocations. These theoretical considerations have been confirmed in the Ge/Si (001) system by the group of Kozlowski et al. [64]. They observed single threading dislocations in nanoheteroepitaxially grown Ge epilayers, which glide out to the sidewalls due to the small volume.

NHE on a Non-Compliant Substrate (Model of Luryi and Suhir)

Luryi and Suhir [61] supposed that the lattice mismatched material is deposited on round substrate seed pads with a diameter *2l*. There is no adhesion of the film to the substrate between the structures. Figure 2.14 shows a schematic drawing of the nanoheteroepitaxial grown epilayer on a patterned (non-compliant) unstrained substrate. The y-axis is located in-plane and the z-axis perpendicular to the seed pads surface and is aligned at the centre point (0) of the seed pad. The distance between the mesas is wide enough to prevent interactions concerning strain fields. It is also shown that the layer has coalesced due to lateral growth with a resulting layer thickness *h*.

It is assumed that in the deposited film, with a misfit strain *f* along the segment *(-l, l)* in y-direction, the in-plane stress $\sigma_{\parallel} \equiv \sigma(y,z)$ along the segment *(-l, l)* in y-direction can be expressed by

$$\sigma_{\parallel} = \frac{Y_{epi}}{1-\nu_{epi}} \varepsilon_{epi} \chi(y,z) \exp\left(-\frac{\pi z}{2l}\right), \tag{14}$$

where Y is the Young´s modulus of the film, ν the Poisson ratio, ε is the strain and the function $\chi(y,z)$ characterizes the lateral stress distribution:

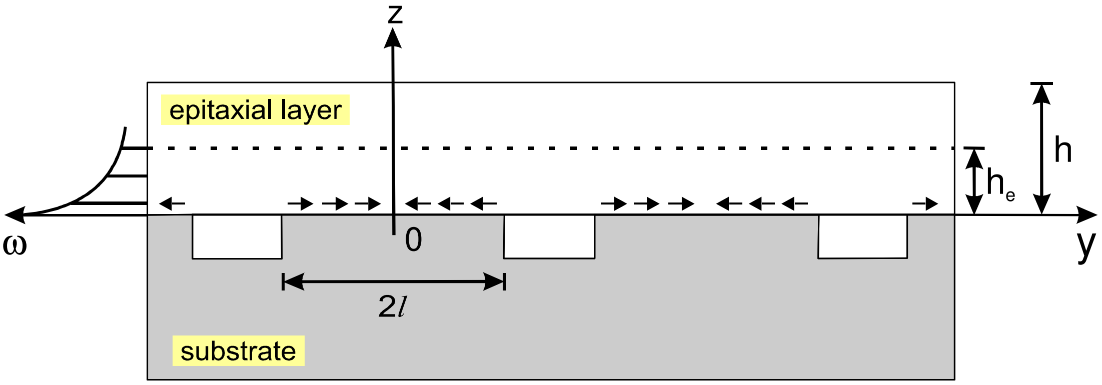

Figure 2.14

Schematic drawing of the nanoheteroepitaxial growth in the model of Luryi and Suhir with the layer thickness height *h* and the effective height of the strained film h^{eff}. A strain energy profile $\omega(0, z)$ for one seed pad is shown on the left side (after [61]).

$$\chi(y,z)=\begin{cases}1-\dfrac{\cosh(ky)}{\cosh(kl)}; & z\le h^{eff}\\ 1 \qquad\qquad ; & z\ge h^{eff}\end{cases} . \tag{15}$$

In z-direction the stress decays exponentially with a length of $2l/\pi$. The value h^{eff} describes the effective range for the strain energy in z-direction and *k* is introduced as interfacial compliance parameter given by

$$k=\left[\frac{3}{2}\left(\frac{1-\nu}{1+\nu}\right)\right]^{1/2}\frac{1}{h^{eff}}\equiv\frac{\xi}{h^{eff}} . \tag{16}$$

The strain energy density per unit volume has its maximum at y = 0 and is determined by

$$\omega(y,z)=\frac{1-\nu}{Y}\sigma_{\parallel}^{2} . \tag{17}$$

The integration of Eq. (17) over the film thickness leads to the strain energy per unit area. The maximum is in the middle of the contact zone and is given by

$$E_s=\int_0^h \omega(0,z)\equiv\frac{Y}{1-\nu}f^{2}h^{eff} . \tag{18}$$

Luryi and Suhir extended the form of χ given by the top line of Eq. (15) to all values of *z*. Together with the right-hand side of Eq. (18) the characteristic thickness h^{eff} is defined to:

$$h^{eff} = h\left\{\left[1-\operatorname{sech}\left(\frac{\xi l}{h^{eff}}\right)\right]^2 \left[1-\exp(-\pi h/l)\right]\frac{l}{\pi h}\right\} = h\left[\phi\left(\frac{l}{h}\right)\right]^2 . \tag{19}$$

The right hand side defines a reduction factor $\phi(l/h)$. The reduction factor is a function of the quotient *(l/h)* (see [61]) which declares that $h^{eff} \approx h$ for $h << l$ and for $h >> l$ the reduction factor approaches to zero resulting in:

$$h^{eff} \approx \frac{1}{h}\left[1 - sech\,(\xi\pi)\right]^2 . \tag{20}$$

If the film thickness *h* is equal to the island radius *l* the reduction factor assumes a value around 0.5.

The critical layer thickness h_c^l for an island of radius *l* can also be found by comparing the maximum strain energy density per unit area in the middle of the seed pad contact zone with the areal energy density associated with a single dislocation line:

$$h_c^l = h_c\left[\varphi\left(l/h_c^l\right) f\right] . \tag{21}$$

Here, Luryi and Suhir used the expression of People and Bean [37] for the critical layer thickness h_c.

NHE on a Compliant Substrate (Model of Zubia and Hersee)

The model of Zubia and Hersee [5] is an extension of the work of Luryi and Suhir [61] discussed above. Firstly, they integrated a strain partitioning in compliant substrates with no patterning of the substrate. Substrate compliance implies that a fraction of the mismatch strain can now move into the substrate resulting in a reduced strain in the deposited layer. This leads to a different compliance factor *K* compared to the model of Luryi and Suhir. The strain partioning varies through the growth process of the epilayer: when the growth process starts the strain is accomodated in the epilayer. Then, with increasing film thickness, more and more of the strain is accomodated in the substrate leading to a partioning of the strain. The partioning depends on the epilayer thickness. Therefore, substrate compliancy is introduced by expressing separately the stresses in the epilayer and in the substrate. The corresponding formulas are shown in appendix B.

After this modification the authors included the substrate patterning by assuming that the lateral stress distribution is uniform until close to the edge of the island where the stress drops down to zero. With these modifications an expression for the total strain energy in the case of NHE is found:

$$\mathrm{E}_{\mathrm{NHE}} = \frac{\mathrm{Y}_{\mathrm{epi}}}{1-\nu_{\mathrm{epi}}}\varepsilon^2_{\mathrm{epi,0}}\mathrm{h}^{\mathrm{eff}}_{\mathrm{epi}} + \frac{\mathrm{Y}_{\mathrm{sub}}}{1-\nu_{\mathrm{esub}}}\varepsilon^2_{\mathrm{sub,0}}\mathrm{h}^{\mathrm{eff}}_{\mathrm{sub}} , \tag{22}$$

where Y_{epi}, Y_{sub} are the Young´s moduli of the epilayer and the substrate, respectively. The expressions of the interfacial (in-plane) partioned strains in the island $\varepsilon_{epi,0}$, $\varepsilon_{sub,0}$ can be found in detail in appendix B as well as the formulas of the effective thicknesses of the epilayer and the substrate h^{eff}_{epi}, h^{eff}_{sub}, respectively. Several approximations given in [63] can be applied to Eq. (22):

$$\varepsilon_{epi,0} = \varepsilon_{sub,0} = \frac{\varepsilon_T}{2} \quad \text{and} \tag{23}$$

$$h^{eff}_{epi} = h^{eff}_{sub} = \frac{l}{\pi}, \tag{24}$$

with ε_T (Eq. (48)) the total lattice mismatch strain and *l* the island diameter. This results (see appendix B) in a simplified term of the total areal strain energy in the case of NHE:

$$E_{NHE} = \left(\frac{Y}{1-\nu}\right)\varepsilon_T^2 \frac{l}{2\pi}. \tag{25}$$

The expression for the total strain energy in the case of NHE shows that the strain energy is finite and proportional to the island radius *l*.

In Fig. 2.15 an illustration of the nanoheteroepitaxial growth in the model of Zubia and Hersee is displayed which is similar to Fig. 2.13. The substrate and the deposit can deform vertically *(i)* and laterally *(ii)* and the strain can decay exponentially away from the interface in both directions. A strain-free region in the coalescencing epi-

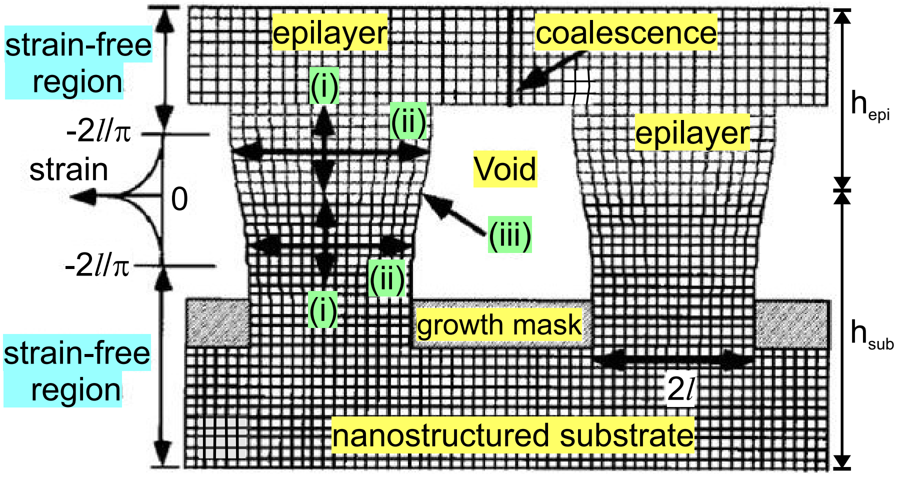

Figure 2.15
Illustration of the nanoheteroepitaxial growth in the model of Zubia and Hersee (after [63]).

layer can be reached. If mismatch dislocations nucleate, they can glide to the mesa edge *(iii)* as shown before in Fig. 2.13.

2.7.2 Nanoheteroepitaxy of Cubic GaN on 3C-SiC (001)

The NHE model of Zubia and Hersee [5] can be applied to semiconductor materials by calculating[1] the areal strain energy in the heteroepitaxial system as a function of the deposited thickness. The results can be compared with the areal energy required to form a dislocation in the deposited film. For this, the areal energy of an already formed dislocation is used. The nucleation process of the dislocations itself is not considered in the NHE model, although it might play a role. Some of the formulars (Eqs. (48)-(75)) used in the following can be looked up in appendix B.

The c-GaN/3C-SiC system has a lattice mismatch of about 3.25% (Eq. (48)) at room temperature (300 K) with the lattice parameter $a_{\text{c-GaN}}$ (300 K)=4.503 Å and $a_{\text{3C-SiC}}$ (300 K)=4.359 Å. The optimal MBE growth conditions of c-GaN on 3C-SiC [9] are found at 720°C. Thus, the best approximation of the NHE model to realistic experimental conditions is found, if the parameters refer to 720°C (993 K). For example, the absolute temperature T affects the lattice parameter a and the stiffness constants C_{ij}, which again define the elastic moduli. Hence, the first basic steps are the calculations of the temperature dependent parameters.

The lattice constants of the 3C-SiC substrate and the c-GaN deposit have been determined as a function of temperature T (with T_0=300 K) by integration about the thermal expansion coefficient $\alpha(\mathrm{T})$:

$$a(\mathrm{T}) = a(\mathrm{T}_0)\cdot\left[1+\int_{\mathrm{T}_0}^{\mathrm{T}}\alpha(\mathrm{T})\,\mathrm{dT}\right]. \tag{26}$$

The thermal expansion coefficients for 3C-SiC and c-GaN are described by:

$$\alpha_{3\text{C}-\text{SiC}}(\mathrm{T}) = 3.19\cdot10^{-6}\ \mathrm{K}^{-1} + 3.60\cdot10^{-9}\ \mathrm{T} - 1.68\cdot10^{-12}\mathrm{T}^2[\mathrm{K}^{-1}]\ [65], \tag{27}$$

$$\alpha_{\text{c}-\text{GaN}}(\mathrm{T}) = 5.174\cdot10^{-6}\ \mathrm{K}^{-1} + 1.466\cdot10^{-9}\ \mathrm{T}\ [66]. \tag{28}$$

Equations (27) and (28) are inserted in Eq. (26) in the case of the substrate or the deposit, respectively. With Eq.(26) the lattice constant of c-GaN at 993 K is determined to $a_{\text{c}-\text{GaN}}(993\text{K}) = 4.5193$ Å and for 3C-SiC to $a_{3\text{C}-\text{SiC}}(993\text{K}) =$ 4.3687 Å, leading to a mismatch of 3.39% (Eq.(48)) at 720°C.

---

[1] Calculations have been performed by Dr. Thomas Riedl (University of Paderborn).

	C_{11} [GPa]	C_{12} [GPa]	C_{44} [GPa]	G^V [GPa]	Y^V [GPa]	ν^V
c-GaN	293	159	155	120	301	0.25
3C-SiC	290	235	55	182	424	0.16

Table 2.3

Elastic stiffness constants C_{ij} at room temperature (300 K) [67] and isotropic mean values of theshear modulus G^V, the Young modulus Y^V and the Poisson ratio ν^V determined by the Voigt formalism expressed by Eqs. (29)-(31).

The values of the stiffness constants at 993 K are not available, because c-GaN is not yet sufficiently characterized in this respect. Thus, the room temperature values of C_{ij} are used here (Table 2.3) to calculate the shear modulus G, the Young modulus Y and the Poisson ratio ν.

In order to approximate the anisotropy characteristics of real crystals, isotropic average elastic constants should be used. With the Voigt average [68] isotropic mean values of the elastic moduli G^V, Y^V and ν^V are specified by averaging the anisotropic properties over all possible orientations:

$$G^V = \frac{C_{11} - C_{12} + 3C_{44}}{5} \tag{29}$$

$$Y^V = 2G(1+\nu) \tag{30}$$

$$\nu^V = \frac{C_{11} + 4C_{12} - 2C_{44}}{4C_{11} + 6C_{12} + 2C_{44}}. \tag{31}$$

The determined isotropic mean values of the elastic moduli are listed in Table 2.3. With these values the parameter *K* (Eq. (56)) is assigned which leads to the interfacial (in-plane) partitioned strains in the deposit (Eq. (60)) and the substrate (Eq. (61)), respectively. Also the compliance paramter *k* (Eq. (16)), Model of Luryi and Suhir) is determined to calculate the effective height h^{eff}. With all these parameters the areal strain energy (Eq. (25)) in a c-GaN/3C-SiC nano-island depending on the island diameter *2l* can then be determined (see also appendix B).

The areal strain energy in the nano-island is compared to the areal strain energy of a 60°-edge dislocation. The total strain energy per unit length of a 60°-edge dislocation $E_{D,\mathrm{line}}$ is approximated by

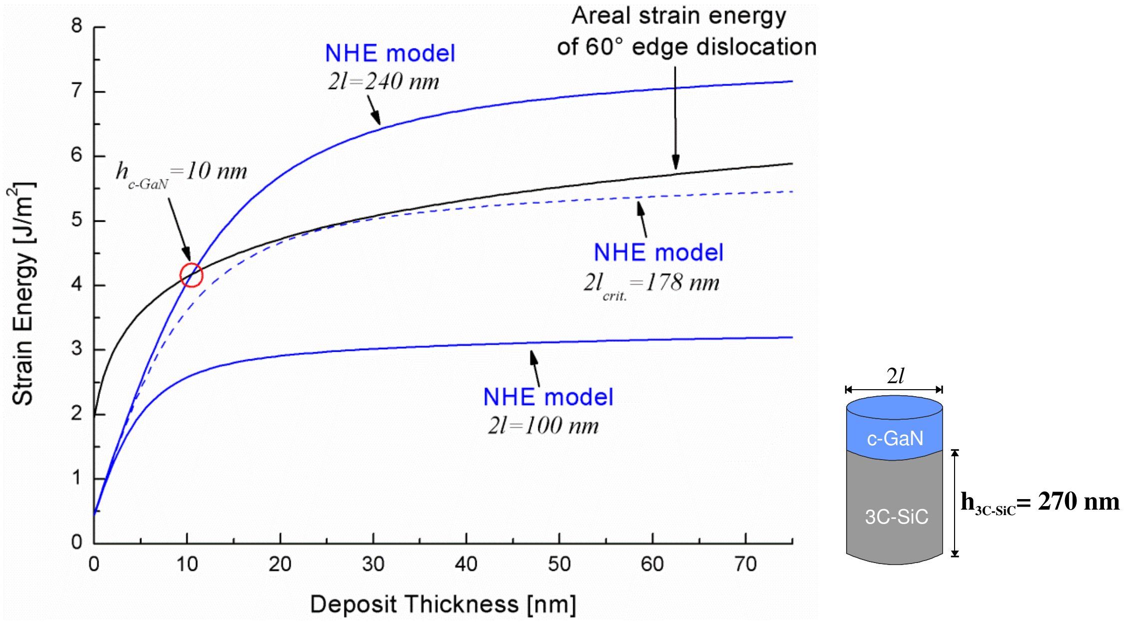

Figure 2.16

Diagram of the strain energy plotted as a function of the deposit thickness in the c-GaN/3C-SiC system with a substrate height of $h_{3C\text{-}SiC}$= *270 nm* calculated by the NHE model of Zubia and Hersee [5].

$$E_{D,\text{line}} = \frac{G_{c-\text{GaN}} G_{3C-\text{SiC}} \cdot b^2}{8\pi (G_{c-\text{GaN}} + G_{3C-\text{SiC}})} \left(1 + \frac{3}{1 - \nu_{c-\text{GaN}}}\right) \cdot \left(\ln\left(\frac{R}{b}\right) + 1\right), \tag{32}$$

where G is the shear modulus, ν the Poisson ratio and$b$ the Burgers vector. The parameter R is a cut-off radius up to which strain energy around a dislocation is taken into account and is equaled to the distance between the dislocation and the nearest free surface and it is assumed that $R = h_{\text{epi}}$. In order to obtain the areal strain energy $E_{D,\text{ area}}$ of a 60°-edge dislocation, Eq. (32) is divided by the effective interfacial width w_{eff} of an isolated linear dislocation, which is assumed by Luryi and Suhir [61] to five atom spacings in the [110] direction ($\Rightarrow w_{\text{eff}} = 5 \cdot b$):

$$E_{D,\text{area}} = \frac{E_{D,\text{line}}}{w_{\text{eff}}} . \tag{33}$$

In Fig. 2.16 the areal strain energy of a c-GaN/3C-SiC island with a substrate height of $h_{3C\text{-}SiC}$ = *270 nm* is plotted as a function of the c-GaN deposit thickness with different island diameters *2l*. The values are adapted to the height and length specifications of real fabricated structures, which will be introduced in section 7.4. The

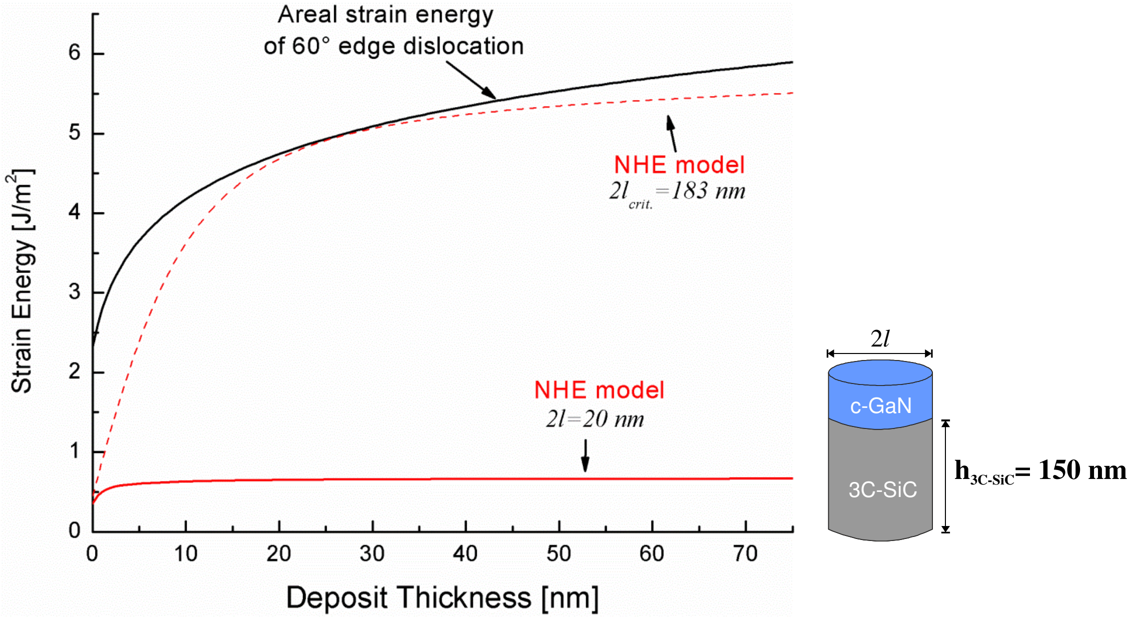

Figure 2.17

Diagram of the strain energy plotted as a function of the deposit thickness in the c-GaN/3C-SiC system with a substrate height of $h_{3C\text{-}SiC}= 150\ nm$ calculated by the NHE model of Zubia and Hersee [5].

black curve presents the areal strain energy associated with a 60°-edge dislocation, which increases with the deposit thickness.

The straight blue curves show the strain energy in the island with a diameter of $2l=240\ nm$ and secondly with a diameter of $2l=100\ nm$ calculated by the NHE model. It is obvious that the strain energy in the NHE configuration with the smaller island diameterof $2l=100\ nm$ remains below the strain energy of a mesa containing on edge dislocation (black curve) throughout the whole thickness range. In this configuration the c-GaN deposit is coherently strainedwithout generating 60°-edge dislocations.

In contrast to this, the blue curve of the *240 nm* diameter island and the black curve intersect at a c-GaN thickness of $h_{c\text{-}GaN}=10\ nm$. At this critical film thickness it is energetically favorable for an island with $2l=240\ nm$ and $h_{3C\text{-}SiC}= 270\ nm$ to create dislocations.

The dashed blue curve represents the areal strain energy of the system with a critical island diameter $2l_{crit.}=178\ nm$. Below this critical island diameter c-GaN can grow in a coherent state without dislocation formation. But above this value dislocation formation appears at a certain deposit thicknesses.

Similar results are found for a smaller substrate height of $h_{3C\text{-}SiC}=150\ nm$ and an island diameter of *20 nm* as plotted in Fig. 2.17. The black curve shows again the increase of the areal strain energy associated with a 60°-edge dislocation. The strain energy in the NHE configuration (solid red curve) remains below this dislocation energy. The critical island diameter of the *150 nm* tall structure is about $2l_{crit}=183$ *nm* and therefore in the same order of the 3C-SiC structure with a substrate height of *270 nm* discussed in Fig. 2.16. In summary, the theoretical calculations predict thatdislocation free c-GaN of arbitrary thickness can be grown on 3C-SiC islands with the configurations of ($h_{3C\text{-}SiC}=270$ *nm, 2l=100 nm*) and ($h_{3C\text{-}SiC}=150$ *nm, 2l = 20 nm*).

In section 7.4 experimental results of c-GaN grown on 3C-SiC structures with heights of *270 nm* and varying top edge lengths of *240 nm* and *100 nm* are presented. Additionally, overgrown SiC structures with a height of *150 nm* and a top edge length of *~20 nm* are analyzed. Comparing the experimental results with the calculations shown here, two differences must be taken into consideration: Firstly, the real structures have a square shape instead of a circular island form as assumed in the NHE model. Secondly, the real 3C-SiC posts are also overgrown on the sidewalls, although the NHE model assumes a selective growth on top of the nanostructures. Besides these differences structural changes, like the reduction of the SF density, in the c-GaN epilayer are clearly observed occurring when the three-dimensional growth surfaces instead of planar ones are used.

3 Characterization Methods

In the following sections the characterization methods used in this thesis are described. Reflection high-energy electron diffraction (RHEED) was used to monitor the MBE growth *in-situ*. The surface morphology of the grown epilayers was characterized with atomic force microscopy (AFM). Optical properties were investigated by cathodoluminescence (CL) and micro-photoluminescence spectroscopy (μ-PL) and the structural properties were studied by high-resolution X-ray diffraction (HRXRD), electron backscatter diffraction (EBSD), and (scanning) transmission electron microscopy (S)TEM.

3.1 Reflection High-Energy Electron Diffraction (RHEED)

During MBE growth the surface of the specimen is investigated *in-situ* by a reflected high-energy electron beam (10-20 kV acceleration voltage, in this work 16 kV), which is focused onto the surface under a small angle of 1°- 3° [69]. The electrons have a de-Broglie wavelength of about 0.06-0.17 Å. Due to the small angle of incidence, the electrons do not significantly penetrate into the sample. As a result the electron beam is mostly diffracted from the two-dimensional lattice on the surface. This method is called reflection high-energy electron diffraction (RHEED) [69].

In order to describe diffraction phenomena it is convenient to describe diffraction geometries in reciprocal space. In reciprocal space sets of parallel (*hkl*) planes are represented by a single point. But because the electron beam interacts only with the surface of the crystal the third dimension in real space is missing. Therefore, the third dimension in reciprocal space is not defined. Thus, the reciprocal space is described by rods perpendicular to the surface with a finite thickness due to lattice imperfections and thermal vibrations.

The Ewald construction [70] is used to explain the conditions for constructive interference of the elastically scattered electrons. The diffraction geometry is defined by wave vectors of the incident $\vec{k}_i$ and the diffracted $\vec{k}_d$ beam. Figure 3.1 reveals the Ewald Sphere of reflection in two dimensions together with a reciprocal lattice. First the wave vector $\vec{k}_i$ of the incident beam is drawn pointing to a lattice point in the reciprocal lattice. Then a circle around the point *M* with the radius $|\vec{k}_i| = 1/\lambda$ is constructed. Constructive interference appears when the Laue condition is fulfilled:

$$\vec{K} = \vec{g}\,, \tag{34}$$

where $\vec{K} = \vec{k}_d - \vec{k}_i$ is the difference between the k-vectors of the diffracted and incident

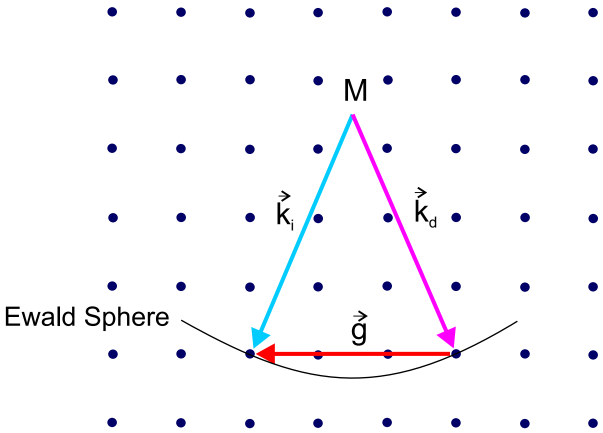

Figure 3.1

Schematically construction of the Ewald Sphere in the general case (after [71]).

waves, respectively. The reciprocal lattice vector is given by $\vec{g} = h \cdot \vec{b}_1 + k \cdot \vec{b}_2 + l \cdot \vec{b}_3$ with the Miller indices *h*,*k*,*l* and the reciprocal vectors $\vec{b}_1$, $\vec{b}_2$ and $\vec{b}_3$.

This condition means in general that the Laue condition is fulfilled if the scattering vector $\vec{K}$ ends at a reciprocal lattice point [71]. The relation of the Laue equation with Bragg´s law is given by $|\vec{K}|^{-1} = \lambda$ and $|\vec{g}|^{-1} = d_{hkl}$ with the distance d_{hkl} between the crystal planes.

In the case of RHEED, constructive interference is given if the Ewald sphere cuts through the reciprocal rods of the two-dimensional surface. A schematic drawing of the RHEED diffraction geometry is shown in Fig. 3.2. The Ewald Sphere has a finite thickness limited by the electron energy spread and by beam convergence. Additionally, the radius of the sphere is much larger than the separation of the rods. This results in the case of a two-dimensionally surface in a streaky diffraction pattern, which is visualized on a fluorescence screen. From the nature of the diffraction pattern e.g. the surface roughness and the epitaxial growth can be monitored. A streaky pattern is an indication of a two-dimensionally flat surface while a spotty pattern represents a three-dimensionally rough surface. In the second case, the electrons penetrate islands which cause diffraction from a three-dimensional instead of a two-dimensional lattice [69].

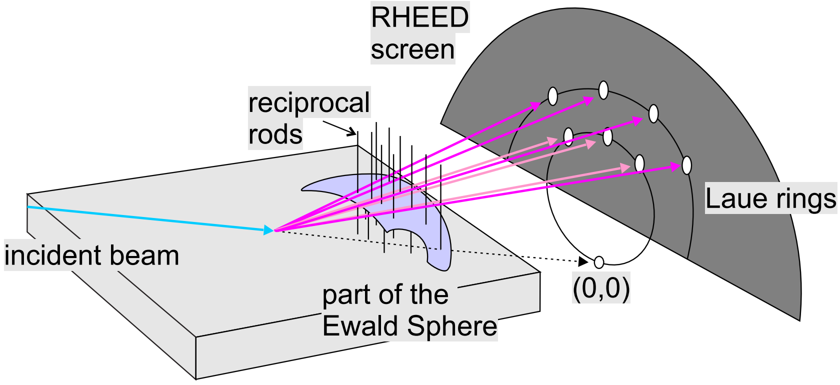

Figure 3.2

Schematic drawing of the RHEED diffraction geometry.

3.2 Atomic Force Microscopy (AFM)

The atomic force microscopy (AFM) is an experimental method to obtain information of the surface morphology, e.g. surface roughness on an atomic scale. Detailed information can be found in Ref. [72].

The operation principle of this method is outlinedin Fig. 3.3. An atomically sharp probe is mounted at the end of a flexible cantilever arm and scanned across the sample surface. When the tip approaches the sample surface forces on the atomic scale interact between the tip and the surface. Mostly van-der-Waals forces are the crucial factor. A laser beam is reflected from the reverse side of the cantilever onto a position-sensitive 4 quadrant photo detector. Any deflection of the cantilever arm produces a change in the position of the reflected laser spot. The deflection changes can be monitored and used to collect relative height information of the surface topography.

There are different operating modes in AFM, like the tapping mode and the non-contact mode, but in this thesis only the contact mode was used. Here, the probe remains in contact with the sample in a constant force mode during the measurement. A feedback mechanism keeps the deflection of the cantilever (hence the force) constant. As the cantilever arm is bent the z-height is altered to cause a return to the original starting point. A change in topography induces a bending of the cantilever, which can be used to create a topographical image. Such images can then be analyzed with regard to the root mean square (*rms*) roughness of the surface, which is defined as

$$rms = \sqrt{\frac{1}{n}\sum_{i=1}^{n}(z_i - \overline{z})^2}\ , \tag{35}$$

where n is the total number of measurement points, z_i the height at every i measurement pointand $\overline{z}$ the median value of the height. Measurements have been performed with a AFM (type MobileS) from Nanosurf and tips from Nanosensors.

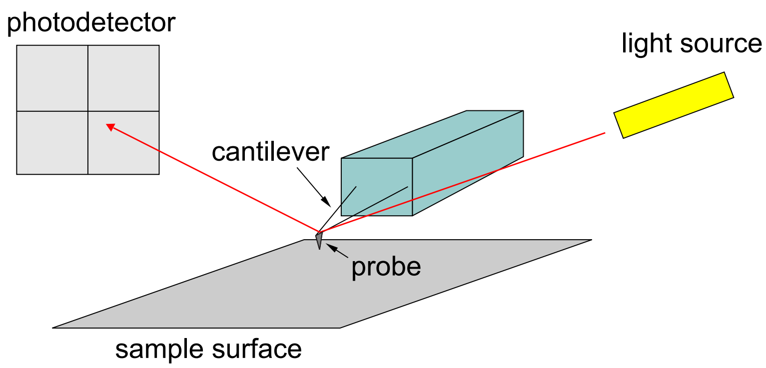

Figure 3.3

Schematic drawing of a basic AFM setup (after [72]).

3.3 Micro-Photoluminescence Spectroscopy (μ-PL)

Photoluminescence (PL) spectroscopy is a non-destructive and sensitive measurement method to analyze the electromagnetic radiation emitted by a semiconductor material [73]. The semiconductor is illuminated by laser light generating electron hole pairs which can recombine under emission of a photon. An electron is lifted from the valence band to the conduction band and is leaving behind a hole. Several excitation sources, like lasers (with energies larger than the band gap of the semiconductor), can be chosen to generate luminescence processes.

After the excitation process the material is in a non-equilibrium state. The thermal equilibrium state can be reached by relaxation and recombination processes of the excited electrons and holes (e,h). In a bulk semiconductor manifold radiative recombination processes are possible (see Fig. 3.4). The transition (e,h) represents an intrinsic band to band recombination process, (FX) a free exciton transition, (D^0,X /A^0,X) bound exciton transitions, (D^0,h), (e,A^0) free to bound and (D^0,A^0) donor to acceptor transitions. The (e,h) band to band transition can be described by the recombination of an electron in the conduction band with a hole in the valence band. The free exciton transition (FX) occurs if the generated electron and the hole are bound into a quasi-hydrogenic exciton by Coulomb interaction. The donor to acceptor transition (D^0,A^0) can appear if the semiconductor is doped or an impurity related level is introduced.

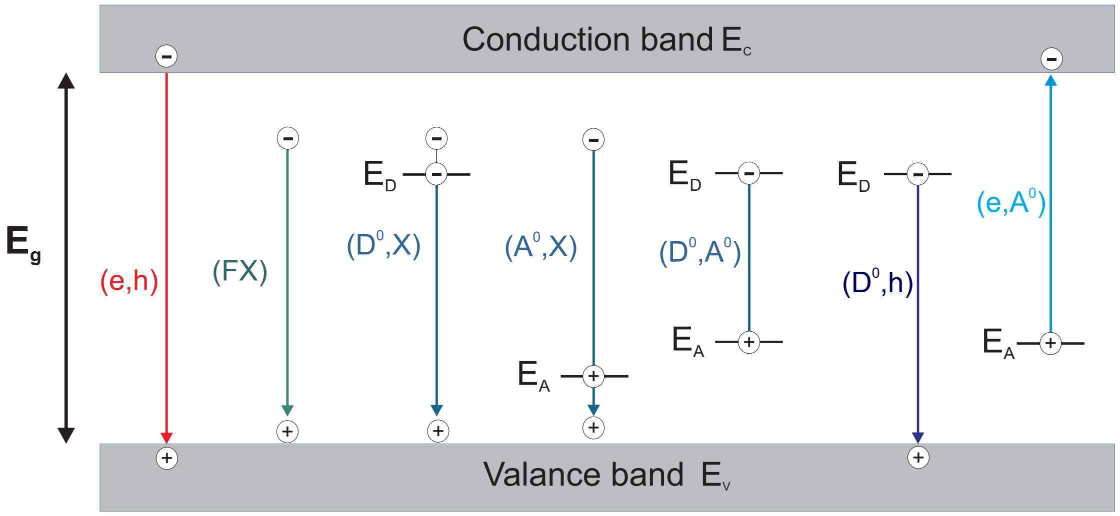

Figure 3.4

Schematic diagram of radiative transitions in a semiconductor with the conduction band E_C, the valence band E_V and the energy band gap E_g: (e,h) represents an intrinsic band to band, (FX) a free exciton, (D^0,h), (e,A^0) free to bound and (D^0,A^0) donor to acceptor transitions.

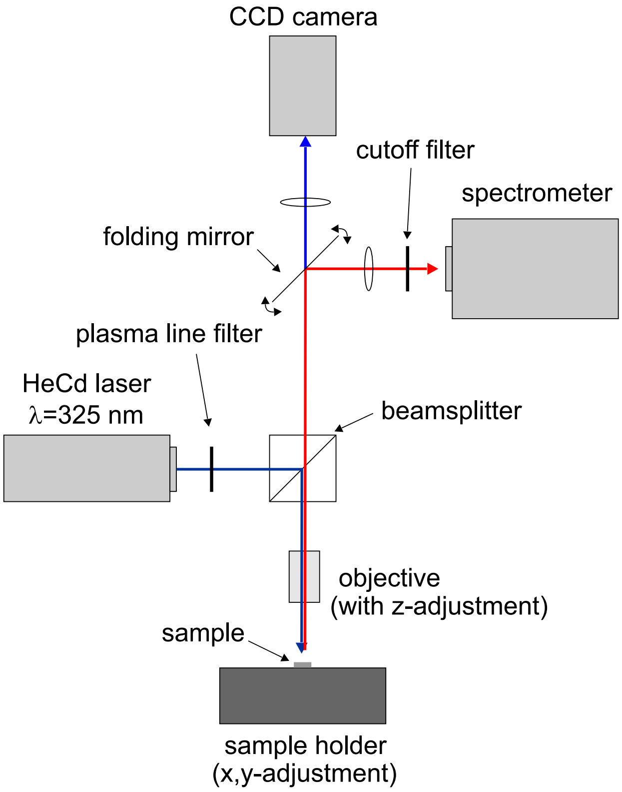

Figure 3.5
Schematic sketch of the μ-PL setup used in this thesis.

Setup

The laser beam of a Helium-Cadmium gas laser from Kimmon with a wavelength of λ = 325 nm and a laser power of 400 μW (max. 38 mW) is focused on the sample. Measurements were performed in the group of Prof. C. Meier, Faculty of Physics, at the University of Paderborn. In Fig. 3.5 a schematic drawing of the μ-PL setup is illustrated. A spatial resolution of less than 1 μm can be reached and is determined by the diameter of the laser spot. For low-temperature measurements (~7 K) the sample is mounted in a continuous liquid helium flowcryostat. In the excitation path plasma lines are eliminated by a plasma filter. The emitted light is spectrally analyzed by a Acton SP2500 spectrometer of Princeton Instruments in combination with an Acton Pixis 256 CCD detector. Additionally, a video camera is integrated in the setup to image the measurement area on the sample surface. This ensures that the collected data belong to the area of interest.

3.4 Cathodoluminescence Spectroscopy (CL)

In cathodoluminescence (CL) spectroscopy measurements electrons instead of laser light are used to generate electron hole pairs in the semiconductor sample. The energy of the electrons is in the order of several keV and therefore convenient to analyze materials with a large bandgap (e.g. GaN, AlN). Another advantage compared to PL is the superior spatial resolution (<100 nm) which depends on the excitation volume. Therefore, this measurement method is an adequate tool to investigate nanometer structures. Useful information can be found in Ref. [74].

Setup

For the CL spectroscopy a JEOL JSM6400 scanning electron microscope (SEM) equipped with a LaB_6- source and a helium cooled cryostat (4.2-300 K) is used in the group of Prof. Christen at the Otto-von-Guericke University of Magdeburg. The sample is mounted on a holder which is tilted about 45° with respect to the impinging electron beam. Here, a spatial resolution of about 40 nm can be achieved. The emitted light is collected by an elliptical half space collimator mirror and then coupled into a Spex 270M monochromator.

To record CL wavelength images (CLWIs) the emission spectra of the local maximum intensity are mapped at each point. To do this, the electron beam is scanned over the area of interest (256× 200 pixels). A complete luminescence spectrum is taken from each pixel with e.g. an acceleration voltage of 10 kV and a beam current of 1.3 nA. Three-dimensional data $I(x,y,\lambda)$ are generated and can be evaluated *ex-situ* to investigate local spectra, monochromatic images and as well as the CLWI maps [75, 76].

3.5 Micro-Raman Spectroscopy (µ-Raman)

In this spectroscopy method the sample is excited by laser light which allows the observation of elementary excitations of the material by measuring the frequency shift between the incident and the scattered photons. The first quantum event in a Raman process is the absorption of an incident photon creating an interband electron-hole pair. This leads to an intermediate electronic state which then may interact with elementary excitations, e.g. phonons. At the end, charges in the intermediate state recombine by emitting a photon with a different frequency. This process, the absorption/emission of elementary excitations via an intermediate state, is named Stokes or Anti-Stokes scattering. In general, if the scattering process takes place without a change in frequency it is called Rayleigh scattering and with a change in frequency it is named Raman scattering. Information about the structural properties can be obtained by this method because e.g. defects and strain affect the phonon frequencies. More detailed information about this method is given in [77], [78].

In this work, Raman measurements were carried out in backscattering $z(x,y)\underline{z}$ geometry where x=[100], y=[010] and z=[001] in the group of Prof. Hoffmann at the TU Berlin. The 532 nm line of a Nd:YAG-laser with a power of 60 mW was used for excitation.In this configuration the incident beam of the laser is parallel to the [001] growth direction. For detailed information line scans with a lateral resolution of 0.25 µm in a measurement area of (20 µm×20 µm) have been executed.

3.6 High-Resolution X-Ray Diffraction (HRXRD)

High-resolution X-ray diffraction (HRXRD) is a non-destructive measurement method which is used to obtain the structural properties like the composition and the crystal quality of semiconductor materials. Here, reciprocal space mapping has been performed to determine the content of hexagonal inclusions in the planar and selective-area-grown c-GaN films. Also, the overall defect density can be assessed by rocking curves.

X-ray diffraction measurements imply the following essential components. The sample, mounted on a goniometer stage, is hit by an incident X-ray beam which is diffracted according to Bragg´s law at the crystal planes. The diffracted X-ray beams are detected with known orientation with respect to the incident beam. Figure 3.6 shows a sketch of the measurement setup with the sample postion. Here, the angle between the incident wave $\vec{k}_i$ and the surface of the sample is called ω and the angle between the crystal planes and the incident wave $\vec{k}_i$ is given by θ, respectively. The angle between the incident beam $\vec{k}_i$ and the diffracted beam $\vec{k}_d$ is 2θ. Constructive interference occurs when the Laue condition is fulfilled (see section 3.1). Diffraction can be described by the construction of the Ewald Sphere as demonstrated for the diffraction process of electrons in section 3.1. But there is a difference between the diffraction of electrons and the diffraction of X-rays. “X-rays are scattered by the electrons in a material through an interaction between the negatively charged electrons and the electromagnetic field of the incoming X-rays. The electrons in the specimen respond to the applied field of the X-ray flux, oscillating with the period of the X-Ray beam. These accelerated charged particles then emit their own electromagnetic field, identical in wavelength and phase to the incident X-rays. The resulting field, which propagates radially from every scattering source is called scattered wave.” [71]. In contrast, in electron diffraction processes the electrons are scattered by the electrons and nuclei in the specimen. More detailed information about X-ray diffraction can be found e.g. in [79] and [80].

Setup

All HRXRD data presented in this work were collected by a Philips X’Pert materials research diffractometer with a copper anode emitting a $K_{\alpha 1}$ radiation of λ=1.54056 Å. Figure 3.6 depicts a schematic drawing of the X-ray measurement setup. The tube is equipped with a line focus and a monochromator resulting in a beam divergence of 47 arcsec. The monochromator consists of a parabolic mirror parallelizing the beam and a (220) channel-cut germanium crystal (2-crystals, 4 reflections) filtering out other wave

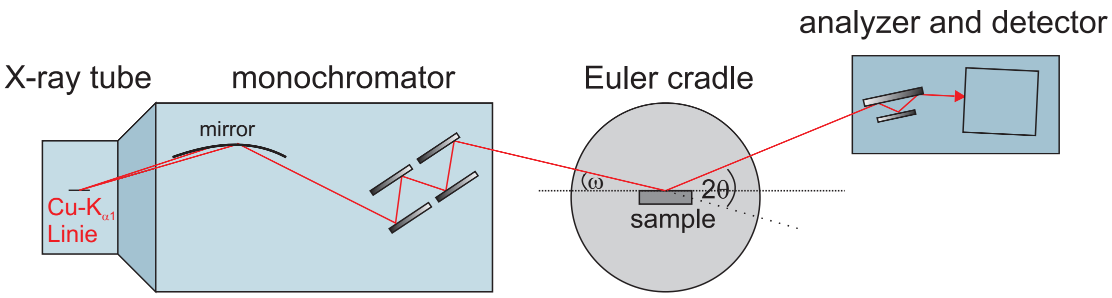

Figure 3.6

Schematic drawing of the X-ray measurement setup with an X'Pert HRXRD diffractometer with X-ray source, monochromator, a sample mounted on an Euler cradle and a detector unit (after [81]).

lengths (e.g. the $K_{\alpha2}$-line). Then the beam hits the sample mounted on an Euler cradle under grazing incidence. Due to the grazing incidence the spot becames elliptical and covers an area of a few mm^2. Using the Euler cradle the sample can be manipulated about six axes. The diffracted beams are detected by a multichannel detector, a Philips Analytical X'Celerator detector, consisting of an analyzer (220 germanium crystal, 3 reflections) and a CCD detector.

Measurement Modes

The detailed analysis of diffraction patterns around reciprocal lattice points is the subject of high-resolution diffractometry. As mentioned at the beginning different measurement modes can be performed, like ω -scans, $\omega - 2\theta$ scans and reciprocal space mapping (RSM) [80].These different scan modes are sketched in the illustration of the diffraction geometry in Fig. 3.7. This sketch tries to connect the sample in real space with its lattice planes, separated by a distance of d_{hkl}, with the reciprocal space where the diffraction geometry can be described (see chapter 3.1). In the case of constructive interference the scattering vector $\vec{K}$ in reciprocal space, which is perpendicular to the real lattice planes of the sample, ends at a reciprocal lattice point (here the [113] reflection). That means that the lattice planes shown inside the sample are {113} planes. If the lattice planes are parallel to the surface the ω and the θ angles are equal. Usually, in X-ray notation the reciprocal lattice vector $\vec{g}$ is called $\vec{q}$. Therefore, the reciprocal lattice parameters are referred to $\vec{q}_\perp$ and $\vec{q}_\parallel$.

ω-scan

The ω-scan is called rocking curve and is a special scan through a reciprocal lattice spot parallel to the reciprocal lattice parameter $\vec{q}_\parallel$. The angle of incidenceω is changed by "rocking" the sample and detecting the signal with the maximum area of the detector.

The broadening of a reciprocal lattice point is correlated to e.g. defects contributing to scattering around the Bragg peaks. Therefore, the FWHM of the diffraction peak contains information about the crystalline quality. The dislocation density D_{disl} can be evaluated from the FWHM by the model of Gay [11] with the relation:

$$D_{disl} = \frac{\Delta\theta^2}{9b^2}, \tag{36}$$

where $\Delta\theta$ is the FWHM of the rocking curve in radians and b the length of the Burgers vector. In literature the dislocation density for zinc blende crystals is often calculated with a Burger´s vector of

$$b = \frac{a}{\sqrt{2}} \tag{37}$$

with the lattice constant a of the material.

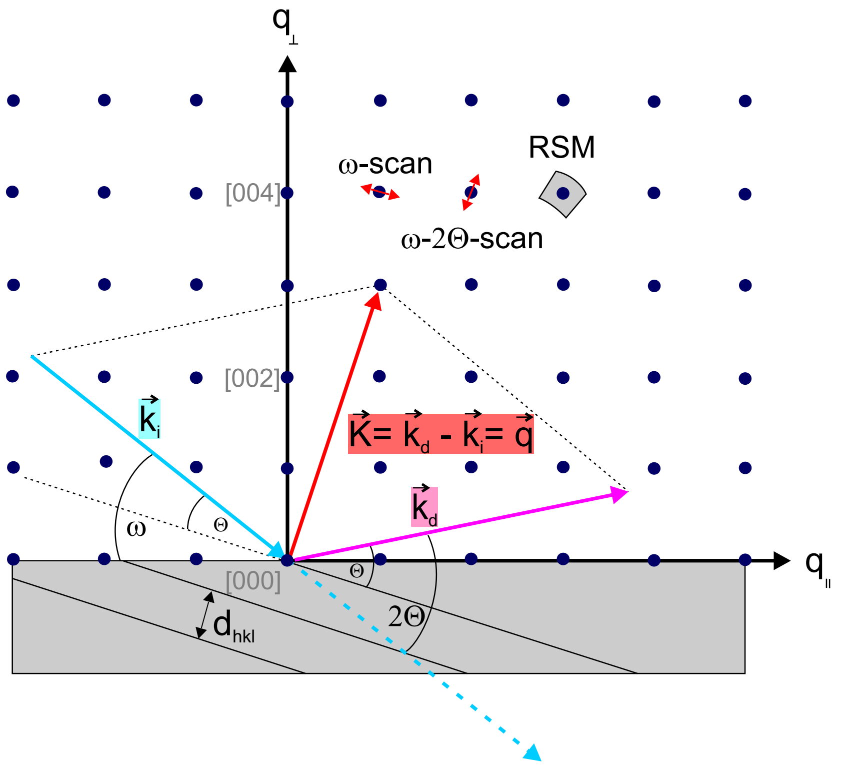

Figure 3.7

Sketch of the diffraction geometry of X-ray measurements. This sketch tries to connect the reciprocal space with the reciprocal lattice parameters $\vec{q}_\parallel$ and $\vec{q}_\perp$ with the real space of the sample. The scattering vector $\vec{K}$ in reciprocal space, which is perpendicular to the real lattice planes, ends at a reciprocal lattice point (here the [113] reflection).

ω -2θ-scan

This mode is realized rotating the detector angle twice of the incidence angle ω. In case of a “symmetrical scan” ($\omega = \theta$) the scan and the crystal planes are parallel to the sample surface. A $\omega - 2\theta$-scan enables to receive information about e.g. the lattice parameter and indirectly the chemical composition.

Reciprocal Space Map (RSM)

For a two-axis reciprocal space map $\omega - 2\theta$-scans are repeated over a small angular range over the area of interest (e.g. a reciprocal lattice point). In a RSM the intensity is plotted graphically as a function of the diffraction vector coordinates $q_{\perp}, q_{\parallel}$. These maps show the exact reflection maximum and contain information about the expansion of the lattice parameter and the strain, respectively. Addionally, for example from a RSM around the (002) reflex of c-GaN, hexagonal inclusions can be determined. If the c-GaN layer contains a significantly fraction of the hexagonal phase, these hexagonal inclusions appear as additional reflections in the RSM. This has been shown by Sun et al. [82] in the c-GaN/GaAs system. From the intensity ratio of the cubic and the hexagonal reflex the percentage of the hexagonal phase can be estimated.

3.7 Electron Backscatter Diffraction (EBSD)

Electron backscatter diffraction (EBSD) is a powerful structural characterization technique integrated in a SEM setup. In this method the primary electron beam is inelastically and elastically scattered by the crystal planes of the sample. This yields so called Kikuchi diffraction patterns, in which each pair of Kikuchi lines represents a crystal plane [83]. With this measurement method surfaces of bulk crystals can be analyzed in view of individual grain orientations, local textures, phase mapsand so on. In this work, EBSD was used for phase identification of different domains in c-GaN (see section 7.1). These measurements were performed in the group of Prof. H.-J. Maier, Lehrstuhl für Werkstoffkunde, at the University of Paderborn. The main references concerning the fundamentals are [84] and [71].

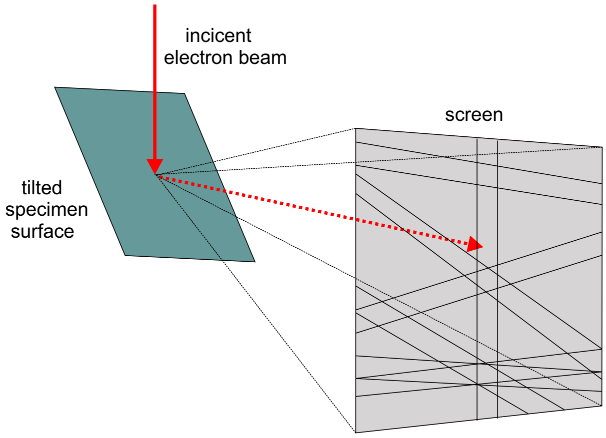

Figure 3.8
Schematic drawing of scattered electrons forming Kossel cones centered in the diffraction plane (after [84]).

Setup and Measurement Method

For the measurements a FEI XL40 ESEM with a tungsten cathode operating at 20 kV was used. The focused primary electron beam is moved across the area of interest on the tilted sample surface with a 0.6 µm stepsize. The sample is tilted by about 70° from the surface normal in order to increase the inelastic signal. Due to the specimen tilt the spatial resolution on the surface along the beam direction is about three times worse than perpendicular to this direction. In general, the resolution is not governed by the diameter of the beam spot on the specimen surface but it is affected by the excitation volume. Figure 3.8 shows a sketch of scattering geometry. The incident beam scans over the raster grid on the tilted sample surface.

The impinging electron beam contains electron waves with a small energy and angular distribution, which are elastically and inelastically scattered in the crystal. In Fig. 3.9 some of the electrons travel at theBragg angle θ_{hkl} to certain *hkl* planes and will be Bragg reflected. The diffracted beam will lie on one of two cones, which are called Kossel cones. The pair of Kossel cones, also called Kikuchi band, can be detected. Inelastic scattering leads to a broadening of the angular distribution of the electron beam. The physical principle is illustrated by the intersection with the detection screen. The geometrical projection of the appropriate *hkl* plane lies in the center of the Kikuchi band. “The width of the Kikuchi band is twice the Bragg angle θ_{hkl}. Thus, the width of the bands is related to the interplanar spacing, d_{hkl}, according to Bragg´s law:

$$2 \cdot d_{hkl} \cdot \sin \theta_{hkl} = n \cdot \lambda \quad , \tag{38}$$

Where n is the order of reflection and λ is the wavelength of the incident electron beam, which is dependent on the accelerating voltage of the SEM.” [84].

The phase identification of GaN was achieved by analyzing the Kikuchi patterns of the crystal planes of the sample. Therefore, the crystal plane identificationwas achie-

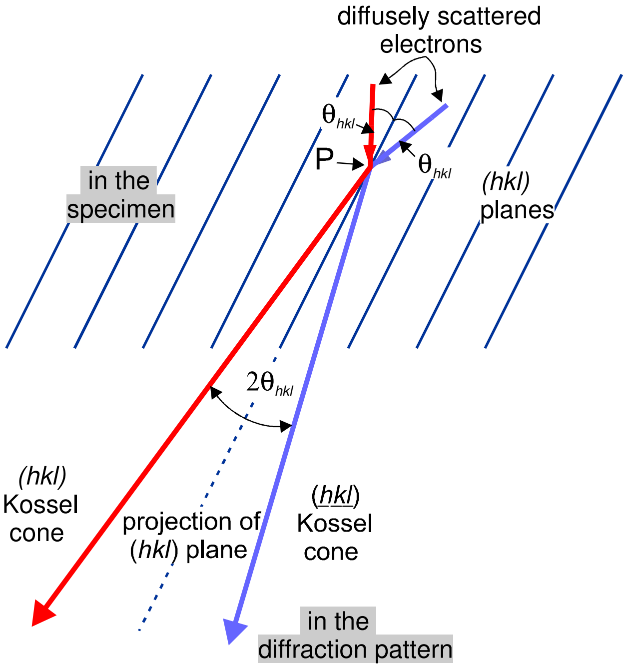

Figure 3.9

Sketch of a digital beam scanning setup (after [71]).

ved by a Hough-transformation [85] of the recorded diffraction patterns followed by a least-square fit to simulated Kikuchi patterns of both the cubic and the hexagonal phase, yielding a phase identification based on the smallest error. The angular resolution of this kind of EBSD method – for e.g. detection of rotational domains inside a crystal – is limited to 1-2°. Figure 3.10a shows a detected Kikuchi diffraction pattern of c-GaN and in Fig. 3.10b a simulated Kikuchi pattern of c-GaN is compared to the experimental pattern of Fig. 3.10a. In Fig. 3.10c a hexagonal GaN pattern is simulated to show the difference between the cubic and the hexagonal patterns.

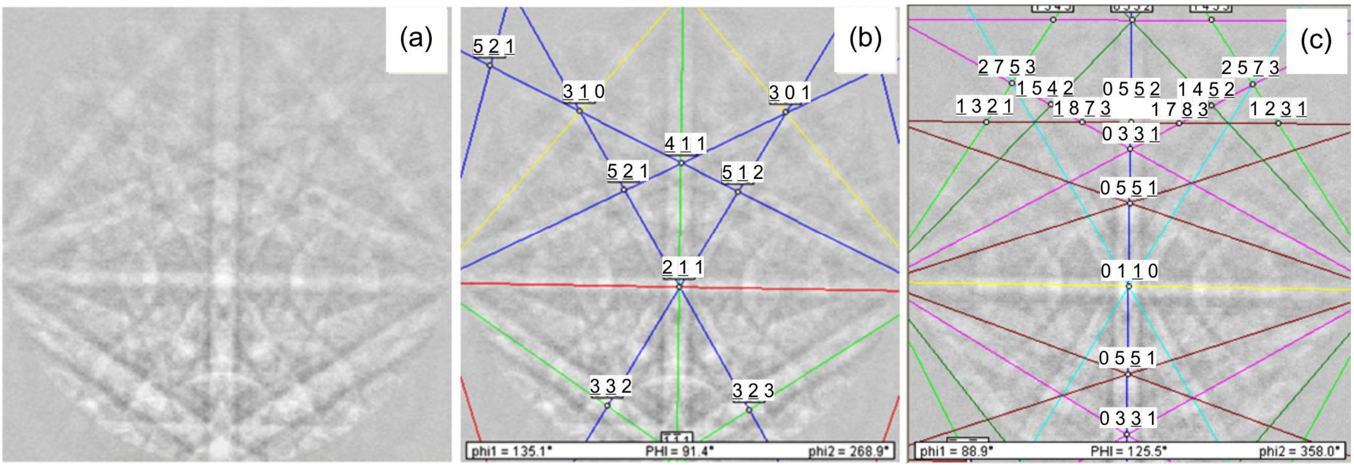

Figure 3.10

(a) Experimental Kikuchi diffraction pattern of c-GaN compared to a cubic simulation **(b)** and a **(c)** hexagonal simulation.

3.8 Transmission Electron Microscopy (TEM)

In this work, (scanning) transmission electron microscopy ((S)TEM) is the method of choice to analyze the structural quality of the overgrown nanostructures (see section 7.3 and 7.4). Some of the investigations were performed with a JEOL FX2000 and a Phillips CM200/STEM both operating at 200 kV at the University at Paderborn. The high-resolution and scanning TEM images were taken with a FEI Tecnai G2 F20 TEM operating at 200 kV, a FEI Titan 80-300 TEM and a FEI Titan 80-300 STEM both operating at 300 kV at the Ernst Ruska-Centre for Microscopy and Spectroscopy with Electrons (ER-C) at the Forschungszentrum Jülich. For conventional TEM and especially for high-resolution TEM the specimens have to be very thin (~10 nm) in the area of interest. Therefore, special preparation techniques have been applied which are described in detail in chapter 6. All TEM specimens presented in this thesis are prepared in cross-section. In the following the general TEM setup, electron diffraction and the imaging in a TEM are briefly discussed. More detailed information can be found in [86] and [71].

Setup

Figure 3.11 illustrates a schematic drawing of a simplified conventional TEM setup. In general the setup can be divided into three parts: the illumination system, the sample stage with the objective lens, and the imaging system. The illumination system includes the electron source which is placed in the upper part of the TEM column, the accelerator and the condenser lenses. The electron beam can be generated by thermionic emission or field-emission depending of the type of electron source. With the electric field from a Wehnelt cylinder the beam is then focused into a “cross-over” which acts as the first source for the following electromagnetic lenses in the illumination system. Then the electrons are accelerated to their maximum velocity and transported to the specimen. This can be realized in two different modes. Either the beam is parallelized which is used primarily for imaging and electron diffraction with a stationary broad, coherent beam or a convergent beam of adjustable convergence angle and spot size is used mainly for STEM imaging and convergent beam electron diffraction. In the scanning mode the beam rasters across the sample like in the SEM.

In the center of the TEM column the electrons interact with the specimen which is placed in a sample holder. Underneath the specimen the objective lens is positioned, which is of crucial importance in the TEM, because it forms the images and the diffraction patterns (DPs). In the imaging system are several lenses which magnify the images produced by the objective lens. At the end, the final projector lens focuses the information on a viewing screen or detector, forming an image of the sample or a diffraction pattern.

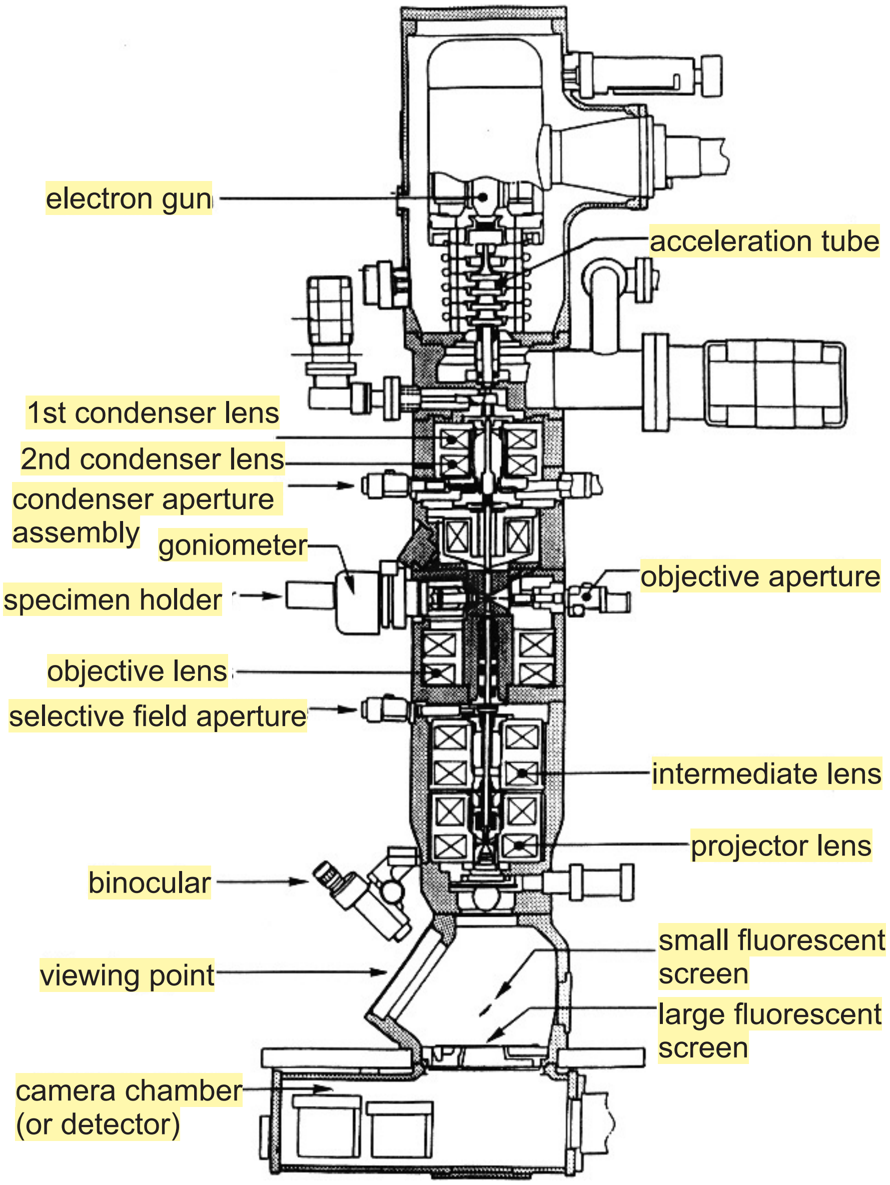

Figure 3.11

Schematic drawing of a simplified conventional TEM setup (after [86]).

Electron Diffraction

Elastic scattering of electrons in the sample, is one of the most important scattering phenomena in the TEM and leads to electron diffraction. Electron diffraction can be used to determine the size and the shape of the unit cells by measuring the positions of the diffracted electron beams. In Fig. 3.12 an overview of different kinds of electron interactions from a thin specimen are shown. Scattering that results in no loss of energy is described with the term *elastic* and if electrons lose energy the process is called *inelastic* scattering. The terms *coherent* and *incoherent* refer to the wave character of

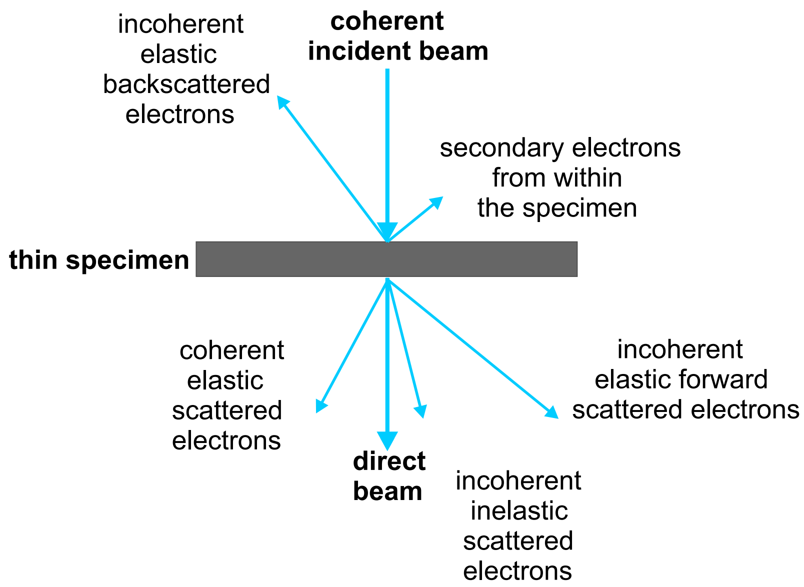

Figure 3.12

Overview of different kinds of electron scattering from a thin specimen (after [71]).

the scattered electrons, which are in a fixed phase with the incident electron wave or have no phase relationship.

The interaction of the electron beam with a crystal can be described to some extent using the so called “kinematical theory”. This is a simplified model which considers one scattering process and not two or more scattering processes like in the “dynamical theory”. Further, it is assumed that the electrons are only scattered elastically and that there is no decrease of intensity of the incident beam. The incident beam can be described as a plane wave with an amplitude ψ_0 and a phase $2\pi\vec{k}\cdot\vec{r}$

$$\psi = \psi_0 \exp(2\pi i\vec{k}\cdot\vec{r}), \tag{39}$$

where $\vec{k}$ is the wave vector and $\vec{r}$ the distance that the wave has propagated. The amplitude of the electron beam $A_{\text{unit cell}}$ scattered from a unit cell is

$$A_{\text{unit cell}} = \frac{e^{2\pi ikr}}{r}\sum_i f_i(\theta)\exp(2\pi i\vec{K}\cdot\vec{r}_i). \tag{40}$$

The summation is taken over all *i* atoms in the unit cell and the angle θ is at which the diffracted beam is traveling relative to the incident beam. Like in X-ray diffraction the scattering vector $\vec{K} = \vec{k}_d - \vec{k}_i$ is the difference between the k-vectors of the diffracted and incident waves, respectively. $f_i(\theta)$ is the atomic scattering factor. All *i* atoms, which location is defined by the vector $\vec{r}_i = x_i\vec{a} + y_i\vec{b} + z_i\vec{c}$ with atomic coordinates x_i, y_i, z_i and crystal lattice translation vectors $\vec{a}, \vec{b}, \vec{c}$ within this unit cell, scatter with a phase difference given by $2\pi i \vec{K} \cdot \vec{r}_i$ .The structure factor $F(\theta)$ is a measure of the amplitude scattered by a unit cell of acrystal and $|F(\theta)|^2$ is proportional to the scattered intensity:

$$F(\theta) = \sum_i^{\infty} f_i(\theta) \exp 2\pi i \left(h x_i + k y_i + l z_i\right) \tag{41}$$

where *h*, *k*, and *l* are Miller indicesand define the plane (*hkl*). Constructive interference appears when the Laue condition $\vec{K} = \vec{g}$ (Eq. 34) is fulfilled (see section 3.1). A more precise description of electron diffraction enabling the description and interpretation of all observable contrast phenomena based on elastic scattering can be achieved using the dynamical theory of electron diffraction which was introduced by Hirsch and Howie in 1962 and is discussed in detail in [87] and other good text books on electron microscopy like [71].

Imaging

There are different imaging techniques available in a TEM. The general ray path in the imaging mode is shown schematically in Fig. 3.13a. The electrons that emerge from the specimen pass through the electromagnetic field of the objective lens. Here, the lens focuses them to create a DP in the back focal plane. After that an image is produced by recombining the DP in the image plane. In the *bright field (BF)* image mode (Fig. 3.13b) an objective aperture is positioned in the back focal plane of the objective lens which only lets the forward scattered ("transmitted") electrons pass. This leads to a contrast rich image in which the contrast results from the weakening of the transmitted electron beam by its interaction with the specimen. Therefore, thick areas and regions where interaction with heavier atoms takes place appear with darker contrast. In this case, the contrast results from a change in the amplitude of the electron wave which isdue to variations in mass or thickness. In the same way, regions of the sample which are oriented in such a way that electrons are strongly scattered out of the forward direction also appear dark, but this time due to diffraction contrast. Another imaging mode is the *axial dark field (DF)* mode (Fig. 3.13c). In this mode, the specimen is illuminated by a tilted incident beam so that a selected beam travels out on the optical axis. In contrast to the BF images, regions that diffract into a specific angle appear bright in DF mode.

The imaging TEM system can also be used to form *selective area diffraction (SAD)* patterns on the viewing screen (see Fig. 3.13d). Therefore, the lenses are adjusted such that the back focal plane of the objective lens acts as the object plane of the intermediate lens. Additionally, a SAD aperture is inserted to limit the sample region from which electrons contribute to the diffraction pattern. The image mode is received again, if the intermediate lens is readjusted so that its object plane is again the image plane of the objective lens.

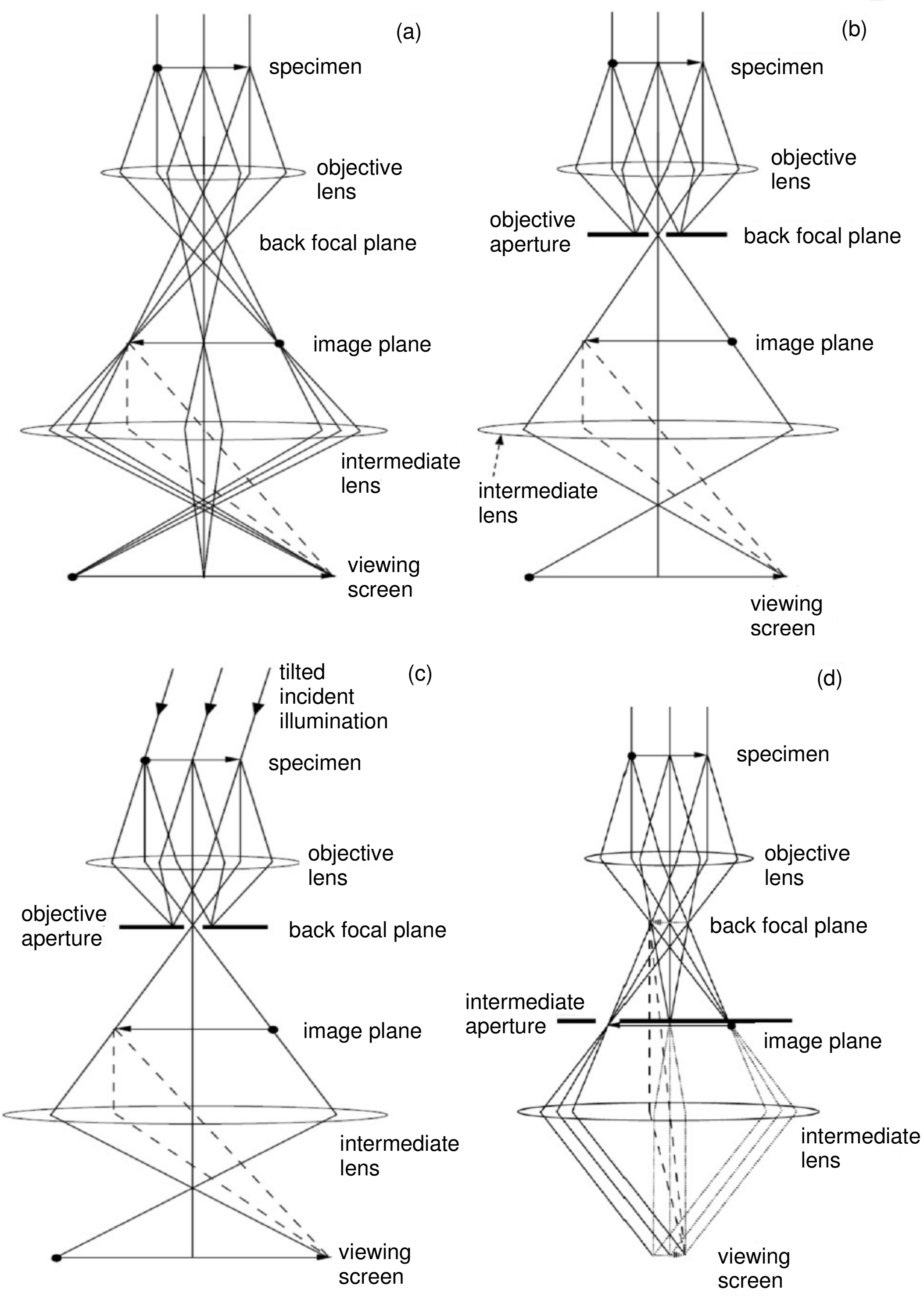

Figure 3.13

Different imaging techniques in a TEM **(a)** general ray path in image mode **(b)** bright field (BF) image mode **(c)** axial dark field (DF) image mode **(d)** selected area diffraction (SAD) mode (after [86]).

In the following experimental results *high-resolution TEM (HRTEM)* images of the crystal structure will be shown. The basic principle of HRTEM is that a very thin (<20 nm) specimen is illuminated by an incident coherent plane electron wave.Inside the specimen the electron wave experiences a phase change and a shift in amplitude and channels along the atom columns of the crystal lattice. Because the specimen is very thin, the change in amplitude can be neglected. The phase change depends on the electrostatical potential of the specimen atoms which the electrons see when they pass through the thin specimen. As a result, the exit electron wave is a superpostion of the the forward scattered incoming wave and the diffracted beams with different scattering angles. The best spatial resolution is achieved if the range of scattered wave fronts with high angles (high values of Δk) large, because they correspond to small distances in real space. Large Δk means that the outer regions of the objective lens are used where the electron waves are affected by the spherical aberration C_s of the lens. The spherical aberration C_s and the focus of the objective lens require phase shifts of the electron waves. In order to get maximum contrast of the lattice planes the sum of these phase shifts have to be considered. Therefore, the so called Scherzer defocus of the objective lens is adjusted which depends on the electron wavelength and the sperical aberration C_s of the objective lens.

Another technique to produce high-contrast images is *scanning TEM (STEM)*, where a narrow incident electron beam is focused and scanned across the specimen using scan coils. In Fig. 3.14 a comparison between the use of an objective aperture in a conventional TEM in BF and DF imaging mode and the use of a detector in a STEM system is shown. With an *annular dark field (ADF)* detector the scattered electrons are detected. Since the cross section for elastic scattering into large scattering angles depends on the atomic number (Z), the ADF detector is very sensitive for the mass-thickness contrast. Thicker or higher Z-areas will scatter more electrons off-axis than thinner regions or areas with lower masses. The Z-contrast could be increased bycollecting electrons with higher scattering angle, because at low scattering angles (<5°) the detected signal contains also Bragg scattered electrons. This is the *high-angle ADF (HAADF)* imaging technique. In the HAADF-STEM modus the contrasts are less influenced by local strains and atomic columns appear as bright dots with the intensity increasing with increasing atomic number.

STEM-CL

A powerful analytical tool in STEM is the integration of a CL setup. A parabolically shaped mirror is located above the specimen which collects the CL emission and focuses it onto the entrance slit of a monochromator (here a Mono CL4 monochromator from Gatan). With this measurement setup it is possible to measure simultaneously STEM images and CL signals with high spatially correlation. This measurement method

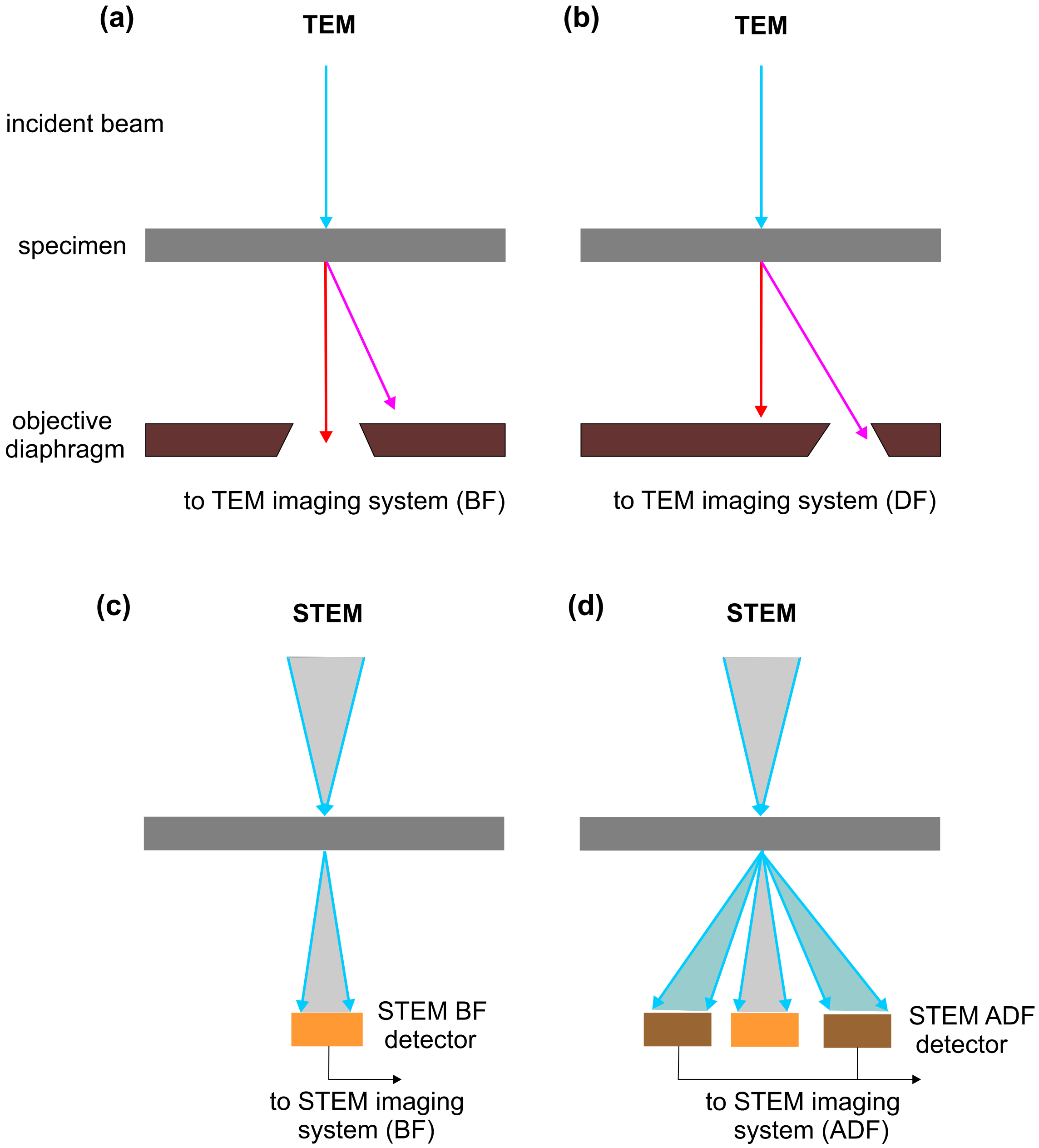

Figure 3.14

Comparison of the use of an objective aperture in a conventional TEM in BF and DF imaging mode (**a-b**) with the use of an detector in a STEM system (**c-d**) is shown (after [71]).

can be applied for example to correlate planar structural defects and their luminescence output (see section 7.2).

In this work the used CL setup is integrated in a Tecnai F20 (S)TEM operating at 80 kV at the Otto-von-Guericke University of Magdeburg in the group of Prof. J. Christen [88]. Within the STEM-CL mode the excitation resolution is about 1 nm at room temperature and <5 nm at 12 K. The lateral resolution of the CL signal with anestimated specimen thickness of 150-200 nm of the cross-section TEM specimens is determined to about <20 nm. The effect of charge carrier diffusion should be also considered, but is not quantified in this work.

JEMS Simulation

Selected area diffraction is used to identify different crystal structures. In chapter 7 SAD patterns of conventional cross-section TEM images and Fast Fourier Transformations (FFTs) of high resolution images along the [110] direction will be used to characterize GaN layers concerning its phase. To this end, SAD patterns from cubic and hexagonal GaN along the [110] zone axis were simulated by the program JEMS version 3.6907U2011 [17]. Therefore, an acceleration voltage of 200 kV and a camera length of 100 cm were assumed.

In Fig. 3.15a the schematic drawing of a c-GaN unit cell with an indexed diffraction pattern along the [110] direction is plotted. Figure 3.15b shows the same for h-GaN viewed along the $[11\underline{2}0]$ zone axis. These two directions are interrelated by the epitaxial relationship of c-GaN and h-GaN of $(110)_{\text{c-GaN}} \parallel (11\underline{2}0)_{\text{h-GaN}}$ together with $(111)_{\text{c-GaN}} \parallel (0002)_{\text{h-GaN}}$. A superposition of both diffraction patterns is observable if hexagonal inclusions are formed within the cubic phase. A simulation of the superposition of both SAD patterns can be found in [89].

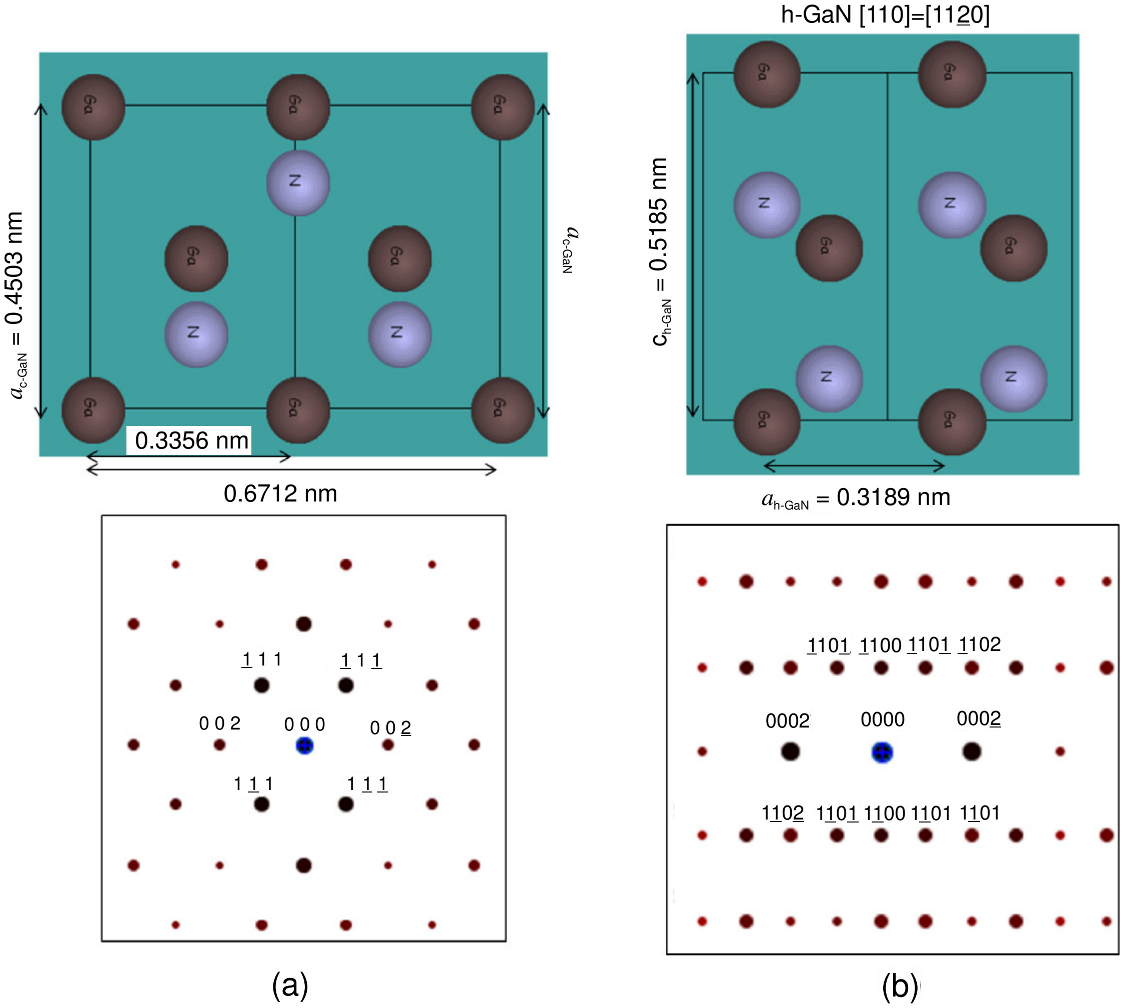

Figure 3.15

Simulated unit cells in [110] and [11$\underline{2}$0] directions together with the associated SAD patterns of **(a)** c-GaN and **(b)** h-GaN, respectively. Calculations were performed by the program JEMS version 3.6907U2011 [17].

4 Substrate Patterning

In the following the different basic steps towards nano-patterning of the 3C-SiC/Si (001) substrate will be explained. Two techniques are used to obtain nano-patterns on the substrate: nanosphere lithography (NSL) and electron beam lithography (EBL). Both methods are followed by a lift-off process and a reactive ion etching (RIE) process. Two sample series with mesa shaped SiC structures fabricated by EBL and RIE will be discussed separately. The first sample series consists of free-standing post shaped structures with a top edge length of ~500 nm and a height of about 700 nm. They have been fabricated by Hiller et al. [90] at the University of Ilmenau. The second sample series has free-standing nanostructures with top edge lengths from ~240 nm down to ~20 nm and heights from ~270 to ~150 nm. This series has been produced at the University of Paderborn.

4.1 Nano-Patterning by Nanosphere Lithography

Nanosphere lithography (NSL) is a low-cost method to produce regular nanoscale surface patterns of scalable size and with a variety of motifs [91]. This method uses a self-organized monolayer of nanobeads as a shadow mask in order to create nanopatterns on a surface. The advantage of this technique is that it can easily produce nanopatterns on areasseveral centimetres large. Therefore, thin film growth studies on NSL patterned surfaces can subsequently employ all of the standard characterization techniques with typical sampling areas of few millimeters diameter. Following infomation is based on previous work [58] and therefore presented here in an abbreviated form.

Due to the hydrophobic character of SiC [92], the substrates were coated with ~16 nm of SiO_2 by plasma enhanced chemical vapour deposition (PECVD) followed by a wet chemical cleaning process (H_2O:NH_3:H_2O_2=3:1:1), which yielded well defined hydrophilic sample surfaces. The surface was subsequently covered with a mask of 600 nm diameter polystyrene (PS) spheres forming a self-organized hexagonally close- packed monolayer throughout most of the sample surface. This was achieved by the controlled drying [93] of a droplet of an aqueous suspension of colloidal PS spheres. In a next step, the spheres were shrunken in oxygen plasma as outlined in [94]. On top of the colloidal mask ~60 nm of Ni was deposited by thermal evaporation and the PS spheres were removed. The resulting Ni-mask coated 3C-SiC/Si (001) was vertically etched by ~300 nm using a RIE system “Plasmalab 80P“ from Oxford Instruments (see section 4.3). After removing the metal by $FeCl_3$ and DI-water (1:3), the samples were cleaned with a buffered oxide etching solution (NH_4F:H_2O:HF=4:6:1). Altogether, this

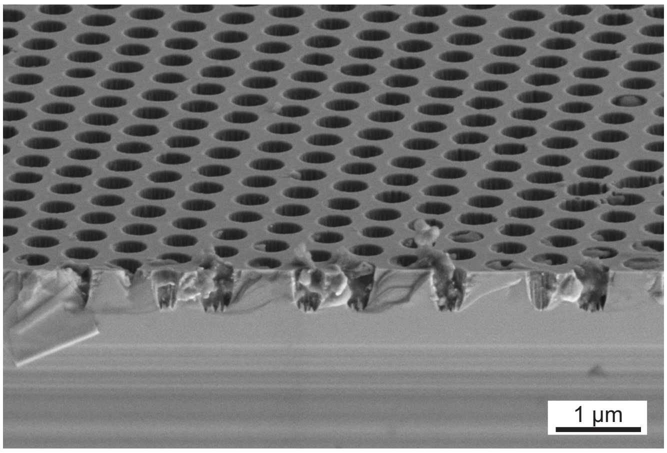

Figure 4.1
Side view SEM image of a 3C-SiC (001) surface nano-patterned by NSL [58].

procedure allows for the creation of surface patterns with a lateral feature sizes of few ten to few hundred nanometers. Figure 4.1 shows a tilted view SEM image of a cleaved nano-patterned 3C-SiC (001) surface. The hole-diameter is about 400 nm and the depth is about 300 nm. Since the cleaving edge cuts through some holes it is obvious that the etching process leads to a high surface roughness at the bottom of the holes. The minimum width of the sidewalls of the holes is determined by the duration of the plasma shrinkage process and amounted to roughly 200 nm in this example.

4.2 Nano-Patterning by Electron Beam Lithography

Electron beam lithography (EBL) [95] is one of the most common techniques to fabricate nanostructure masks. Even though for time reasons one would typically fabricate nanostructures only in small areas of few hundret µm^2, the high flexibility in motive shapes and the excellent precision at which motives can be reproduced make EBL attractive for patterning substrates for selected-area growth studies.

In order to produce small pattern sizes in the range of 100 nm for nano-heteroepitaxy, an individual patterning process with a new designed lithography mask was developed. Therefore, the substrate was covered with a ~130 nm thick layer of positive photoresist (type PMMA 950k (AR-P 671.02)). After spinning the resist for 30 s with 2000 rpm the sample is baked for about 2 min at 150 °C on a hot plate. The mask for the EBL process consists of 7x8 arrays with different sizes of nanotructures and was designed with a Pioneer software from Raith GmbH [96].

Figure 4.2 shows an overview of the mask design. The columns are marked with capital letters (A-D) and the lines are marked with numbers (1-8). The size and the distance of the square shaped structures within one array are listed in Table 4.1.

A square shape is used, because the pattern symmetry may play an important role if coalescent layers are achieved after prolonged layer growth. Zubia et al. [63] expect that a hexagonal symmetry yields a superior coalescent hexagonal GaN film in comparison to asquare symmetry. Therefore, a rectangular symmetry is fabricated to support the cubic crystal structure.The edges of the squares are aligned with the (110) plane of the 3C-SiC/Si (001) substrate wafer.

The writing of the mask was performed in a NanoSuite Raith Pioneer microscope with a field emission cathode. The masks were exposed with a dose of 300 µC/cm^2, a beam diameter of <20 nm and a stepsize of 0.0016 µm. After exposure the resist was developed for 70s in a developer solution (AR 600-56), which removes the electron beam exposed areas, followed by a stop bath of 60 s in isopropanol. Next, a 45 nm thick Ni layer was thermally evaporated, which acts as a hard mask for the following RIE process. For the lift-off process the sample is put into:

1. 5 min. aceton,
2. 30 min.(fresh) aceton,
3. 10 min. isopropanol,
4. short DI water bath.

In the second step the aceton bath is renewed to remove metal residuals in the solution, which have been already taken off from the sample. A helpful tool is toput the beaker with the sample and the solution on a rotation plate during the lift-off process.

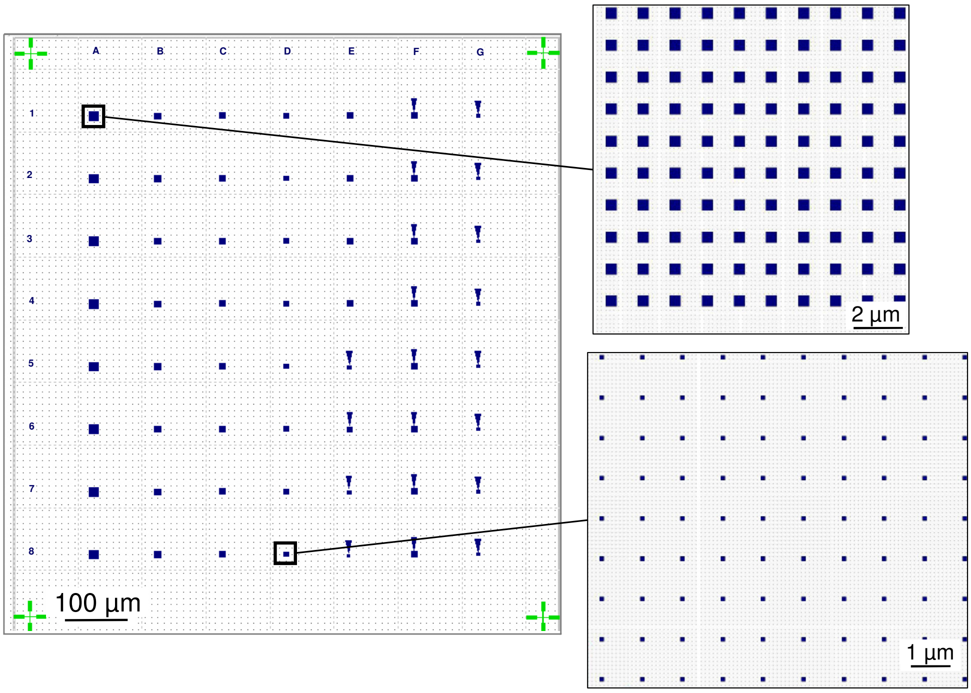

Figure 4.2

Electron beam lithography mask containing fields (marked in blue) with arrays of post shaped structures. The appropriate sizes are listed in Table 4.1.

Column	Row	Size of individual structures	Distance between structures within one array
A	1-8	500 nm x 500 nm	1000 nm
B	1-8	500 nm x 500 nm	500 nm
C	1-8	250 nm x 250 nm	750 nm
D	1-8	250 nm x 250 nm	500 nm
E	1-4	100 nm x 100 nm	900 nm
E	5-8	100 nm x 100 nm	100 nm
F	1-8	50 nm x 50 nm	950 nm
G	1-8	50 nm x 50 nm	450 nm

Table 4.1
Summary of the different structure sizes and distances of the several mask fields in Fig. 4.2.

4.3 Reactive Ion Etching

In the previous sections, two different lithography techniques have been introduced. To transfer the pattern into the third dimension reactive ion etching (RIE) processes are used. Due to the chemical inertness of the 3C-SiC substrate a dry etching instead of wet etching techniques has been selected. An important benefit of dry etching processes are highly anisotropic etch profiles.

Plasma etching processes are performed in a vacuum chamber where a plasma generates reactive species which chemically or physically remove the material. Usually, the setup in the vacuum chamber consists of two flat and parallel arranged electrodes. The sample lies on the lower electrode. After inserting the gas the plasma is initiated by applying a radio frequency (rf) electromagnetic field to the electrodes. The oscillating electrical field dissociates the gases into ions creating electrons and positvely charged ions. The electrons have a greater mobility than the heavier ions. Thus, the electrons follow the oscillating rf field and move onto the electrode surfaces charging them negatively with respect to the plasma. Due to this charge an electric field between the electrodes is build up which accelerate the ions towards the sample where they react with the material. Due to the perpendicular impingement of the ions a highly anisotropic etching process can be realized [95].

Hiller and coworkers [90] have shown how to produce 3C-SiC sub-micrometer structures which are aligned parallel to the [110] directions of the substrate using a electron cyclotron resonance (ECR) plasma system. They modified their system by a special gas inlet unit which is suitable for injecting SF_6 into the high-density down-

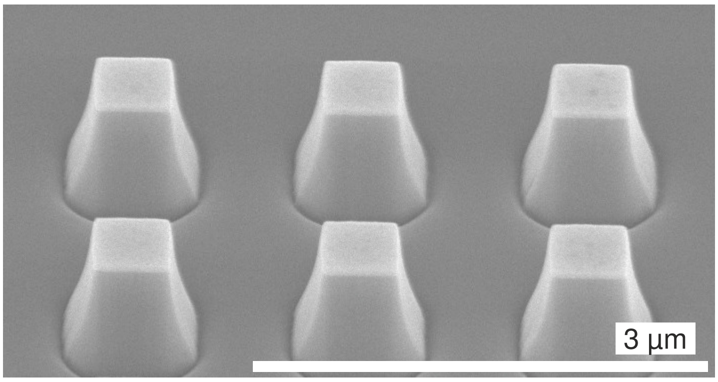

Figure 4.3

Side view SEM images of the 3C-SiC (001) surface with post shaped nanostructures fabricated by Hiller et al. [90].

stream Ar/O_2 ECR plasma. They achieved side wall steepnesses of up to 83° in 3C-SiC with an etching rate of about 100 nm/min. Figure 4.3 shows a side view SEM image of the 3C-SiC (001) surface with post shaped nanostructures. The posts have top edges with a length of about 500 nm and a height of about 700 nm. These types of structures have been used to investigate the growth of c-GaN and c-AlN/GaN on sub-micrometer SiC structures (see section 7.3).

To analyze the influence of growth area reduction on the c-GaN growth, an own dry etching process of 3C-SiC was developed using a RIE system “Plasmalab 80P“ from Oxford Instruments with all mask parameters described in subsection 4.2. The etching process was performed at a SF_6 flux of ~73 sccm and a O_2 flux of ~8 sccm, a chamber pressure of ~100 mTorr, and a rf power of ~100 W. The etching time was about 10 min resulting in a 3C-SiC etching rate of around 30 nm/min. Concerning the reproducibility of this process two features have to be mentioned. First, the 1 cm^2 large samples were fixed with a double-faced adhesive carbon tape on a (2x3) cm^2 p-doped Si wafer piece. Second, at the beginning of each process the same etching process has been run without a sample in the chamber for about 5 minutes.

After the RIE process the Ni mask is removed innitrid acid heated in a water bath to ~75°C. Figure 4.4 shows arrays of 3C-SiC structures after removing the Ni mask fabricated by this patterning technique. In Fig. 4.4a the posts have top edges with a length of about 500 nm, in Fig.4.4b of about 250 nm and in Fig.4.4c of about 100 nm. The insets in (a) and (b) show top view SEM images of the square shaped structures. Slightly chipped edges can be identified which result from the lift-off process. During the lift-off process the Ni mask on top of the photoresist is ripped away causingroughened edges which are transferred by the RIE process into the SiC substrate. This tearing has been reduced by optimizing the metal and photoresist thickness ratio. Another distinctive feature is observed in Fig. 4.4c. The shape of the 3C-SiC structures has no longer a clear square form but shows a mixture of a square and

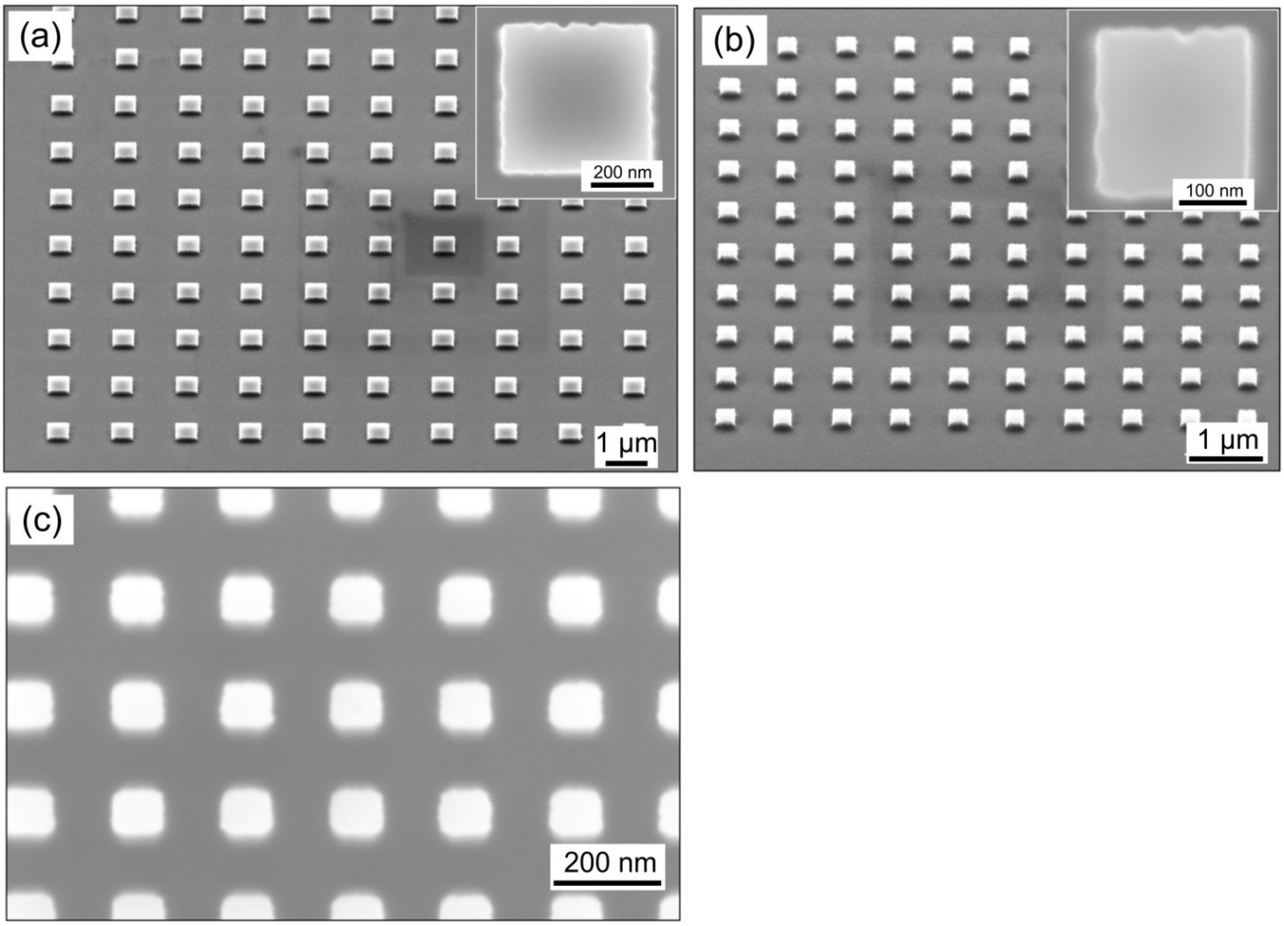

Figure 4.4

(a), **(b)** Side view SEM images of the 3C-SiC (001) surface after removing the Ni mask with post shaped nanostructures fabricated by a dry etching process with (a) ~500 nm top edge length and (b) ~250 nm top edge length. The insets in (a) and (b) show top view SEM images of the square shaped structures. **(c)** Top view SEM image of the 3C-SiC (001) surface with post shaped nanostructures fabricated by a dry etching process with a edge length of about 100 nm.

a round shape. This effect is due to a non ideally focused electron beam during the EBL process.

5 MBE on Pre-Patterned 3C-SiC/Si (001)

In this chapter the growth of c-GaN and c-AlN/GaN QWs on pre-patterned 3C-SiC (001) substrates by MBE will be explained. Optimized conditions for the growth of c-GaN on 3C-SiC/Si (001) substrates have been developed in the last ten years and are described e.g. in [9], [97-99] and in section 2.5. The growth processes on patterned substrates are based on this previous work.

To control the growth parameters the sample surface is monitored *in-situ* by RHEED. The electron beam hits the surface under grazing incidence (1-3°) resulting in a broadened beam on the surface. To guarantee that the electron beam for RHEED touches the patterned area on the surface and monitors information about the growth on top of the structures the surface patterns have to be large. Pre-patterning of the substrate by NSL (see section 4.1) offers a patterned surface area which is large enough for this purpose and therefore guarantees that the electron beam contains information about the growth on top of the nanostructures [58]. Parts of this work focus on the overgrowth of single post shaped SiC structures located in arrays in the middle of the (1x1) cm^2 sample. Compared to the unpatterned sample area these structured areas are small. Therefore, they can not easily be captured in a RHEED pattern. To overcome this problem planar reference samples with the same layer thickness were grown before each patterned sample to determine the optimized growth parameters and the surface area next to the structures has been monitored by RHEED during growth.

Before starting growth the 3C-SiC/Si (001) substrates [27] are cleaned in

1. 10 min. aceton,
2. 10 min. isopropanol,
3. short DI-water bath,
4. 10 min. buffer oxide etching solution (BOE) ($NH_4F:H_2O:HF=4:6:1$),
5. short DI-water bath.

Subsequently, they were dried with nitrogen and loaded into the MBE UHV chamber with a base pressure of $\sim10^{-9}$-10^{-10} mbar. Prior to growth the planar reference samples were subject to an aluminium (Al) deoxidation process at a substrate temperature of T_S = 910°C in order to remove native oxides and other residues. Therefore, Al (~2-3 MLs) is given 10 times on the sample surface for a time of 5 s. With recording a transient of the RHEED intensity versus the time the adsorption and desorption processes were monitored. This procedure was not executed with the patterned samples, because former studies [58] have shown that the Al is not completely desorbed from the structured surface. Hence, this preparation step was skipped and the patterned samples were heated up to T_S=910°C to facilitate the vaporization of impurities but without using Al flashes.

In the next step, the surface temperature was lowered to an optimized growth temperature of T_S=720°C. The sticking coefficient was adjusted to 0.5 by varying the substrate temperature at a constant gallium flux of $3.5 \cdot 10^{14}\ cm^{-2} s^{-1}$. Therefore, Ga flashes (Ga shutter open for a time of 10 s) were used to analyze the deposition and desorption rate of Gaby recording the RHEED intensity. The gallium (Ga) flux was measured before by a Bayard-Alpert ion gauge tube. The Ga flashes also effect a removing of native oxides from the surface.

The nucleation process is performed in 10 cycles: At first the Ga shutter is opened and after 5 s the nitrogen shutter is also opened and the GaN deposition process starts. After 30 s a growth interruption of 30 s follows. During the nucleation process of c-GaN on the 3C-SiC/Si substrate a *pseudo* Frank van der Merve growth can be observed [100]. Sequences of RHEED patterns show that during the first 3 minutes three-dimensional islands are formed. After 5 minutes a smoothening of the surface is observed again [98]. The streaky RHEED pattern after the nucleation process indicates a smooth 2D surface. In Fig. 5.1 the RHEED intensity is plotted versus the time during the growth of c-GaN after the nucleation process on a pre-patterned surface. At the beginning, the gallium shutter is opened for about 5 s. The RHEED intensity drops down to a characteristic kink and then the shutter of the nitrogen source is released.

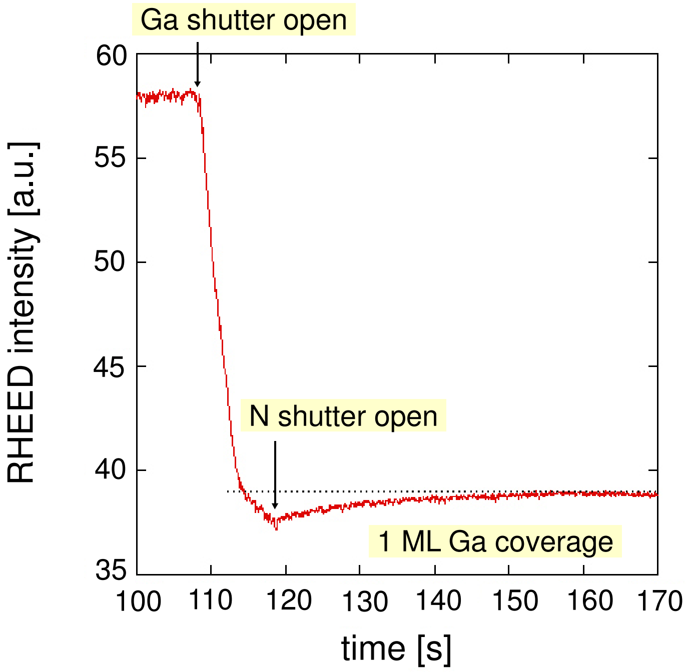

Figure 5.1

RHEED intensity versus time during c-GaN growth.

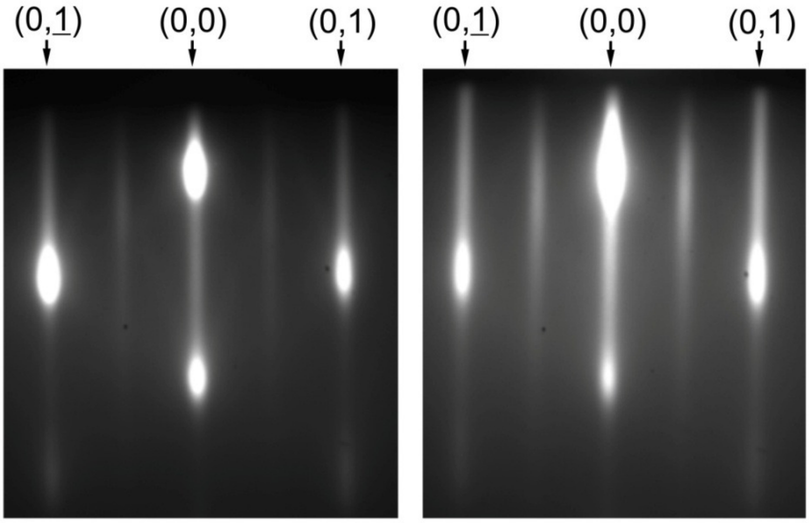

(a) (b)

Figure 5.2

RHEED pattern of the [110] azimuth taken from **(a)** a pre-patterned sample overgrown with 75 nm c-GaN (sample GNR 2298) and from **(b)** the corresponding reference sample with a planar 75 nm c-GaN epilayer (sample GNR 2297).

The GaN growth starts by opening the nitrogen shutter, which is indicated by a minimum of the RHEED intensity. If the intensity rises to a characteristic kink and saturates at a constant value the surface is covered with one monolayer of Ga. A deviation from these metal rich conditions leads to stoichiometric or even nitrogen rich conditions resulting in an increased roughness of the surface as well as to a higher dislocation density [97]. During c-GaN growth the temperature is increased with increasing layer thickness according to the optimized growth conditions.

Figure 5.2 shows two RHEED patterns of the [110] azimuth taken from (a) an EBL structured sample overgrown with 75 nm c-GaN and from (b) a reference layer with a planar 75 nm c-GaN epilayer. Both RHEED images show a streaky pattern with three-dimensional spots and a (2x2) surface reconstruction indicated by the light streaks in between the (0,-1), (0,0) and the (0,1), (0,0) reflections. The reflections can be allocated to the cubic symmetry [97]. The influence of the patterned surface cannot be monitored here.

The growth of c-AlN/GaN MQWs (shown in subsection 7.3.2) is realized under similar growth conditions as described above at a substrate temperature of T_S=720°C. At first c-AlN is grown in 3 cycles for a time of 20 s with a growth interruption of 30 s. Therefore, the Al shutter and the nitrogen shutter are opened simultaneously, so that there is no Al termination on the surface. Then 10 periods of c-GaN/AlN MQWs are grown starting with a 4-5 nm thick c-GaN QW followed by a ~2 nm c-AlN barrier [101].

6 TEM Specimen Preparation

There are several ways to prepare TEM specimens in cross-section geometry with final thicknesses of 10–100 nm. In the following I will concentrate on two preparation methods which were applied in this work. Firstly, the conventional cross-section preparation method will be explained. This procedure contains individual time-consuming steps, but it is a well established thinning technique. Secondly, the specimen preparation using a focused-ion beam (FIB) system is introduced. With the controlled use of an ion beam, specimens from a defined area can be selectively cut out and thinned. This method is necessary to prepare the nano-posts fabricated in this work. Specimens prepared with the conventional cross-section method were produced at the University of Paderborn while FIB sample preparation was performed at the Ernst-Ruska Centre (E-RC), Forschungszentrum Jülich.

6.1 Conventional Cross-Section Preparation

The cross-section specimen preparation process is based on several steps. In the end of cross-sectioning the c-GaN/SiC sample the interface is parallel to the electron beam. In Fig. 6.1 a-f the basic steps are schematically illustrated. General information can be found in Ref. [71].

At the beginning, two stripes with a width of 2 mm are cut with a saw from the sample (see Fig. 6.1a). The two blocks are glued together with epoxy (Fig. 6.1b) so that the sample surfaces are in contact with the epoxy layer. The glue is hardened 2 hours at 130°C. The result is a sandwich consisting of the substrate stripes with athin layer of epoxy in between. Next, the sandwich slice is cut into smaller pieces with a width of ~900 µm (Fig. 6.1c). These pieces are glued in a laser-cut CuZn-grid (Fig. 6.1d). The sandwich piece within the CuZn-grid is thinned and polished mechanically from both sides until a final thickness of ~100 µm is reached. Further, the center of the disk is thinned by a dimpling process (see Fig. 6.1e). For that process, a Model 656 dimple grinder from Gatan is used. With the mechanical dimple process the disk is ground and polished to a fixed radius and curvature in the area of interest. The aim is to leave a final thickness within the dimple of about ~30 µm. The rest of the material is then thinned by sputtering with Ar^+-ions in a Model 691 Precision Ion Polishing System (PIPS) instrument from Gatan. This system contains a dual beam source with two Penning ion guns. The operating angles of each gun are independent, but the ion beams are centered onto the specimen. A schematic side-view is depicted in Fig. 6.1f. The specimen is ion milled under a vacuum of ~$5\text{x}10^{-5}$ Torr and room temperature conditions with an accelerating voltage of 4.5 kV. The angles of incidence (-3° and +4.5°) are chosen in a

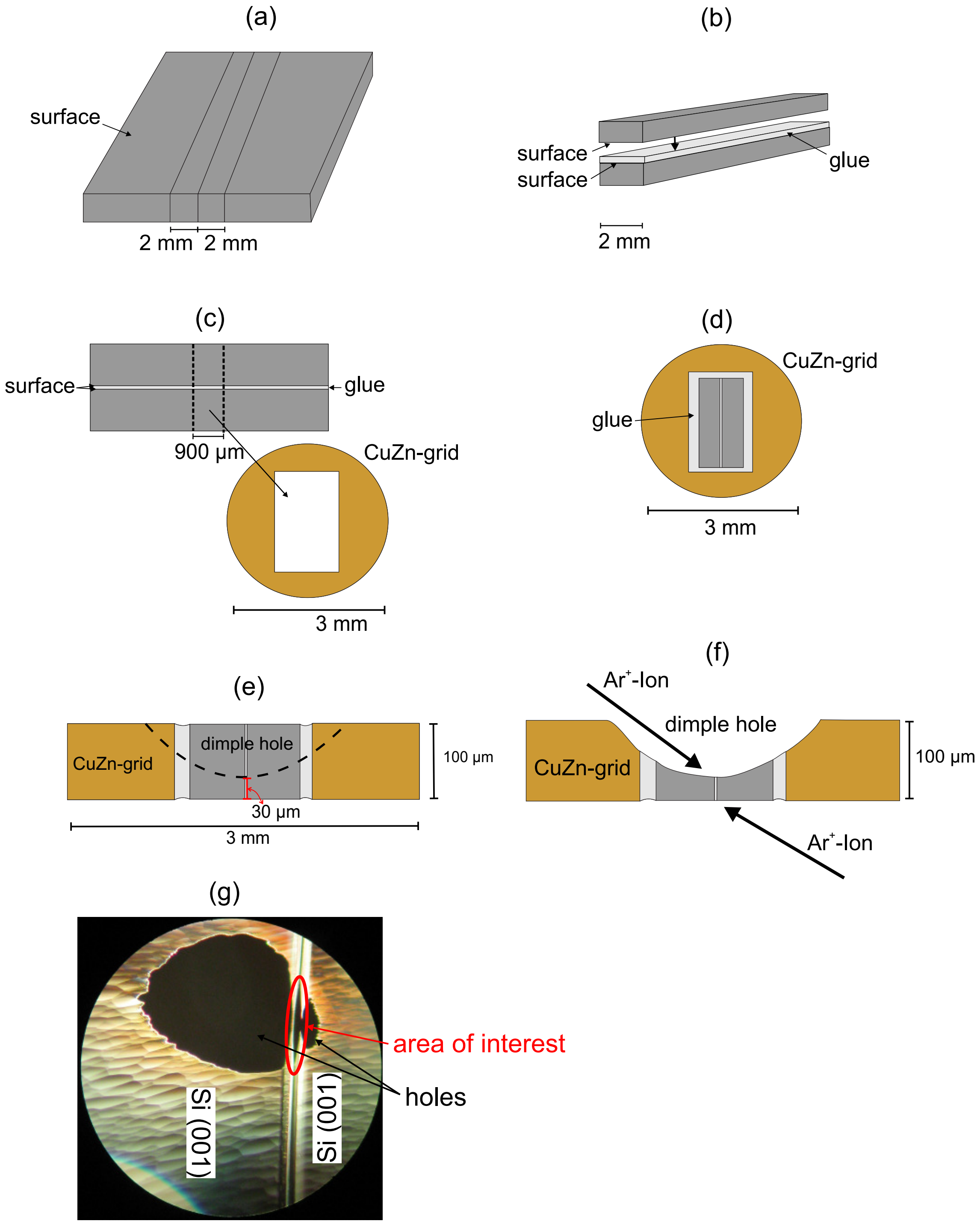

Figure 6.1
(a-f) Schematic drawings with arbitrary unity scales of the basic steps of cross-section TEM specimen preparation. **(g)** Top view optical microscopy image of a thinned c-GaN/SiC/Si (001) cross-section sample after ion milling.

way that the rotating specimen is sputtered from the back and from the front side. The ideal milling result is a small hole with electron-transparent wedges in the area of interest. Subsequently, the specimen surface is polished for 2 min at 1.8 keV in the ion milling system in order to remove previously amorphized sample material. The optical microscope image in Fig.6.1g shows a top view of a thinned c-GaN/SiC/Si (001) cross-section sample after ion milling. The sample consists of a 3C-SiC/Si (001) substrate with 400 nm c-GaN on top. The image shows a TEM specimen “sandwich” of two sample slices glued together. A hole was thinned into the glue line, the surfaces of the slices and the substrate. The region of interest is close to the glue line at the surfaces of the slices. The specimen is now ready for TEM investigations.

6.2 Preparation of TEM Specimens with Focused-Ion Beam

Focused-ion beam (FIB) sample preparation was carried out in a Helios NanoLab 400S system from FEI at the E-RC Jülich. This system is based on a digital field emission SEM supplemented with a FIB column and a flipstage assembly.

Figures 6.2a-i showall the stages in the specimen preparation process. An array of 5x5 post shaped structures is displayed. At first a ~200 nm thin bar of platinum (Pt) is deposited by decomposition from a metalorganic gas by the electron beam on the area of interest (here the front row of the array). Figure 6.2a-b reveal SEM images of the coated row in top view (a) and from the side (b). This metal layer serves as a protective coating for the Ga ion beam. Platinum is the preferred metal for deposition if a high deposition rate and a high spatial precision of the deposition are required. Then another ~3 µm thick Pt film is deposited (Fig. 6.2c) by the ion beam to enhance the conservation of the structures. Next, two trenches in the front and in the back of the structures are cut out (Fig. 6.2d,e) until a thin wall (~2 µm thick) within the sample is left. Now the sample is tilted to undercut the wall until it is connected only on one side with the rest of the sample. In Fig. 6.2f a needle-arm of a micromanipulator is fixed with Pt on top of the slice and the wall is lifted out of the trench. The lamella is transported by the needle to a 3 mm in diameter grid and fixed there with two stripes of Pt (Fig. 6.2g). In this position the lamella can be thinned by a Ga ion beam from both sides. In Fig. 6.2h a cross-section top view of the lamella is shown to estimate the thickness (~0.3 µm) and the bending of the TEM specimen.

In order to achieve thinner TEM lamellas or to remove armorphous layers an additional post FIB thinning step can be performed. Therefore, a low-energy (500 V) argon beam with a beam size of ~1 µm is focused and scanned over the TEM lamella (Nanomill System (Fischione)). This step is repeated until the area of interest is thin enough, for example ~10 nm for high-resolution TEM imaging.

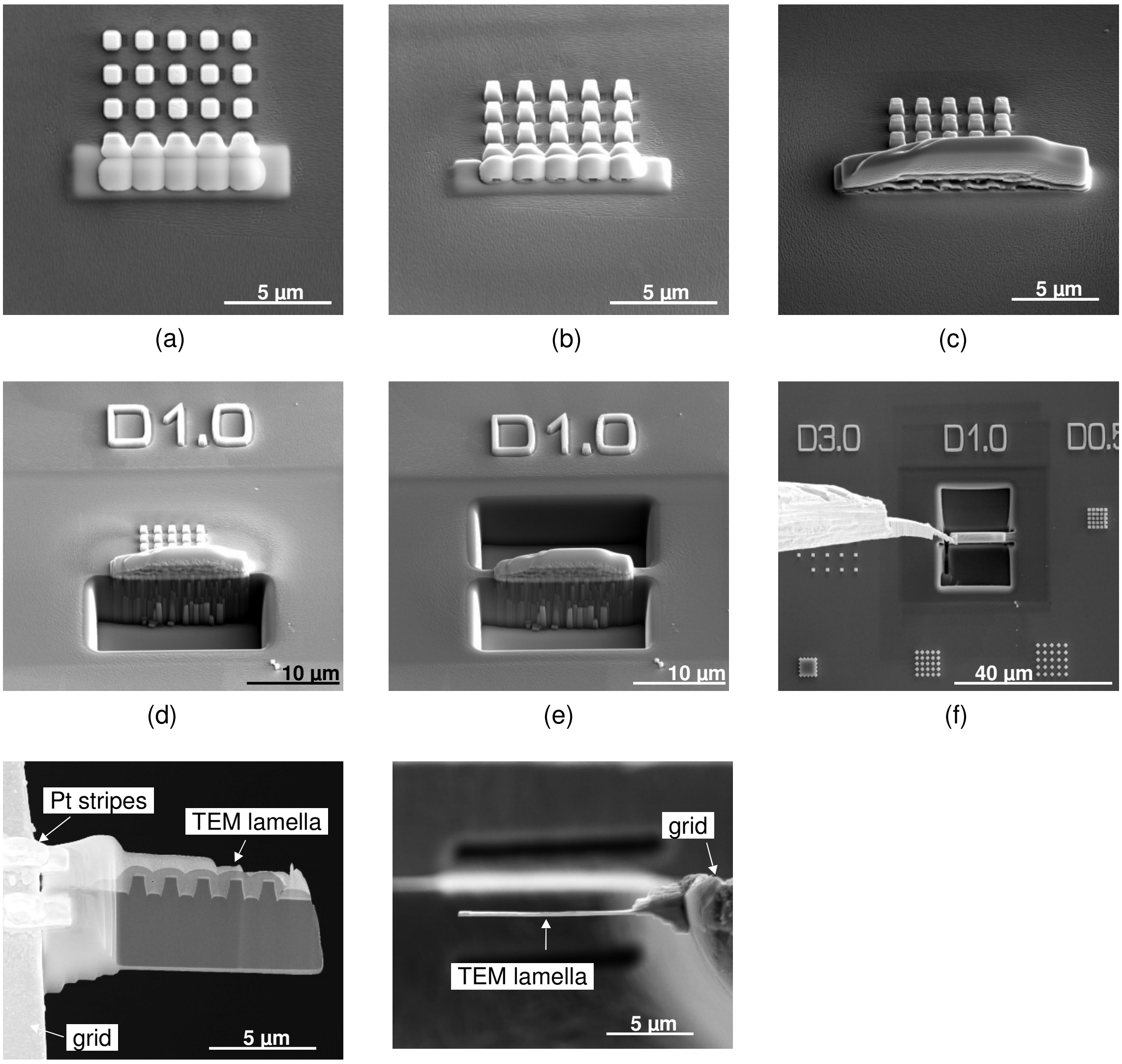

(a) (b) (c)

(d) (e) (f)

(g) (h)

Figure 6.2
(a-h) Various stages of TEM specimen preparation via FIB system, see text.

7 Experimental Results

In this chapter the experimental results concerning the overgrown pre-patterned substrates are discussed. This chapter is structured as follows: First, the influence of the substrate morphology on planar and selective-area-grown c-GaN layers will be described (section 7.1). Then, in section 7.2, the influences of SFs on the optical properties of c-GaN and c-AlN/GaN MQWs are investigated. The following section 7.3 will focus on the analysis of c-GaN and c-AlN/GaN QWs grown on sub-micrometer square shaped 3C-SiC structures. At the end, in section 7.4, the influence of growth area reduction down to ~20 nm islands on the structural properties of c-GaN is analyzed.

7.1 Anti-Phase Domains in Cubic GaN

In this chapter the heteroepitaxial growth of c-GaN by MBE on planar and nano-patterned 3C-SiC/Si (001) substrates is investigated. Parts of the results of section 7.1.1 are already published in [13], [102] and the results of section 7.1.2 are published in [14], [102].

7.1.1 Anti-Phase Domains in Planar Cubic GaN Epilayers

To enable these studies two samples with different c-GaN layer thicknesses of ~450 nm (sample A (GNR 2100)) and ~1.7 µm (sample B (GNR 2104)) grown on the same planar 3C-SiC/Si (001) substrate are investigated.

Scanning Electron Microscopy and Atomic Force Microscopy

Figure 7.1 shows a SEM top view surface image of sample B. The surface exhibits surface striations in two perpendicular orientations parallel to [110] and $[1\underline{1}0]$, respectively. Regions with striations in either of these directions form islands of arbitrary shape with sizes between 10 and 100 µm. The two types of regions are considered to be anti-phase domains (APDs) with boundaries in between. One type of domains shows surface facetselongated perpendicular to the [110] direction, this domain is called APD ⊥[110] and the other type with surface facetselongated parallel to the [110] direction is labeled with APD ||[110].

To verify the results of the SEM analysis, AFM measurements in contact mode were carried out for sample A and B. The AFM image of sample A is shown in Fig. 7.2a. This image reveals two clearly distinguishable domains. In these APDs the elongated facets have a length of 400-500 nm and exhibit two perpendicular orientations.

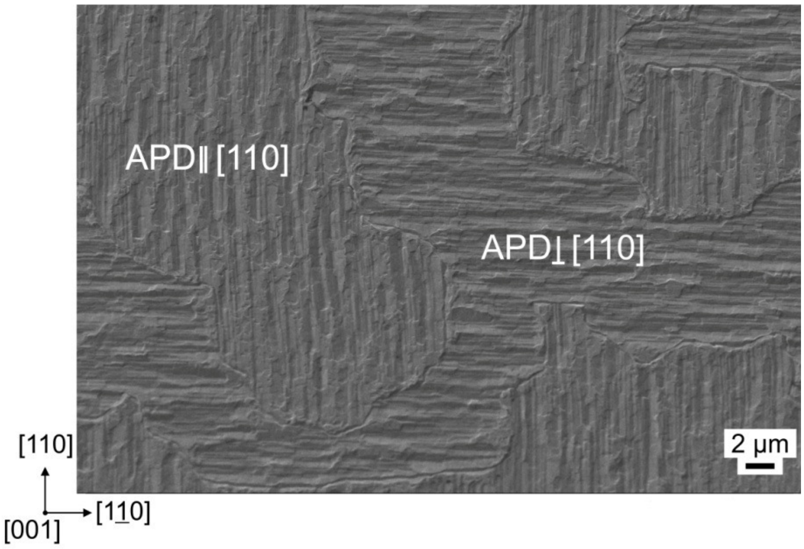

Figure 7.1
Top view SEM (secondary electron (SE) detector) surface image of sample B. Clearly distinct islands with striations exhibiting perpendicular orientation are an indication of APDs.

Figure 7.2b shows the surface image of sample B showing domain formation as well. The comparison between Fig. 7.2a and b reveals that the presence of domains in the c-GaN layer is independent of the layer thickness. However, with increasing layer thickness the length of the elongated micro crystals within the APDs becomes larger to about 1-2 µm in sample B. Consequently the facet formation becomes more pronounced. One reason for this could be a different lateral growth rate between the APDs in dependence of the polarity of {111} facets. For example, the polar gallium

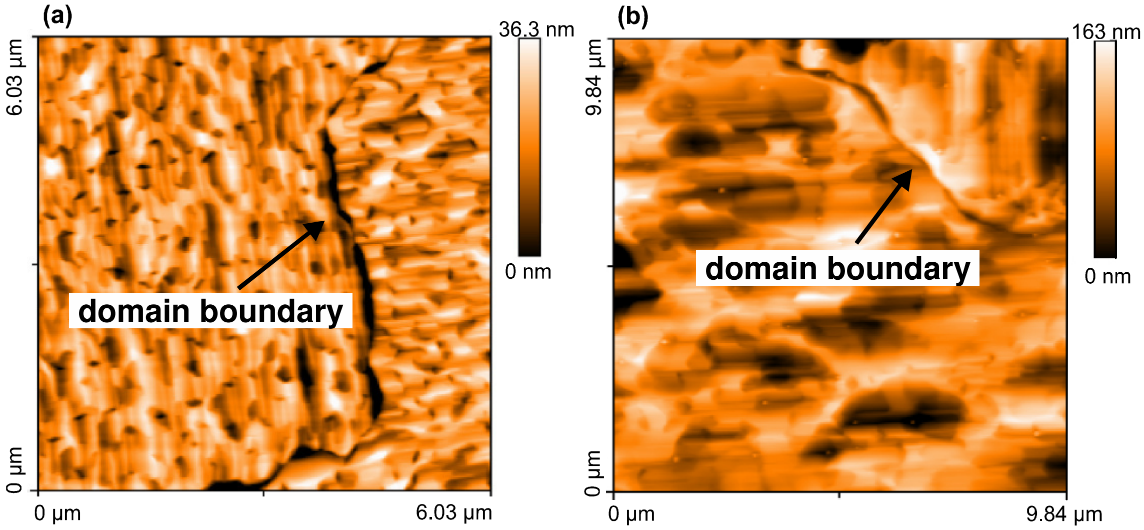

Figure 7.2
AFM surface images of **(a)** sample A (~450 nm thick c-GaN layer) and **(b)** sample B (~1.7 µm thick c-GaN layer) establish the existence of APDs in c-GaN.

(Ga)- and nitrogen (N)-terminated {111} facets possess different lateral growth rates, as shown for c-GaN grown by metal organic chemical vapor deposition [103]. The polar faces result because in contrast to the diamond structure with one type of atoms A, which has a point inversion symmetry center in the middle of the A-A bonds, the inversion symmetry in a zinc blende crystal with two types of atoms A and B is missing. Therefore, the {111}and {001} planes of the zinc blende crystal structures have polar faces containing either type A or type B atoms. In the case of c-GaN the {111} planes are terminated either with Ga- or with N-atoms as shown in Fig. 7.3.

A first indication of the origin of domain formation in the c-GaN with these characteristic surface morphology can be found in the 3C-SiC/Si (001) substrate. During the nucleation of the 3C-SiC on an elementary Si substrate APDs are formed which can be interpreted as 3C-SiC domains that are rotated by 90° around the [001] axis (see section 2.2). The surface of one type of domains is terminated by Si atoms and the other type has C atoms on its surface. The different surface terminations seem to be decisive for the formation of domains in the c-GaN. To determine which face type in 3C-SiC induces the face type in c-GaN the electronegativity in the Linus Pauling scale is utilized as means for the Gibbs free energy. The electronegativities for the involved elements are: Ga 1.81, Si 1.90, C 2.55, and N 3.04 [104]. As a result, it is concluded that the Si-face type planes of the substrate induce Ga-face type planesin the c-GaN and C-face type planes of the substrate induce N-face type planes. If the c-GaN nucleates on the 3C-SiC (001) surface a transition from 2D to 3D and then back to a smooth 2D growth mode during the nucleation of the first MLs c-GaN is oberved by RHEED mea-

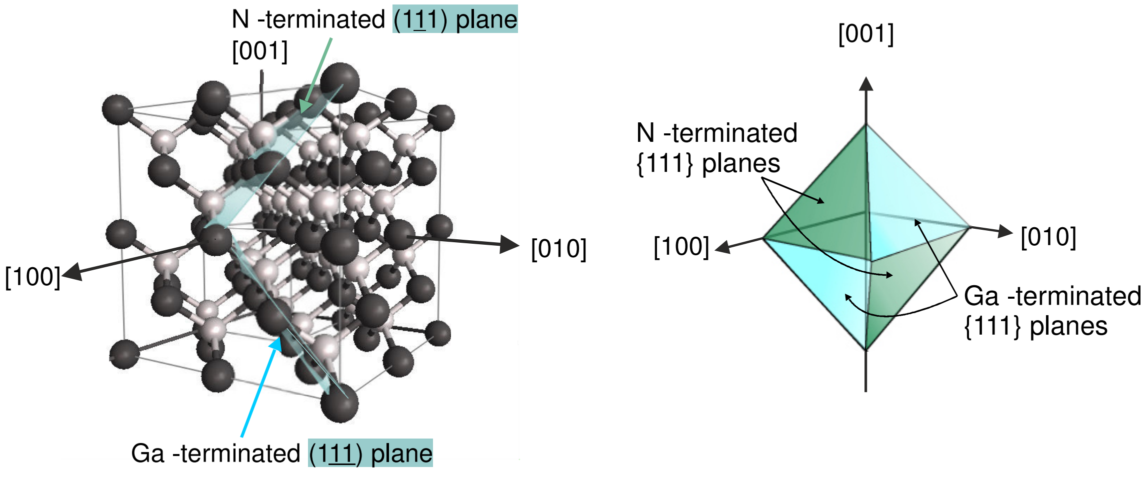

(a) (b)

Figure 7.3

The {111} planes of c-GaN are terminated either with gallium (Ga) or with nitrogen (N) atoms shown in the **(a)** simulation and in a **(b)** schematically drawing.

surements [98]. The influence of facet formation during that nucleation process on the c-GaN growth process including the substrate properties is not investigated until now. In literature [105] it has been shown that the {111} facets have a lower surface energy compared to the {001} and {110} planes in the zinc blende crystal structure, and therefore they are favoured and should play an important role during the nucleation process and for the formation of the APDs. In order to get a proper understanding of domain formation in c-GaN, detailed structural investigation of the nucleation process on the 3C-SiC surface are needed. Therefore, TEM investigations of different c-GaN layer thicknesses from 1-2 MLs up to 1 µm would be desirable. All in all, the AFM analysis supports the results of the SEM images and confirms the existence of grains elongated either parallel of perpendicular to the [110] direction.

High-Resolution X-Ray Diffraction

HRXRD allows the investigation of the defect density and phase purity of the c-GaN layer (see section 3.6) averaged about all domains. Figure 7.4 shows a HRXRD reciprocal space map of sample B. The content of hexagonal inclusions was determined by the intensity ratio of the c-GaN (002) and h-GaN $\{10\underline{1}1\}$ reflections in the reciprocal space map. The hexagonal content increases with the layer thickness from < 1 % in sample A to 15 % in sample B. The defect density, determined from the FWHM of the rocking curve of the c-GaN (002) reflection according to [11], decreases from $8.4 \cdot 10^{10}$ cm^{-2} to $4.5 \cdot 10^{9}$ cm^{-2} with increasing c-GaN layer thickness from ~450 nm to ~1.7 µm. These results show that with increasing layer thickness the defect density decreases, which are mainly SFs on the {111} planes as shown in the following by TEM measurements, but the hexagonal inclusions increase. This seems to be a contradiction, because we assume that the hexagonal inclusions are caused by {111} SFs. One possible reason for this might be that also the surface roughness increases with increasing film thickness and therefore facet formation at the surface becomes pronounced, which favours the growth of hexagonal inclusions. This have been monitored by RHEED investigations (private communications by Dipl. Phys. Ing. Thorsten Schupp). The hexagonal inclusions are most probably caused by {111} facets, but they are mainly not due to the high SF densityat the c-GaN/SiC interface, because reciprocal space mapping from different samples with varying layer thicknesses shows that the hexagonal $\{10\underline{1}1\}$ reflections firstly occur over a c-GaN layer thickness of ~600 nm.

Furthermore, the hexagonal reflections in Fig. 7.4 show different intensities, indicating different h-GaN contents along the [110] and $[\underline{11}0]$ directions. In Ref. [106] it is mentioned that the content of hexagonal inclusions in c-GaN grown on GaAs (001) is different between Ga-terminated {111} planes and that grown on N-terminated {111} planes. In order to clarify this discussion detailed TEM studies of thick (~1 µm) c-GaN layers are necessary.

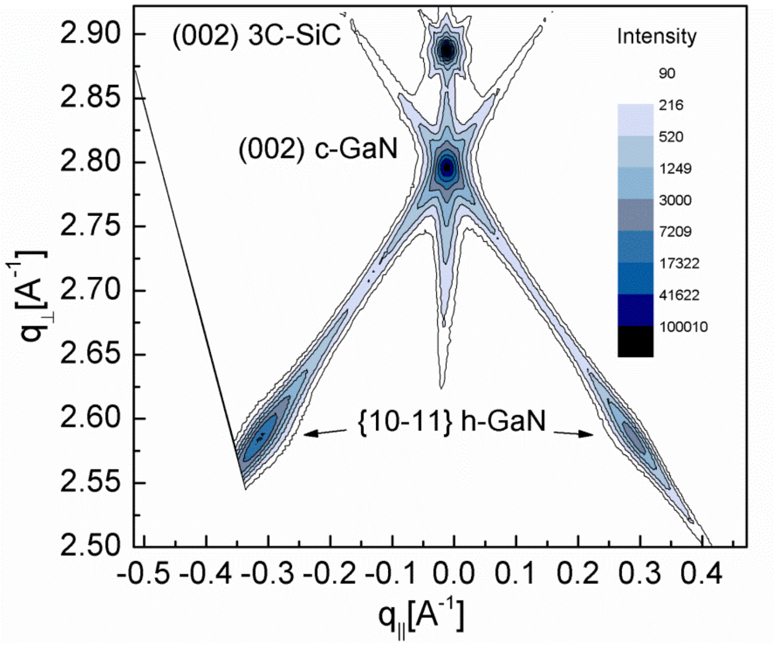

Figure 7.4

Symmetrical reciprocal space map around the (002) c-GaN reflection of sample B (1.7 µm thick c-GaN layer).

Electron Backscatter Diffraction

The phase identification in the thick GaN film of sample B was achieved by EBSD, where Kikuchi diffraction patterns have been correlated to the crystal planes of cubic and hexagonal GaN (see section 3.7). The measurement area on the sample surface, which was tilted by about 70° in the measurement setup to increase the EBSD signal, is shown on the left side of Fig. 7.5. The EBSD data were recorded with a step size of 0.6 µm and an angular resolution of 1-2°. Figure 7.5 (right) shows the corresponding phase map, where the cubic phase is depicted in red and the hexagonal phase is shown in green. The comparison between the SEM image of the measurement area and the phase map clearly indicates a different fraction of h-GaN for adjacent domains. For reference one APD with facet orientation $\perp$[110] is marked by a white line in the SEM image (Fig. 7.5). This domain can be identified in the phase map as cubic phase containing hexagonal inclusions. In contrast to this domain, the APDs $||$[110] contain themajor fraction of the hexagonal phase. Thus, the fraction of hexagonal inclusions within the ADPs is different and depends on the crystal direction. The color distribution in the phase map shows that there should be a huge amount (~50%) of hexagonal inclusions inside the sample, which is in contrast to the HRXRD measurements. Therefore, it has to be mentioned that the phase identification by these EBSD measurements, whether the Kikuchi pattern is related to the cubic or the hexagonal phase, has a 50 % threshold. The computer program gets the information that the sample consists of cubic or hexagonal GaN and then it decides whether the measured Kikuchi pattern matches to the hexago-

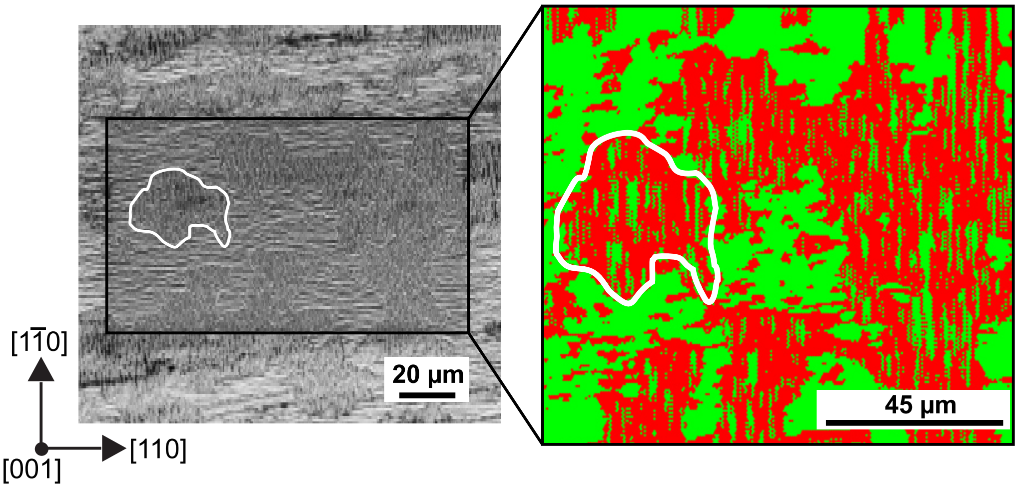

Figure 7.5

Left: Tilted view (~70°) SEM image of the EBSD measurement area on the surface of sample B. *Right*: Phase map showing regions of predominantly cubic (red) and hexagonal (green) GaN. The APD ⊥ [110], marked by a white line in the SEM image, can be identified in the phase map as cubic phase containing hexagonal inclusions.

nal or the cubic phase. But in this mode a clearly distinction between a cubic phase containing many SFs and the hexagonal phase was not possible. Nonetheless, these results are evidence for the micro crystals within the APDs not being structurally equal.

Micro-Raman Spectroscopy

Further structural information about the APDs is given by µ-Raman measurements. Figure 7.6 shows a top view optical image of the measurement area with two adjacent domains of sample B. Two typical Raman spectra, taken at room temperature at the position 1 and 2 marked by crosses in Fig. 7.6, are shown in Fig. 7.7. At position 1, facets are alongated parallel to [110] where EBSD measurements have indicated a high fraction of hexagonal inclusions, while at position 2 the facet orientation is perpendicular to the [110] direction and here the cubic phase dominates. The blue curve (position 1) presents a spectrum of mainly the hexagonal content in the c-GaN with a dominating hexagonal E_2(high) mode at 565 cm^{-1} [107]. The small FWHM of about 4.3 cm^{-1} indicates a low defect density in the hexagonal phase.

As expected, the µ-Raman spectrum recorded at position 2 (red curve) looks very different and clearly shows the c-GaN TO mode at 551 cm^{-1}and the longitudinal optical (LO) modes are located at 735 cm^{-1}. These values can be compared to the literature values of c-GaN grown on GaAs [107]. To provide a better overview the phonon frequencies of cubic, hexagonal GaN [107] and 3C-SiC [108] at room temperature are summarized in Table 7.1.

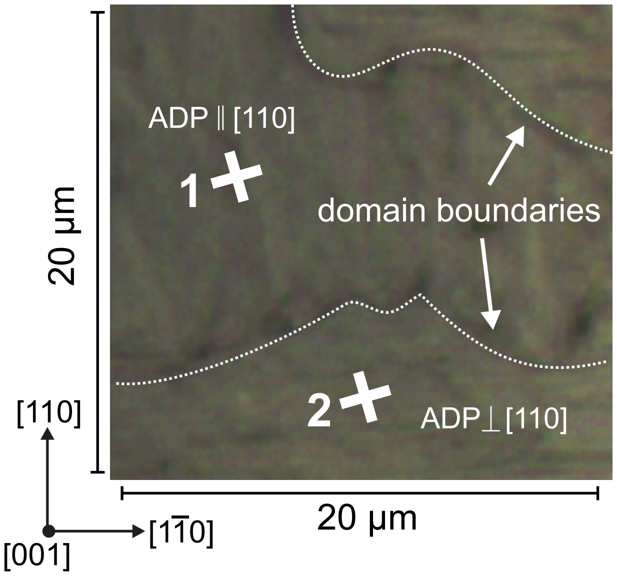

Figure 7.6
Optical image of the (20 µm×20 µm) µ-Raman measurement area of sample B. Position 1 and 2 mark the measurement area of the µ-Raman spectra 1 and 2 in Fig. 7.7 in adjacent APDs.

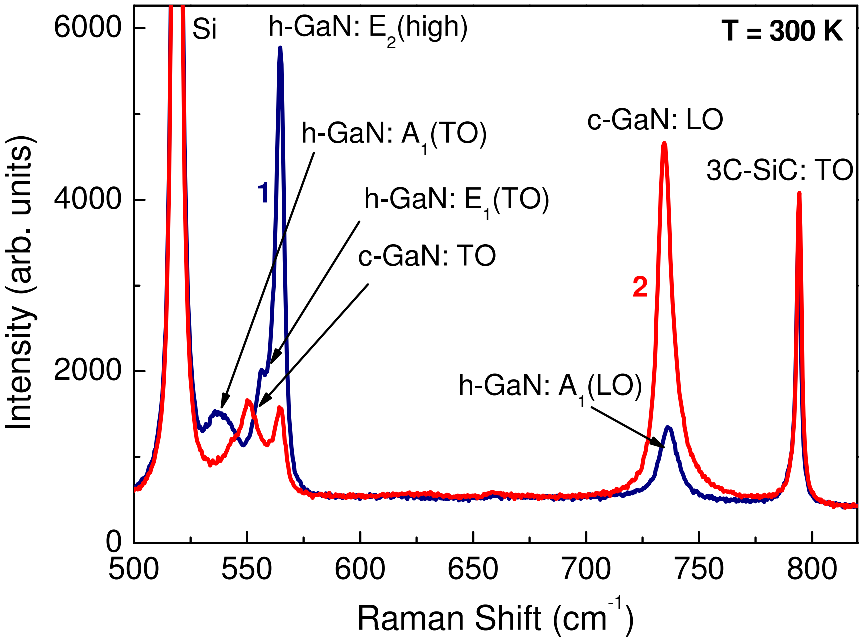

Figure 7.7
Two typical µ-Raman spectra (1 and 2) normalized to the silicon (Si) peak at room temperature taken from the measurement area in Fig. 7.6.

Cubic Modes		**TO**		**LO**	
Frequency [cm^{-1}] of c-GaN		555[107] 551		740[107] 735	
Frequency [cm^{-1}] of 3C-SiC		793[108] 794		969	
Hexagonal Modes	**A_1(TO)**	**E_1(TO)**	**E_2**	**A_1(LO)**	**E_1(LO)**
Frequency [cm^{-1}] of h-GaN	533[107] 537	561[107] 557	570[107] 565	735[107] 736	742

Table 7.1

Literature values of the phonon frequencies of cubic and hexagonal GaN [107] and 3C-SiC [108] at room temperature compared to the measured data from Fig. 7.7.

Figure 7.8a shows a map of the wavelength of the cubic TO mode and the TO component of the hexagonal E_1 mode, measured in the area displayed in Fig. 7.6. A correlation between the image of the measurement area (Fig. 7.6) and the plotted data affirm the dominance of the cubic phase in the APD⊥[110] and the dominant presence of the hexagonal phase in the APD ∥ [110]. These results are in good agreement with the observations made by EBSD. Additionally, the map in Fig. 7.8a shows streaks related to the cubic phase along the [010] direction in the APD ∥ [110]. The reason for this streaky pattern can be found in a detailed analysis of the substrate. Figure 7.8b shows a map of the Raman shift of the 3C-SiC TO mode varying from 793.7 to 794.3 cm^{-1} [108]. This variation is ascribed to local strains and exhibits also a streaky pattern. Thus, the substrate does not only transfer the APDs into the c-GaN layer, but also the local strain fields influence seemingly the growth of c-GaN in the APDs.

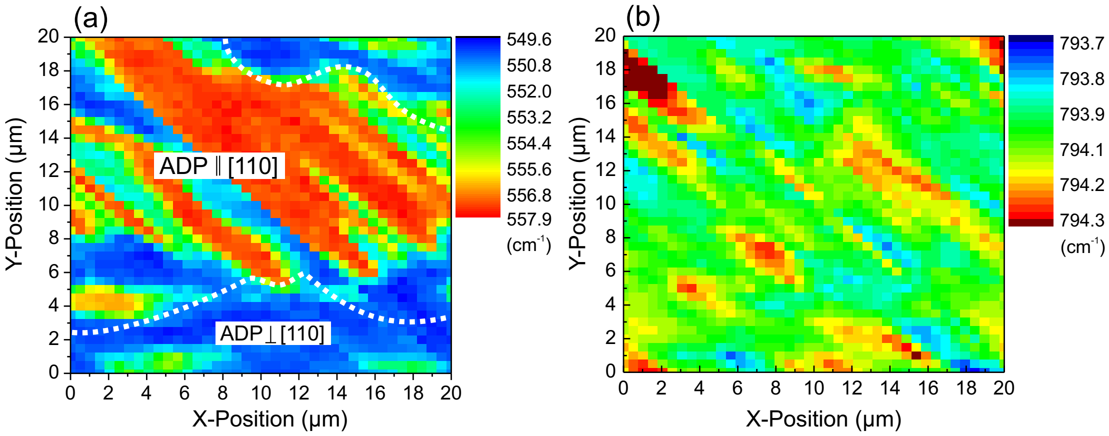

Figure 7.8

(a) Map of the position of the cubic TO mode and the hexagonal E_1 component of the TO mode (cm^{-1}). **(b)** Micro-Raman map of the Raman shift of the TO mode (cm^{-1}) of the 3C-SiC substrate.

Cathodoluminescence Spectroscopy

The optical properties of the APDs were recorded spatially resolved by low-temperature (6 K) CL measurements. In a dedicated SEM at the University of Magdeburg, the electron beam with an acceleration voltage of 10 kV and a beam current of 1.3 nA [75, 76] was scanned over the area of interest (256 × 200 pixels). A complete luminescence spectrum was taken from each pixel.

Figure 7.9 shows local CL emission spectra of sample B. The corresponding measurement areas are marked in the SEM image in Fig. 7.10a. The CL emission spectra a) and b) (dashed lines) are taken from measurement areas located in an APD with facets ∥[110] and the measurement areas of the emission spectra c) and d) (solid lines) are positioned in the adjacent APDs with facets ⊥[110]. The corresponding CL emission spectra shown in Fig. 7.9contain four dominant peaks: The peak at 3.25 eV is due to the radiative recombination of the free exciton (FX) in c-GaN [109]. It is visible in all of the spectra, but most clearly in the spectra c) and d) recorded in the mostly cubic regions with APD ⊥[110]. Additionally, there is a donor-acceptor (D^0,A^0) pair recombination peak at 3.14 eV again most clearly visible in the APDs ⊥[110], a C-related donor-acceptor transition (D^0,A^0_C) at 3.04 eV exclusively in the APDs ⊥[110] and a deep compensating complex in the range from 2.2-2.9 eV [110] mostly in the domains with dominant hexagonal fractions (spectra a) and b)). Furthermore, there is an interesting emission line at 3.33 eV, which is assigned to defect luminescence related to the hexagonal phase. In comparison, the local CL spectra between the APDs significantly differ from each other, because the spectra a) and b), marked in dashed lines, show more intensity of the hexagonal defect luminescence at 3.33 eV and a pronounced defect luminescence in the range of 2.2 -2.9 eV. This indicates a different defect density in adjacent domains. Figure 7.10a shows the SEM image of the whole (70 µm×50 µm) CL measurement area with the corresponding CL wavelength map (Fig. 7.10b). The CLWI displays the emission wavelength of the local maximum CL intensity of each pixel [75]. The color distribution of this map reproduces the sample morphology (Fig. 7.10a) showing domains. The APDs ⊥[110] contain on average more regions dominated by luminescence of the donor-acceptor pair recombination around 3.14 eV than APDs ∥[110]. In addition these domains show a smaller amount of areas with dominant defect luminescence around 3.33 eV than the adjacent domains. The CLWI measurements show that APDs ∥[110] contain a higher fraction of defects than APDs ⊥[110].

Summary

The studies presented above show the existence of APDs in c-GaN grown on 3C-SiC/Si (001) substrates by MBE. The GaN growth is governed by the APDs of the 3C-SiC/Si (001) substrate, resulting in equal orientations and the same anti-phase boundaries. The presence of the APDs is independent of the GaN layer thickness. AFM

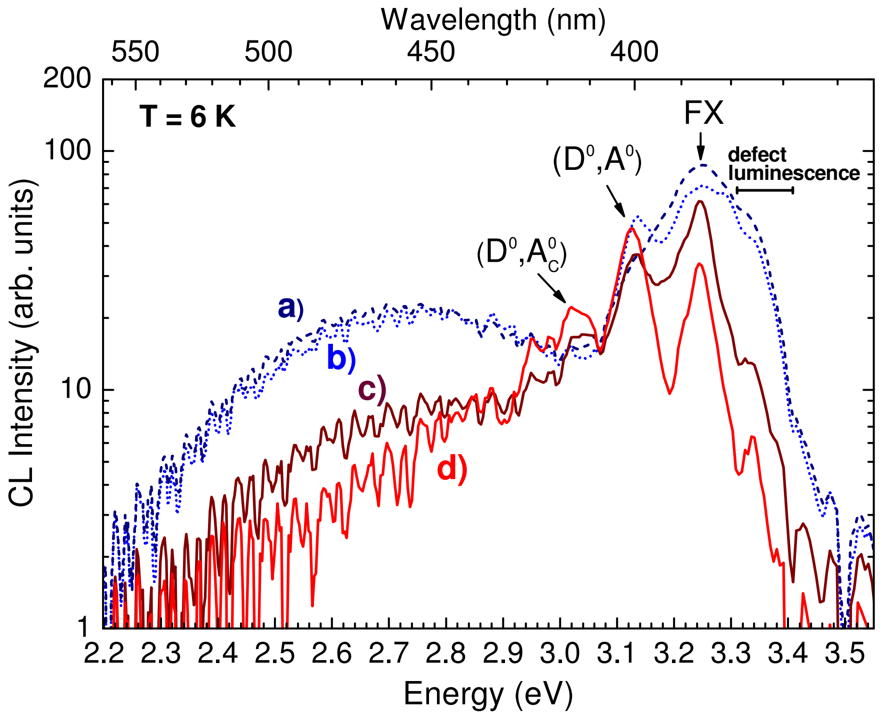

Figure 7.9
Local low-temperature CL spectra of APDs of sample B. The corresponding measurement areas of the CL emission spectra are marked in the SEM image in Fig. 7.10a. Spectra a) and b) (dashed lines) are taken from measurement areas located in an APD ∥[110] and the measurement areas of the emission spectra c) and d) (solid lines) are positioned in the adjacent APD ⊥[110].

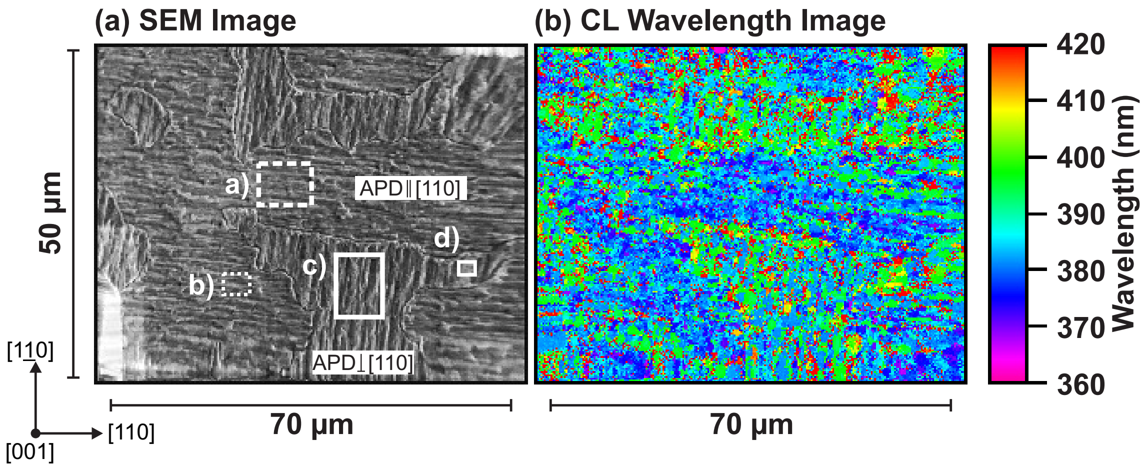

Figure 7.10
SEM image **(a)** of the whole (70 µm × 50 µm) CL-measurement area with matching CL wavelength image **(b)** of sample B. The marked measurement areas a), b), c) and d) in the SEM image correspond to the CL emission spectra in Fig. 7.9.

and SEM images confirm the existence of grains elongated either parallel to [110] or $[1\underline{1}0]$ direction. Several independent measurement techniques like EBSD, µ-Raman and CL demonstrate the formation of hexagonal inclusions and defects preferentially in one type of the APDs. Since according to HRXRD measurements the hexagonal fraction of GaN increases with increasing layer thickness along with the supposed growth of surface facets, it is concluded that the presene of {111} facets plays an improtant role in the formation of hexagonal inclusions. Micro-Raman measurements indicate an additional influence of the 3C-SiC substrate: Local strain fields are extending through the 3C-SiC into the c-GaN layer and affect the growth of the cubic or the hexagonal phase.

7.1.2 Influence of the Substrate Morphology on the Selective-area-grown Cubic GaN

In the previous subsection it was shown that c-GaN growth on 3C-SiC/Si (001) is governed by the APDs of the substrate and that the APDs are transferred into the c-GaN films. The presence of the APDs is independent of the GaN layer thickness. Moreover, in subsection 7.3.1 it will be demonstrated by TEM images that the two types of domains exhibit a largely different stacking fault density. In the following the influence of the APDs in the 3C-SiC/Si substrate on a thick selective-area-grown c-GaN film will be discussed. Here, a large layer thickness of ~1.4 µm (sample GNR 2103) was grown to achieve a pronounced lateral growth and to promote the formation of surface facets.

Scanning Electron Microscopy and Atomic Force Microscopy

Figure 7.11a shows a top view SEM image of the surface of a ~1.4 µm thick c-GaN layer grown on a NSL nano-patterned (see Fig. 4.1) 3C-SiC/Si (001) substrate exhibiting a hexagonally close-packed array of cylindrical pits at the surface. Even though the film thickness is as large as ~1.4 µm the GaN film is still discontinuous and exhibits a close packed array of residual holes. In the SEM image domains with an arbitrary shape and with lateral dimensions varying from a few microns up to about 100 µm can be seen. Different surface morphologies are present in the two types of domains, as is clearly visible in the SEM detail image of Fig. 7.11b. The residual hole openings in domain 1 are smaller than in domain 2 and their long axis is rotated by 90° with respect to each other in the two domains. NSL patterned surfaces may contain distortions of the periodicity (e.g. grain boundary like mask defects) but a close inspection of the domains reveals that irregularities in the periodicity of the nano-pattern on the substrate do not influence the surface morphology of the GaN grown within the

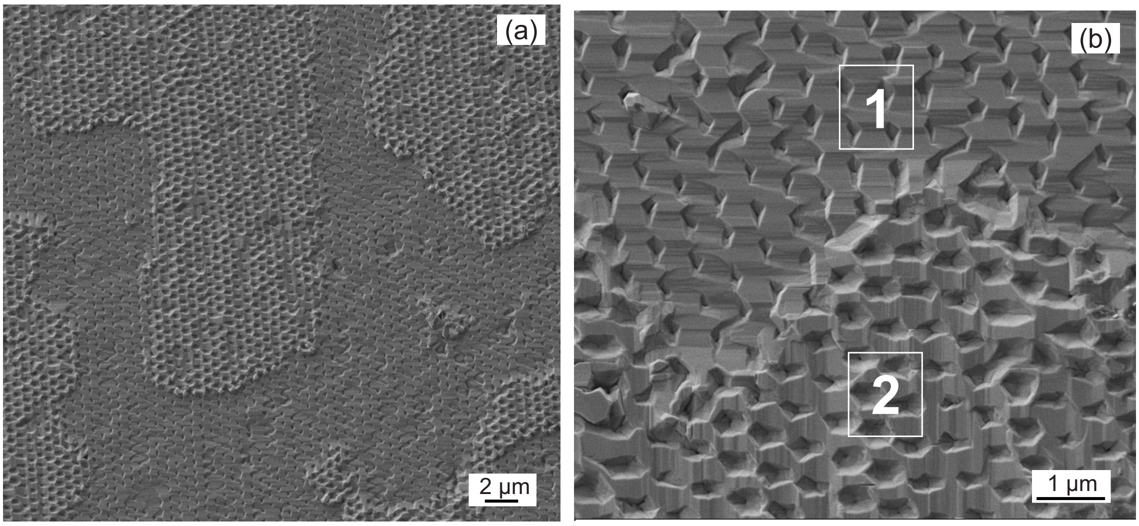

Figure 7.11

(**a**) Top view SEM image of the surface of a ~1.4 µm thick c-GaN layer grown on a NSL nano-patterned 3C-SiC/Si (001) substrate (sample GNR 2103). The surface consists of domains, which have an arbitrary shape with lateral dimensions varying from a few micrometers up to about 100 µm. (**b**) Enlarged section showing the different size and orientation of residual holes in the two domains (1 and 2).

same domain. This is a clear indication that the different morphologies originate from the domain structure of the substrate. The reason for these different GaN growth types is assumed to be the APD structure of the substrate discussed above, i.e. the differently terminated surfaces of the SiC substrate, leading to different polarities of the GaN film and thus a different growth behavior.

Figure 7.12 shows an AFM image of two adjacent domains on the surface of GaN grown on the pre-patterned substrate. In domain 1 GaN grows with atomically smooth facets, indicating that in this region a more Frank-Van-der-Merwe-like growth mechanism dominates. Due to the lateral growth the shape of the nanostructures changes from circular holes before GaN growth into triangle-shaped openings afterwards. The diameter of the holes is reduced from 500 nm before to 100-200 nm after GaN growth. In contrast to the more step-flow-like growth mechanism in domain 1, cubic GaN seems to grow in form of islands in domain 2 (Fig. 7.12). The shape of the holes after GaN growth has changed into squares with diameters from 200 to 350 nm.

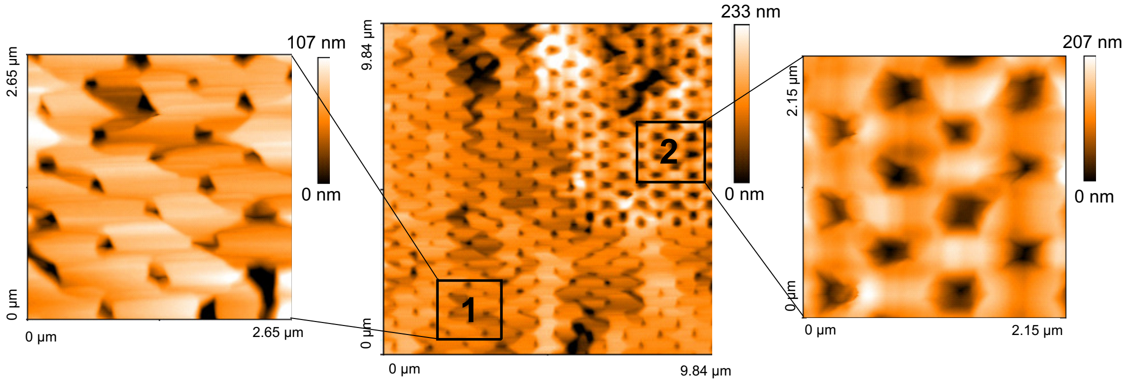

Figure 7.12
AFM image of the surface of the selective-area-grown c-GaN with two adjacent domains. Zoom-in sections on the left and on the right show a step-flow-like flat surface in domain 1 and a more three-dimensional surface morphology in domain 2.

High-Resolution X-Ray Diffraction

Figure 7.13 shows a symmetric reciprocal space map around the c-GaN (002) reflection. The FWHM of the (002) rocking curve of the selective-area-grown c-GaN is about 25 arcmin. In addition to the (002) c-GaN reflection, there is a strong (10-11) reflection of h-GaN visible in Fig. 7.13. From this, an amount of 78 % hexagonal inclusions in the selective-area-grown c-GaN is estimated. This value is very high compared to the c-

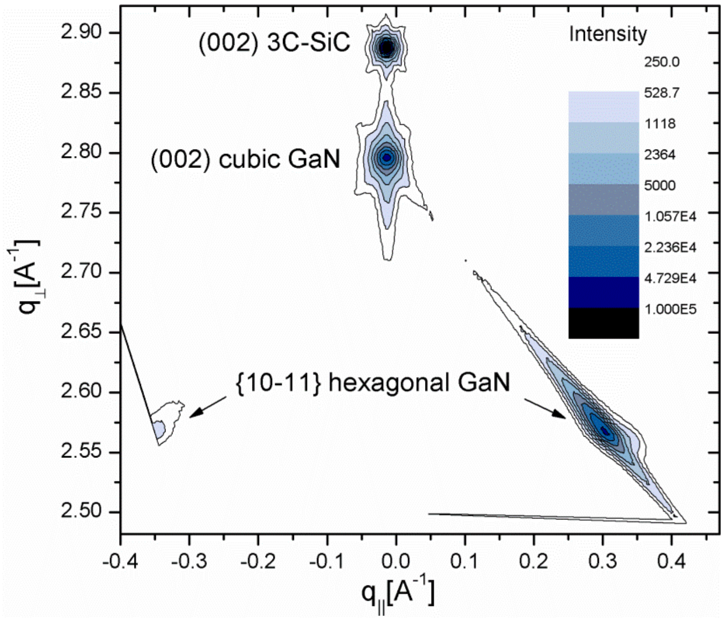

Figure 7.13
A symmetrical reciprocal space map around the (002) reflection of a selective-area-grown ~1.4 µm thick GaN film on NSL pre-patterned 3C-SiC/Si (001).

GaN reference layer grown on a planar substrate, where only 17% hexagonal inclusions and a FWHM of the (002) rocking curve of 21 arcmin were observed at similar film thickness. Thus, the quality of the cubic phase related to the FWHM of the rocking curve of the selective-area-grown GaN and the reference layer are almost in the same range. It will be shown below that enhanced formation of SFs takes place on the sidewalls of SiC nanostructures (see section 7.3) and that the hexagonal volume fraction in thin GaN films is negligible (see section 7.3). Therefore, it is concluded that substrate patterning enhances the formation of SFs and hexagonal inclusions mainly at the sidewalls, leading to substantial fractions of hexagonal GaN upon the growth of thick layers.

Electron Backscatter Diffraction

EBSD measurements were used for phase identification of the selective-area-grown GaN domains. Figure 7.14a shows a top view SEM image of the EBSD-measurement area on the surface of the selective-area-grown c-GaN sample, which is tilted to about 70° in the microscope. The domains described above are clearly visible in this image.

The diffraction pattern of the cubic and the hexagonal phase of GaN are the measured raw data and lead to the phase map in Fig. 7.14b. The cubic phase is displayed in red color and the hexagonal phase of GaN in green, where a 50 % threshold is used to assign either phase to a measurement position. Even though it is assumed that both phases are present in the domains, a sharp discrimination of the two pure phases is made in this diagram, and it obviously strongly correlates with the SEM image in

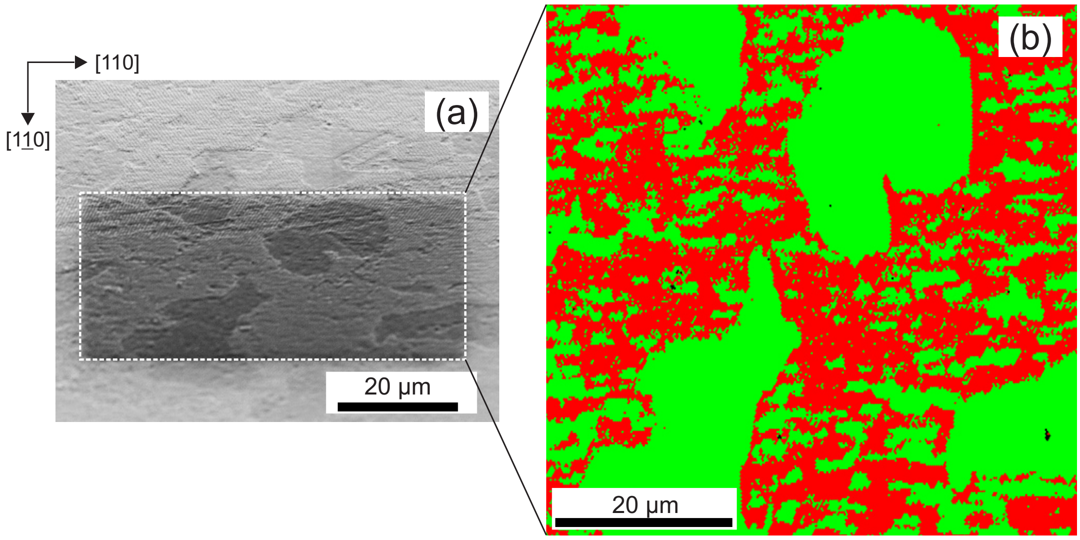

Figure 7.14
(**a**) SEM image of the EBSD-measurement area on the surface of the 1.4 µm thick selective-area-grown c-GaN film, which is tilted to about 70° in the measurement setup. (**b**) Phase map showing regions of predominantly cubic (red) and hexagonal (green) GaN.

Fig. 7.14a. It is clearly visible that the fraction of hexagonal phase between close-by domains varies. The domains with mainly cubic phase (red) contain hexagonal inclusions (green). Additionally, there are domains where the hexagonal phase (green) dominates. The correlation between SEM images and AFM measurements demonstrates that in domains with smaller lateral growth the cubic phase is dominant. Furthermore, the domains with a smooth layer-by-layer growth can be identified to contain a high fraction of the hexagonal phase.

Micro-Photoluminescence Spectroscopy

The optical properties of the domains of the selective-area-grown GaN layer were studied by room temperature μ-PL measurements (see section 3.3). The spot diameter of this method is smaller than the domain size. In the inset of Fig. 7.15 a top view SEM image of the μ-PL measurement area on the sample surface is displayed. The different domains show a different secondary electron yield and thus can be clearly distinguished. In order to find appropriate positions in the optical measurements, contamination markers (dark rectangles in the inset of Fig. 7.15) were deposited with a SEM. Position 1 (green) is allocated to a domain which according to EBSD results is mainly hexagonal GaN, while position 2 (red) marks a domain consisting mainly of c-GaN. The μ-PL luminescence was excited by the 325 nm line of a HeCd laser with a power of 5 mW (beam diameter ~1 μm). The spectra of two domains (position 1 green curve and position 2 red curve) of the selective-area-grown GaN are depicted in Fig. 7.15. The band-edge luminescence of position 1 (green curve) is at 3.38 eV and is assigned to defect luminescence related to the hexagonal phase. An additional emission shoulder at 3.20 eV related to the cubic phase is also visible. This value agrees well with the band-edge transition at 3.21 eV for c-GaN grown on GaAs [109]. Spectrum 1 implies that in this domain the cubic phase with dominant defect formationexists. It should be noted that a pure hexagonal phase is expected to show a luminescence peak at 3.42 eV, which would be clearly separated from the peak observed here. By comparison, the μ-PL peak of domain 2 has more intensity and occurs at 3.20 eV. Furthermore, there is an emission shoulder with low intensity at 3.38 eV, which is an indication for defects and hexagonal inclusions in the selective-area-grown c-GaN. A further luminescence peak in the red curve at 2.23 eV is related to defect luminescence. These spectra demonstrate clearly that in addition to thestructural differences shown by EBSD the optical properties between two adjacent domains are quite different.

Summary

Using SEM and AFM measurements it is demonstrated that selective-area-grown c-GaN growson pre-patterned SiC/Si (001) in two different domains. Nano-patterning of the substrate does not influence the shape of these domains, which most probably ori-

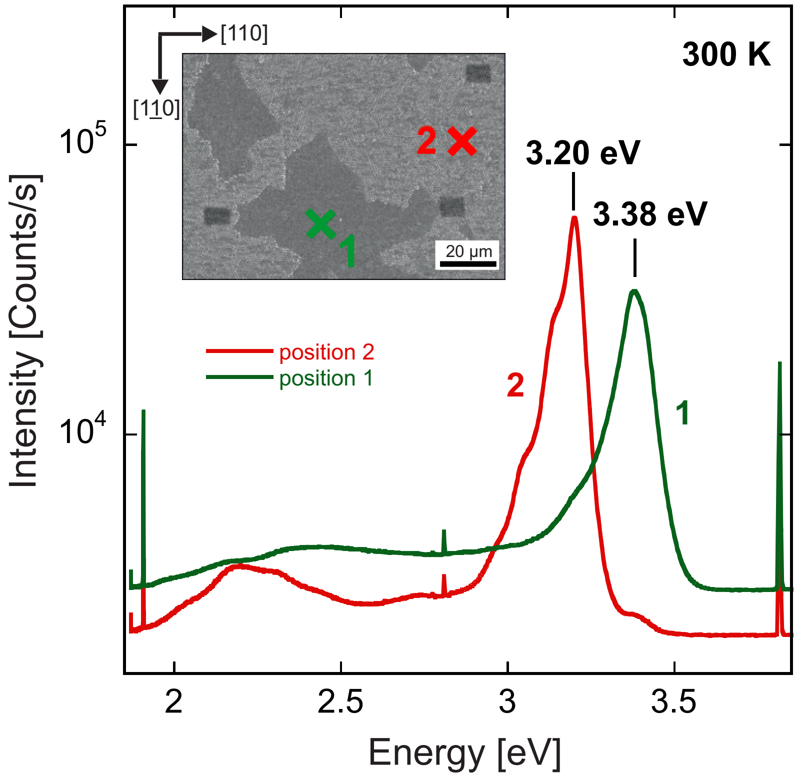

Figure 7.15

Micro-PL spectra of adjacent domains (position 1 green curve and position 2 red curve) of the selective-area-grown c-GaN at room temperature. Inset: Top view SEM image of the µ-PL measurement area on the sample surface. Each domain is identified with markers (dark rectangles) positioned by a SEM.

ginate from the substrate. It is likely that the domains are due to the presence of two different sets of {111} planes in c-GaN, which are either Ga- or N-terminated and which in metal organic chemical vapour deposition [103] were shown to have clearly different growth behaviour, like different growth rates. HRXRD measurements show that at large layer thicknesses the hexagonal fraction in selective-area-grown c-GaN is strongly enhanced. Several independent measurement techniques reveal that there is a largely differing amount of hexagonal inclusions and defects in the two sets of domains. Depending on the fraction of cubic or hexagonal phase the lateral growth rate varies accordingly. These observations need to be considered carefully in order to further reduce SF densities and hexagonal phase content in MBE grown selective-area-grown c-GaN layers.

7.2 Influences of Stacking Faults on Optical Properties of Cubic GaN Films and Cubic GaN/AlN MQWs

In the following the correlation between structural defects and the optical emission intensity of asymmetric c-GaN/AlN MQWs and c-GaN films is investigated by cathodoluminescence in the STEM (STEM-CL) at room temperature performed at the University of Magdeburg.

Two types of samples were fabricated. The sample structures are shown schematically in Fig.7.16. Sample A consists of a ~450 nm thin c-GaN layer on the 3C-SiC/Si substrate. Sample B is built up of a 50 nm c-GaN buffer layer on the substrate followed by 40 periods of asymmetric c-AlN/GaN QWs. In each period the active region is formed by a 2.1 nm c-GaN QW coupled by a 0.9 nm c-AlN barrier with a 1.6 nm c- GaN QW and embedded in 3 nm c-AlN barriers. Altogether the cubic MQW film on top of the c-GaN buffer has a film thickness of ~307 nm.

The samples were prepared usingthe cross-section preparation process described in section 6.1. Before STEM analysis the samples were cleaned in an oxygen plasma and then examined in a Tecnai F20 (S)TEM operating at 80 kV with an integrated CL setup (see section 3.8).

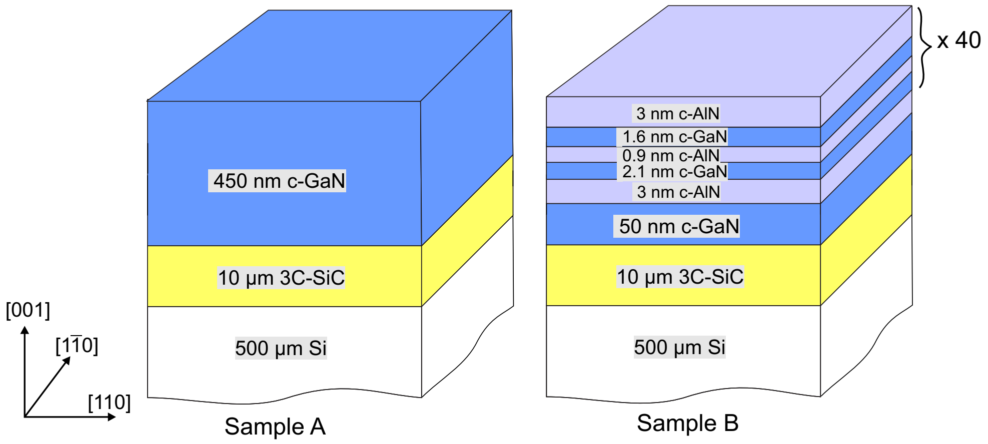

Figure 7.16

Sample structure of sample A (GNR 2151) and B (GNC 2206, fabricated by Dr. C. Mietze [101]).

Cubic GaN (Sample A)

Figure 7.17 shows a cross-section STEM image of sample A in ADF contrast along the [110] zone axis. The 450 nm thin c-GaN epilayer on top of the 3C-SiC substrate is revealed. Planar defects, identified as SFs on the {111} planes, extend from the c-GaN/SiC interface with an inclination of 57.4° towards the sample surface. Individual and also bunches of SFs can be observed. A general tendency that the SF density is reduced with increasing film thickness is visibly. A systematic decrease of the SF density as a function of layer thickness has also been verified by the group of Daudin et al. [51]. They explain this trend by annihilation mechanisms resulting in an improved crystalline quality towards the sample surface (see section 2.5). Moreover, it is mentioned in section 2.5 that the glide model by Ayers [50] implies that the dislocation density N_{disl} is inversely proportional to the layer thickness *d*. This can be proved performing HRXRD (002) rocking curves and using the model of Gay et al. [11] as demonstrated in section 2.5 (Fig. 2.9) and section 3.6. The inset in Fig. 2.9 (see section 2.5) exemplarily reveals the rocking curve of sample A (GNR 2151) with a FWHM of ~29 arcmin corresponding to a dislocation density N_{disl} in the order of 10^{10} cm^{-2}. The plot unambiguously shows that the FWHM decreases with increasing epilayer thickness. There is a correlation between the FWHM, respectively the dislocation density N_{disl}, and the film thickness. Similar results for c-GaN epilayers on 3C-SiC (001) substrates can be found in [51] and also in the 3C-SiC/Si (001) system [49].

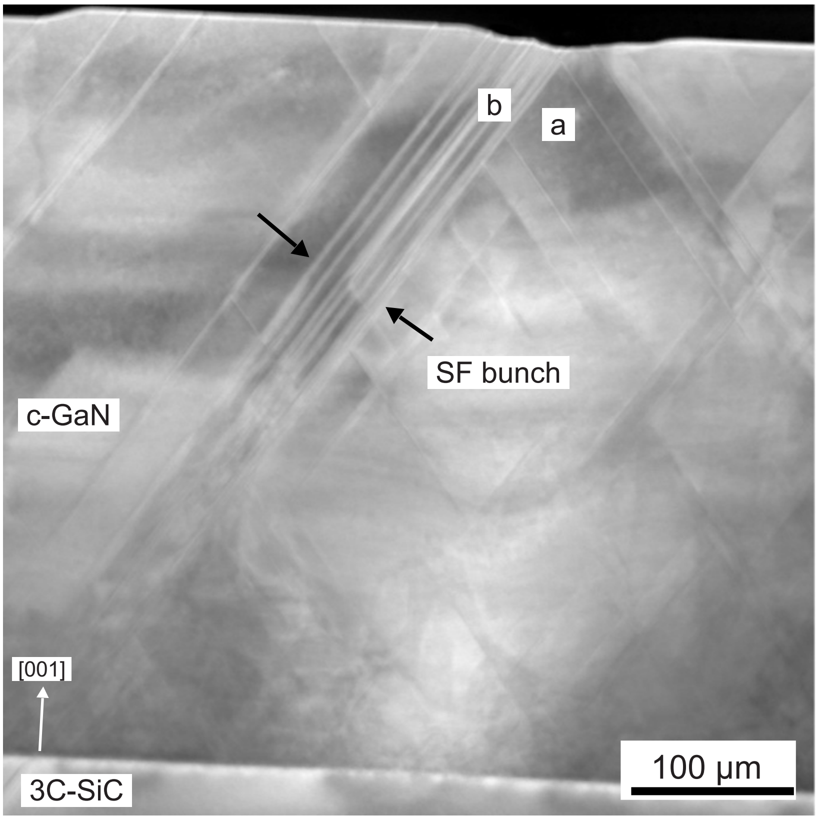

Figure 7.17

Cross-sectional STEM image in ADF contrast along the [110] zone axis of sample A. Individual and also bunches of SFs run from the c-GaN/3C-SiC (001) interface to the c-GaN surface. Local CL spectra, shown in Fig. 7.18, were taken from the measurement areas *a* and *b* marked near the surface.

In order to obtain information about the influences of the SFs on the optical properties of c-GaN local room temperature emission CL spectra (Fig.7.18) were taken from regions marked with *a* and *b* in the STEM image in Fig.7.17. Spectrum *a* is taken from a nearly defect free c-GaN region while spectrum *b* is detected from a defect rich area where a bunch of SFs runs through the crystal. The corresponding CL emission spectra shown in Fig. 7.18 contain two dominant maxima. The peak at 3.23 eV is due to the radiative recombination of the free exciton (FX) in c-GaN [109]. Also the luminescence of a deep compensating complex in the range of 1.8-2.8 eV is observed [110]. This red luminescence is comparable to the yellow defect luminescence in the hexagonal phase. In comparison, both spectra show the same emission characteristics, but the position and the intensity of the (FX) emission peak are different. In spectrum *b* there is a shift of the excitonic emission peak to 3.20 eV combined with a reduced intensity anda broadening of the peak. As anticipated, the undisturbed c-GaN region has a higher CL emission intensity of the (FX) transition than the structural defective region. Unfortunately, individual emission lines from these SFs, as shown in the hexagonal phase [111], cannot be resolved here.

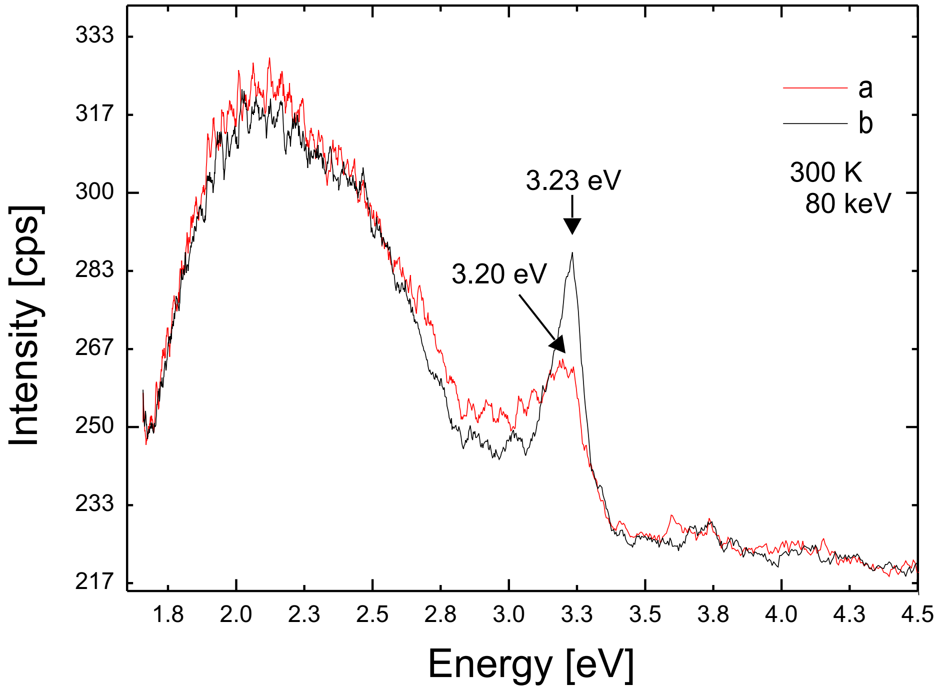

Figure 7.18

Local room temperature CL emission spectra *a* and *b* correspond to the marked regions *a* and *b* in the STEM in Fig. 7.17.

Cubic GaN/AlN MQWs (Sample B)

Since in PL and CL measurements MQW samples exhibit a particulary strong luminescence, a c-GaN/AlN MQW film (sample B) is investigated in the following. Figure 7.19a shows a cross-sectional HAADF-STEM image taken along the [110] zone axis of sample B. On top of the 50 nm c-GaN buffer the MQW layer stack can be seen. In the HAADF-STEM mode the c-GaN layers can be clearly distinguished from c-AlN layers by their higher intensity. In regions without any planar defects a straight sequential arrangement of c-GaN and c-AlN layers can be noticed with homogeneous thickness [16]. Again, a decreasing SF density with increasing film thickness due to annihilation processes can be noticed, but is not well resolved in this image. The entire MQW film exhibits undulations of the individual MQW layers. These undulations are caused by the surface shape of the c-GaN buffer and by bunches of SFs extending from the c-GaN/SiC interface up to the surface, as TEM studies [16] have shown. These TEM studies (see also subsection 7.3.2) also revealed that SFs emerging from the substrate interface are not stopped at the c-AlN/GaN interfaces of the different layers and lead to the undulation of the MQWs. Superimposed to theundulation of MQWs, the STEM image shows slight image distortions in the vertical scanning direction, visible by the rough appearance of the atomically sharp GaN/SiC interface (compare Fig. 7.20b). For the conclusions on the optical emission properties of the sample, which will be presented in the following, these image distortions are not important.

To analyze the influence of SFs on the luminescence output of the MQW film a panchromatic image within a wavelength range of 160-930 nm of the CL emission intensity is displayed in 7.19b. This image is spatially correlated to the STEM image in Fig. 7.19a and both images were collected simultaneously at room temperature.

The panchromatic (Fig. 7.19b) image reveals an inhomogeneous distribution of the CL intensity. The spatial correlation of Fig. 7.19a and b shows that the emission intensity increases with increasing MQW film thickness, i.e. towards the sample surface. High emission intensities (hot spots) appear in regions with a lower defect density, which are mostly located near the sample surface. In regions with bunches of SFs (marked with white arrows in Fig. 7.19a and b) the intensity of the CL signal is much lower and no hot spots can be detected here compared to areas with an improved crystal quality. In these regions, non-radiative recombination seems to be the predominant process. In order to find an explanation for SFs acting as non-radiative recombination centers, they are considered to be hexagonal inclusions in a cubic matrix. In this case, the carriers generated in the hexagonal QW would diffuse into the cubic matrix and recombine there due to the smaller band gap of the cubic phase compared to the hexagonal. The minory carrier diffusion length is determined in Ref. [112] to ~20 nm. This simplification includes no internal polarisation fields and should be verified by simulations of the band diagram like shown for cubic inclusions in hexagonal GaN nanowires [113]. These measurements directly demonstrate that the CL emission intensity can be correlated to the structural crystal quality.

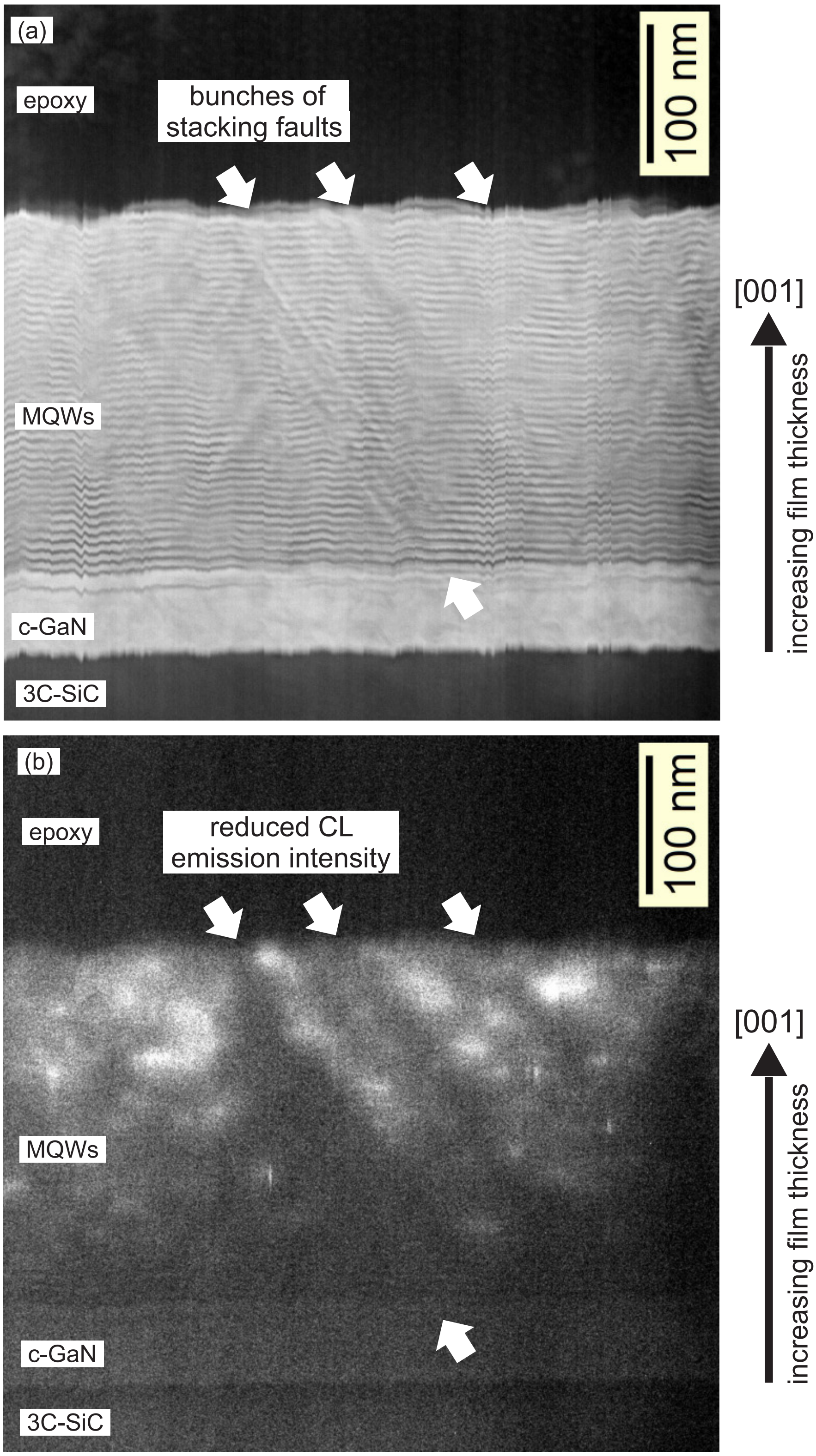

Figure 7.19

(a) Cross-sectional STEM image in HAADF contrast along the [110] zone axis of sample B. **(b)** Corresponding panchromatic image of the CL signal of the STEM image in (a) at room temperature.

The correlation between the CL emission intensity and the film thickness dependent crystal quality can be analyzed in more detail. In Fig. 7.20a local room temperature CL spectra *1-4* taken from sample B are displayed. The corresponding measurement spots *1-4* are marked in the STEM image in Fig. 7.20b and are ascendingly positioned with increasing film thickness. The CL emission spectrum *1* belongs to the 3C-SiC substrate, spectrum *2* to the c-GaN buffer layer, spectrum *3* to the area of the first c-AlN layer embedded in c-GaN and spectrum *4* was taken from the MQW layer near the surface of the sample, respectively. All emission spectra shown in Fig. 7.19a contain two dominant peaks at 3.26 eV and 3.64 eV plus the emission from the deep compensating complex in the range from 2.3-2.9 eV. The peak at 3.26 eV is due to the radiative recombination of the (FX) transition in c-GaN [109], and the emission peak at 3.64 eV can be related to asymmetric coupled c-MQWs [114]. The emission is assigned to the wider 2.1 nm QW, because the charge carriers tunnel from the smaller QW through the c-AlN barrier into the wider QW.

Because of the indirect band gap of the 3C-SiC substrate no CL emission signal can be detected in spectrum *1*. Spectrum *2* is assigned to the c-GaN buffer with anemission peak at 3.26 eV of the (FX) transition and a low emission signal at 3.64 eV. Thus, the slightly and homogeneously enhanced intensity of the c-GaN buffer layer in the panchromatic CL image of Fig. 7.19b is mainly attributed to the presence of free ecxitons. Spectrum *3* belongs to the first c-AlN layer embedded in c-GaN and shows two maxima at 3.26 eV and 3.60 eV with low intensity. The slightly lower emission energy of spectrum 3 at 3.60 eV may indicate that the thickness of the first QW may be about one monolayer wider than the QWs near the surface. Spectrum *4* represents the emission of the asymmetric c-MQWs at 3.64 eV near the surface in a defect reduced area. Here, the c-MQW emission intensity at 3.64 eV is drastically increased compared to spectra *2* and *3*.

In the inset of Fig. 7.20a the maximum intensities of the MQW peak around 3.64 eV from spectra *2-4* are plotted *versus* the film thickness on a double logarithmic scale. Here, the underground in Fig. 7.20a has been substracted from the maximum intensity values. A simple relationship between the film thickness and the MQW emission intensity isobserved pointing out that the emission intensity increases with decreasing defect density. It should be mentioned that the measurements shown here are not statistically averaged. Each measurement is afflicted by errors, because the intensity strongly depends on the defect density at the measurement point. Nonetheless, these results are in good qualitative agreement with the correlation of the FWHM of the rocking curves and the film thickness in c-GaN layers plotted in section 2.5: A decrease of the dislocation density N_{disl} and an increase of CL emission intensity with increasing film thickness is observed.

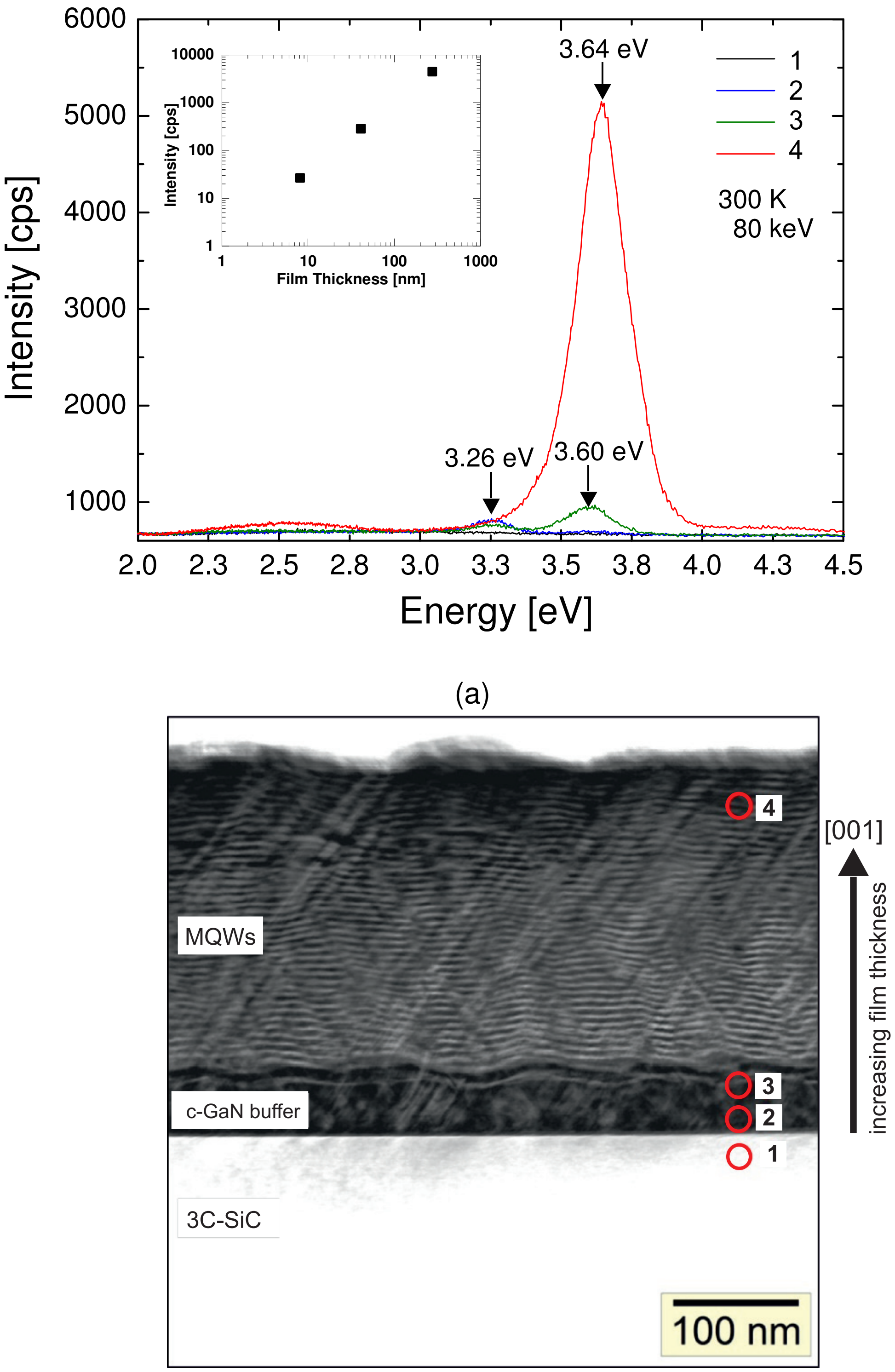

(a)

(b)

Figure 7.20

(a) Room temperature CL spectra *1-4* corresponding to the marked regions *1-4* in the STEM image (b). In the inset the maximum intensities of the MQW peak at 3.64 eV from spectra *2-4* are plotted *versus* the film thickness in a double logarithm scale. **(b)** Cross-sectional STEM image in ADF contrast along the [110] zone axis of sample B.

Conclusions

In summary, correlated room temperature STEM-CL measurements from c-GaN and asymmetric c-GaN/AlN MQWs films have been acquired and discussed. An increasing CL emission intensity with increasing film thickness due to the improved crystal quality is observed. This correlation can be connected to the reduction of the FWHM of ω-rocking curves with increasing film thickness of c-GaN films. Defects like SFs on the {111} planes lead to a decrease of the CL emission intensity.

7.3 Cubic GaN and AlN/GaN MQWs on Sub-Micrometer Structures

The former sections have demonstrated that {111} SFs lower the structural quality and reduce the CL emission intensity in planar cubic III-nitride films. Thus, the reduction of the SF density seems to be essential for improving the structural film quality and to enhance the optical emission intensity. The approach of this work receiving defect reduction is to grow on pre-patterned 3C-SiC structures. Therefore, the fundamentally structural characteristics of c-GaN and c-AlN/GaN MQWs films grown on sub-micrometer square shaped 3C-SiC structures are investigated by TEM. The SiC structures in this section have a top edge length of ~500 nm, a height of ~700 nm and were fabricated by the group of J. Pezoldt at the TU Ilmenau [90]. The section is divided into two parts: first a ~400 nm thin c-GaN film is analyzed and then c-AlN/GaN QWs are elucidated. Parts of the results of subsection 7.3.1 have already been published in [15], [102] and the results of subsection 7.3.2 are published in [16], [102].

7.3.1 Cubic GaN Films on Sub-Micrometer Structures

In this section the growth of GaN on post shaped 3C-SiC structures is investigated and the influence of substrate domains on the defect structure is analyzed. Therefore, the following analysis is also separated into two parts.

Arrays of 5x5 posts are repeated several times on the substrate surface with etched down spaces in between. The posts have top edges with a length of about 500 nm, a height of about 700 nm and are aligned parallel and perpendicular to the [110] direction of the substrate. The possibility to align the sidewalls parallel to {110} lattice planes and therby forming clearly arranged growth conditions is the main reason why these patterns were created by EBL. The posts and the etched down 3C-SiC surface in between were overgrown with ~400 nm GaN. After growth the c-GaN epilayer was characterized by EBSD and the GaN grown on the structures was analyzed by cross-

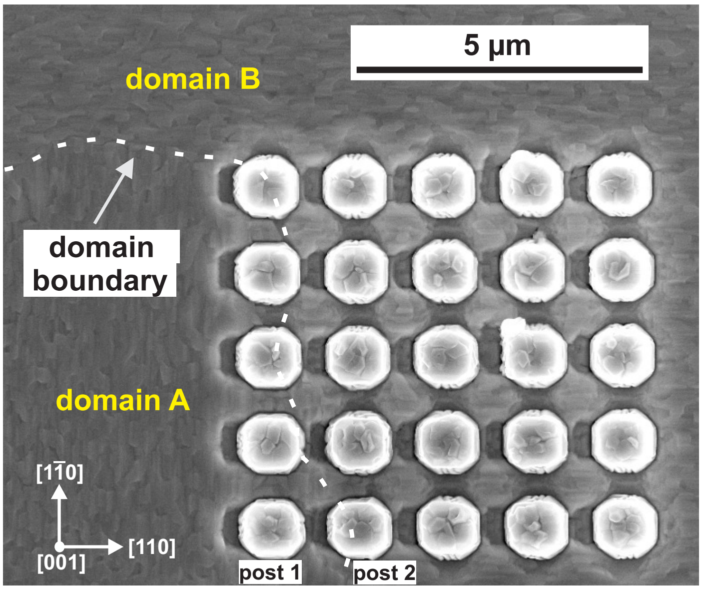

Figure 7.21

Top view SEM image of a nanostructure array overgrown with ~400 nm c-GaN (sample GNR 2152). The c-GaN surface exhibits surface striations in two perpendicular orientations parallel to [110] and [1$\underline{1}$0], which are considered to belong to be APDs with a boundary in between.

sectional TEM. For this purpose, the post structures were prepared using a focused ion beam (see section 6.2). The TEM lamellas were cut from different post arrays parallel to the [110] direction.

Cubic GaN Grown on 3C-SiC (001) Posts

In section 7.1 it is shown that planar c-GaN surfaces grown on 3C-SiC/Si (001) substrates exhibit surface striations in two perpendicular orientations parallel to the [110] and [1$\underline{1}$0] direction of the substrate. Corresponding surface regions are considered to belong to two APDs with a boundary in between. The structural quality within these APDs is not equal meaning that the amount of hexagonal inclusions and defects within the domains is different (see section 7.1).

Figure 7.21 shows a top view SEM image of post shaped 3C-SiC (001) structures overgrown with ~400 nm c-GaN. The edge length of the post structures is increased after GaN overgrowth from about 500 nm to about 1 µm. Furthermore, there are contrasts in the areas in between neighbouring posts, the darker regions indicating deepenings in the GaN layer. They arise probably due to shadowing in particular when the rotation of the sample holder is stopped during MBE growth for RHEED inspection of the growth surface.

A domain boundary, separating two domains with their characteristic orientation of surface striations, is clearly visible. In domain A the surface striations are perpendicular to the [110] direction and in domain B the striation orientation is parallel

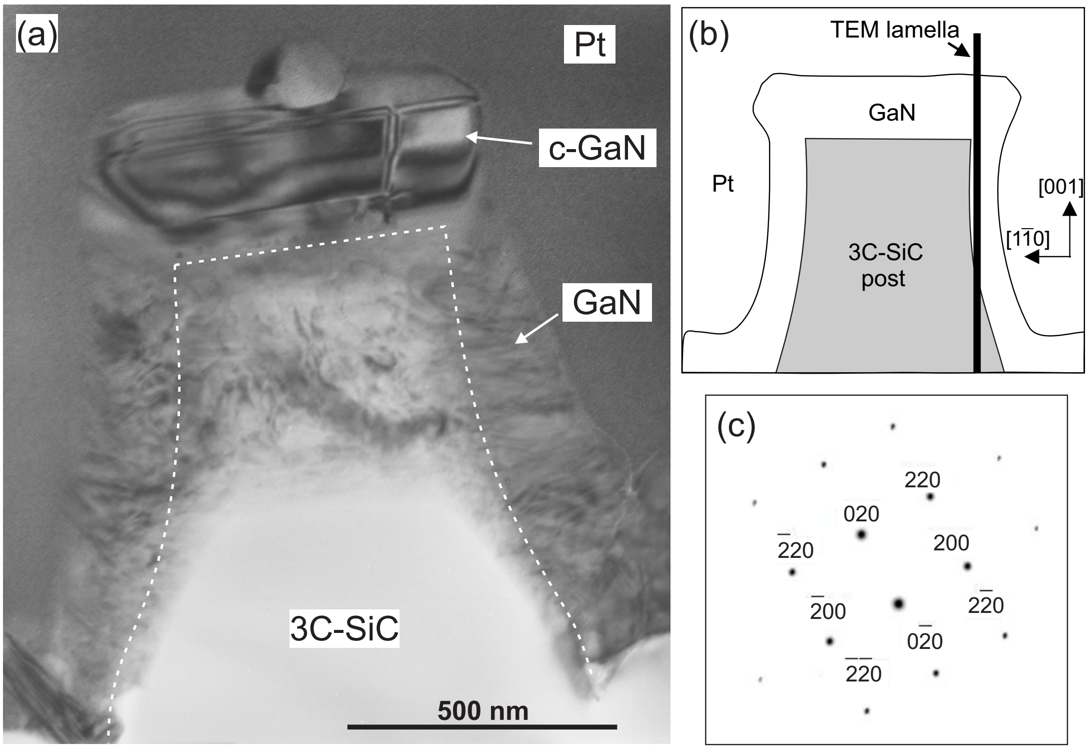

Figure 7.22

(a) Cross-sectional TEM image of an individual 3C-SiC post overgrown with 400 nm c-GaN taken along the [110] zone axis. **(b)** A schematic cross-section view through the center of a typically overgrown SiC post parallel to the [11̲0] direction. The TEM lamella cuts through the sidewall of the post perpendicular to the [11̲0] direction. **(c)** SAD pattern (contrast inverted) taken from the middle c-GaN island in (a) along the [001] c-GaN zone axis with the main reflections indexed.

to the [110] direction. The array of posts is located in both types of domains. In the bottom row, the domain boundary passes through post 2 (see Fig. 7.21).

To have a closer look to the selective-area-grown GaN on the post structures, Fig. 7.22a displays a cross-sectional TEM bright-field micrograph of an individual overgrown 3C-SiC (001) post taken along the [110] zone axis. The GaN surface is covered with a Pt protection film (dark in Fig. 7.22a) necessary in the TEM lamella preparation process (see subsection 6.1). The image shows that the GaN grows on the top of the 3C-SiC post and on its sidewalls. Since the TEM lamella was taken through the sidewall of the post and not through the center (Fig. 7.22b), the GaN is visible on threesidewalls of the post. This leads to the strongly varying contrasts within the upper part of the SiC post, since here the almost defect free crystal lattice of the SiC post is superimposed with the defect rich GaN growing on the flanks of posts. The GaN on the top of the post grows in individual crystals. It should be emphasized that the part of the GaN film displayed in Fig. 7.22a is located at the edge of the GaN top layer. The homogeneous contrasts within this part of the GaN film indicates a very low defect den-

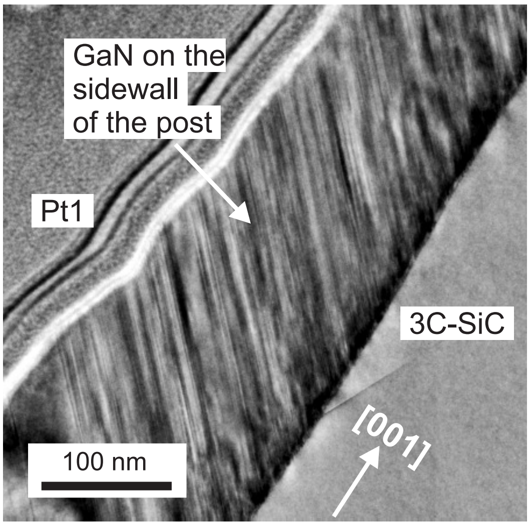

Figure 7.23

TEM image of GaN grown on a SiC post sidewall taken along the [110] zone axis. The GaN growth is dominated by {111} planar defects. The parallel lines along the GaN surface are thickness fringes of the TEM lamella.

sity of the GaN growing on top of the SiC post. There is only one dislocation like defect running vertically in the GaN top bit. The corresponding SAD pattern taken from the central GaN area on top of the post in (a) is shown in (c). The diffraction pattern can be completely assigned to the lattice of c-GaN with the [001] zone axis oriented parallel to the electron beam. The SAD pattern contains no further reflections indicating a crystal with a pure cubic phase. These are the first steps towards defect reduced c-GaN grown via MBE on a dimensionally limited 3C-SiC (001) growth area. However, there is also a small misaligned GaN crystal centered on top of the epitaxial GaN film, not contributing to the SAD pattern shown.

Figure 7.23 shows a TEM image of GaN grown on a SiC post sidewall taken along the [110] zone axis at higher magnification. The inner structure of the GaN sidewall is dominated by planar defects occupying one of the {111} planes. One reason for this could be the sidewall surface roughness resulting from the etching process during substrate patterning. Another reason is probably the deviation from an ideal 90° slope of the flanks. The GaN layer thickness on the sidewalls is smaller than on top of the post. Hence, there is a lower GaN growth rate on the sidewalls (in this region approximately 2.5 times less) than on top of the 3C-SiC post. It is conspicuous that the {111} SFs, here lying on the $(1\underline{1}\underline{1})$ plane, are all oriented in the same direction. The investigation of the sidewalls of other SiC posts have shown that the SFs can also all lie on the $(\underline{1}1\underline{1})$ plane. A relation of this orientation with regard to the APDs is not determined here due to the lack of adequate TEM samples.

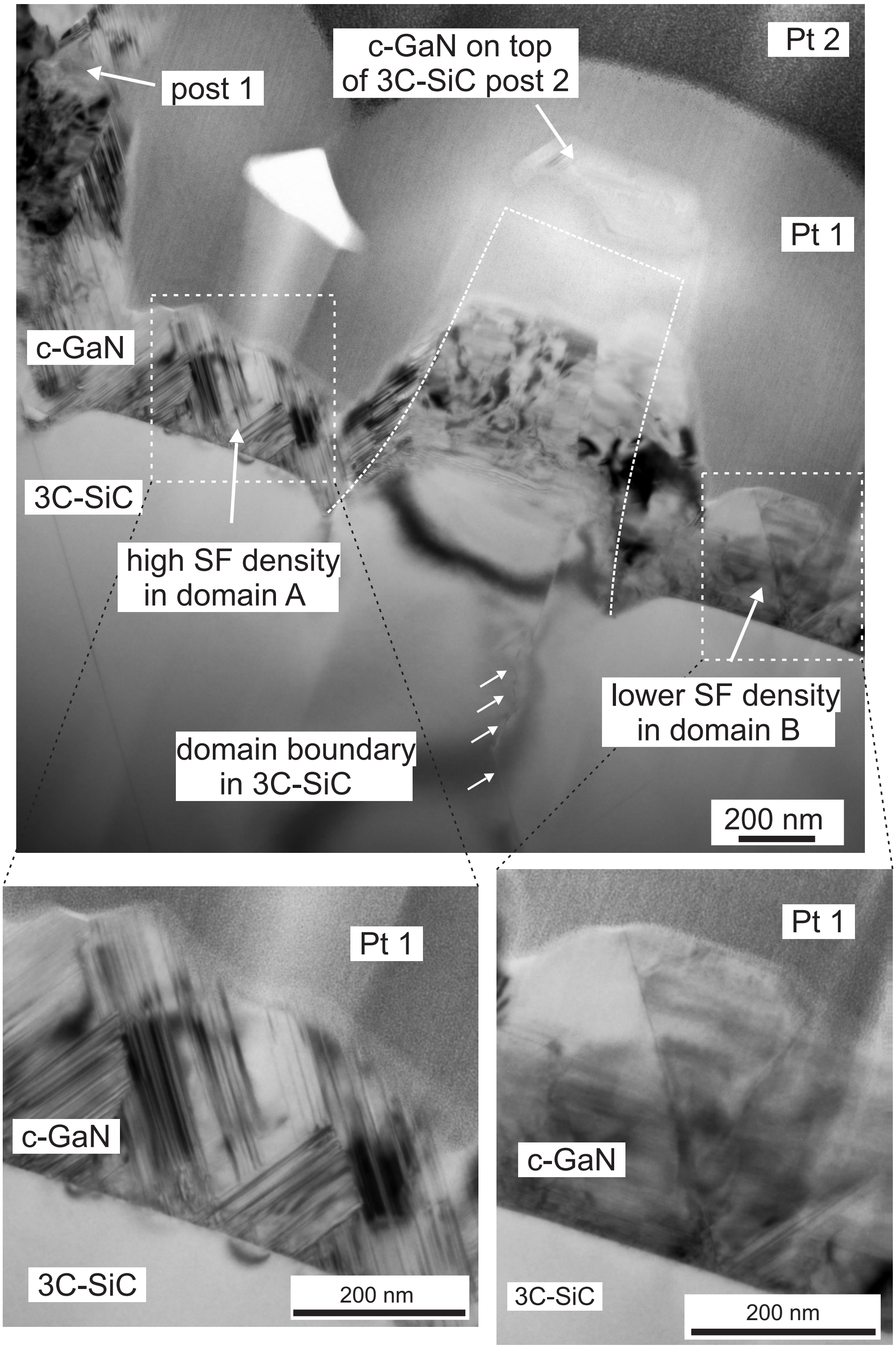

Figure 7.24

Cross-sectional TEM image of an individual 3C-SiC post overgrown with 400 nm c-GaN taken along the [110] zone axis. A domain boundary coming from the 3C-SiC substrate runs through the 3C-SiC post (post 2 in Fig. 7.21). Hence, the c-GaN grown on the left and the right side of the post belong to adjoining APDs (domain A and B in Fig.7.21). The SF density on the left side of the post is significantly higher than on the right side.

Figure 7.24 shows a cross-sectional TEM image of post 2 taken from the bottom row of the post array in Fig. 7.21. The bright-field image was taken along the [110] zone axis where the typical {111} planar defects appear edge-on and lead to line shaped contrasts. Next to post 2 the GaN epilayer grown between the posts is visible, together with post 1 on the left. Again, a low defect density GaN top film is observable on top of the SiC post, which due to the non-central FIB cut appears to be disconnected from the SiC post. The GaN grown on the SiC post sidewalls and on the right sidewall of post 1 is dominated by {111} planar defects.

The domain boundary visible in the SEM image of the GaN surface in Fig. 7.21 running through post 2 of the bottom row of posts is visible in the cross-sectional TEM image of Fig. 7.24, too. It clearly runs through the 3C-SiC substrate and passes through post 2. Hence, the c-GaN grown on the left and the right side of the post belong to adjoining APDs, called domain A and B, respectively, in Fig. 7.21. It is obvious that the SF density left to the domain boundary, e.g. in domain A, is significantly higher than in domain B. Therefore, it is evident that at the same growth conditions, the two different domains in the SiC substrate lead to largely different c-GaN crystal qualities.

Summary

The results in this subsection show first steps towards the MBE growth of defect reduced c-GaN on a dimensionally limited 3C-SiC (001) growth area. The overgrown 3C-SiC (001) sub-micrometer structures are post shaped and aligned parallel and perpendicular to the [110] directions of the substrate. On top of the 3C-SiC posts nearly defect-free phase-pure c-GaN with excellent structural properties is grown. On the sidewalls of these posts, however, the GaN layer contains a high density of {111} planar defects. For c-GaN grown in the intermediate area between the 3C-SiC posts the SF density in adjoining anti-phase domains is markedly different, with the domain boundary clearly separating regions of low and high planar defect densities. It is likely that the SF density on top of the posts varies as well, depending on whether the post belongs to either type of domain, but such an observation was not possible yet due to the limited number of TEM samples that could be prepared by FIB.

7.3.2 Cubic AlN/GaN MQWs on Sub-Micrometer Structures

Next, the structural quality of c-AlN/GaN MQWs on pre-patterned 3C-SiC/Si (001) substrates is investigated. The growth of such a layer system on a pre-patterned surface gives the opportunity to study both the influence of defects on layer growth and the observation of the growth behavior at edges of the surface pattern.

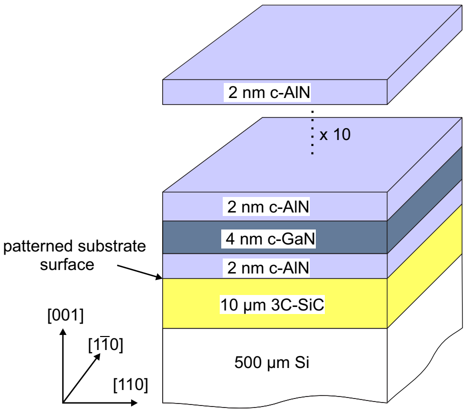

Figure 7.25

Schematic drawing of the sample structure (GNRC 2284).

The surface pattern consists of posts with edges aligned parallel to the <110> directions with a length of about 550 nm and a height of about 700 nm. On these patterned substrates 10 periods of ~2 nm c-AlN barriers with a 4-5 nm c-GaN layer in between were grown by MBE. Altogether a film thickness of ~62 nm in [001] growth direction was deposited. Figure 7.25 illustrates the sample structure. Because of the smaller mismatch between 3C-SiC and c-AlN of about -0.25% compared to c-GaN the MQW growth is started with a c-AlN layer. This should lead to a slightly lower dislocation density of about $8 \cdot 10^{9}$ cm^{-2} [115] and should be the first approach towards defect reduction in c-GaN.

Scanning Electron Microscopy

Figure 7.26 shows a side view SEM image of an 5x5 array of 3C-SiC posts overgrown with the MQW film. The sidewalls of the posts have a varying steepness. At the bottom the posts are surrounded by trenches due to the etching process [90]. One explanation for this so called trenching effect is given by ions arriving at grazing incident angles on sloped sidewalls and getting reflected there leading to a localized higher etching rate atthe bottom of the structure [116]. Film deposition takes place on the top, on the sidewalls and between the posts. The whole patterned area is covered with the MQW

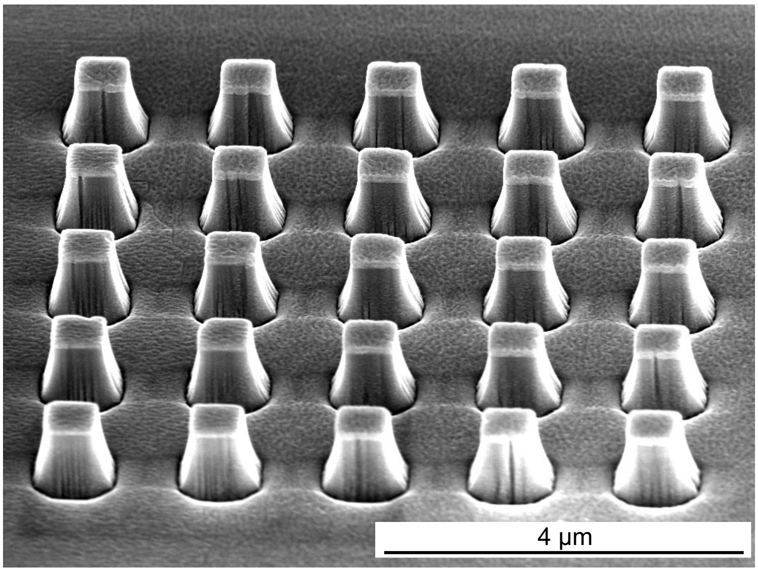

Figure 7.26
Side view SEM image of an array of overgrown 3C-SiC (001) posts.

film. In between neighbouring posts deepenings in the layer are seen, probably due to shadowing in particular when the rotation of the sample holder is stopped for RHEED inspection.

Transmission Electron Microscopy

Figure 7.27 shows a cross-sectional TEM image of an individual 3C-SiC post overgrown with 10 periods of c-AlN/GaN QWs taken along the [110] zone axis. The post is covered by the two Pt layers used in the FIB-TEM specimen preparation process. The post has slightly curved sidewalls. V-groove trenches are formed at the bottom of the post (seesubsection 7.3.2.1). The top of the post and also the sidewalls as well as the free surface in between are covered with the MQW film. It should be noted that all posts exhibit almost identical growth morphologies of the MQW film and an identical internal defect distribution.

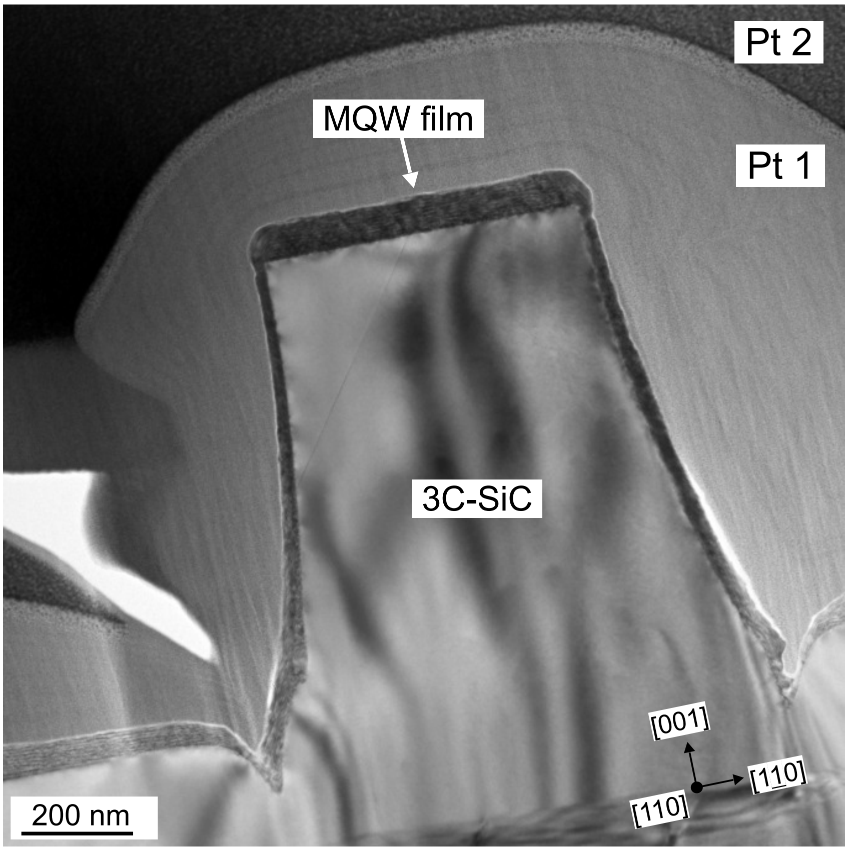

Figure 7.27

Cross-sectional TEM bright-field image of an individual 3C-SiC post overgrown with 10 periods of c-AlN/GaN MQWs taken along the [110] zone axis.

Figure 7.28a shows a more detailed bright-field TEM image of the MQW film on top of the 3C-SiC post in Fig. 7.27. Due to the difference in electron extinction lengths the c-GaN layers (dark) and the c-AlN barriers (bright) can be clearly separated. In Fig. 7.28a bunches of {111} SFs can be seen propagating through the entire MQW layer stack. The SFs emerge from the 3C-SiC/c-AlN interface and are not stopped at the c-GaN/AlN interfaces of the different layers. In regions with a high SF density the sequential arrangement of c-AlN/GaN layers is disturbed which generates an undulating shape of the MQWs. In contrast in regions without any planar defects a planar sequential arrangement of c-AlN and c-GaN layers is observed with uniform growth rate. Strong undulations may occur right within the first few layers of the MQW stack. In some cases these undulations are transferred up to the surface, leading to surface hillocks. In other cases these undulations are smoothened in subsequent layers, leading to a smooth surface at the top. Care must be taken therefore if one would try to judge the smoothness of MQW layer stacks from measurements of the surface smoothness of a layer stack (using SEM or scanning probe techniques). It should be emphasized that undulations generated in the first few layers on the substrate are not transferred vertical-

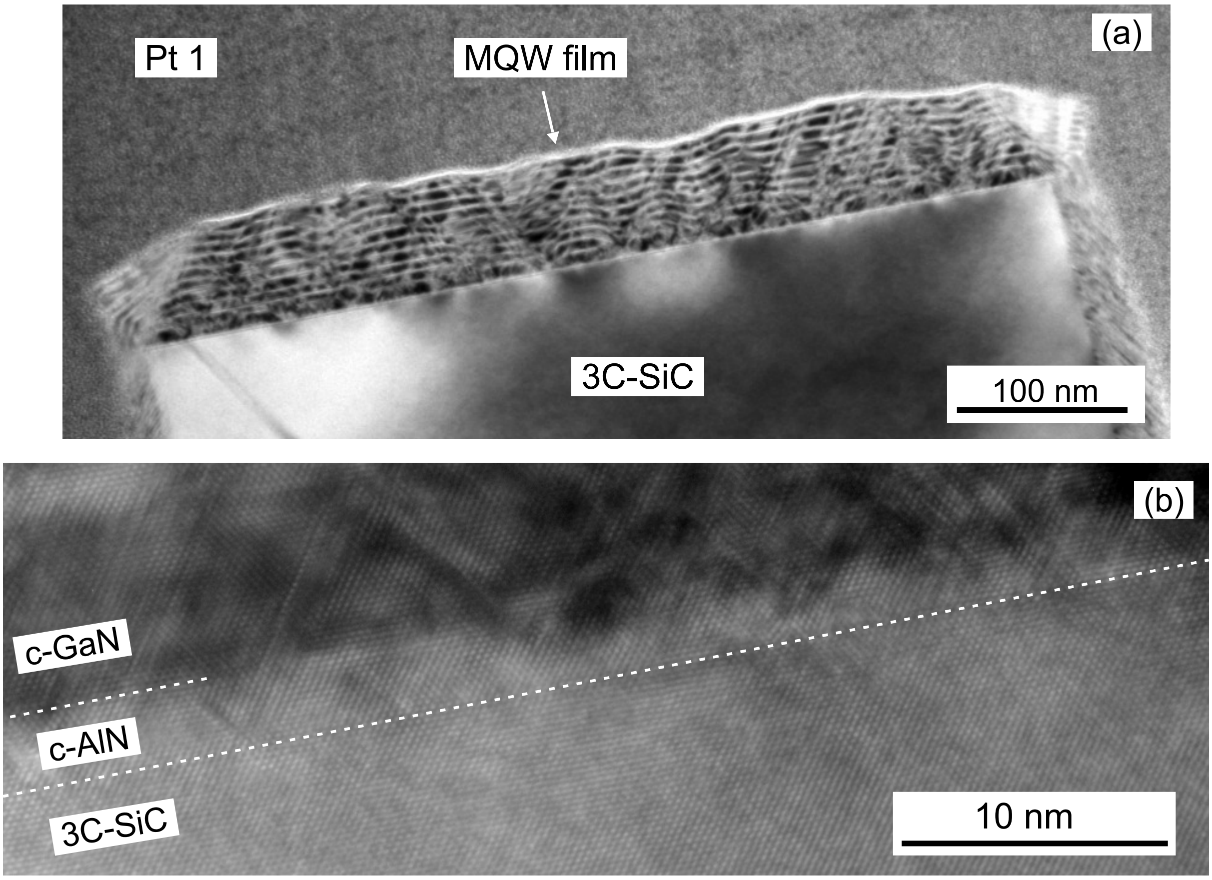

Figure 7.28

(a) TEM image along the [110] zone axis of the MQWs on top of the 3C-SiC post. In regions with a high SF density the sequential arrangement of the MQWs is disturbed. **(b)** High-resolution TEM image along the [110] zone axis of the 3C-SiC/c-AlN interface on top of the post.

ly towards the surface but follow the propagation of the SFs, indicating a locally reduced growth rate around the SFs. The SFs arise although the misfit between the 3C-SiC substrate and the first c-AlN layer is small. To understand the growth process of the first c-AlN layer a high-resolution TEM image of the interface of the 3C-SiC substrate and the c-AlN is shown in Fig. 7.28b. It is observed that the c-AlN/3C-SiC interface is atomically smooth and exhibits an undisturbed crystalline structure. The first c-AlN layer has an average thickness of 6 ML and a comparatively rough, three-dimensional interface to the c-GaN film on top. One explanation for this tendency to island formation can be the difference in surface energies of the 3C-SiC substrate and the c-AlN as described in detail in Ref. [115]. It is reported that after 6 ML c-AlN growth a roughness transition of the surface from 2D into 3D-islands is observed. After a growth of 10-20 MLs the surface transforms back into a smooth 2D state. This transformation depends on the Al coverage of the growth front [115].

It is obvious that optimized growth conditions of the first c-AlN layer are essential to improve the MQW growth. The growth of the following (first) c-GaN layer is affected by the rough surface and the lattice mismatch with the first c-AlN layer. These may be the main reasons for the formation of {111} SFs with a 54.7° slope towards the surface which occur at a high density in this layer and all layers on top, frequently forming bunches of planar defects. The density of planar defects seems to be largest within the first c-GaN layer (Fig. 7.28b) but is similar in the AlN layer underneath. This might indicate that the SFs nucleate at the c-AlN/GaN interface and then extend into both, the c-GaN and the c-AlN film underneath.

Occasionally it is also observed that SFs originating from the 3C-SiC substrate extend into the MQW film. However, since the density of SFs in the 3C-SiC substrate is comparatively small this mechanism plays a minor role for the SF formation in the MQW layer stack.

Due to the contrast between c-AlN and c-GaN layers in STEM images the MQW structure investigated here provides an indication of the general growth kinetics on patterned substrates. The individual MQW layers can be regarded as “annual rings” which give information about the growth behaviour especially around the edges of the posts.

Figure 7.29a displays a HAADF STEM image of a part of the MQW film grown on top of a 3C-SiC post and on the sidewall. In the HAADF STEM modus the contrasts are less influenced by local strains and atomic columns appear as bright dots with the intensity increasing with increasing atomic number. Therefore, GaN layers can be distinguished from AlN by their higher intensity, e.g. the contrasts are inverted with respect to the TEM images in Fig. 7.28. The MQW film on top of the post in [001] growth direction encloses the almost perfectly rectangular edge of the post. Judging from the progress of the individual layers it looks like the MQW film is bent around the 3C-SiC edge. Further the growth morphology on the (001) plane is not influenced by the growth on the sidewall of the post. The inset in Fig. 7.29a displays an annotated section of the overgrown post edge with indexed facets. It is obvious that the MQW layers cover the (nearly) 90° edge by developing a low-index facet rather than by forming a conformal system of 90° angled layers. Most pronounced is the (111) facet, which – in each layer – ends directly above the 90° edge of the 3C-SiC post.

In Fig. 7.29b a TEM bright-field image along the [110] zone axis of the MQW film around the 3C-SiC post edge is shown. A bunch of SFs on the $(1\underline{1}1)$ plane occurs directly at the edge. In the area above (the beginning is marked with a dashed line in Fig. 7.29b) the individual MQWs are bent parallel to the $(1\underline{1}1)$ SFs and the growth direction is changed to the $[1\underline{1}1]$ direction. Additionally, the thickness of the individual MQW layers is varying compared to the growth in [001] growth direction indicating a different growth rate (around 1.6 times less) in this region. Here thecrystalline nature is dominated by SFs which promotes the hexagonal phase. Infact, Fourier transformed

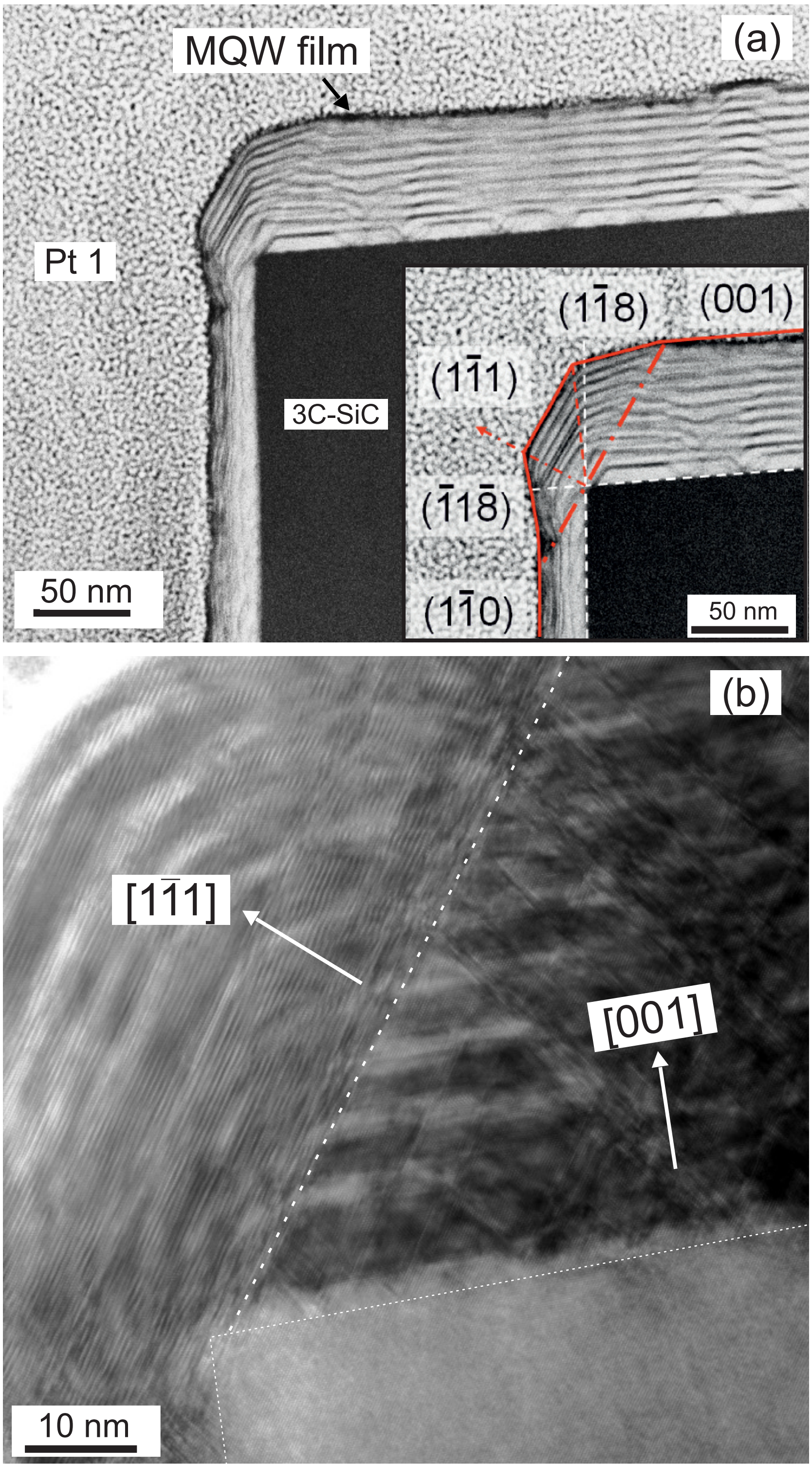

Figure 7.29

(a) STEM image along the [110] zone axis of a part of the MQW film grown on top of a 3C-SiC post with ~500 nm top edge length and around the edge. Inset: the MQW layers cover the (nearly) 90° edge by developing (low-index) facets. **(b)** TEM bright-field image along the [110] zone axis of the MQW film around the 3C-SiC post edge. At the edge the individual MQWs are bent parallel to the {111} SFs. The diffuse contrast results from the high SF density.

images of the region above the $(1\underline{1}1)$ facet give a hexagonal rather than a cubic reciprocal lattice.The diffuse contrasts in this region result from the high defect density. So far it is not clear whether the shape of the substrate edge influences the formation of SFs. The investigation of the detailed growth kinetics especially on substrate edges should be the subject of further studies.

Summary

In summary, these results show that it is possible to grow c-AlN/GaN MQWs on pre-patterned 3C-SiC substrates by means of MBE. {111} SFs occur and continue through the entire layer stack and generate regions with locally reduced growth rate. This leads to an undulated shape of the MQW film. The SFs are mainly induced by the three-dimensional morphology of the first AlN layer on the SiC substrate. Therefore, any major improvements of the MQW morphology can be achieved only by eliminating the island growth of these initial layers. It is shown that MQW films do not grow conformally around (nearly) 90° SiC edges along <110> directions, but form {111} facets which promote the formation of hexagonal inclusions in both, the c-GaN and the c-AlN films.

7.3.2.1 Cubic AlN/GaN in 3C-SiC V-grooves

Low-dimensional systems, like quantum wires (QWRs), have attracted great interest during the last years. One advantage of these structures is an increased exciton binding energy resulting from lateral confinement, which gives rise to enhanced linear and nonlinear optical excitonic effects [117]. One fabrication technique to achieve QWRs is the epitaxial growth on nonplanar substrates for producing V-groove QWRs (V-QWRs) [118,119]. Until now these V-QWRs have not yet been realized in the cubic AlN/GaN/SiC system. In the following, a possible route to obtaining c-GaN V-QWRs encapsulated in c-AlN shall be presented, as observed accidentaly in the studies reported above.

Due to trenching effects during the 3C-SiC etching process, V-grooves are formed around the post shaped structures described in the previous section. In Fig. 7.30a a schematic cross-section view of a 3C-SiC post is illustrated. The V-shape trench runs around the bottom of the entire SiC post. The deposition of a sequence of AlN, GaN and again AlN films on such a V-groove gives rise to the formation of a GaN V-QWR looping around the bottom of the SiC post. High-resolution STEM images were performed to analyze the structural quality of the V-QWRs. Figure 7.30b reveals a cross-section high-resolution STEM image of such a V-groove. In the groove, a layer of c-AlN covers the {111} 3C-SiC V-groove sidewalls. Then the c-GaN QW follows which due to the given form has a triangular cross-section and which is covered again

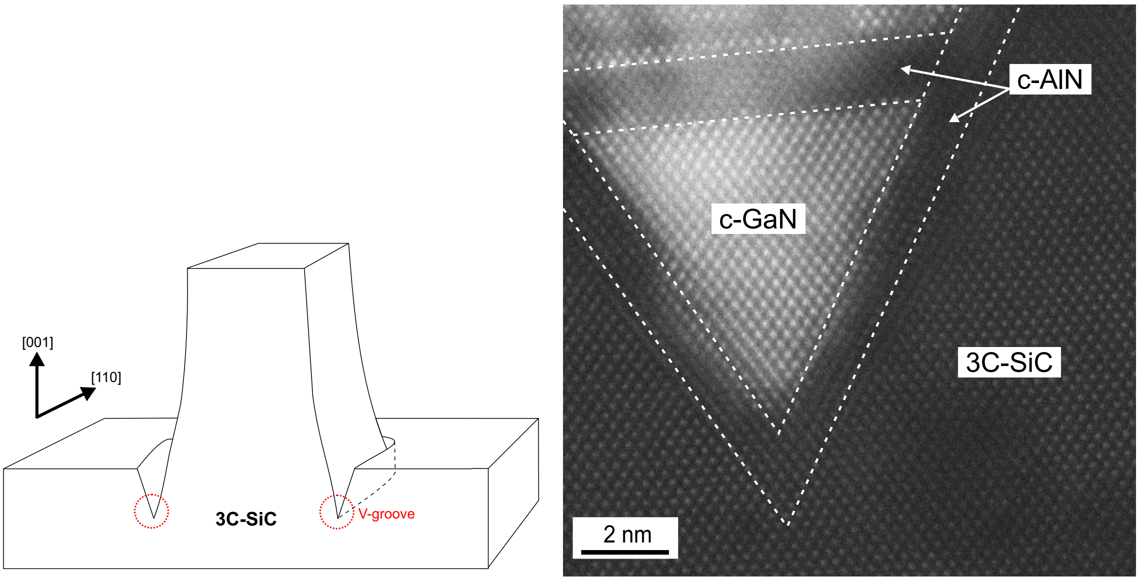

(a) (b)

Figure 7.30

(a) Schematic cross-section drawing of a 3C-SiC post. A V-groove trench runs around the hole structure. **(b)** High-resolution STEM image of almost defect-free c-AlN/GaN layers grown in a 3C-SiC V-groove with {111} sidewalls.

with a c-AlN layer. Thus, the c-GaN is surrounded by c-AlN. Due to the difference in contrast the different materials can be clearly distinguished, while AlN and SiC show little contrast due to similar atomic numbers. It can also be seen that the regular arrangement of the atom columns is not disturbed and that this V-QWR seems to be defect free. These investigations show the possibility to grow c-AlN/GaN QWs on V-groove patterned 3C-SiC substrates.

7.4 Influence of Growth Area Reduction on Cubic GaN

In the previous section, the top edge lengths of the square-shaped 3C-SiC (001) structures were about 500 nm. It was demonstrated that it is possible to grow c-GaN and c-AlN/GaN MQWs by means of MBE on top of these structures. In order to investigate the influence of growth area reduction on the growth of c-GaN, the top edge length of the 3C-SiC (001) structures is now reduced to ~240 nm, ~100 nm and ~20 nm (see Fig. 7.31). To guarantee the comparability of the films grown on these structures, individual arrays are arranged on the same sample (here GNR 2298). They were simultaneously fabricated and overgrown with ~85 nm GaN by MBE. The different heights of the 3C-SiC structures seem to be a result of different etching rates in the RIE process and shadowing phenomena.

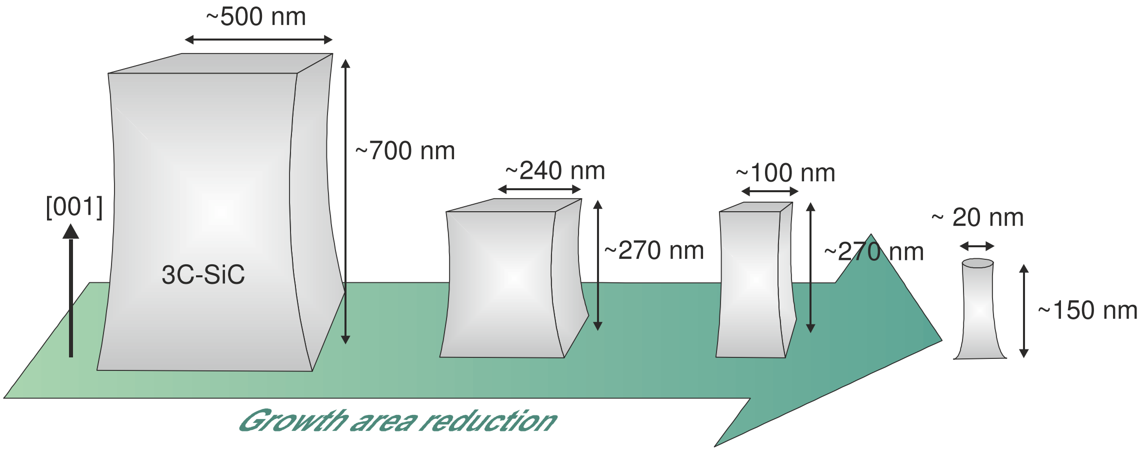

Figure 7.31

Overview: Schematic drawing of different types of 3C-SiC (001) structures investigated in this section. The post-shaped SiC structures with top edge lengths of ~500 nm are analyzed in section 7.3, the others located on one sample will be introduced in the following.

7.4.1 3C-SiC (001) Posts with ~240 nm Top Edge Length

Figure 7.32 displays a side-view SEM image of a part of array 8D (see section 4.2) from sample GNR 2298 consisting of 3C-SiC (001) structures with top edge lengths of ~240 nm and heights of ~270 nm which were overgrown with 85 nm GaN. The original distance between the uncovered structures is ~500 nm.

It is obvious that growth takes place on the top, on the sidewalls and between the posts, like mentioned before in section 7.3. The c-GaN surface between the structures shows the characteristical c-GaN morphology with elongated surface striations which

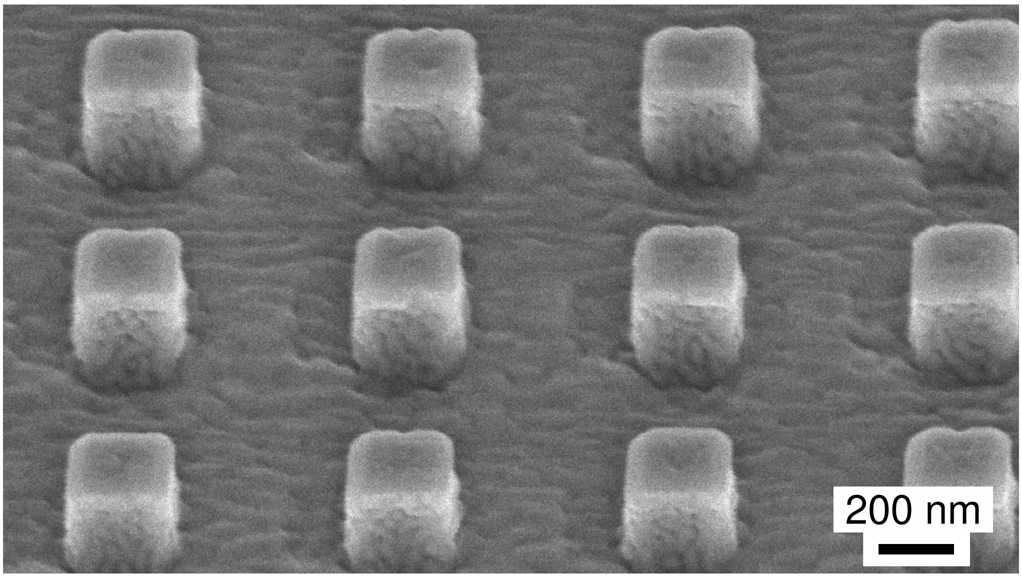

Figure 7.32

Side-view SEM image of an array with 3C-SiC (001) structures with top edge lengths of ~240 nm and heights of ~270 nm which were overgrown with ~85 nm GaN (sample GNR 2298, array 8D).

have also been presented by SEM and AFM measurements in the previous sections. Additionally, the typical deepenings in the c-GaN layer next to each post, are also observed. As mentioned in section 7.3 they arise due to shadowing in particular when the rotation of the sample holder is stopped during MBE growth for RHEED monitoring.

The upper part of Fig. 7.33 shows an overview cross-sectional TEM image of a TEM lamella containing a row of SiC structures from the array shown in Fig. 7.32. Five overgrown SiC posts can be identified which are surrounded by two Pt protection films (Pt1 and Pt2). Taking into account that the FIB cut is not exactly parallel to [110] and therefore only passes through the middle of the first two posts (from the left), the posts are regularily arranged and largely have the same dimensions. This overview image demonstrates that the SiC structures have been fabricated reproducibly and consistently. Moreover, the GaN film on top of the posts seems to show comparable structural characteristics. Therefore, one individual post is analyzed in detail representative for all structures and is shown in the enlarged TEM image in Fig. 7.33. The dashed white line indicates the SiC/GaN interface and thus the shape of the post. The side walls are slightly curved especially at the edges of the (001) growth area. Because the TEM lamella was taken through the sidewall of the post and not through the center (see section 7.3, Fig. 7.22), GaN is visible on three sidewalls of the post. This results in varying Moiré contrasts within the upper part of the SiC post, since here the almost defect free crystal lattice of the SiC post is superimposed with the defect rich GaN grown on the posts sidewalls.

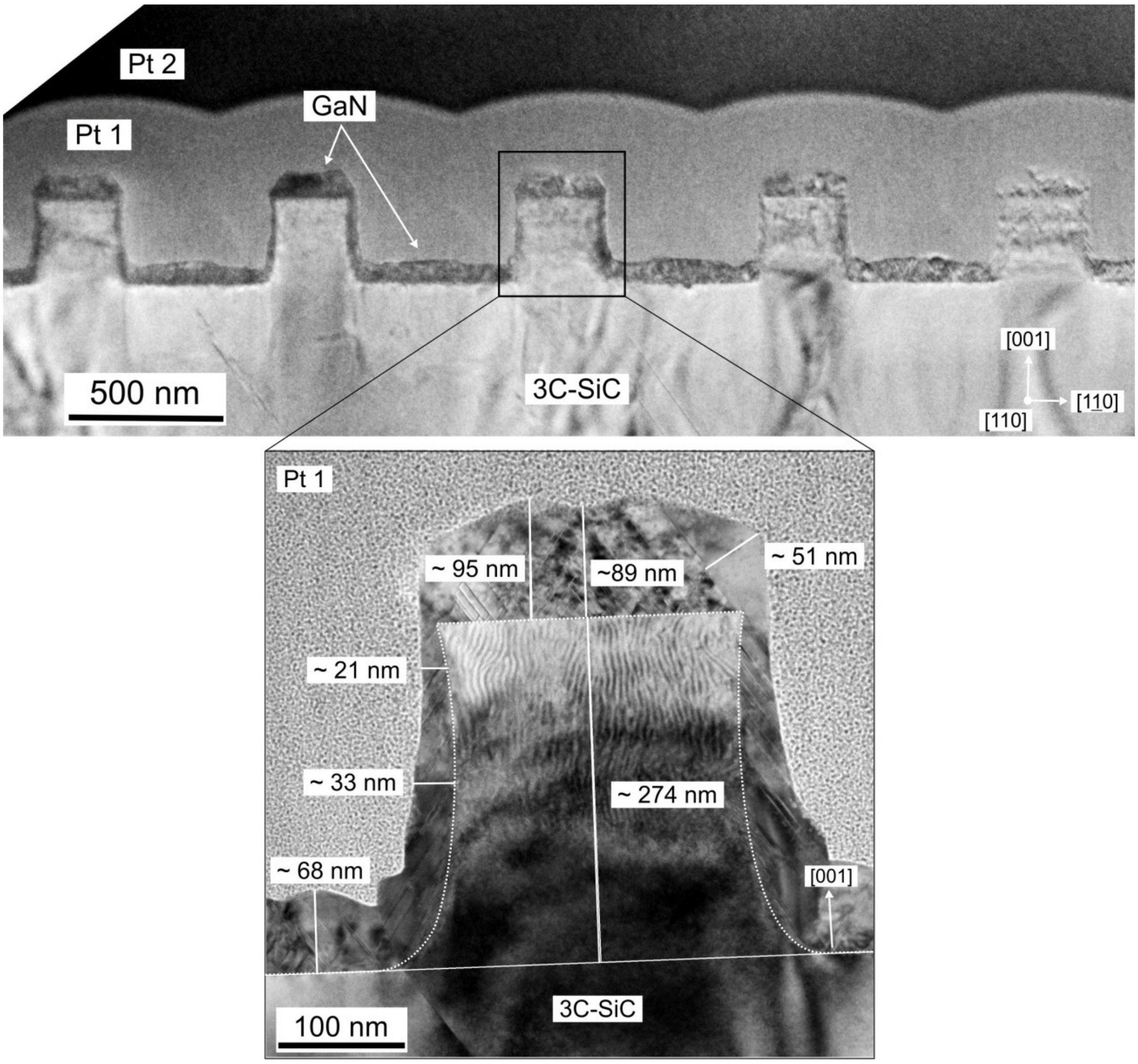

Figure 7.33

Overview cross-sectional TEM image along the [110] zone axis of a TEM lamella taken of a row of SiC structures from the array shown in Fig. 7.32. Zoom-in: Individual 3C-SiC (001) post with associated length specifications. The SiC/GaN interface is indicated by a white dashed line.

Several length measurements are superimposed to the image: the height of the pure 3C-SiC post can be determined to ~274 nm and the length to about ~238 nm. The GaN thickness on top, on the sidewalls and also next to the post varies. The layer thickness on the (001) growth area on top differs between ~95 nm and ~89 nm due to different surface facet formations. This leads to an average vertical [001] GaN growth rate of ~184 nm/h on top of the post. Furthermore, a reduced thickness of only ~21 nm is measured on the sidewalls, but it is increased to ~33 nm towards the bottom of the post. The layer thickness next to the post is ~68 nm and thus lower than on top of the post. The reason for this is the shadowing during growth which has been observed in the SEM image (Fig. 7.32).

The structural properties of the GaN film on top of this post are analyzed particulary by high-resolution TEM along the [110] direction in Fig. 7.34. In the overview cross-section TEM image the shape of the individual 3C-SiC post is again indicated by a white dashed line like in Fig. 7.33. Four areas (1)-(4) on the top of the post are marked. The areas are enlarged in the corresponding images (1)-(4). For reasons of clarity image (1) is still shown in Fig. 7.34 and images (2)-(4) are depicted in Fig. 7.35 following on the next page.

In image (1) the SiC/GaN interface in the center of the post is pictured. An almost atomically smooth interface is observed showing that the patterning process (see chapter 4) works quite well. There are no residues of the metal mask or damage resulting from the RIE process at the GaN/SiC interface visible, which could affect the epitaxial GaN growth. The GaN layer contains SFs on the {111} planes which pass from the interface to the surface. A Fast Fourier Transformation (FFT), taken from the white highlighted area in image (1), shows the typical c-GaN reflections along the [110] direction indicating that the cubic phase is grown on the reduced (001) growth area. The SFs within the film lead to streaks along the <111> directions in the FFT. These characteristics can be found in the entire GaN film on top of the (001) growth plane except the posts edges.

Areas (2) and (3) contain regions where GaN is grown on the left top side of the post and area (4) reveals the growth next to the right SiC edge. In image (2) the left hand SiC edge of the (001) growth area is magnified. The SiC edge has a slope < 90°. In this image the GaN layer on the (001) growth area can be divided into two regions. While on the (001) growth plane the cubic phase with SFs dominates, a nearly defect-free hexagonal phase is formed above the SiC edge. The FFT of this region shows the typical diffraction spots of h-GaN in the [11$\underline{2}$0] direction. Between the (0000) and the (0002) reflections additional spots appear due to dynamic diffraction events.

A (1$\underline{1}$1) facet separates the cubic and the hexagonal region (marked with a yellow dashed line). The SFs within the cubic phase are terminated at this facet and a nearly defect free region of the thermodynamically stable hexagonal phase follows. The change from the cubic to the hexagonal phase within the GaN epilayer at the post´s edge can also be seen in image (3). The critical (1$\underline{1}$1) facet is again marked with a yellow dashed line. Here, a nearly defect-free cubic crystal structure merges into the hexagonal phase and the individual SFs in the cubic phase are stopped at this “boundary”. Comparable growth characteristics are observed at the right top side of the post in area (4). In image (4) it becomes also appearent that on the post´s sidewall SFs dominate as already pointed out in image (2) and section 7.3. Probable reasons for the formation of this hexagonal “wing” at the post´s edge are the formation of the {111} facets. Also SFs nucleated on the sidewalls are observable and may influence the growth characteristic around the edge. A SF on a {111} facet is a local deviation from the cubic (111) stacking sequence to the stacking sequence in the hexagonal phase. Therefore, SFs can lead to hexagonal inclusions.In the opposite case, basal-plane SFs in a hexagonal crys-

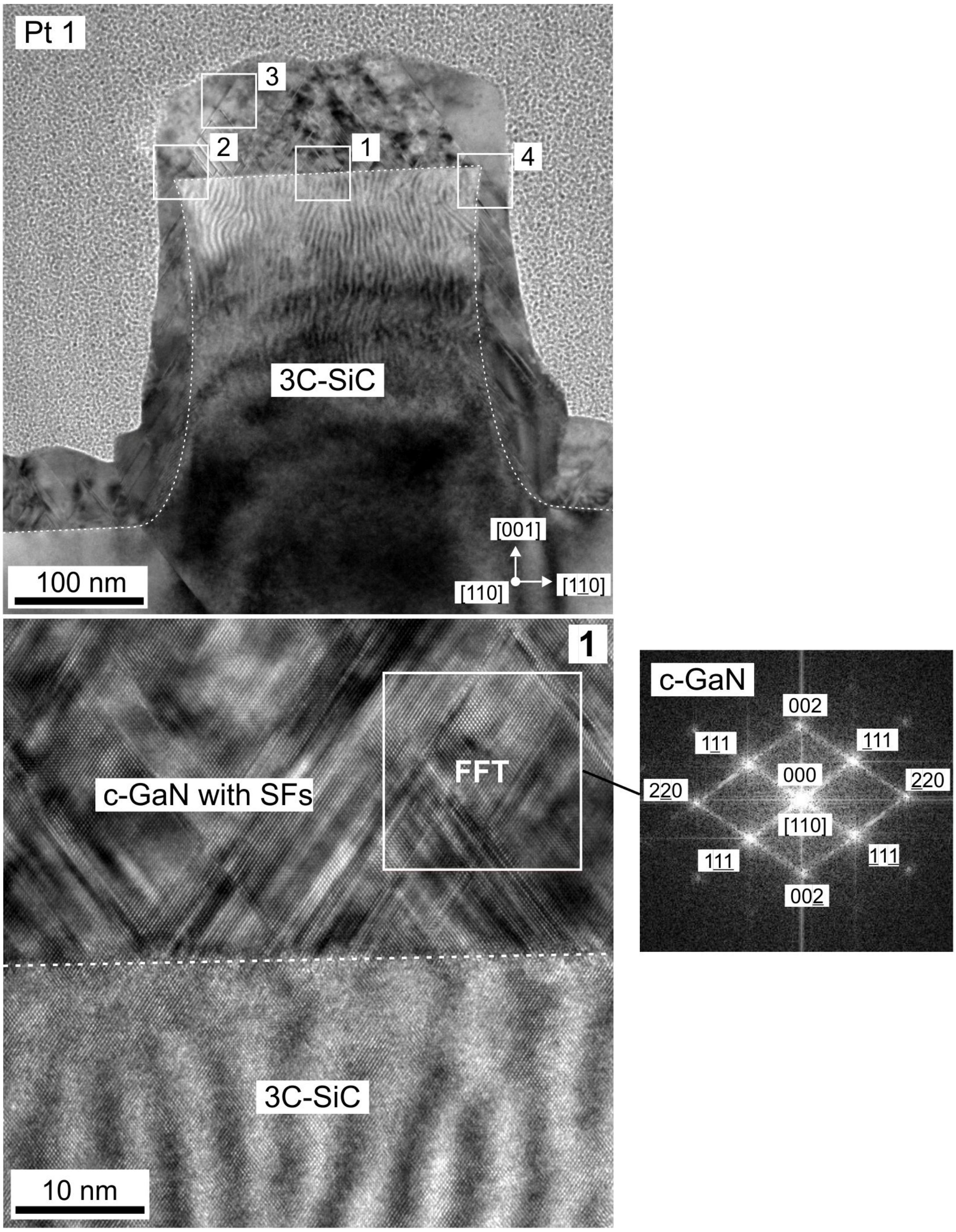

Figure 7.34

The upper TEM image shows an overview of the individual post with a top edge length of ~240 nm (see Fig. 7.33) along the [110] zone axis with marked areas (1)-(4). Image (1) depicts a high-resolution TEM image of the highlighted area (1) in the overview image. Image (2)-(4) follow in Fig. 7.35.

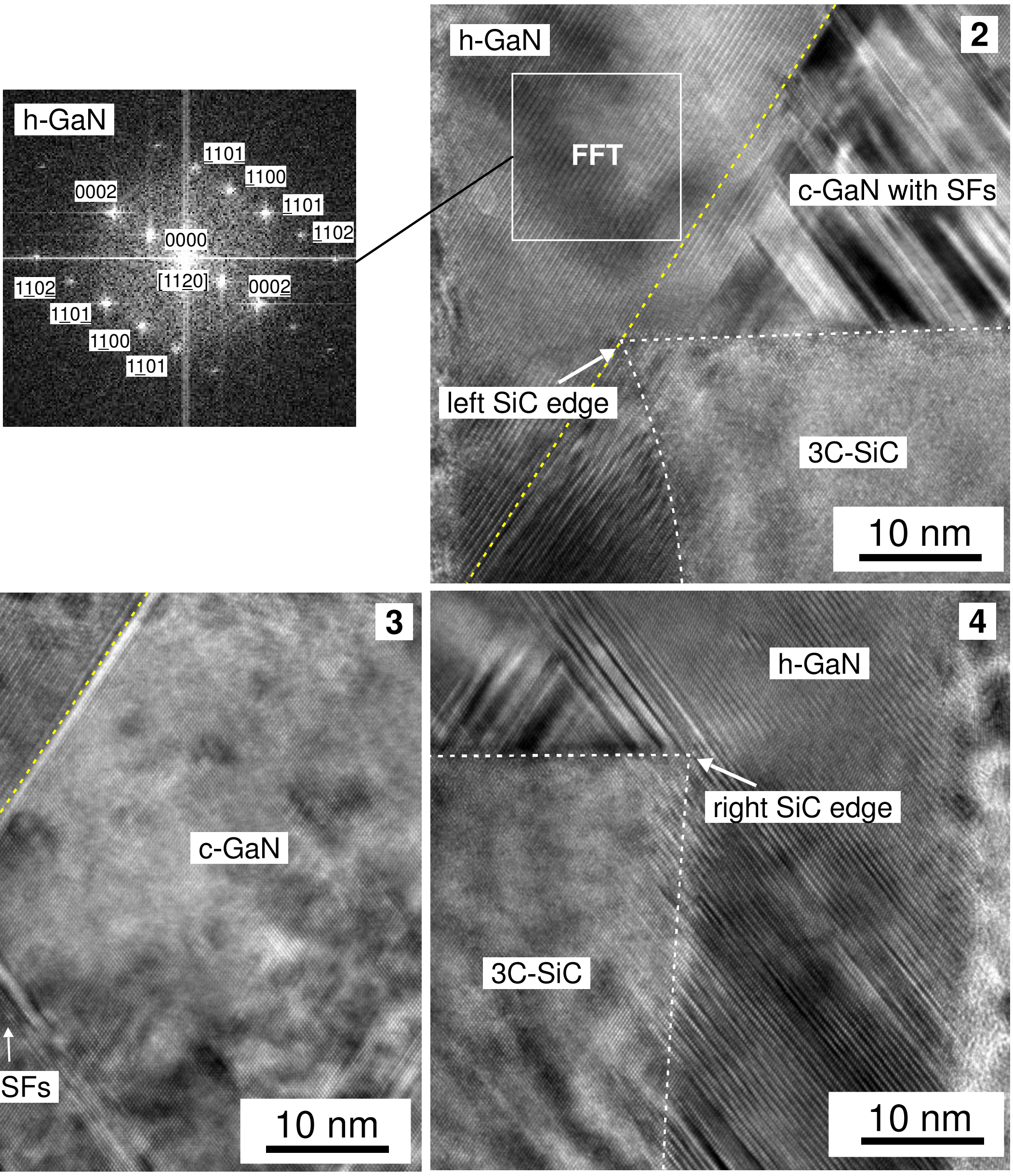

Figure 7.35

Enlarged high-resolution TEM images of the highlighted areas (2)-(4) in the overview image in Fig. 7.34. Detailed information is given in the text.

tal also result in cubic inclusions in the hexagonal crystalstructure and if the stable hexagonal phase is formed once, it remains, especially if the cubic substrate information is lost. The influence of potential strain fields at the post´s edge should also be considered but is not quantified in this work. Similar to the growth of the c-AlN/GaN MQW film on 3C-SiC (001) posts with top edges of ~500 nm length (see section 7.3.2) the growth direction changes at the edges from the [001] to the [111] direction. In general, the growth characteristics of the c-AlN/GaN MQW on a (001) growth area with a length of ~500 nm is comparable to the characteristics of the GaN film on top of the ~240 nm 3C-SiC (001) post. Growth area reduction from ~500 nm to ~240 nm does not significantly influence the growth characteristics of the cubic III-nitrides.

Figure 7.36 summaries the experimental findings. It shows the upper part of the 3C-SiC (001) post analyzed before in Fig. 7.34. The cubic phase grows on the reduced(001) growth area on top of the SiC post along the [001] growth direction with {111} SFs propagating from the SiC interface to the c-GaN surface. At certain {111} facets (yellow dashed lines) the hexagonal phase grows nearly defect-free at the right and the left edge. These observations are in good agreement with the results from section 7.3, where c-AlN/GaN MWQs were grown on larger 3C-SiC posts.

A closer view still shows that the GaN layer exhibits low-indexed surface facets. With reference to the cubic crystal structure the facets are indexed in Fig. 7.36. Similar facet formation of c-GaN has been observed by Sanorpim et al. [120] who studied the epitaxial lateral overgrowth of (001)-oriented stripe-patterned GaAs with c-GaN by

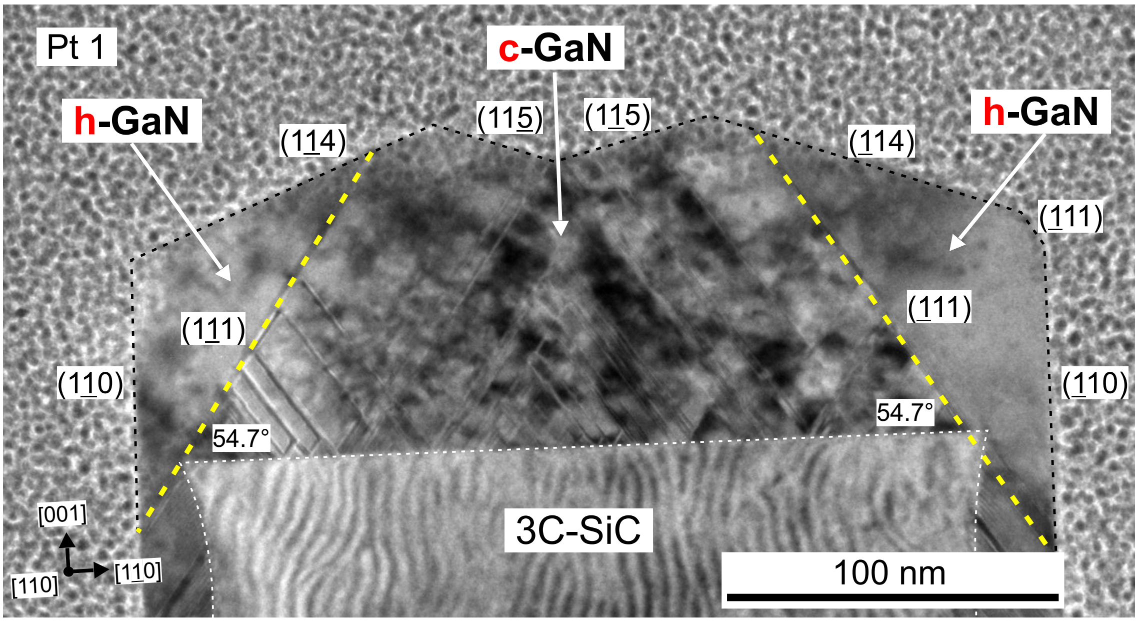

Figure 7.36

Cross-sectional TEM image along the [110] zone axis showing the upper part of the individual 3C-SiC (001) post with a top edge length of ~240 nm described in detail in Fig. 7.34.

metal organical vapor phase epitaxy (MOVPE). In this context also a similar facet formation of c-GaN, grown on substrates patterned by the NSL technique, was demonstrated in previous work [89]. Until now the mechanism of facet formation is not yet completely understood.

7.4.2 3C-SiC (001) Posts with ~100 nm Top Edge Length

In this subsection the growth of GaN on 3C-SiC (001) structures with top edge lengths of ~100 nm and heights of ~270 nm is investigated. The nanostructures were overgrown with ~85 nm GaN and are located on the same sample (GNR 2298) as the array described in subsection 7.4.1. The difference is that the top edge length is reduced to~100 nm and the distance between the uncovered structures is ~100 nm.

Figure 7.37a depicts a side-view SEM image of an array (array 8E) with periodically arranged 3C-SiC structures overgrown with GaN. In Fig. 7.37b a top view SEM image with higher magnification shows that the GaN surface on top of the structures forms surface facets, which are analyzed more in detail later in Fig. 7.39.

To investigate the nanostructures with TEM, a lamella is prepared from a row of structures (see section 6.2) depicted in the SEM image (Fig. 7.37a). Figure 7.38 pictures an overview cross-section TEM image along the [110] zone axis of this lamella containing a row of the nanostructures. All structures have a very regular and consistent shape, which can also be seen in the SEM image of Fig. 7.37. Between the structures holes appear in the Pt1 layer (bright areas) due to shadowing effects when the structures

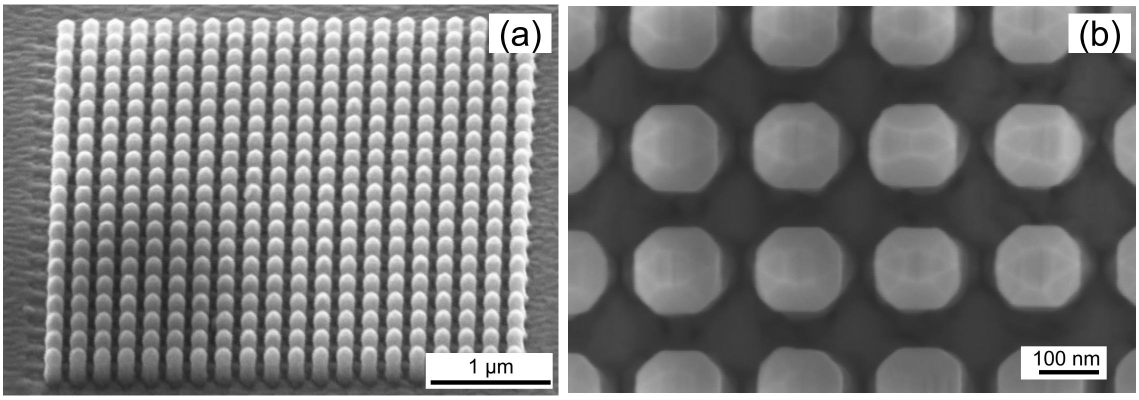

Figure 7.37

(a) Side view SEM image with 3C-SiC (001) structures with top edge lengths of ~100 nm overgrown with 85 nm GaN (sample GNR 2298, array 8E)). **(b)** Top view SEM image showing that the GaN grown on top of the structures exhibits surface facets.

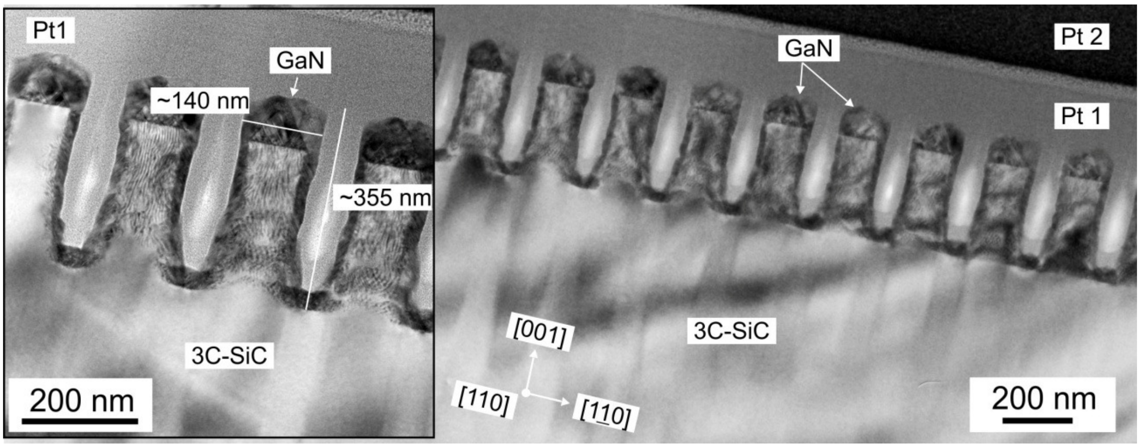

Figure 7.38

Overview cross-sectional TEM image along the [110] zone axis of a TEM lamella taken from the array shown in Fig. 7.37. Zoom-in: Individual posts with associated length specifications.

are covered with the Pt protection film during the TEM lamella preparation. The streaky contrasts within the SiC substrate result from different specimen thicknesses in this area due to the thinning process of the TEM lamella ("curtain effect" [121]). The inset displays four individual posts with top diameters of the c-GaN layer up to ~140 nm and total island heights of ~355 nm after the MBE growth process. On the SiC front sidewalls Moiré contrasts are again observed in all but the thinnest posts resulting from superpositions of the defect rich GaN and the 3C-SiC substrate itself. The GaN film thickness and the surface contours on top and between the posts have very similar characteristics in all posts, indicating that the crystalline constitution is dictated by the shape of SiC posts.

One individual post is analyzed in detail in Fig. 7.39. The measured geometrical dimensions are: The top edge length of the raw SiC post is ~101 nm, about 85 nm GaN was grown on the (001) top growth area and about ~25 nm on the sidewalls. This results in a vertical (001) GaN growth rate on top of the post of ~170 nm/h. The GaN on top of the post exhibits surface facets (marked with black lines) as already observed for broader posts in section 7.3 and subsection 7.4.1. The sidewall facets are (110) planes and the top surface facets are {119} and {137} facets referring to the cubic phase nomenclatur. The facet orientations on the top surfaces may vary slightly from post to post. On the post´s sidewalls the GaN film exhibits no clearly surface facets. On the right SiC sidewall of the post in Fig. 7.39 the GaN film is even interrupted. Strong thickness variations of the GaN film in the concave part of the sidewalls are seen on all posts and are ascribed to shadowing effects between the narrow posts.

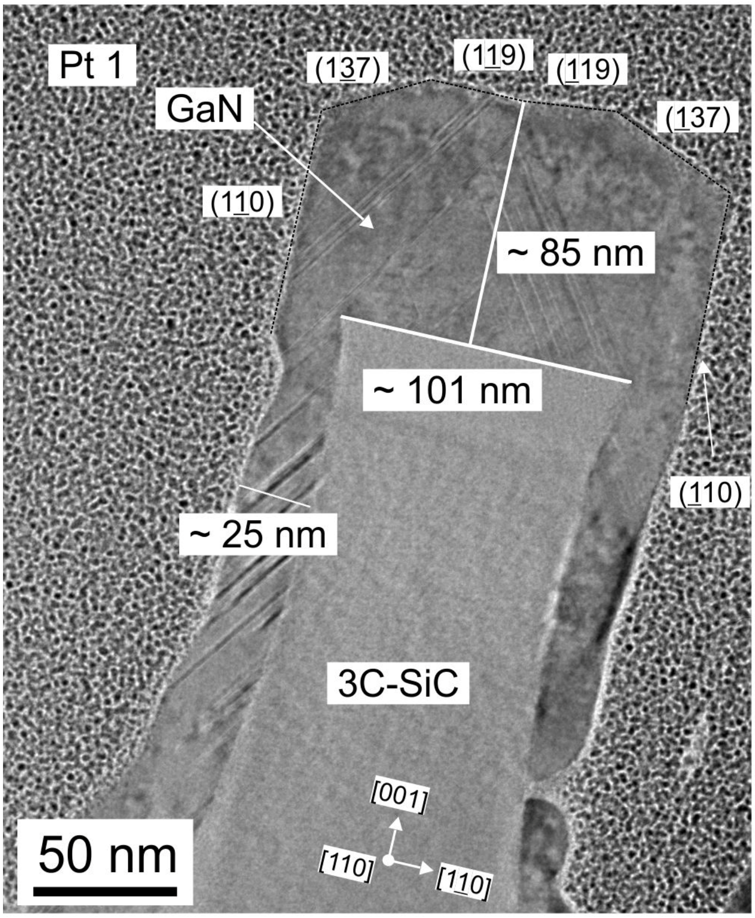

Figure 7.39

Cross-sectional TEM image along the [110] zone axis of an individual 3C-SiC post with a top edge length ~100 nm. Around 85 nm GaN are grown in (001) growth direction on top of the post.

The structural properties of the GaN film are analysed in more detail by high-resolution TEM along the [110] zone axis in Fig. 7.40. In the upper overview cross-sectional TEM image five areas (1)-(5) are marked on top of the post, which are individually enlarged in the high-resolution images (1)-(5). For better clarity image (1) is still displayed in Fig. 7.40 and images (2)-(5) follow in Fig. 7.41 on the next page.

Image (1) shows the upper left hand corner of the SiC post. A smooth GaN/3C-SiC (001) interface is observed showing that the fabrication process of even smaller structures (see chapter 4) works also well. There are no residues of the metal mask or damage resulting from the RIE process identifiable. The left SiC corner does not have a 90° angle but a small undercut resulting from the etching process. On the (001) SiC growth area GaN grows in the cubic phase, which can be determined by the arrangement of the lattice planes and FFT images as in Fig. 7.40a and b depicted on the right side of image (1). The FFT image (a) corresponds to a [110] DP of c-GaN,

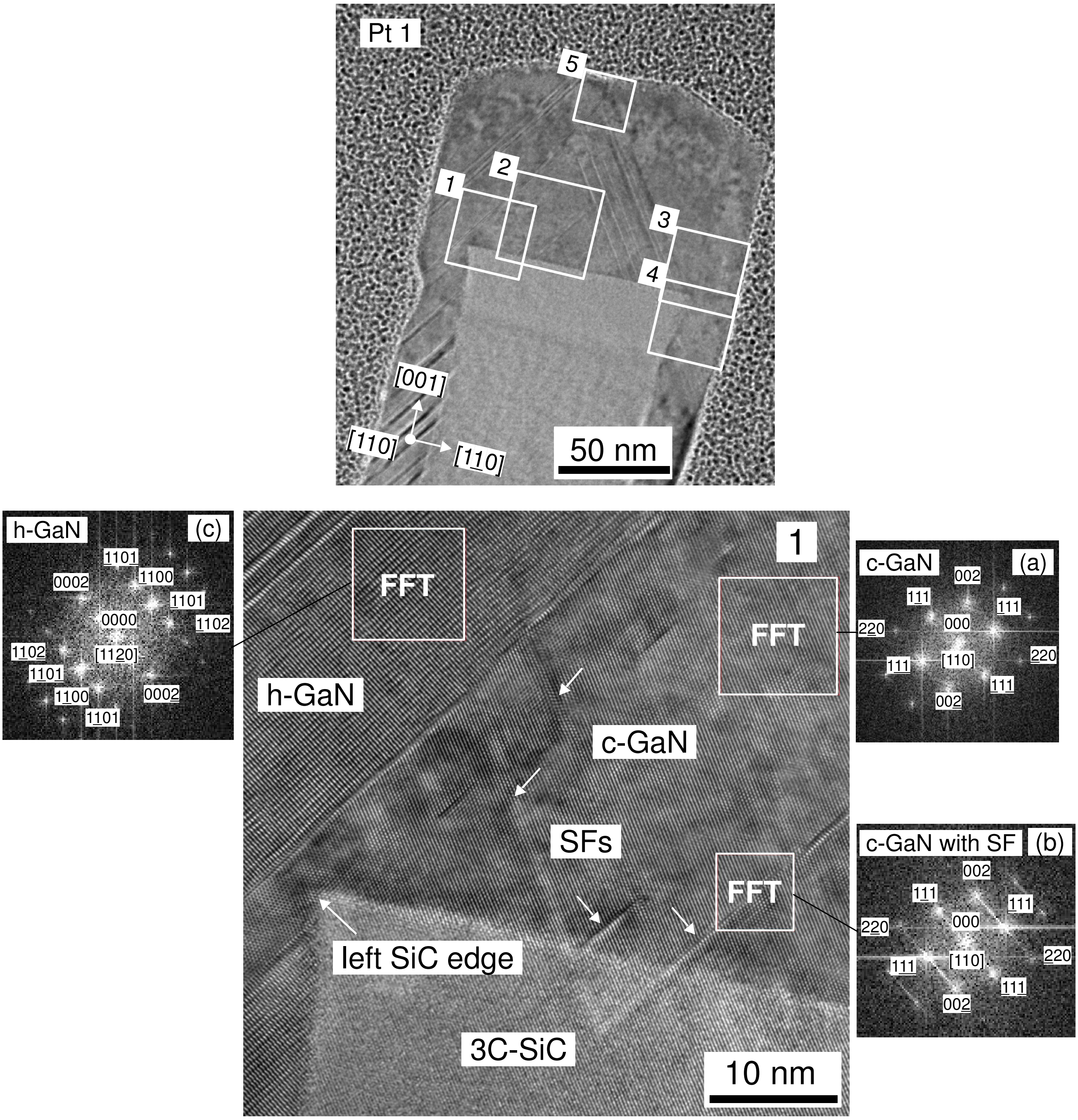

Figure 7.40

Top: TEM image of the upper part of the individual post with a top edge length of ~100 nm (see Fig. 7.39) along the [110] zone axis with marked areas (1)-(5). Image (1) shows a high-resolution TEM image of the marked area (1) in the overview image with FFT images (a)-(c) of three individual regions. Image (2)-(5) follow in Fig. 7.41.

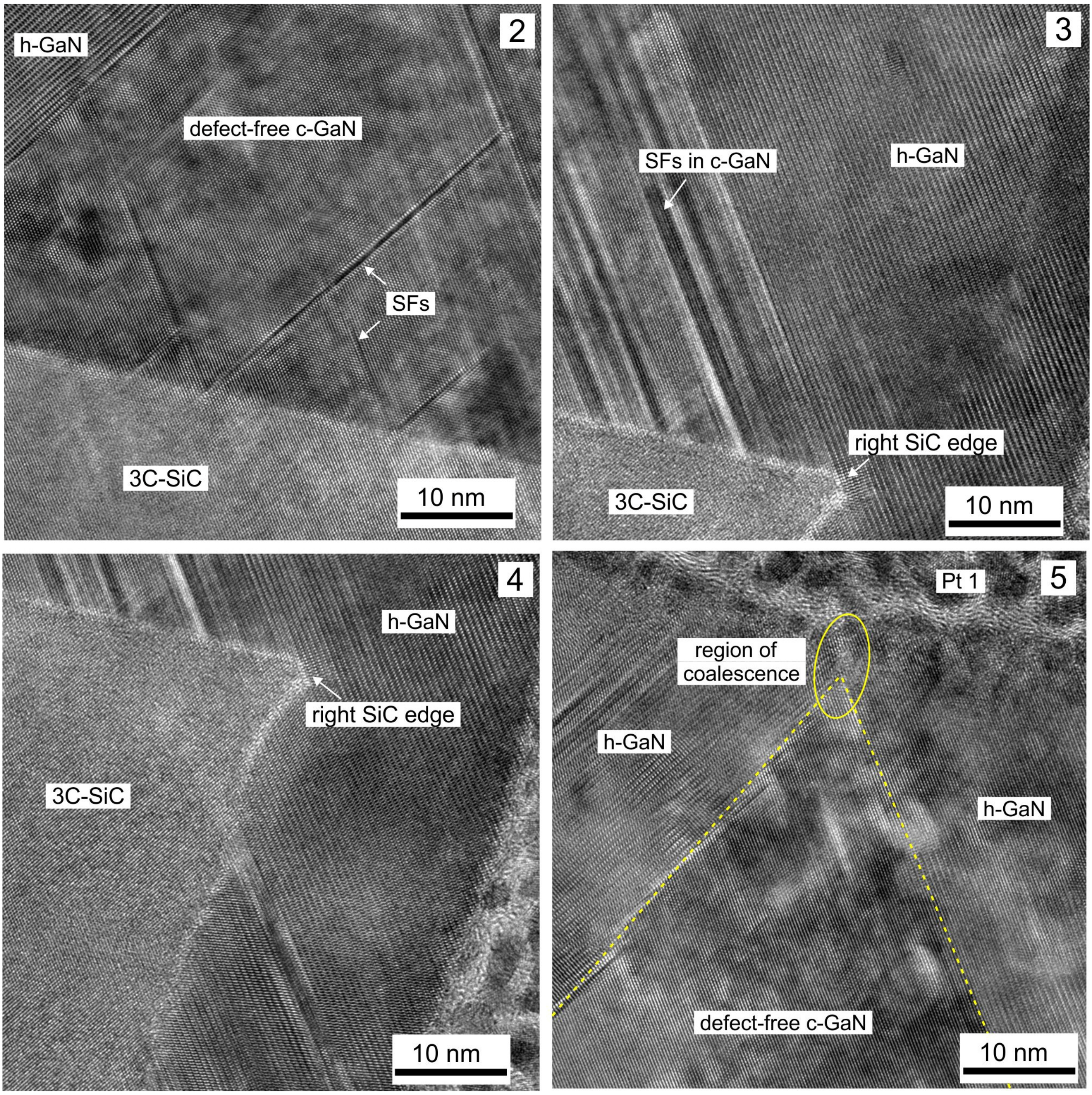

Figure 7.41

Enlarged high-resolution TEM images of the marked areas (2)-(5) in the overview image in Fig. 7.40.

proving that c-GaN is grown on top of the post. Isolated SFs, marked with white arrows, can be identified which disturb the regular arrangement of the atomic lattice. Several SFs extend into the substrate. This is the first time to observe individual SFs and not bunches of SFs originating from the c-GaN/SiC interface. This gives the possibility to count individual SFs and obtain information about the SF density, which will be demonstrated in the end of this section in Fig. 7.42. Until now the SF density close to the interface was too high so that individual SFs could not be separated in conventional TEM images due to indistinguishable contrasts.

The FFT image (b), from a square shaped area containing an individual SF, shows that this SF leads to streaks along the $[\underline{1}1\underline{1}]$ direction. In contrast theDP (a) observed in the undisturbed cubic region above contains no streaks showing an almost defect-free and phase-pure area.

Around the left SiC edge, GaN grows also in the cubic phase. The substrate information seems to be sufficient to force the Ga and N atoms in the cubic phase.Up to now the reason is not known, but after a few atomic planes the hexagonal phase is formed at the post´s edge on a {111} plane and remains stable. This nearly defect free region is marked in image (1) with “h-GaN”. The associated FFT image (c) of this $[11\underline{2}0]$ zone axis region is shown on the left side. The unambiguously phase boundary between the cubic and the hexagonal crystal structure is highlighted by a dashed yellow line. One reason for this phase change may be the influence of the SFs grown on the SiC sidewall, where they dominate the lattice of the GaN film. But also facet formation of the growing film, here e.g. the formation of {111} planes, supporting the growth of the hexagonal phase, is a possible reason for the phase change.

In image (2) (Fig. 7.41) the SiC/GaN (001) interface in the center of the post is shown. The GaN layer on top has again a cubic crystal structure containing isolated SFs on the $(1\underline{1}1)$ and $(\underline{1}11)$ planes. Here, a partly annhilation process of the individual SFs is clearly visible. Two SFs intersect, but only one of these SFs is continued. This incomplete annhilation process is also observed at the 3C-SiC/Si (001) interface as shown in [49]. But up to now this process is not fully understood. Image (2) is representative for the growth on the whole (001) growth area of the post besides the post edges.

Images (3) and (4) display the GaN grown on the right top side of the post. In contrast to image (1) the hexagonal phase already grows around the SiC edge (image (3)) which is also undercut with an angle < 90°. Two main reasons are responsible for the hexagonal growth around the right corner. Firstly, next to the right SiC edge (see image (3)) more SFs in the cubic phase on top of the (001) growth area occur then close to the left edge. If the substrate information is lost at the edge the thermodynamically stable hexagonal phase dominantes. Secondly, the GaN growth on the post´s sidewall is also dominated by SFs supporting the formation of a hexagonal flank as shown in image (4). An additional consideration for the reason of the formation of the cubic or the hexagonal phase around the SiC edges could be different (Si- or C-) terminated surfaces. This is an open question which ought to be in focus of further research.

Image (5) reveals the upper part of the GaN film at the center of the post where the left and the right hexagonal flanks coalesce. The cubic phase grows in the [001] direction while the hexagonal phase grows on the {111} flanks. Within a film thickness of ~80 nm these hexagonal flanks grow together and stop the cubic growth in [001] direction. In order to assess whether the hexagonal phase coalesces by generating a defect, which will expand into the coalescent film, a higher film thickness is necessary, because the region of coalescence is immediately below the sample surface. If the hexagonal flanks coalesce without theformation of a defect a nearly defect-free hexagonal film on top of the SiC post could grow surrounding a c-GaN region.

Up to now the determination of the SF density was very difficult due to a usually high density of planar defects at the interface and the fact that SFs often appear in bunches, where individual planar defects cannot be distinguished. Now, the high-reso-

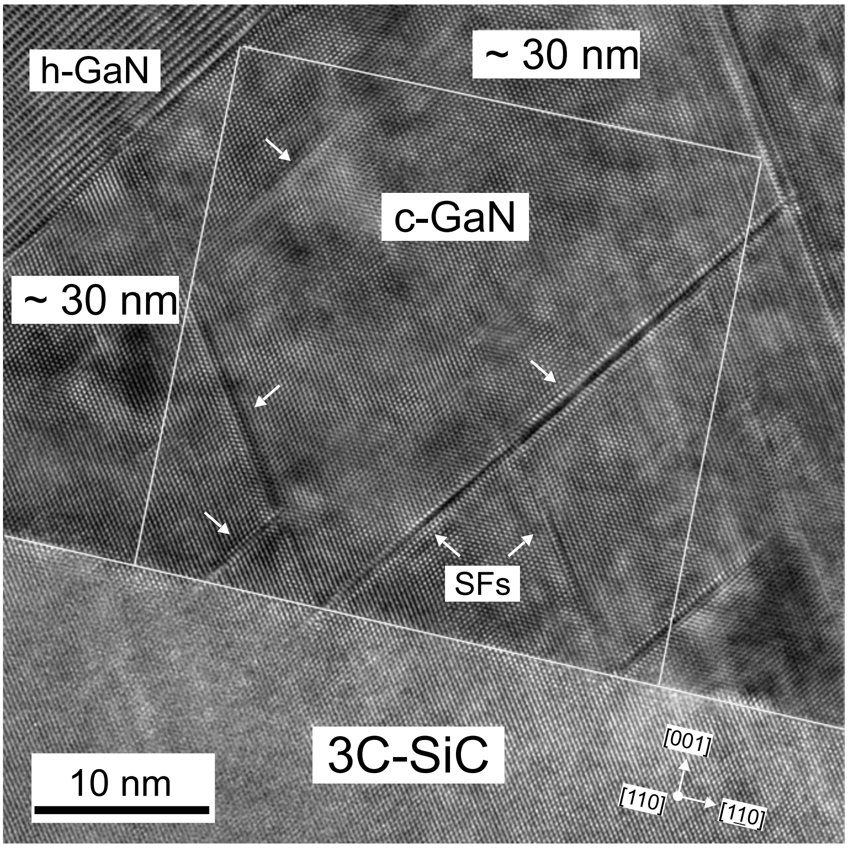

Figure 7.42

High-resolution TEM image along the [110] zone axis of the c-GaN/3C-SiC interface in the center of the post described in detail in image (2) in Fig. 7.41. Within the white square with a side length of ~30 nm five SFs can be counted near the interface.

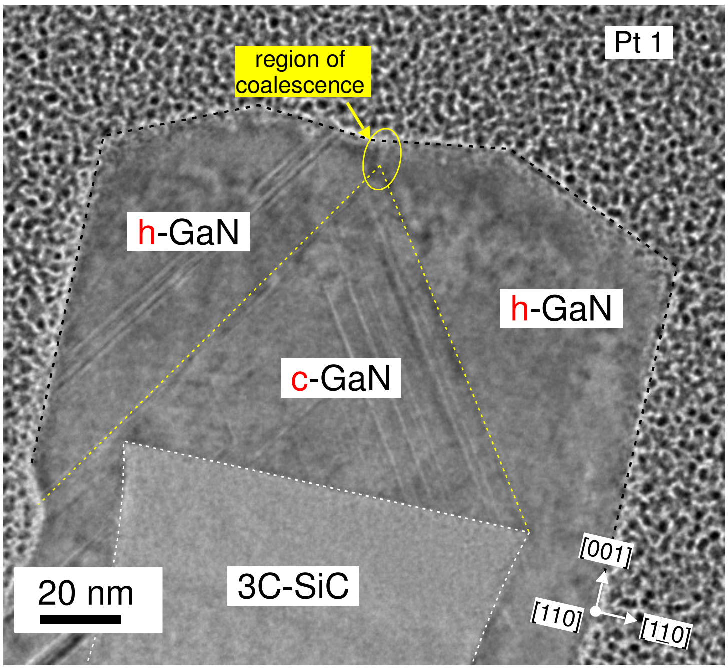

Figure 7.43

Cross-sectional TEM image along the [110] zone axis showing the upper part of the individual 3C-SiC (001) post with a top edge length of ~100 nm which is described in detail in Fig. 7.40.

lution images in Fig. 7.40 and 7.41 demonstrate that on top of the SiC post isolated SFs exists in the c-GaN which can be separated. To determine a SF density per unit length Fig. 7.42 shows again the high-resolution TEM image of the c-GaN/SiC interface in the center of the post from image (2) in Fig. 7.41. Stacking faults, marked with white arrows, run through the c-GaN film and partly annihilate pairwise. In the white square of ~ (30x30) nm^2 five SFs can be counted near the interface. At a [001] film thickness of ~15 nm only two of these SFs remain, but two other SFs run from the surrounding area into the marked area of interest. This results in a line density of five SFs per ~30 nm (SF density $D_{SF}/\text{line} \approx 1.7 \cdot 10^6/\text{cm}$) at the interface in this special highlighted area.

Figure 7.43 gives a summary of the results. On the complete (001) growth area on top of the 3C-SiC post c-GaN grows along the [001] growth direction containing individual {111} SFs. The single SFs at the interface can be separated and do not appear in bunches as observed in the previous chapters except in the region next to the right SiC edge (see image (3), Fig. 7.41). At both edges the {111} facets lead to the formation of almost defect-free stable h-GaN “wings”. These flanks coalesce at the GaN surface in the middle of the post at a [001] film thickness of ~80 nm. In this region the cubic growth in [001] direction is stopped.

7.4.3 3C-SiC (001) Posts with ~20 nm Top Edge Length

A free-standing nanostructure array with a post diameter of ~20 nm overgrown with GaN (sample GNR 2298, array 6G) is shown in the side view SEM image in Fig. 7.44a. The array consists of 10x10 nanostructures which are arranged regularly with a distance of ~450 nm between each other. Figure 7.44b displays a side-view SEM image of four 3C-SiC (001) structures with higher magnification. Next to the nanostructures the typically GaN surface morphology is observed indicating that growth takes place on top, on the sidewalls and between the posts, like mentioned before. Deepenings due to shadowing in the GaN layer next to each nanostructure are noticed again. The layer on top of the nanostructures forms tapered surface facets in (001) growth direction.

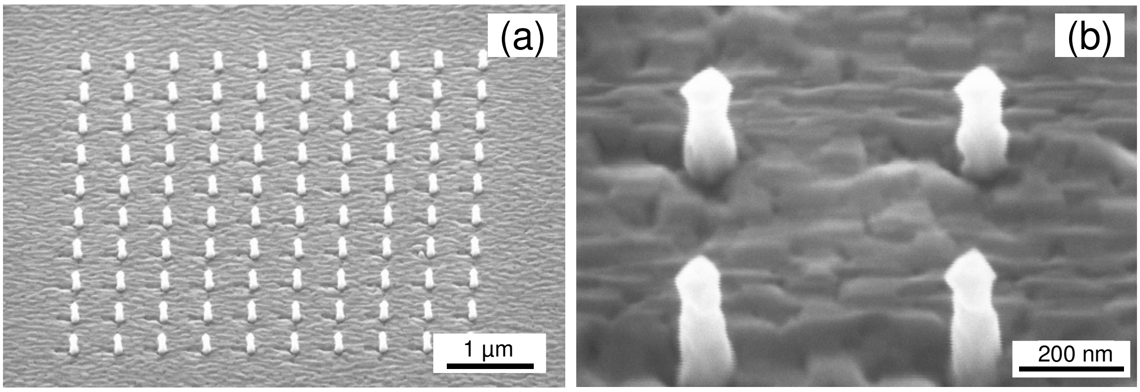

Figure 7.44

(a) Side view SEM image of array 6G (sample GNR 2298) with 3C-SiC (001) structures with top edge lengths of approximately 20 nm overgrown with GaN. **(b)** Enlarged side view SEM image of four nanostructures showing that the deposit on top of the structures forms tapered surface facets.

In Fig. 7.45 an cross-section TEM overview image of a TEM lamella containing a row of the nanostructures from Fig. 7.44a is depicted. Three overgrown SiC nanostructures are identified which are surrounded by two Pt protection films (Pt1 and Pt2). Due to the small post dimensions, the TEM lamella cuts not through the center of the nanostructures but in tendency more through their sidewalls. Therefore, the original 3C-SiC post is difficult to identify and varying contrasts on the post´s front sidewall are observed which are caused by superpositions of the 3C-SiC post and the GaN grown on the front or back sidewall.

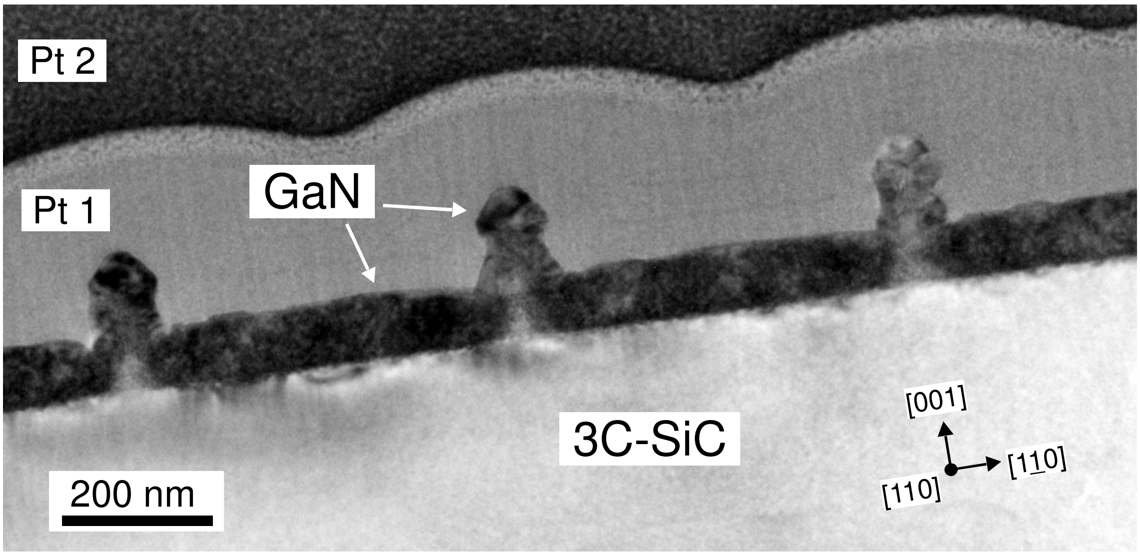

Figure 7.45

TEM image along the [110] direction of a TEM lamella taken from the array shown in the SEM image in Fig. 744a. Three individual posts can be identified. The top, the sidewalls and the space in between the structures are overgrown with GaN. The lamella cuts not through the middle of the nanostructures but in tendency more through their sidewalls.

Figure 7.46 shows a cross-sectional TEM imagetaken along the [110] zone axis of an individual overgrown nanostructure. The dashed white line indicates the 3C-SiC posts. It must be mentioned that the SiC/GaN interface is not unambiguously reconstructible, but the geometrical dimensions of the 3C-SiC postare approximated by the varying Moiré contrasts induced by the superimposed GaN grown on the SiC sidewalls. The post´s height in Fig. 7.46 is assumed to be ~150 nm and the top edge length of the SiC (001) growth area is approximately 20 nm. As a consequence of the reconstruction of the form of the SiC post it is not quite sure if the (001) growth surface of the nanostructure was damaged during the RIE process. There are no apparently signs for a disturbed SiC surface, but unfortunately, this issue remains unclear. With the assumption that on top of the (001) growth area ~48 nm GaN was grown the deposit has a diameter of ~97 nm at the broadest part on top. Thus, the growth rate in [001] direction is determined to ~96 nm/h. The film thickness on top of this nanostructure is thinner than the film thicknesses (~85 nm) on top of the broader structures described in subsections 7.4.1 and 7.4.2. Local variations of the growth parameters may be the origin of the film thickness differences, but all fabricated structures are located in the middle of the sample and were simultaneously overgrown. Another reason is possibly the form of the SiC posts. It is noticeable, that in contrast to the broader square shaped SiC strutures and compared to the volume grown on the (001) growth area there is a high GaN growth rate on the SiC sidewalls. In some parts the ratio between the (001) growth

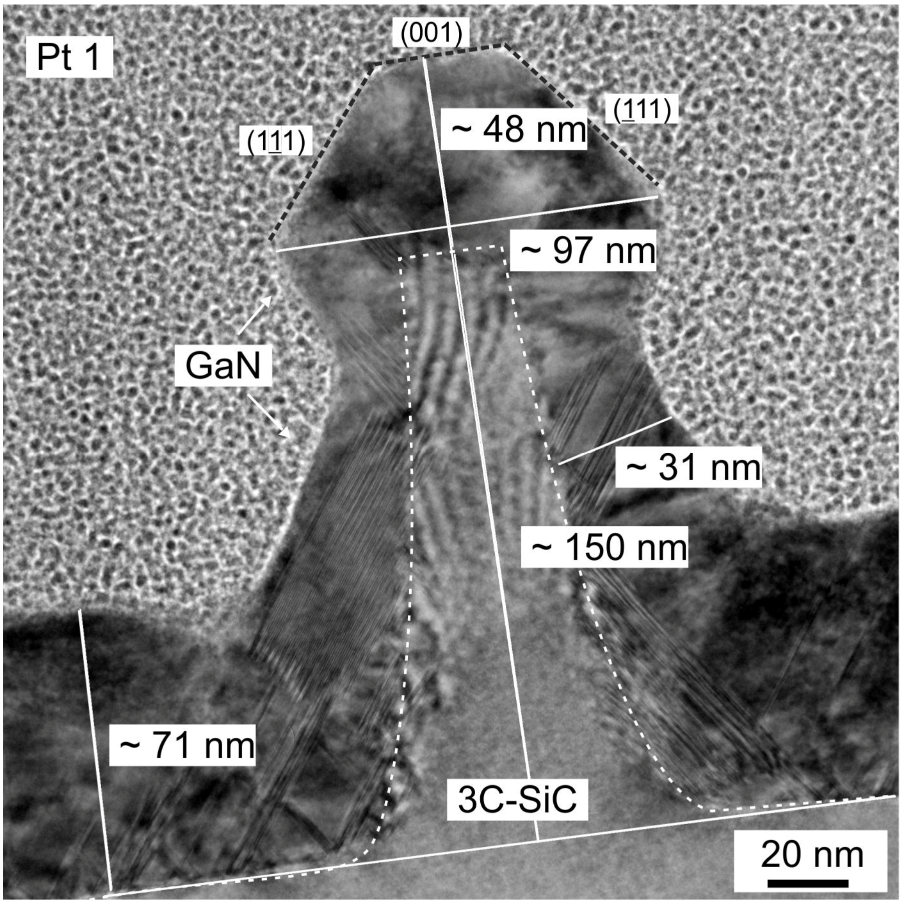

Figure 7.46

Cross-sectional TEM image along the [110] zone axis of an individual overgrown nanostructure. The dashed white line indicates the 3C-SiC post, but the SiC/GaN interface is not unambiguously reconstructible. But it is assumed that the post´s height is about ~150 nm and the top edge length ~20 nm.

rate and the growth rate on the sideswalls is about 1. This is in contrast to the broader SiC structures with top edge lengths of ~240 nm and ~100 nm. Their sidewalls are almost {110} planes. This may indicate that the sidewalls of the ~20 nm top length SiC structures are possibly no {110} planes. A detailed TEM analysis of the SiC posts before MBE growth would give more insight about the form and facets of the SiC sidewalls.

The surface facets on top of the post can be indexed with {111} planes at the sides and as (001) on top. The layer thickness on the sidewalls narrows upwards and has a thickness in the range of ~30 nm. The GaN film between the posts has a height of ~71 nm.

The structural properties of the deposit are analysed more in detail by high-resolution TEM along the [110] zone axis in Fig. 7.47. In the overview TEM image the assumed shape of the 3C-SiC nanostructure is reproduced by a white dashed line (see

Fig. 7.46). On the sidewalls of the post SFs within the GaN can be identified. Three areas on the top of the nanostructure ((1)-(3)) and one at the bottom of the post (area (4)) are marked, which are individually magnified in the high-resolution images (1)-(4). The TEM images are separated in three figures for reasons of clarity. Image (1) is still visible in Fig. 7.47, images (2), (3) can be found in Fig. 7.48 and image (4) is shown in Fig. 7.49.

Image (1) depicts the left side of the top of the layer. The GaN surface is marked by a white dashed line. Varying contrasts caused by thickness fluctuations of the specimen owing to the Pt1 protection film cover the GaN. Within the GaN nearly undisturbed lattice planes which are arranged in the cubic phase are observed. This is confirmed by the FFT from the marked region showing the typical spots of c-GaN in the [110] DP. The FFT verifies that phase pureand almost defect-free c-GaN is grown on the top left side of the SiC nanostructure. One defect is recognized in the lower part of the image as indicated by an arrow.

In image (2) (Fig. 7.48) the GaN region on top of the nanostructure is shown. Due to radiation damage the GaN layer on top of the post appears partially disturbed. Nevertheless, a FFT of a well preserved region close to the assumed SiC post exhibits again spots of the [110] DP of c-GaN without any streaks caused by SFs. The same results are found on the top right side of the nanostructure (image (3)). Again, only the cubic phase is present. Here, there are no {111} SFs which promote the growth of h-GaN.

Image (4) in Fig. 7.49 taken from the bottom of the post also demonstrates the formation of the cubic phase. However, here a higher density of {111} SFs is obvious, in contrast to the c-GaN deposited on top of the nanostructure. This is a particulary clear indication that the morphology of the growth surface leads to a reduction of the SF density.

In summary on the left top side of the post (image (1)), in the center (image (2)) and on the top right side (image (3)) almost defect-free c-GaN was grown. Moreover, no hexagonal inclusions were formed on the sides like on top of the larger SiC structures described in the former subsections.

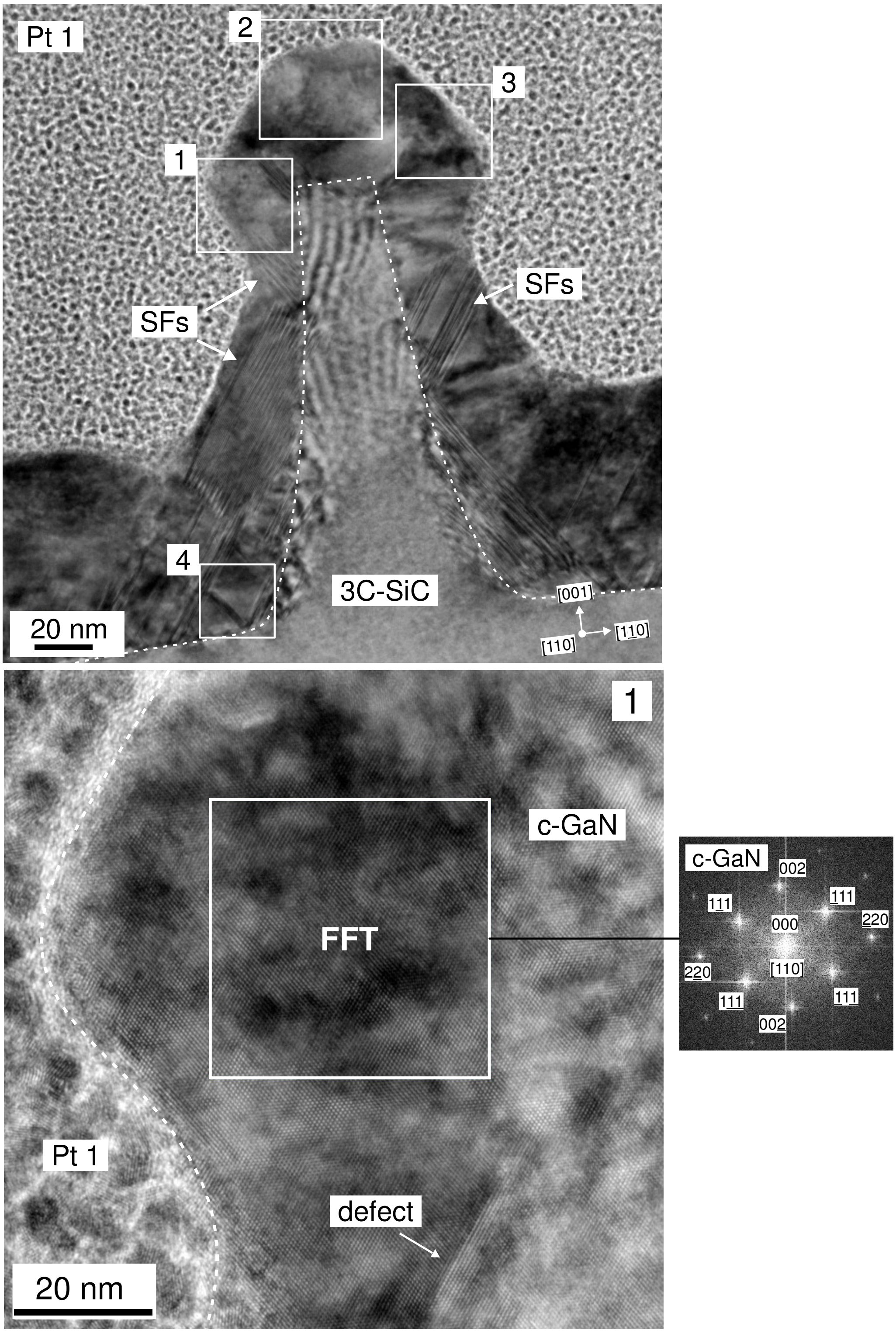

Figure 7.47

Top: Overview TEM image of the individual post with a top edge length of ~20 nm (see Fig. 7.46) along the [110] zone axis with marked areas (1)-(4). Buttom: Image (1) reveals a high-resolution TEM image of the assigned area (1) in the overview image with FFT showing the typically spots of c-GaN in the [110] DP. Image (2)-(4) follow on the next two pages.

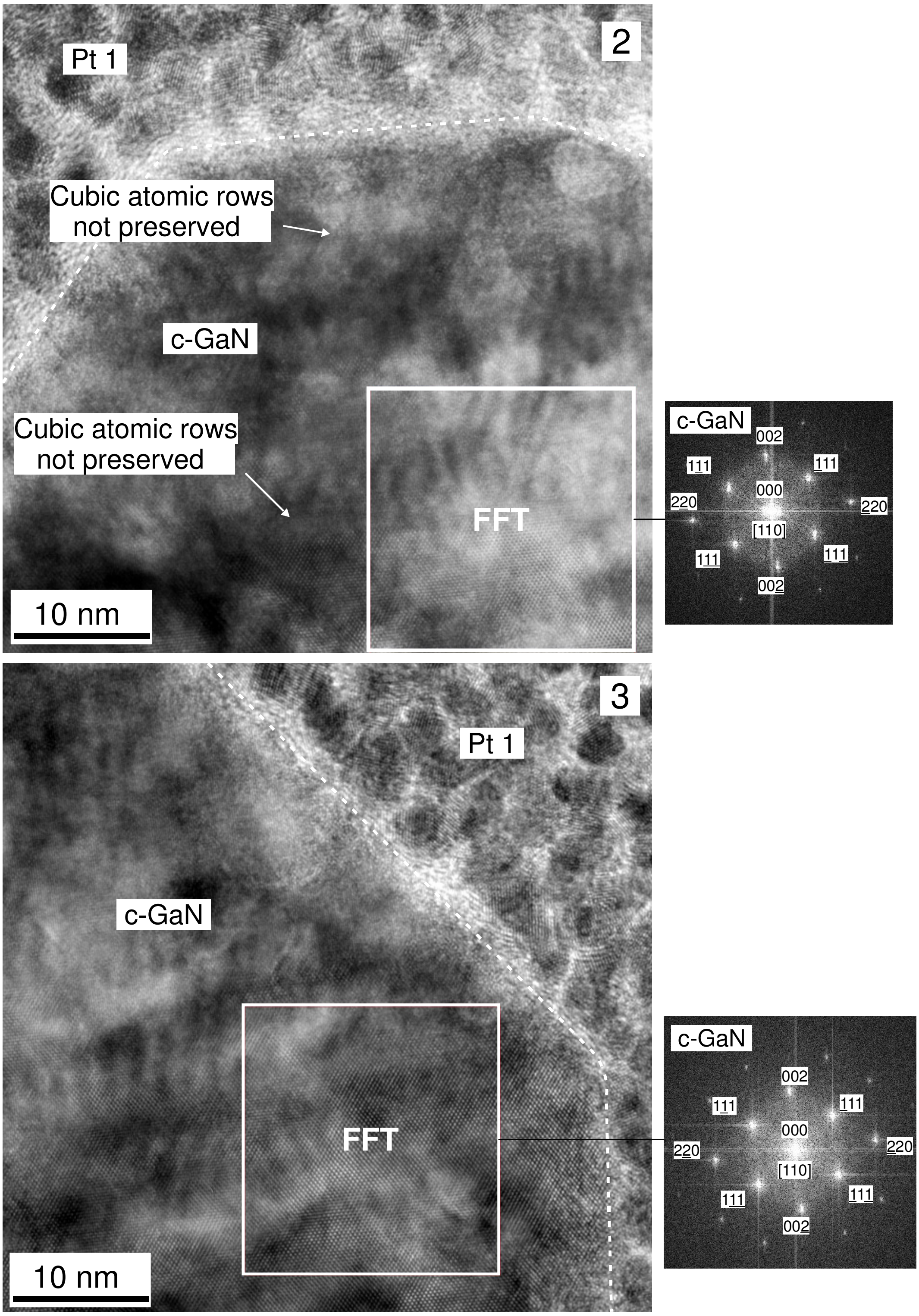

Figure 7.48

Enlarged high-resolution TEM images (2) and (3) of the marked areas (2), (3) in the overview TEM image in Fig. 7.47.

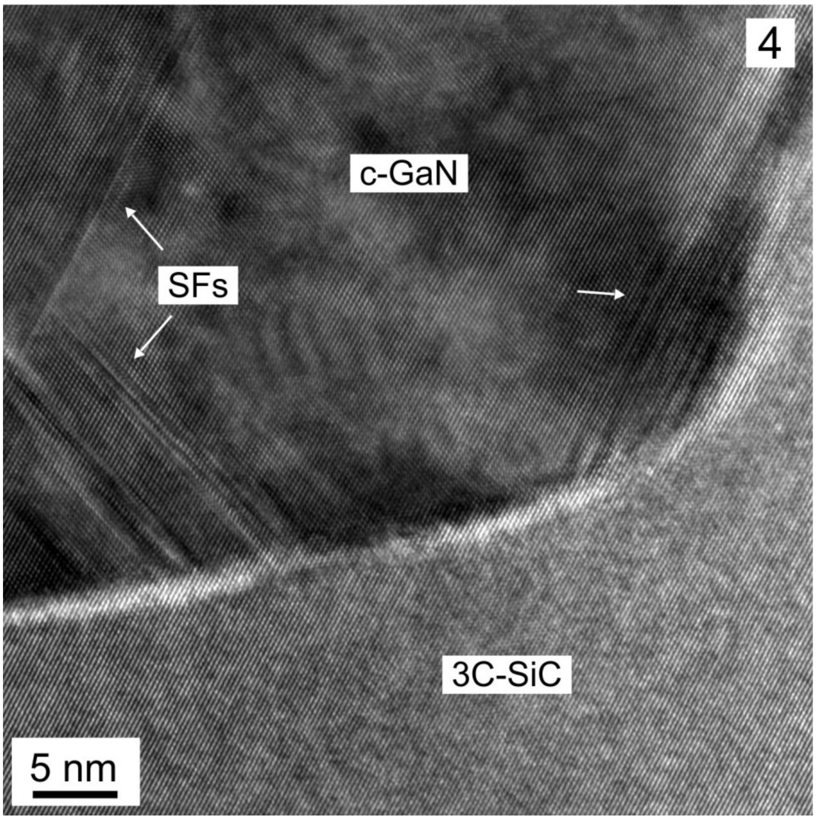

Figure 7.49

Enlarged high-resolution TEM image of the marked areas (4) in the overview TEM image in Fig. 7.47.

7.4.4 Conclusions

To summarize the results ofsection 7.4 an overview of the investigated 3C-SiC (001) structures is given in Fig. 7.50. On the right side the uncovered SiC structures are shown schematically. On the left side TEM images taken along the [110] direction of the corresponding overgrown 3C-SiC (001) posts are depicted. The (001) growth area was reduced from a length of ~240 to ~100 nm and finallydown to ~20 nm. The structural analysis of the GaN deposited on top of the different structures revealed that on larger structures the cubic phase with {111} SFs forms on the complete (001) growth area while at the SiC edges hexagonal regions are created. Already the growth area reduction from ~240 nm towards ~100 nm results in a reduction of the SF density. On top of the ~240 nm post the SF density cannot clearly be determined due to indistinguashable constrasts of the bunches of planar defects. In contrast, on top of the ~100 nm SiC post, the SF density is low enough to identify individual SFs at the inter-

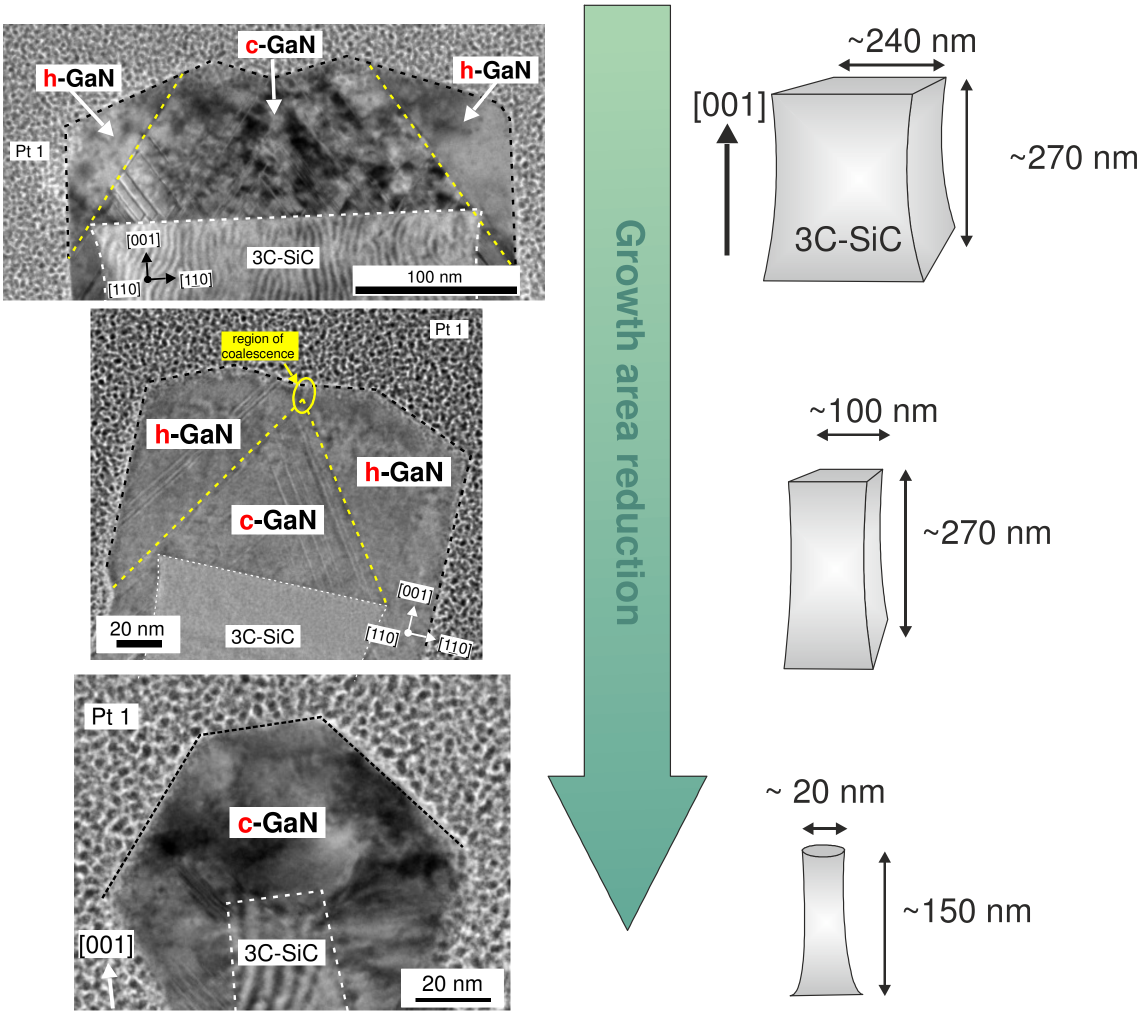

Figure 7.50

Overview about the three types of 3C-SiC (001) posts with different (001) growth area sizes. On the right side the uncovered SiC structures with assumed shapes are drawn schematically. On the left side TEM images along the [110] direction of the correspondig overgrown 3C-SiC (001) structures are depicted. The growth area length is reduced from ~240 nm to approximately 20 nm.

face. Within a length of ~30 nm five SFs appear at the c-GaN/3C-SiC (001) interface. But nonetheless, at the edges hexagonal regions occur and coalesce at a [001] film thickness of ~80 nm. However, on top of the post with approximately 20 nm (001) top edge length exculsively the cubic phase grows epitaxially without the formation of hexagonal flanks and almost no planar defects. The reason why the formation of hexagonal flanks is not obvious is maybe due to the form of the SiC nanostructure. The influence of the SiC (001) growth area form, e.g. square shaped or nearly round, on the facet formation of the growing c-GaN film should be investigated more in detail.

In general, these experimental results confirm the theoretical calculations according to the theory of NHE in subsection 2.7.2. The calculations predict that on 3C-SiC structures with a height of ~270 nm and a diameter of ~240 nm defects should nucleate as proved by the TEM images of the center of the posts. However, the c-GaN should nucleate defect-free on structures with a further reduced diameter of ~100 nm, but TEM images show individual planar defects in the c-GaN grown on the (001) growth area of the nanostructures. Finally, the NHE calculations predict that on the smallest nano-islands, with ~150 nm height and a diameter of ~20 nm, no dislocation formation should occur. The high-resolution TEM images in subsection 7.4.3 verify these theoretical calculations. Although there are differences between the calculations and the experiment. For example, in the experiment the GaN film grows on the hole SiC structure and not selectively on top as assumed by the theory of NHE. However, this structural improvement demonstrates the potential of reduced area growth for defect reduced/free c-GaN.

8 Summary and Outlook

In this work c-GaN films grown on pre-patterned 3C-SiC/Si (001) substrates by means of MBE are analyzed. The experimental results can be divided into two sections: Firstly, the influence of the substrate morphology on c-GaN grown on planar and on pre-patterned 3C-SiC/Si (001) substrates is investigated. Secondly, the influence of growth area reduction towards length scales predicted to be effective for defect reduction by the theory of nanoheteroepitaxy (NHE) is demonstrated.

In the first part the existence of anti-phase domains (APD) in c-GaN grown on planar and on pre-patterned 3C-SiC/Si (001) substrates has been revealed. SEM and AFM images show two sets of domains with grains elongated either parallel to the [110] or [1$\underline{1}$0] direction in the planar c-GaN films. The origin of the domains is found in the 3C-SiC/Si (001) substrate, which itself contains APDs generated during the nucleation of 3C-SiC on Si (001). The GaN nucleation is governed by the APDs of the substrate, which are transferred into the GaN film independently of the GaN film thickness. However, in contrast to 3C-SiC, a large variation in the GaN phase composition and the density of planar defects, like {111} SFs, for the two types of APDs is demonstrated by independent measurement methods. This is in particular shown in GaN films grown on 3C-SiC/Si substrates which are pre-patterned by nanosphere lithography followed by a lift-off and a RIE process. It is revealed that nano-patterning of the substrate does not influence the formation of domains in the c-GaN film. Here, the two sets of domains in the overgrown GaN have a largely differing amount of hexagonal inclusions and planar defects.

Stacking faults on the {111} planeslower not only the structural crystal quality but also reduce the luminescence intensity in planar c-GaN layers and c-GaN/AlN MQWs as highlighted by STEM-CL measurements. A reduction of the SF density with increasing film thickness through annihilation processes is demonstrated resulting in an increased CL emission intensity towards the film surface. This correlation could be connected to the reduction of the FWHM of the (002) rocking curves of HRXRD measurements with increasing c-GaN film thickness.

In order to investigate the influence of growth area reduction 3C-SiC mesa structures with varying (001) top edge lengths from ~500 nm down to ~20 nm are analyzed in the second part. The post shaped mesa structures are aligned parallel and perpendicular to the [110] directions of the substrate and were fabricated using electron beam lithography followed by a lift-off and a RIE process. These nanostructures were overgrown with c-GaN by means of MBE. Extensive TEM invetigations demonstrate that, regardless of the pattern size and symmetry, the cubic phase nucleates epitaxially on top of all analyzed 3C-SiC structures. The influence of growth area reduction is indicated by a drastical reduction of the SF density on top of the mesa structures with decreasing (001) growth area dimensions. While on top of the larger SiC posts with top edge lengths of ~500 nm and ~240 nm planar defects occur in bunches, only individual SFs at the c-GaN/SiC interface can be counted on top of the ~100 nm wide posts and almost defect-free c-GaN grows on top of the nanostructures with a top edge length of ~20 nm. At the top edges of the larger posts (~500- ~100 nm SiC top edge length) h-GaN flanks are formed. These hexagonal flanks can coalesce, as seen on top of the posts with ~100 nm top edge length. Similar formation of hexagonal flanks can also be seen in a complex c-AlN/GaN MQW layer structure which has been realized on larger SiC structures with top edge lengths of ~500 nm. The MQW film does not grow conformally around the (nearly) 90° SiC edges along [110] directions, but forms {111} facets which promote the formation of hexagonal inclusions in both, the c-GaN and the c-AlN films. Within the c-MQW film {111} SFs occur and continue through the entire layer stack and generate regions with a locally reduced growth rate. This leads to an undulated shape of the MQW film on top of the SiC post.

If the growth area is further scaled down to approximately 20 nm top edge length a significantly change in the c-GaN growth characteristics is observed. The cubic phase grows almost without planar defects and the formation of hexagonal flanks on the top sides cannot be observed. This structural improvement gives the evidence that growth area reduction significantly influences the growth of c-GaN as predicted by theoretical calculations according to the theory of NHE.

These results show that the heteroepitaxy of non-polar c-GaN on pre-patterned substrates is possible and that it bears the potential to be a powerful method for improving the structural quality of cubic nitrides.

Outlook

At the very end of this thesis I would like to provide a brief outlook concerning open questions and further conceivable experiments. Firstly, the influence of the pattern symmetry on the c-GaN growth on top of the structures should be investigated more in detail. Therefore, free-standing post shaped structures orientated e.g. parallel to the [001] direction should be fabricated as well as round structures. Secondly, growth series with increasing layer thickness starting with 2-3 monolayers would be useful to understand the nucleation process on such mesa structures especially around the mesa edges. Furthermore, the influence of the GaN grown at the post´s sidewalls on the layer on top and around the SiC post top edges ought to be in focus of further research. The GaN nucleation on the sidewalls could be prevented by a selectively growth on top of the posts. This would involve a protecting layer on the sidewalls where the GaN nucleation will be suppressed. Such an experiment would also lead to an experimental situation closer to the theoretical assumptions of NHE. Another idea towards NHE and towards extensively high-quality c-GaN films is the realization of coalesced thin films. Therefore, the distances between the SiC structures should be sufficiently small to ensure a coalescence of the individual islands within a low film thickness. However, in all these conceivable experiments the influence of the domains originating from the substrate should be taken into consideration. Up to now it is unclear how these domains affect the defect formation on top of the nanostructures. This question would likely not be posed, if the domain formation itself will be suppressed. One possible way to eliminate the two types of domains is the growth of 3C-SiC on tilted Si (001) substrates. Those substrates should be more appropriate for an improved c-GaN growth.

9 Appendix

Appendix A: Elastic Moduli of Cubic Crystals

(after Ref. [32])

- **Hooke´s Law**:

$$\vec{\sigma} = C \cdot \vec{\varepsilon}$$

  or

$$\begin{bmatrix} \sigma_{xx} \\ \sigma_{yy} \\ \sigma_{zz} \\ \sigma_{yz} \\ \sigma_{zx} \\ \sigma_{xy} \end{bmatrix} = \begin{bmatrix} C_{11} & C_{12} & C_{12} & 0 & 0 & 0 \\ C_{12} & C_{11} & C_{12} & 0 & 0 & 0 \\ C_{12} & C_{12} & C_{11} & 0 & 0 & 0 \\ 0 & 0 & 0 & C_{44} & 0 & 0 \\ 0 & 0 & 0 & 0 & C_{44} & 0 \\ 0 & 0 & 0 & 0 & 0 & C_{44} \end{bmatrix} \begin{bmatrix} \varepsilon_{xx} \\ \varepsilon_{yy} \\ \varepsilon_{zz} \\ \varepsilon_{yz} \\ \varepsilon_{zx} \\ \varepsilon_{xy} \end{bmatrix} \tag{42}$$

- The **shear modulus G** is defined as the shear stress to shear strain:

$$G = (C_{11} - C_{12})/2 \tag{43}$$

- The **Young´s modulusY** is defined as the ratio of stress and strain:

$$Y = \frac{(C_{11} + 2C_{12})(C_{11} - C_{12})}{(C_{11} + C_{12})} \tag{44}$$

- The **Poisson ratio ν** is definded as the transverse contraction to the longitudinal extension for a uniaxial tensile stress in the longitudinal direction:

$$\nu = \frac{C_{12}}{(C_{11} + C_{12})} \tag{45}$$

- The **biaxial modulus Y_B**, commonly used in mismatched heteroepitaxy in the case of biaxial stress:

$$Y_B = C_{11} + C_{12} - \frac{2C^2{}_{12}}{C_{11}} = \frac{Y}{1 - \nu} \tag{46}$$

- The **biaxial relaxation constant R_B** is analogous to the Poisson ratio but in the case of biaxial stress, so it is the ratio of in-plane strain to the out-of plane-strain:

$$R_B = \frac{2C_{12}}{C_{11}} \tag{47}$$

Appendix B: Theory of Nanoheteroepitaxy (NHE)

NHE on a Compliant Substrate (Model of Zubia and Hersee)

The NHE model of Zubia and Hersee [5] is an extension of the work of Luryi and Suhir [61]. Firstly, they integrated a strain partitioning in compliant substrates with no patterning of the substrate. Therefore, a fraction of the mismatch strain can now move into the substrate resulting in a reduced strain in the deposited layer. This leads to a different compliance factor *K* compared to the model of Luryi and Suhir. After this modification the authors included the substrate island patterning and found an expression for the total strain energy in the case of NHE.

Primarily, Zubia and Hersee assume that in a coherent surface, the total lattice mismatch strain ε_T is

$$\varepsilon_T = 2 \cdot \left| \frac{a_{epi} - a_{sub}}{a_{epi} + a_{sub}} \right| , \tag{48}$$

where a_{epi} and a_{sub} are the equilibrium lattice parameters of the epilayer and the substrate. Equation (48) must be equal to the sum of the strains in the deposit and in the substrate:

$$\varepsilon_T = \varepsilon_{epi} + \varepsilon_{sub} \quad , \tag{49}$$

where ε_{epi} and ε_{sub} are the partioned in-plane strains in the deposit and in the substrate, respectively. For cubic $\{100\}$ interfaces, the isotropic elastic constants are assumed to have equal biaxial stresses $\sigma_{11} = \sigma_{22} = \sigma$ and strains $\varepsilon_{11} = \varepsilon_{22} = \varepsilon$ with zero shear stresses and strains. The static equilibrium in the structure dictates that the net force at a point at the interface must be zero:

$$\sigma_{epi} h_{epi} + \sigma_{sub} h_{sub} = 0 , \tag{50}$$

where σ_{epi} and σ_{sub} are the in-plane stresses and h_{epi} and h_{sub} are the layer thicknesses of the epilayer and the substrate, respectively.

Together with the in-plane strain-stress relationship

$$\sigma = \frac{Y}{1-\nu} \varepsilon \tag{51}$$

it can be shown that:

$$\sigma_{epi} = \frac{Y_{epi}}{1-\nu_{epi}} \varepsilon_{epi} \quad \text{and} \quad \sigma_{sub} = \frac{Y_{sub}}{1-\nu_{sub}} \varepsilon_{sub} , \qquad (52), (53)$$

where Y_{epi} and Y_{sub} are the Young´s moduli and ν_{epi} and ν_{sub} are the Poisson ratios of the epilayer and the substrate, respectively.

Combining Eqs. (52), (53) and (49) expressions for the strains in the film and the substrate can be found. The authors predict the dependence of the strains on the thickness ratio h_{epi}/h_{sub}:

$$\varepsilon_{epi} = \frac{\varepsilon_T}{1+\left(K\dfrac{h_{epi}}{h_{sub}}\right)} \quad \text{and} \quad \varepsilon_{sub} = \frac{\varepsilon_T}{1+\left(\dfrac{1}{K}\dfrac{h_{sub}}{h_{epi}}\right)}, \qquad (54), (55)$$

where the parameter *K* is given by

$$K = \frac{Y_{epi}}{(1-\nu_{epi})}\frac{(1-\nu_{sub})}{Y_{sub}}. \qquad (56)$$

Now, the authors follow an approach of the model of Luryi and Suhir considering substrate compliancy by expressing the stresses in the film and the substrate:

$$\sigma_{epi}(y,z) = \frac{Y_{epi}}{1-\nu_{epi}}\varepsilon_{epi,0}\chi(y,z)\exp\left(-\frac{\pi z}{2l}\right), \qquad (57)$$

$$\sigma_{sub}(y,z) = \frac{Y_{sub}}{1-\nu_{sub}}\varepsilon_{epi,0}\chi(y,z)\exp\left(-\frac{\pi z}{2l}\right), \qquad (58)$$

where $\varepsilon_{epi,0}$ and $\varepsilon_{sub,0}$ are the partioned film and substrate strains at the interface. Now, static equilibrium conditions are adopted assuming that the lateral stress distribution is highly uniform up to close to the edges of the structures where the stress quickly drops to zero. This was also calculated by Luryi and Suhir before:

$$\int_0^{h_{epi}} \sigma_{epi}(z)\,dz = \int_{-h_{sub}}^{0} \sigma_{sub}(z)\,dz = 0. \qquad (59)$$

This yields in the interfacial (in-plane) partitioned strains in the island:

$$\varepsilon_{epi,0} = \frac{\varepsilon_T}{1+\left(K\dfrac{(1-\exp(-\pi h_{epi}/2l))}{(1-\exp(-\pi h_{sub}/2l))}\right)}, \quad \varepsilon_{sub,0} = \frac{\varepsilon_T}{1+\left(\dfrac{1}{K}\dfrac{\left(1-\exp\left(-\pi h_{sub}/2l\right)\right)}{\left(1-\exp\left(-\pi h_{sepi}/2l\right)\right)}\right)}. \qquad (60), (61)$$

According to Luryi and Suhir the strain energy density per unit volume can then be expressed by

$$\omega(y,z) = \frac{1-\nu}{Y}\sigma(y,z)^2 \ . \tag{62}$$

With this relation the areal strain energy in the system can be described as the sum of the individual strain energies in the film and in the substrate:

$$E(y) = \int_0^{h_{epi}} \omega_{epi}(y,z)\,dz + \int_{-h_{sub}}^{0} \omega_{sub}(y,z)\,dz. \tag{63}$$

The integration over these terms results in the maximum strain energy density in the film and in the substrate:

$$E_{epi} = \frac{Y_{epi}}{1-\nu_{epi}}\varepsilon_{epi,0}^2\left[1-\sec\mathrm{h}\left(k_{epi}l\right)\right]^2 \cdot \frac{l}{\pi}\left[1-\exp\left(-\pi h_{epi}/l\right)\right] \tag{64}$$

$$E_{sub} = \frac{Y_{sub}}{1-\nu_{sub}}\varepsilon_{sub,0}^2\left[1-\sec\mathrm{h}\left(k_{sub}l\right)\right]^2 \cdot \frac{l}{\pi}\left[1-\exp\left(-\pi h_{sub}/l\right)\right] \ . \tag{65}$$

Now, the authors proceed like Luryi and Suhir by comparing Eqs. (64) and (65) with the strain energy *E* for a planar grown epilayer on a conventional substrate:

$$E = \frac{Y}{1-\nu}\varepsilon^2 h \ . \tag{66}$$

This comparison leads to the definition of the effective layer thickness (similar expression for the substrate)

$$h_{epi}^{eff} = \left[1-\sec\mathrm{h}\left(k_{epi}l\right)\right]^2 \cdot \frac{l}{\pi}\left[1-\exp\left(-\pi h_{epi}/l\right)\right] \ . \tag{67}$$

With this definition Eqs. (64) and (65) can be written into the final expressions for the areal strain energy density of the film and the substrate, respectively:

$$E_{epi} = \frac{Y_{epi}}{1-\nu_{epi}}\varepsilon_{epi,0}^2 h_{epi}^{eff} \quad , \quad E_{sub} = \frac{Y_{sub}}{1-\nu_{esub}}\varepsilon_{sub,0}^2 h_{sub}^{eff} . \qquad (68), (69)$$

In summary, the areal strain energies of a conventional planar epilayer, a planar compliant substrate and of a patterned structure can be compared:

$$E_{CONVENTION\ AL} = \frac{Y}{1-\nu}\varepsilon_T^2 h_{epi} \tag{70}$$

$$E_{\mathrm{COMPLIANT}} = \frac{Y_{\mathrm{epi}}}{1-\nu_{\mathrm{epi}}}\varepsilon_{\mathrm{epi}}^{2} h_{\mathrm{epi}} + \frac{Y_{\mathrm{sub}}}{1-\nu_{\mathrm{sub}}}\varepsilon_{\mathrm{sub}}^{2} h_{\mathrm{sub}} \tag{71}$$

$$E_{\mathrm{NHE}} = \frac{Y_{\mathrm{epi}}}{1-\nu_{\mathrm{epi}}}\varepsilon_{\mathrm{epi},0}^{2} h_{\mathrm{epi}}^{\mathrm{eff}} + \frac{Y_{\mathrm{sub}}}{1-\nu_{\mathrm{esub}}}\varepsilon_{\mathrm{sub},0}^{2} h_{\mathrm{sub}}^{\mathrm{eff}} \tag{72}$$

There are several approximations given in [63] which can be applied to Eq. (72):

$$\varepsilon_{\mathrm{epi},0} = \varepsilon_{\mathrm{sub},0} = \frac{\varepsilon_{\mathrm{T}}}{2} \text{ and} \tag{73}$$

$$h_{\mathrm{epi}}^{\mathrm{eff}} = h_{\mathrm{sub}}^{\mathrm{eff}} = \frac{l}{\pi}. \tag{74}$$

This results in a simplified term of the total areal strain energy in the case of NHE:

$$E_{\mathrm{NHE}} = \left(\frac{Y}{1-\nu}\right)\varepsilon_{\mathrm{T}}^{2}\frac{l}{2\pi}. \tag{75}$$

This shows that the strain energy is finite and proportional to the island radius *l*.

Appendix C: List of Symbols

Symbol	**Description**
[..]	Real space: particular direction;
{..}	Real space: general plane;
(..)	Real space: particular plane;
<..>	Real space: general direction;
a	Lattice constant
A	Amplitude
$\alpha(T)$	Thermal expansion coefficient
(A^0,X), (D^0,X)	Bound exciton transitions
b	Burgers vector
C_{ij}	Elastic stiffness constants
C	Compliance matrix of elastic stiffness constants
d_{hkl}	Spacing of the lattice planes
D_{SF}	Stacking fault density
δ	Lattice relaxation
(D^0,A^0)	Donor to acceptor transition
(D^0,h), (e,A^0)	Free to bound transitions
E_C	Conduction band
$E_{D,line}$	Total strain energy per unit length of an edge dialocation
E_g	Energy gap
E_V	Valence band
E_ε	Total strain energy
ε_T	Total lattice mismatch strain
(e,h)	Intrinsic band to band transition
$\varepsilon_{\parallel}$	In-plane strain
f	Lattice mismatch
(FX)	Free exciton
$F(\theta)$	Structure factor
G	Shear modulus
$\vec{g}$	Reciprocal lattice vector
h	Epilayer thickness
h_e	Effective range for stress distribution
h^{eff}	Effective layer thickness
h_c	Critical layer thickness
h_c^l	Critical layer thickness for an island of radius l
(hkl)	Miller indices
k	Interfacial compliance parameter in the model of Luryi and Suhir
$\vec{k}$	Wave vector
$2l$	Island diameter
N	Number of atoms
N_{Disl}	Dislocation density
$q_{\perp}$, $q_{\parallel}$	Diffraction vector coordinates

Symbol	**Description**
R	Distance between the dislocation and the nearest free surface
R_B	Biaxial relaxation constant
r_0	Dislocation core radius
θ	Incident angle
λ	Wavelength
S	Sticking coefficient
$\sigma_{\parallel}$	In-plane stress
$\sigma_{\perp}$	Out-of-plane stress
T_S	Substrate temperature
ν	Poisson ratio
$\chi(y, z)$	Lateral stress distribution
Y	Young modulus

Appendix D: List of Abbreviations

Abbreviation	**Description**
ADF	Annular Dark Field
APD	Anti-phase Domain
AFM	Atomic Force Microscope/Microscopy
BEP	Beam Equivalent Pressure
BF	Bright Field
BOE	Buffered Oxide Etching
c-AlN	Cubic AlN
c-AlN/GaN MQW	Cubic AlN/GaN Multi-Quantum Well
c-GaN	Cubic GaN
CL	Cathodoluminescence
CCD	Charge-Coupled Device
CLWI	Cathodoluminecence Wavelength Image
DI-water	Deionized-water
DF	Dark Field
DP	Diffraction Pattern
EBL	Electron Beam Lithography
EBSD	Electron Backscatter Diffraction
ECR	Electron Cyclotron Resonance
ELO	Epitaxial Lateral Overgrowth
fcc	Face Centered Cubic
FFT	Fast Fourier Transformation
FIB	Focused-Ion Beam
FWHM	Full Width at Half Maximum
HAADF	High-angle annular Dark Field
h-GaN	Hexagonal GaN
HRXRD	High-Resolution X-Ray Diffraction
HRTEM	High-Resolution Transmission Electron Microscopy
IDB	Inversion Domain Boundary
LO	Longitudinal Optical
MBE	Molecular Beam Epitaxy
ML	Monolayer
MOCVD	Metall Organic Chemical Vapor Deposition
MQW	Multi-Quantum Well
NHE	Nanoheteroepitaxy
NSL	Nanosphere Lithography
PECVD	Plasma Enhanced Chemical Vapour Deposition
PL	Photoluminescence
PS	Polystyrene Sphere
µ-PL	Micro-Photoluminescence
µ-Raman	Micro-Raman
rf	Radio Frequency

RHEED	Reflection High Energy Electron Diffraction
RIE	Reactive Ion Etching
rms	Root Mean Square
RSM	Reciprocal Space Map
RT	Room Temperature
SAD	Selected Area Diffraction
SEM	Scanning Electron Microscope/Microscopy
SF	Stacking Fault
STEM	Scanning Transmission Electron Microscope/Microscopy
TEM	Transmission Electron Microscope/Microscopy
TO	Transversal Optical
UHV	Ultra-High Vacuum

Appendix E: List of Samples

Sample No.	Date of Growth	Substrate	Substrate Pattern Patterning Technique	 Place of Patterning	Layer
2095	30.11.10	NOVASiC Unipad 10-03	-	-	10 nm c-AlN/c-GaN QDs
2096	30.11.10	NOVASiC Unipad 10-03	-	-	10 nm c-AlN/c-GaN QDs
2097	30.11.10	NOVASiC Unipad 10-03	-	-	10 nm c-AlN/c-GaN QDs/40 nm c-AlN Caplayer
2098	30.11.10	NOVASiC Unipad 10-03	NSL	Paderborn	10 nm c-AlN/c-GaN QDs
2099	30.11.10	NOVASiC Unipad 10-03	NSL	Paderborn	c-GaN QDs
2100	01.12.10	NOVASiC Unipad 10-03	-	-	450 nm c-GaN
2101	02.12.10	NOVASiC Unipad 10-03	NSL	Paderborn	440 nm c-GaN
2102	03.12.10	NOVASiC Unipad 10-03	NSL	Paderborn	110 nm c-GaN
2103	06-07.12.10	NOVASiC Unipad 10-03	NSL	Paderborn	1450 nm c-GaN
2104	08-09.12.10	NOVASiC Unipad 10-03	-	-	1735 nm c-GaN
2151	13.06.11	NOVASiC Unipad 10-03	-	-	440 nm c-GaN
2152	14.06.11	NOVASiC Unipad 09-02	EBL	Ilmenau	370 nm c-GaN
2153	16.06.11	NOVASiC Unipad 09-02	EBL	Ilmenau	195 nm c-GaN
2154	17.06.11	NOVASiC Unipad 09-02	-	-	320 nm c-GaN

2155	20.06.11	NOVASiC Unipad 09-02	-	-	200 nm c-GaN
2156	21.06.11	NOVASiC Unipad 09-02	EBL	Ilmenau	100 nm c-GaN
2157	22.06.11	NOVASiC Unipad 09-02	-	-	100 nm c-GaN
2280	10.04.12	NOVASiC Unipad 09-02	-	-	400 nm c-GaN
2281	11.04.12	NOVASiC Unipad 09-02	EBL	Ilmenau	400 nm c-GaN
2282	11.04.12	NOVASiC Unipad 09-02	-	-	10 periods: 2.2 nm c-AlN 4-5 nm c-GaN QW plus 2.2 nm c-AlN caplayer
2283	12.04.12	NOVASiC Unipad 09-02	-	-	10 periods: 2.2 nm c-AlN 4-5 nm c-GaN QW plus 2.2 nm c-AlN caplayer
2284	12.04.12	NOVASiC Unipad 09-02	EBL	Ilmenau	10 periods: 2.2 nm c-AlN 4-5 nm c-GaN QW plus 2.2 nm c-AlN caplayer
2293	20.08.12	NOVASiC Unipad 10-03	-	-	765 nm c-GaN
2294	21.08.12	NOVASiC Unipad 10-03	EBL	Paderborn	765 nm c-GaN
2295	03.09.12	NOVASiC Unipad 10-03	-	-	150 nm c-GaN
2296	04.09.12	NOVASiC Unipad 10-03	EBL	Paderborn	150 nm c-GaN
2297	05.09.12	NOVASiC Unipad 10-03	-	-	75 nm c-GaN

2298	06.09.12	NovaSic Unipad 10-03	EBL	Paderborn	75 nm c-GaN

Bibliography

1 Introduction

[1] S. Nakamura, I. Mukai, and M. Senok, *Candelaclass high brightness InGaN/AlGaN double heterostructure bluelight emitting diodes*, Appl. Phys. Lett. **64**, 1687 (1994).

[2] S. Rajan, P. Waltereit, C. Poblenz, S.J. Heikman, D.S. Green, J.S. Speck and U.K. Mishra, *Power Performance of AlGaN–GaN HEMTs Grown on SiC by Plasma-Assisted MBE*, IEEE Electron Device Lett. **25**, 247 (2004).

[3] E. Tschumak, R. Granzer, J.K.N. Lindner, F. Schweiz, K. Lischka, H. Nagasawa, M. Abe, and D.J. As, *Nonpolar cubic AlGaN/GaN heterojunction field-effect transistor on Ar+implanted 3C–SiC (001)*, Appl. Phys. Lett. **96**, 253501 (2010).

[4] E.A. Fitzgerald, G.P. Watson, R.E. Proano, and D.G Ast, *Nucleation mechanisms and the elimination of misfit dislocations at mismatched interfaces by reduction in growth area*, J. Appl. Phys. **65**, 2220 (1989).

[5] D. Zubia and S.D. Hersee, *Nanoheteroepitaxy: The Application of nanostructuring and substrate compliance to the heteroepitaxy of mismatched semiconductor materials,* J. Appl. Phys. **85**, 6492 (1999).

[6] F. Bernardini, V. Fiorentini and D. Vanderbilt, *Spontaneous polarization and piezoelectric constants of III-V nitrides*, Phys. Rev.B **56**R10 024 (1997).

[7] O. Ambacher, J. Majewski, C. Miskys, A. Link, M. Hermann, M. Eickhoff, M. Stutzmann, F. Bernardini, V. Fiorentini, V. Tilak, B. Schaffand L.F. Eastman, *Pyroelectric properties of Al(In)GaN/GaN hetero- andquantum well structures*,J. Phys. Condens. Matter **14**, 3399 (2002).

[8] P. Waltereit, O. Brandt, A. Trampert, H.T. Grahn, J. Menninger, M. Reiche, K.H. Ploog, *Nitride semiconductors free of electrostatic fields for efficient white light-emitting diodes*, Nature **406**, 865 (2000).

[9] J. Schörmann, S. Potthast, D.J. As and K. Lischka, *In situ growth regime characterization of cubic GaN using reflection high energy electron diffraction*, Appl. Phys. Lett. **90**, 041918 (2009).

[10] S.V. Novikov, N.M. Stanton, R.P. Campion, C.T. Foxon, and A.J. Kent, *Free-standing zinc-blende (cubic) GaN layers and substrates*, J. Crystal Growth **310**, 3964 (2008).

[11] P. Gay, P.B. Hirsch, and A. Kelly, *The estimation of dislocation densities in metals from X-ray data*, ActaMetallurgica**1**, 315 (1953).

[12] E.A. DeCuir, Jr., M.O. Manasreh, E. Tschumak, J. Schörmann, D.J. As, and K. Lischka, *Cubic GaN/AlN multiple quantum well photodetector*, Appl. Phys. Lett. **92**, 201910 (2008).

[13] R.M. Kemper, T. Schupp, M. Häberlen, T. Niendorf, H.-J. Maier, A. Dempewolf, F. Bertram, J. Christen, R. Kirste, A. Hoffmann, J.K.N. Lindner, and D.J. As, *Anti-phase domains in cubic GaN*, J. Appl. Phys. **110**, 123512 (2011).

[14] R.M. Kemper, M. Häberlen, T. Schupp, M. Weinl, M. Bürger, M. Ruth, C. Meier, T. Niendorf, H.J. Maier, K. Lischka, D.J. As and J.K.N. Lindner, *Formation of defects in cubic GaN grown on nano-patterned 3C-SiC (001)*, phys. stat. sol. (c) **9** (3-4), 1028 (2012).

[15] R.M. Kemper, L. Hiller, T. Stauden, J. Pezoldt, K. Duschik, T. Niendorf, H.J. Maier, D. Meertens, K. Tillmann, D.J. As and J.K.N. Lindner, *Growth of cubic GaN on 3C-SiC/Si (001) nanostructures*, Journal of Crystal Growth **378**, 291 (2013).

[16] R.M. Kemper, C. Mietze, L. Hiller, T. Stauden, J. Pezoldt, D. Meertens, M. Luysberg, D.J. As, and J.K.N. Lindner, *Cubic GaN/AlN multi-quantum wells grown on pre-patterned 3C-SiC/Si (001),* phys. stat. sol. (c)**11** (2), 265 (2014).

2.1 Properties of Cubic III-Nitrides

[17] P.A. Stadelmann, *EMS – A Software package for electron diffraction analysis and HREM image simulation in materials schience*, Ultramicroscopy **21** (2), 131 (1987).

[18] D. Hull and D. J. Bacon, *Introduction to Dislocations*, Elvesier Ltd., 5th Edition (2011).

[19] J.H. Edgar,*Properties of Group III Nitrides,*INSPEC, London (1994).

[20] M. Röppischer, C. Cobet, N. Esser, J. Schörmann, T. Schupp, D.J. As, F. Hörich, J. Bläsing, A. Krost, and R. Goldhahn, *Optical properties of cubic GaN from 1 to 20 eV*, Phys. Rev. B **85**, 155207 (2012).

[21] M.E. Sherwin and T.J. Drummond, *Predicted elastic constants and critical layer thicknesses for cubic phase AlN, GaN, and InN on β-SiC*, J. Appl. Phys.**69**(12), 8423(1991).

[22] M. Röppischer, R. Goldhahn, G. Rossbach, P. Schley, C. Cobet, N. Esser, T. Schupp, K. Lischka, and D.J. As, *Dielectric function of zinc-blende AlN from 1 to 20 eV: Band gap and van Hove singularities*, J. Appl. Phys.**106**(7), 076104(2009).

2.2 Properties of 3C-SiC

[23] G.R. Fischer and P. Barnes, *Towards a unified view of polytypism in silicon carbide*, Phil. Mag. B **61**, 217 (1990).

[24] L.S. Ramsdell, *Studies on silicon carbide*, Am. Miner. **32**, 64 (1947).

[25] G.L. Harris, *Properties of Silicon Carbide*, INSPEC London(1995).

[26] M.E. Levinshtein, S.L. Rumyantsev and M.S. Shur (eds), *Properties of Advanced Semiconductor Materials GaN, AIN, InN, BN, SiC, SiGe*, John Wiley & Sons (2001).

[27] T. Chassagne, A. Leycuras, C. Balloud, P. Arcade, H. Peyre and S. Juillaguet, *Investigation of 2 inch SiC layers grown in a resistively-heated LP-CVD reactor with horizontal "hot-walls"*, Materials Science Forum Vols. **457**-**460**, 273 (2004).

[28] D.E. Aspnes and J. Ihm, *Biatomic steps on (001) silicon surfaces*, Phys. Rev. Lett. **57**, 3054 (1986).

[29] P. Pirouz, C.M. Chorey, and J.A. Powell*, Antiphase boundaries in epitaxially grown SiC*, Appl. Phys. Lett. **50**, 221 (1987).

[30] K. Korizane, *Antiphase domain structures in GaP and GaAs epitaxial layers grown on Si and Ge*, J. Cryst. Growth **38**, 249 (1977).

2.3 Principle of Molecular Beam Epitaxy (MBE)

[31] M. Herman and H. Sitter, *Molecular beam epitaxy: fundamentals and current status*, Springer Series in Materials Science **7**, Springer Berlin (1989).

2.4 Strain Relaxation in Heteroepitaxial Systems

[32] J.E. Ayers, *Heteroepitaxy of Semiconductors: Theory, Growth and Characterization*, CRC Press, Taylor&Francis Group (2007).

[33] L. Dong, J. Schnitker, R.W. Smith and D.J. Srolovitz,*Stress relaxation and misfit dislocation nucleation in the growth of misfitting films: A molecular dynamics simulation study*, J. Appl. Phys. **83** (1), 217 (1998).

[34] J.H. van der Merwe, *Crystal Interfaces. Part II. Finite Overgrowths*, J. Appl. Phys. **34**, 123 (1963).

[35] J.W. Matthews and A.E. Blakeslee, *Defects in epitaxial multilayers*, J. Cryst. Growth **27**, 118 (1974).

[36] M.E. Sherwin and T.J. Drummond, *Predicted elastic constants and critical layer thicknesses for cubic phase AlN, GaN, and InN on SiC*, J. Appl. Phys. **69**(12), 8423(1991).

[37] R. People and J.C. Bean, *Calculation of critical layer thickness versus lattice mismatch for Ge x Si1x /Si strained layer heterostructures*, Appl. Phys. Lett. **47**, 322 (1985).

2.5 MBE of Cubic GaN on Planar 3C-SiC (001)

[38] RiberInstruction Manual (608 26G 52 DOCTEPAO OCT/92), *MBE 32*, (1992).

[39] J.E. Northrup, J. Neugebauer, R.M. Feenstra, and A.R. Smith, *Structure of GaN (0001): The laterally contracted Ga bilayer model,*Phys. Rev. B **61**, 9932 (2000).

[40] G. Koblmüller, J. Brown, R. Averbeck, H. Riechert, P. Pongratz, and J.S.Speck, *Continuous evolution of Ga adlayer coverages during plasma-assisted molecular-beam epitaxy of (0001) GaN*, Appl. Phys. Lett. **86**, 041908 (2005).

[41] O. Brandt, Y.J. Sun, L. Däweritz, and K.H. Ploog, *Ga adsorption and desorption kinetics on M-plane GaN*, Phys. Rev. B **69**, 165326 (2004).

[42] D.J. As in *Optoelectronic Properties of Semiconductors and Superlattices*, in "III-Nitride Semiconductor materials: Growth"edited by M. O. Manasreh, Taylor & Francis, New York, Vol.**19**, Chap. 9, pp. 323–450 (2003).

[43] D. Schikora, M. Hankeln, D.J. As, K. Lischka, T. Litz, A. Waag, T. Buhrow, and F. Henneberger, *Epitaxial growth and optical transitions of cubic GaN films*, Phys. Rev. B **54**, 8381 (1996).

[44] G. Feuillet, H. Hamaguchi, K. Ohta, P. Hacke, H. Okumura, and S. Yoshida, *Arsenic mediated reconstructions on cubic (001) GaN*, Appl. Phys. Lett. **70**, 1025 (1997).

[45] J. Neugebauer, Z. Zywietz, M. Scheffler, J.E. Northrup, and C.G. Van der Walle, *Clean and As-Covered Zinc-Blende GaN (001) Surfaces: Novel Surface Structures and Surfactant Behavior*, Phys. Rev. Lett. **80**, 3097 (1998).

[46] G. Mula, C. Adelmann, S. Moehl, J. Oullier, and B. Daudin, *Surfactant effect of gallium during molecular-beam epitaxy of GaN on AlN (0001)*,Phys. Rev. B **64**, 195406 (2001).

[47] C. Adelmann, J. Brault, D. Jalabert, P. Gentile, H. Mariette, G. Mula, and B. Daudin, *Dynamically stable gallium surface coverages during plasma-assisted molecular-beam epitaxy of (0001) GaN*, J. Appl. Phys. **91**, 9638 (2002).

[48] A. Nagayama, H. Sawada, E. Takuma, R. Katayama, K. Onabe, H. Ichinose, Y. Shiraki, *Structural Study on Stacking Faults in GaN/GaAs (001) Heterostructures*, Inst. Phys. Conf. Ser. **170**, 749 (2002).

[49] J. Yamasaki, S. Inamoto, Y. Nomura, H. Tamaki and N. Tanaka, *Atomic structure analysis of stacking faults and misfit dislocations at 3C-SiC/Si(001) interfaces by aberration-corrected transmission electron microscopy*, J. Phys. D:Appl. Phys. **45**, 494002 (2012).

[50] J.E. Ayers, *New model for the thickness and mismatch dependencies of threading dislocation densities in mismatched heteroepitaxial layers*, J. Appl. Phys. **78**, 3724 (1995).

2.6 Extended Defects in Cubic GaN

[51] E. Martinez-Guerrero, E. Bellet-Amalric, L. Martinet, G. Feuillet, B. Daudin, H. Mariette, P. Holliger, C. Dubois, C. Bru-Chevallier, P. Aboughe Nze, T. Chassagne, G. Ferro, and Y. Monteil,*Structural properties of undoped and doped cubic GaN grown on SiC(001)*, J. Appl. Phys. **91**, 4983 (2002).

[52] A. Trampert, O. Brandt, H. Yang, and K.H. Ploog, *Direct observation of the initial nucleation and epitaxial growth of metastable cubic GaN on (001) GaAs*, Appl. Phys. Lett. **70**, 583 (1997).

[53] H. Okumura, K. Ohta, G. Feuillet, K. Balakrishnan, S. Chichibu, H. Hamaguchi, P. Hacke, S. Yoshida, *Growth and characterization of cubic GaN*, J. Cryst. Growth **178**, 113 (1997).

[54] D. Wang, Y. Hiroyama, M. Tamura, M. Ichikawa, S. Yoshida, *Initial growth of cubic GaN on Si(001) coated with a thin flat SiC buffer layer*, J. Cryst. Growth **220**, 204 (2000).

[55] M.N. Shetty, *Dislocations and Mechanical Behaviour of Materials*, Prentice-Hall of India Pvt.Ltd (2013).

[56] H. Föll, *Defects in crystals*, Hyperscript, University of Kiel, Faculty of Engineering, (http://www.tf.uni-kiel.de/matwis/amat/def_en/index.html) (2014).

2.7 Defect Engineering for Improved Epilayer Growth

[57] T.S. Zheleva, O.Nam, M.D. Bremser, and R.F. Davis, *Dislocation density reduction via lateral epitaxy in selectively grown GaN structures*, Appl. Phys. Lett.**71**, 2472 (1997).

[58] R.M. Kemper, *GaN-Epitaxie an nanostrukturierten 3C-SiC Substraten*, Masterthesis, University of Paderborn (2010).

[59] X.Y. Sun, R. Bommena, D. Burckel, A. Frauenglass, M.N. Fairchild, and S.R.J. Brueck, G.A. Garett, M. Wraback, S.D. Hersee, *Defect reduction mechanisms in the nanoheteroepitaxy of GaN on SiC*, J. Appl. Phys. **95**, 1450 (2004).

[60] S.D. Hersee, D. Zubia, X. Sun, R. Bommena, M. Fairchild, S. Zhang, D. Burckel, A. Frauenglass ,and S.R.J. Brueck, *Nanoheteroepitaxy for the Integration of Highly Mismatched Semiconductor Materials*, IEEE J. Quantum Electronics **38**(8), 1017 (2002).

2.7.1 Theory of Nanoheteroepitaxial Growth

[61] S. Luryi and E. Suhir, *New approach to the high quality epitaxial growth of*

latticemismatched materials, Appl. Phys. Lett. **49**, 140 (1986).

[62] H. Ye, P. Lu, Z. Yu,and L. Han, *Critical lateral dimension for a nanoscale-patterned heterostructure using the finite element method*, Semicond. Sci. Technol. **24**, 025029 (2009).

[63] D. Zubia, S. H. Zaidi, S. D. Hersee, and S. R. J. Brueck, *Nanoheteroepitaxy: Nanofabrication route to improved epitaxial Growth*, J. Vac. Sci. Technol. B **18** (6), 3514 (2000).

[64] G. Kozlowski, P. Zaumseil, M.A. Schubert, Y. Yamamoto, J. Bauer, J. Matejova, T. Schulli, B. Tillack, and T. Schroeder, *Compliant substrate versus plastic relaxation effects in Ge nanoheteroepitaxy on free-standing Si(001) nanopillars*,Appl. Phys. Lett. **99**, 141901 (2011).

2.7.2 Nanoheteroepitaxy of Cubic GaN on 3C-SiC (001)

[65] Z. Li and R.C. Bradt, *Thermal Expansion and Thermal Expansion Anisotropy of SiC Polytypes*, J. Am. Ceram. Soc.**70** (17), 445(1987).

[66] W.H. Moon and H.J. Hwang, *Structural and thermodynamic properties of GaN: a molecular dynamics simulation*, Phys. Lett. A **315**, 319 (2003).

[67] Database. Physical Properties of Semiconductors. h*ttp://www.ioffe.ru/SVA/NSM/Semicond/index.html.*

[68] W. Voigt, *Lehrbuch der Kristallphysik*, Teubner Verlag Leipzig (1928).

3.1 Reflection High Energy Electron Diffraction (RHEED)

[69] W. Braun, *Apllied RHEED: Reflection High-Energy Electron Diffraction during Crystal Growth*, Springer Tracts in Modern PhysicsVol. **154**, Springer Verlag Berlin Heidelberg New York (1999).

[70] D.W.J. Cruickshank, H.J. Juretschke, N. Katō (eds.), *P.P. Ewald and His Dynamical Theory of X-ray Diffraction: A Memorial Volume for Paul P. Ewald, 23 January 1888-22 August 1985*, International Union of Crystallography (1992).

[71] D. B. Williams and C. B.Carter, *Transmission Electron Microscopy; A Textbook for Materials Science*, Springer Science+Business Media, LLC, 2nd Edition (2009).

3.2 Atomic Force Microscopy (AFM)

[72] D. Johnson, N. Hilal and W.R. Bowen, *Atomic Force Microscopy in Process Engineering*, Elsevier Ltd., Chapter 1 and 2 (2009).

3.3 Photoluminescence Spectroscopy (PL)

[73] S. Perkowitz, *Optical Characterization of Semiconductors: Infrared, Raman, and Photoluminescence Spectroscopy*, Academic Press Limited (1993).

3.4 Cathodoluminescence Spectroscopy (CL)

[74] B. G. Yacobi and D.B. Holt, *Cathodoluminescence of Inorganic Materials*, Springer Science+Business Media New York (2009).

[75] J. Christen, M. Grundmann, and D. Bimberg, *Scanning cathodoluminescence microscopy: A unique approach to atomic scale characterization of heterointerfaces and imaging of semiconductor inhomogeneities*, J. Vac. Sci. Technol. B **9**, 2358 (1991).

[76] F. Bertram, T. Riemann, J. Christen, A. Kaschner, A. Hoffmann, C. Thompsen, K. Hiramatsu, T. Shibata, and N. Sawaki, *Strain relaxation and strong impurity incorporation in epitaxial laterally overgrown GaN: Direct imaging of different growth domains by cathodoluminescence microscopy and micro-Raman spectroscopy*, Appl. Phys. Lett. **74**, 359 (1999).

3.5 Micro-Raman Spectroscopy (μ-Raman)

[77] T. Ruf, *Phonon Raman Scattering in semiconductors, quantum wells and superlattices*, edited by G. Höhler, Vol. 142 of Springer Tracts in Modern Physics, Springer-Verlag Berlin (1998).

[78] W.H. Weber and R. Merlin (eds), *Raman Scattering in Materials Science*, Springer Series in Materials Science ISSN 0933-033X; 42, Springer-Verlag Berlin Heidelberg (2000).

3.6 High-Resolution X-Ray Diffraction (HRXRD)

[79] M. Birkholz, *Thin Film Analysis by X-Ray Scattering*, Wiley-VCH Verlag GmbH&Co. KGaA,Weinheim (2006).

[80] P. F. Fewster, *X-Ray Scattering from Semiconductors*, 2nd edition, Imperial College Press (2003).

[81] P. Kidd, *XRD of gallium nitride and related compounds: strain, composition and layer thickness*, The Analytical X-ray Company, ISBN: 978-90-809086-7-3(2013).

[82] X.L. Sun, Y.T. Wang, Hui Yang, J.B. Li, L.X. Zheng, D.P. Xu, Z.G. Wang, *The content calculation of hexagonal phase inclusions in cubic GaN films on GaAs(001) substrates grown by metalorganic chemical vapor deposition*,Thin Solid Films **368**, 237 (2000).

3.7 Electron Backscatter Diffraction (EBSD)

[83] L. Reimer, *Scanning Electron Microscopy*, 2nd ed. New York: Springer, pp. 368-374 (1998).

[84] A.J. Schwartz, M. Kumar, B.L. Adams, D.P. Field (eds.), *Electron Backscatter Diffraction in Materials Science*, 2nd edition Springer Science+Business Media (2009).

[85] R.O. Duda and P.E. Hart, *Use of the Hough Transformation to detect lines and curves in pictures*, Comm. ACM **15** (1), 11 (1972).

3.8 Transmission Electron Microscopy (TEM)

[86] B. Fultz and J.M. Howe,*Transmission Electron Microscopy and Diffractometry of Materials*, Third Edition, Springer-Verlag Berlin Heidelberg (2008).

[87] P.B. Hirsch, A. Howie and M. J. Whelan, *On the Production of X-rays in Thin Metal Foils*, Phil. Mag. **7**, 2095 (1962).

[88] J. Christen, F. Bertram, G. Schmidt, S. Petzold, P. Veit, R. Ravash, A. Dadgar, and A. Krost, *Cathodoluminescence Directly Performed in a Transmission Electron Microscope: Nanoscale Correlation of Structural and Optical Properties*, Microsc. Microanal. 18 (Suppl 2) (2012).

[89] R.M. Kemper, M. Weinl. C. Mietze, M. Häberlen, T. Schupp, E. Tschumak, J.K.N. Lindner, K. Lischka, D.J. As, *Growth of cubic GaN on nano-patterned 3C-SiC (001) substrates,*J. Crys. Growth **323**, 84 (2011).

4 Substrate Patterning

[90] L. Hiller. T. Stauden, R.M. Kemper, J.K.N. Lindner, D.J. As, J. Pezoldt, *ECR-Etching of Submicron and Nanometer Sized 3C-SiC (100) Mesa Structures*, Materials Science Forum Vols. **717-720**, 901 (2012).

4.1 Nanosphere Lithography

[91] C.L. Haynes and R.P. Van Duyne, *Nanosphere Lithography: A Versatile Nanofabrication Tool for Studies of Size-Dependent Nanoparticle Optics*, J. Phys. Chem. B **105** (24), 5599 (2001).

[92] G. Cicero, A. Catellani and G. Galli, *Interaction of Water Molecules with SiC(001) Surfaces*, J. Phys. Chem. B **108**, 16518 (2004).

[93] J.K.N. Lindner, C. Seider, F. Fischer, M. Weinl, B. Stritzker, *Regular surface patterns by local swelling induced by He implantation into silicon through nanosphere lithography masks*, Nuclear Instruments and Methods in Physics Research B **267**, 1394 (2009).

[94] D. Gogel, M. Weinl, J.K.N. Lindner, B. Stritzker,*Plasma modification of nanosphere lithography masks made of polystyrene beads*, J. Optoelectronics and Adv. Materials **12**, 740 (2010).

4.2 Nano-Patterning by Electron Beam Lithography

[95] M. Razeghi, *Technology of Quantum Devices*, Springer Science+Business Media, LLC, 114 (2010).

[96] Pioneer Sytem Manual, Document number 2-08-1.1, Raith GmbH (2011).

5 MBE on Pre-Patterned 3C-SiC/Si (001)

[97] J. Schörmann, S. Potthast, D. J. As, and K. Lischka, *In situ growth regime characterization of cubic GaN using reflection high energy electron diffraction*, Appl. Phys. Lett. **89**, 131910 (2006).

[98] B. Schöttker, *Molecular Beam Epitaxy and characterization of doped and undoped cubic Gan layers*, Dissertation,University of Paderborn (1999).

[99] D.J.As, *Cubic group III-nitride based nano-structures - basics and applications in optoelectronics*, Microelectronics Journal **40**, 204 (2009).

[100] E. Bauer and J. H. van der Merwe, *Structure and growth of crystalline superlattices: From monolayer to superlattice*, Phys. Rev. B **33** (6), 3657 (1986).

[101] C. Mietze, *Cubic AlN/GaN multi-quantum-wells for unipolar device applications*, Dissertation, University of Paderborn (2013).

7.1 Anti-Phase Domains in Cubic GaN

[102] R.M. Kemper, D.J. As and J.K.N. Lindner, *Cubic GaN on nano-patterned 3C-SiC/Si (001) substrates,* in "Silicon-based Nanomaterials" edt. Z.M. Wang, Springer Series in Materials Sciences **187**, chapter 15 (2013).

7.1.1 Anti-Phase Domains in Planar Cubic GaN Epilayers

[103] Y. Fu, H. Yang, D.G. Zhao, X. H. Zheng, S.F. Li, Y.P. Sun, Z.H. Feng, Y.T. Wang and L.H. Duan, *Epitaxial lateral overgrowth of cubic GaN by metalorganic chemical vapor*

deposition, J. Cryst. Growth **225**, 45 (2001).

[104] D.R. Lide, CRC Handbook of Chemistry and Physics: *A Ready-Reference Book of Chemical and Physical Data*, 90th ed, CRC Taylor & Francis, Boca Raton, Fl., pp. 9–98(2009).

[105] H. Ibach, *Physics of Surfaces and Interfaces*, Springer-Verlag Berlin Heidelberg (2006).

[106] X.H. Zheng, B. Qu, Y.T. Wang, Z.H. Feng, J.Y. Han, H. Yang, and J.W. Liang, *Investigation of {111}A and {111}B planes of c-GaN epilayers grown on GaAs(001) by MOCVD*, J. Cryst. Growth **233**, 52 (2001).

[107] H. Siegle, L. Eckey, A. Hoffmann, C. Thomson, B. K. Meyer, D. Schikora, M. Hankeln, and K. Lischka, *Quantitative determination of hexagonal minority phase in cubic GaN using raman spectroscopy*, Solid State Commun. **96** (12), 943 (1995).

[108] Z.C. Feng, C.C. Tin, R. Hu, and J. Williams, *Raman and Rutherford backscattering analyses of cubic SiC thin films grown on Si by vertical chemical vapor deposition*, Thin Solid Films **266**, 1 (1995).

[109] D.J. As, F. Schmilgus, C. Wang, B. Schöttker, D. Schikora, and K. Lischka, *The near band edge photoluminescence of cubic GaN epilayers*, Appl. Phys. Lett. **70**, 1311 (1997).

[110] D.J. As and U. Köhler, *Carbon - an alternative acceptor for cubic GaN*, J. Phys.: Condens. Matter **13**, 8923(2001).

7.2 Influence of Stacking Faults on Optical Properties of Cubic GaN Films and Cubic GaN/AlN MQWs

[111] J. Lähnemann, O. Brandt, U. Jahn, C. Pfüller, C. Roder, P. Dogan, F. Grosse, A. Belabbes, F. Bechstedt, A. Trampert, and L. Geelhaar, *Direct experimental determination of the spontaneous polarization of GaN*, Phys. Rev. B **86**, 081302(R) (2012).

[112] D. J. As, S. Potthast, U. Köhler, A. Khartchenko and K. Lischka, *Cathodoluminescence of MBE-grown cubic AlGaN/GaN multiquantum wells on GaAs (001) substrates*, MRS Symp. Proc. Vol. **743** L5.4 (2003).

[113] G. Jacopin, L. Rigutti,L. Largeau, F. Fortuna, F. Furtmayr, F.H. Julien, M. Eickhoff, and M. Tchernycheva, *Optical properties of wurtzite/zinc-blende heterostructures in GaN nanowires*, J. Appl. Phys. **110**, 064313 (2011).

[114] C. Mietze, M.Bürger, S. Sakr, M. Tchernycheva, F.H. Julien, and D.J. As, *Cubic III-nitride coupled quantum wells towards unipolar optically pumped lasers*, Phys. Stat. Sol. (a)**210** (3), 455 (2013).

7.3.2 Cubic AlN/GaN MQWs on Sub-Micrometer Structures

[115] T. Schupp, K. Lischka, and D.J. As, *MBE growth of atomically smooth non-polar cubic AlN*, J. Cryst. Growth **312**, 1500 (2010).

[116] S. Van Nguyen, D. Dobuzinsky, S.R. Stiffler, and G. Chrisman, *Substrate Trenching Mechanism during Plasma and Magnetically Enhanced Polysilicon Etching*, J. Electrochem. Soc.**138**(4), 1112 (1991).

[117] E. Kapon, *Quantum wires and quantum dots for optoelecronics: Recent advances with epitaxial growth on nonpolar substrates*, Frontiers of Nano-Optoelectronic Systems NATO Science Series Vol. **6**, pp 41-64 (2000).

[118] C.J.M. Stark, T. Detchprohm, S.C. Lee, Y.-B. Jiang, S.R.J. Brueck, and C. Wetzel, *Green Cubic GaInN/GaN light-emitting diode on microstructured silicon (100),* Appl. Phys. Lett. **103**, 232107 (2013).

[119] D.X. Xia, Z. Ku, and S.R.J. Brueck, *Nanostructures and Functional Materials Fabricated by Interferometric Lithography*, Adv. Mater. **23**, pp. 147-179 (2011).

7.4.1 3C-SiC (001) Posts with ~240 nm Top Edge Length

[120] S. Sanorpim, E. Takuma, H. Ichinose, R. Katayama, and K. Onabe, *Structural transition control of laterally overgrown c-GaN and h-GaN on stripe-patterned GaAs (001) substrates by MOVPE*, Phys. Stat. Sol. (b) **244**(6), 1769(2007).

7.4.2 3C-SiC (001) Posts with ~100 nm Top Edge Length

[121] E.Montoya, S. Bals,M.D. Rossel, D. Schryvers, G. van Tendeloo, *Evaluation of Top, Angle, and Side Cleaned FIB Samples for TEM Analysis*, Microsc. Res. and Techniques **70**, 1060 (2007).

Publication List

1. D.J. As, E. Tschumak, I. Laubenstein, **R.M. Kemper**, K. Lischka, *Schottky and ohmic contacts on non-polar cubic GaN epilayers*, MRS. Symp. Proc. **1108**, A01-02 (2009).
2. **R.M. Kemper**, M. Weinl. C. Mietze, M. Häberlen, T. Schupp, E. Tschumak, J.K.N. Lindner, K. Lischka, D.J. As, *Growth of cubic GaN on nano-patterned 3C-SiC (001) substrates,* J. Crys. Growth **323**, 84 (2011).
3. **R.M. Kemper**, T. Schupp, M. Häberlen, T. Niendorf, H.-J. Maier, A. Dempewolf, F. Bertram, J. Christen, R. Kirste, A. Hoffmann, J.K.N. Lindner, and D.J. As, *Anti-phase domains in cubic GaN*, J. Appl. Phys. **110**, 123512 (2011).
4. **R.M. Kemper**, M. Häberlen, T. Schupp, M. Weinl, M. Bürger, M. Ruth, C. Meier, T. Niendorf, H.J. Maier, K. Lischka, D.J. As and J.K.N. Lindner, *Formation of defects in cubic GaN grown on nano-patterned 3C-SiC (001)*, Phys. Stat. Sol. (c) **9** (3-4), 1028 (2012).
5. L. Hiller. T. Stauden, **R.M. Kemper**, J.K.N. Lindner, D.J. As, J. Pezoldt, *ECR-Etching of Submicron and Nanometer sized 3C-SiC (100) Mesa Structures*, Materials Science Forum Vols. **717-720**, 901 (2012).
6. J. Achtelik, **R.M. Kemper**, W. Sievers and J.K.N Lindner, *Self-organized nanostructure formation for anti-reflex glass surfaces*, MRS Online Proceedings Library Vol.**1389**, mrsf11-1389-g03-18 doi:10.1557/opl.2012.491, (2012).
7. M. Bürger, **R.M. Kemper**, C. Bader, M. Ruth, S. Declair, C. Meier, J. Förstner and D.J. As, *Cubic GaN quantum dots embedded in zinc-blende AlN microdisks*, J. Crys. Growth **378**, 287 (2013).
8. **R.M. Kemper**, L. Hiller, T. Stauden, J. Pezoldt, K. Duschik, T. Niendorf, H.J. Maier, D. Meertens, K. Tillmann, D.J. As and J.K.N. Lindner, *Growth of cubic GaN on 3C-SiC/Si (001) nanostructures*, J. Crys. Growth **378**, 291 (2013).
9. **R.M. Kemper**, C. Mietze, L. Hiller, T. Stauden, J. Pezoldt, D. Meertens, M. Luysberg, D.J. As, and J.K.N. Lindner, *Cubic GaN/AlN multi-quantum wells grown on pre-patterned 3C-SiC/Si (001),* Phys. Stat. Sol. (c)**11** (2), 265 (2014).
10. L. Hiller. T. Stauden, **R.M. Kemper**, J.K.N. Lindner, D.J. As, J. Pezoldt, *Hydrogen Effects in ECR-Etching of 3C-SiC(100) Mesa Structures*, ICSCRM 2013 (accepted) (2014).

Book Chapter

R.M. Kemper, D.J. As and J.K.N. Lindner, *Cubic GaN on nano-patterned 3C-SiC/Si (001) substrates*, Silicon-based Nanomaterials edited by Z.M. Wang, J. Wu, and H. Li, Springer Series in Materials Science **187**, chapter 15,ISBN: 978-1-4614-8168-3, (2013).

Invited Talk

Seminar “Neue Materialien-Halbleiter“, 03.12.2012, „*Cubic GaN on nano-patterned 3C-SiC/Si (001) substrates*“, Faculty of Natural Sciences, Institute of Experimental Physics (IEP), Otto-von-Guericke University Magdeburg.

Additional Contributions

1. **R.M. Kemper**, T. Riedl, L. Hiller, T. Stauden, J. Pezoldt, D. Meertens, M. Luysberg, K. Tillmann, D.J. As, and J.K.N. Lindner, *TEM investigation of GaN thin films grown on nanostructured 3C-SiC/Si(001) substrates*, European Microscopy Conf. EMC2012, Manchester (UK).
2. J.K.N. Lindner, **R.M. Kemper**, D.J. As, D. Meertens, A. Kovács and K. Tillmann, *Characterization of cubic GaN/AlN multi-quantum wells using state-of-the-art analytical STEM,* Microscopy Conf. MC2013, Regensburg (Germany).

Conference Contributions

08/2010	Oral presentation, 16th International Conference on Molecular Beam Epitaxy, Berlin (Germany)
05/2011	Oral presentation, Spring Meeting European Materials Research Society (E-MRS), Nice (France)
09/2012	Poster presentation, 17th International Conference on Molecular Beam Epitaxy, Nara (Japan)
05/2013	Oral presentation, Spring Meeting European Materials Research Society (E-MRS), Strasbourg (France)

Cooperation Partners

- FG Nanotechnology, Institute of Micro- und Nanotechnologies MacroNano®, Technical University of Ilmenau, Group of Dr. Jörg Pezoldt
- Ernst Ruska-Centre for Microscopy and Spectroscopy with Electrons, Forschungszentrum Jülich
- University of Paderborn, Lehrstuhl für Werkstoffkunde (Materials Science), Group of Prof. Dr. J.-H. Maier
- Otto-von-Guericke University Magdeburg, Institute of Experimental Physics, Group of Prof. Dr. Jürgen Christen
- Technical University Berlin, Institute of Solid State Physics, Group of Prof. Dr. Axel Hoffmann

Acknowledgements

I would like to thank all people who supported me during this research project. Moreover, my special thanks go to my supervisors

- Prof. Dr. Jörg K. N. Lindner for this fascinating subject and the opportunity to realize this work. His personal dedication and helpful discussions enabled this project.
- apl. Prof. Dr. Donat J. As for his encouragement in difficult research and also private situations. With his expertise and feedback he ensured a pleasant working atmosphere.

Furthermore, I am very grateful to all colleagues and group members without whom this dissertation would not have been possible

- Prof. Dr. Klaus Lischka for many interesting scientific discussions. He taught me to approach problems keeping a clear head!
- Prof. Dr. Dirk Reuter for his continuous interest in my work.
- Prof. Dr. Cedrik Meier for access to the electron beam lithography system.
- Dr. Maik Häberlen, who laid the foundation of this research project and who became a friend.
- My office mate M. Sc. Matthias Bürger for a pleasant work atmosphere and outstanding teamwork. Furthermore, Dr. Christian Mietze, M. Sc. Alexander Zado, Dr. Marcel Ruth, and Dipl.-Phys. Ing. Thorsten Schupp for their help with fabricating my samples, measurements and their teamwork.
- Dr. Thomas Riedl for theoretical calculations.
- PD Dr. Alexander Pawlis and Dr. Detlef Schikora for thought-provoking questions during the group meetings.
- M. Sc. Tobias Wecker, M. Sc. Katharina Brassat, M. Sc. Mefer Dogan and all members of the group meetings for their teamwork and their interest in my work.
- Irmgard Zimmermann, Anja Blank, Dipl.-Phys. Ing. Werner Sievers, Dipl.-Ing. Bernhard Volmer and Siegfried Igges for administrative and technical support.

I would like to thank all coworkers for cooperative work at the

- *Technical University of Ilmenau*
  Dipl.-Wirtsch.-Ing. Lars Hiller, Dr. Ing. Thomas Stauden and Dr. Jörg Pezoldt.
- *Ernst Ruska-Centre Jülich*
  Doris Meertens, Dr. András Kovács, Dr. Martina Luysberg and Dr. Karsten Tillmann.

- *University of Paderborn (Faculty of Mechanical Engineering)*
  Dipl.-Ing. Kristina Duschik, Dr. Thomas Niendorf and Prof. H.-J. Maier.
- *University of Magdeburg*
  Dr. habil. Frank Bertram, Dr. Peter Veit, Dipl. Phys. Sebastian Metzner, Dipl. Phys. Anja Dempewolf and Prof. Dr. Jürgen Christen.
- *Technical University of Berlin*
  Dr. Ronny Kirste and Prof. Dr. Axel Hoffmann.

In particular, I owe thanks to my friends Inga Krutmann, Marie Wiegand, Martin Rohrmüller, Alexander Leier and Kamill Eliasch for making this time easier! And last but in no way least, I would like to express my heartfelt gratitude to my parents, Ramona, my sister, and especially to Philipp for their love and encouragement, and for making everything possible.